NORTHWESTERN UNIVERSITY

Atomic-Scale Studies of Oxides Supported Catalysts by X-ray and Imaging Methods

A DISSERTATION

SUBMITTED TO THE GRADUATE SCHOOL
IN PARTIAL FULLFILLMENT OF THE REQUIREMENTS

for the degree

DOCTOR OF PHILOSOPHY

Field of Materials Science and Engineering

By

Zhenxing Feng

EVANSTON, ILLINOIS

August 2011

ABSTRACT

Atomic-Scale Studies of Oxides Supported Catalysts by X-ray and Imaging Methods

Zhenxing Feng

Oxide supported metal and metal oxide catalysts have been synthesized by molecular beam epitaxy (MBE) and atomic-layer deposition (ALD). To obtain a general idea of how a catalyst behaves chemically and structurally during reduction-oxidization (redox) reaction at atomic-scale, oxide single crystals with well-defined surfaces are used as supports to grow monolayer (ML) and sub-ML catalysts. Several model catalysis systems are investigated: $Pt/SrTiO_3(001)$, $WO_X/\alpha\text{-}Fe_2O_3(0001)$, $VO_X/\alpha\text{-}TiO_2(110)$ and mixed $VO_X/WO_X/\alpha\text{-}TiO_2(110)$. For purposes of comparison the catalysts include a noble metal (Pt), inert oxide (WO_X) and active oxide (VO_X). The oxide supports are categorized as a reducible substrate, $\alpha\text{-}Fe_2O_3(0001)$, and non-reducible substrates, $\alpha\text{-}TiO_2(110)$ and $SrTiO_3(001)$. To obtain *in situ* information, a variety of X-ray and scanning imaging methods have been applied together to study the atomic-scale surface morphology, structure and cation dynamics during chemical reactions. These characterization techniques are: X-ray standing wave (XSW), grazing-incident small angle X-ray scattering (GISAXS), X-ray absorption fine structure (XAFS), X-ray reflectivity (XRR), X-ray fluorescence (XRF), X-ray photoelectron spectroscopy (XPS), atomic-force microscopy (AFM) and scanning electron microscopy (SEM). Our studies show that different combinations of catalysts and substrates give distinct structural and chemical state changes in redox reactions.

For MBE deposited sub-monolayer (sub-ML) Pt on the 2 × 1 $SrTiO_3(001)$ surface, AFM shows the formation of nanoparticles and XSW atomic imaging shows that these nanoparticles are composed of Pt face-centered-cubic nanocrystals with cube-on-cube epitaxy coherent to the substrate unit cell. Different Pt coverages lead to differences in the observed XSW image of the interfacial structure, which is explained by the Pt-Pt interaction becoming stronger than the Pt-substrate interaction as the coverage is increased from 0.2 to 0.6 ML. For ALD grown Pt on $SrTiO_3(001)$ surface, AFM combined with SEM, XRR, reciprocal space mapping and GISAXS together show the dramatic surface morphology changes before and after UHV annealing. These thermally induced structural changes are explained by surface diffusion, and the surface/interface energies for noble metals on oxides.

For ALD deposited sub-ML $WO_X/\alpha\text{-}Fe_2O_3(0001)$ and $VO_X/\alpha\text{-}TiO_2(110)$, redox-induced surface cation dynamics were observed by a combination of *in situ* XSW, *ex situ* XPS and AFM. Direct atomic-scale images created from XSW show how W or V cation responds to redox reactions, which are further compared and explained with density functional theory calculations. Extended work on mixed catalysts $VO_X/WO_X/\alpha\text{-}TiO_2(110)$ demonstrates that a synergistic effort is developed when a proper amount of WO_X is mixed with VO_X. This effect is further explained by the W-introduced surface density of Brønsted acid sites.

Approved:

Professor Michael J. Bedzyk

Department of Materials Science and Engineering

Northwestern University

Evanston, Illinois

ACKNOWLEDGEMENT

I would like to thank my supervisor Prof. Michael Bedzyk for his support and guidance during my work at Northwestern University and Argonne National Laboratory. He taught me various X-ray techniques, generously answered my questions, and gave me great freedom on my research. I am indebted to him for his innumerable discussions on projects and his patience to edit my papers.

I thank Dr. Jeffrey Elam, Prof. Peter Stair, Prof. Mark Hersam and Prof. Chris Wolverton for serving on my thesis committee. The high quality films grown by Dr. Jeff Elam were essential for my research project. Prof. Peter Stair provided great insight into catalysis. I thank Prof. Mark Hersam and Prof. Chris Wolverton for many valuable discussions.

I thank Drs. Chang-Yong Kim, Zhan Zhang and Steven Christensen for helping me getting started with my research. I thank Drs. Jui-Ching Lin, Qing Ma, Byeongdu Lee, Xianghui Xiao, John Okasinski, and Steven Weigand for many useful instructions on my experiments and research. I especially thank Dr. Denis Keane at the DND-CAT for helping me on EPICS systems development.

I am also thankful to many past and present members of the Bedzyk research group: Dr. Alexander Kazimirov, Dr. Yuan-Chieh Tseng, Dr. Jeff Klug, Dr. Vaibhav Kohli, Curtis Leung, Jon Emery, Martin McBriarty, I-Cheng Tung, Dr. Sumit Kewalramani, Dr. Sven Stoltz and Dr. Sudeshana Chattopadhyay. I am especially grateful to those discussions about life and research with Curtis Leung and my roommate Zhaoyang Fan. I appreciate the encouragements given by my friends who also enrich my graduate life.

Finally, I would like to dedicate this dissertation to my dear parents in China. It is their encouragements and long-lasting support that helped me conquer many difficulties in life and work.

Table of Contents

LIST OF FIGURES

LIST OF TABLES

Introduction

Metal oxide monolayers or clusters anchored to an oxide support are important catalysts for hydrocarbon transformations, industrial catalytic processes[1], and gas sensors[2]. In spite of extensive efforts to define the molecular-scale structure of supported metal oxides, there is little direct, experimental information on the atomic positions of the metal cations on the support. Figure 1.1 taken from Weckhuysen and Keller[1] shows a hypothesized surface structure for vanadium oxides. However, these cartoon drawings cannot reflect the real atomic arrangements. In many cases theoretical calculations have not been performed for a surface structure that is found experimentally, but rather for some other simplified or model structure. How representative these conclusions are remains open to questions.

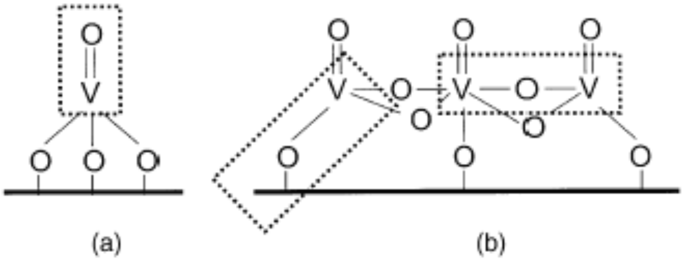

Figure 0.1 Chemical-intuition inspired schematic of three possible V–O bonds involved in the selective oxidation of methanol to formaldehyde: (a) monomeric VO_4 species and (b) polymeric VO_4 species characterized by V=O, V–O–V and V–O–support bonds. This figure is reproduced from Ref. [1].

Therefore, it is necessary to understand the atomic-scale electronic and geometric structure of a catalyst. Among all catalysts supported platinum, vanadium oxide (vanadia or VO_X) and tungsten oxide (WO_X) have received the most attention in literature. Supported vanadia, tungsten oxide and their mixed oxides have also been widely used in the manufacture of important chemicals and in the reduction of environmental pollution.[1] Typically when a catalyst is active in a chemical reaction, its catalytic performance relies on its oxidation states. For example, the existence of the 5+ oxidation state for vanadium is crucial for catalytic reactions.[3, 4] Furthermore, previous studies have shown that a catalyst exhibits greater activity as a monolayer than as a thicker film.[5] The monolayer catalysis indicates significant role of the supporting oxide substrate. Significance of reducibility of the supporting oxide has also been proposed.[6] More important, if the surface structure of these supported metal oxides could be predicted, this would have an enormous impact upon our understanding of numerous chemical processes.

Taking vanadia as an example, previous studies[7] only give a general consensus that supported vanadium oxide exists as an isolated or polymerized VO_4 unit. However studies for the positions of vanadium cations with respect to the support and its sensitivity to the oxidation-reduction cycle, at the atomic scale, are rare. Recently efforts have been made within our research group by Kim et al[8] to show atomic-scale view of redox changes to VO_X / α-$Fe_2O_3(0001)$. They show that X-ray techniques are excellent tools to study cation structural changes at the atomic scale. X-ray fluorescence (XRF) can determine the coverage of the vanadium in the sub-monolayers. X-ray photoelectron spectroscopy (XPS) can be used to trace the electronic structural changes of a supported vanadium oxide system at different stages of its oxidation-reduction cycle. X-ray standing wave (XSW), a combination of single crystal X-ray diffraction and XRF, is a powerful tool to probe the elements' 3-D positions with 0.03 Å resolution.

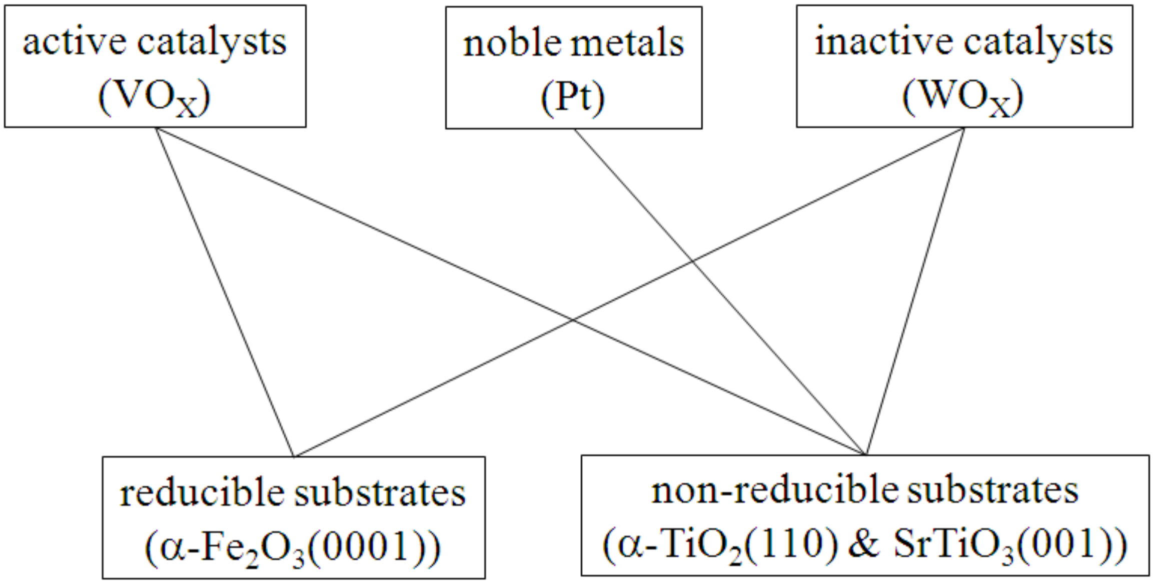

Figure 0.2 Combinations of catalysts and substrates used in this thesis

Therefore, my thesis work is to use various X-ray techniques, combined with other surface characterization tools, for *in situ* studies of the atomic structural changes of metal and metal oxides (Pt, VO_X, WO_X and their mixed oxides) supported on a single crystal ($SrTiO_3$(001), α-TiO_2(110) and α-Fe_2O_3(0001)) or powder, in redox reactions. As shown in Figure 1.2, different combinations of catalysts and substrates studied in this thesis will provide general ideas of how a catalyst performs structurally and electronically and how important the substrate is during redox reactions.

Chapter 1: Background

1.1 Substrate: Rutile (α-TiO_2)

Rutile (α-TiO_2) is a popular substrate material in surface science, especially the (110) surface, which has evolved as a model system in the surface science of metal oxides for a number of reasons. First, titanium dioxide has many applications in heterogeneous catalysis, photocatalysis in solar cells for the production of hydrogen and electric energy and in gas sensors [9]. Second, TiO_2 is a preferred system for experimentalists. It can be prepared simply by sputtering and annealing, and thus various companies and vendors provide polished crystals with a high surface quality.

TiO_2 is found as three different crystallographic structures: rutile (tetragonal, D^{14}_{4h}-$P4_2/mnm$, $a = b = 4.584$ Å, $c = 2.953$ Å[10]), anatase (tetragonal, D^{19}_{4h}-$I4_1/amd$, $a = b = 3.782$ Å, $c = 9.502$ Å [11]), and brookite (rhombohedral, D^{15}_{2h}-Pbca, $a = 5.436$ Å, $c = 5.135$ Å [12]). However, only rutile and anatase surfaces have been studied. Rutile is thermodynamically the most stable phase and the (110) face is the most intensely studied surface.[11] Figure 2.1 shows the bulk-terminated (1 × 1) surface. Along the [001] direction, rows of six-fold-coordinated Ti atoms (as in the bulk) alternate with five-fold-coordinated Ti atoms with one ‘dangling bond’ perpendicular to the surface. Oxygens within the main surface plane are three-fold-coordinated as in the bulk.[1] The so-called bridging oxygen atoms are two-fold-coordinated.[9]

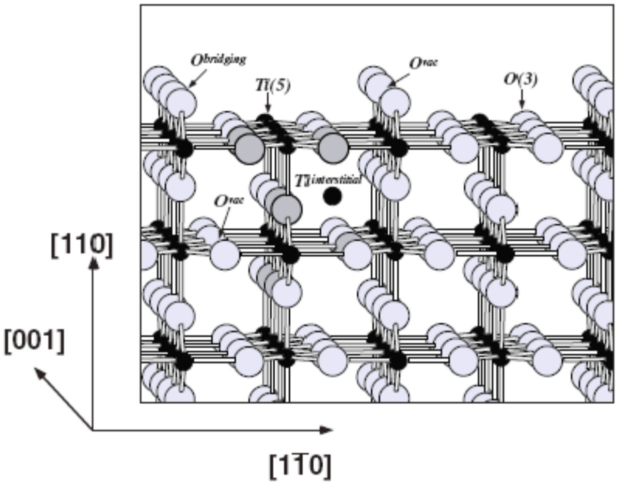

Figure 1.1 Ball-and-stick model of the rutile TiO_2 (110)-(1×1) surface. Large light balls, oxygen; small black balls, titanium. The two types of bulk defects that are prevalent in reduced TiO_2 crystals, i.e. oxygen vacancies and titanium interstitials, are also indicated. Such bulk defects can often affect surface chemistry. This figure is reproduced from Ref. [9].

For the surface of TiO_2, different treatments (annealing in vacuum vs. annealing in oxygen) can result in different surface structures, such as two different (1 × 2) reconstructions, a 'rosette' overlayer, and crystallographic shear planes. Annealing in UHV or in oxygen at elevated temperature can both lead to a terrace structure.[11] In our surface treatment, we anneal the substrate at 400 ^{o}C first to burn away contamination like carbon, then anneal at 900^{o}C to form a terrace structure. These will be further discussed in Chapter 2.4.

The typical Rutile (110) surface, as shown in Figure 2.2, has three possible terminating planes in theory. Termination #1 has both a surface oxygen bonded to two Ti atoms (named bridging oxygen or BO) and an oxygen singly bonded to the surface (named terminal oxygen or TO) present on the surface. Termination #2 is terminated with only BO atoms present on the surface. Termination #3 is terminated with neither BO or TO, but only a bare Ti-O plane, as shown shaded in green in Figure 2.2(a), which we define as the surface Ti-O plane. Based on the crystal symmetry and the charge balance, termination #2 should be favored in vacuum. For instance, a simplified consideration is that when a rutile crystal is cleaved at this position, the two newly created surfaces would be identical and charge neutral. In fact that is the stable rutile (110) surface observed in vacuum.[13, 14] The surface relaxation was both calculated[15-18], and measured[19, 20] for this termination, which shows significant relaxations occurring along the surface normal direction.

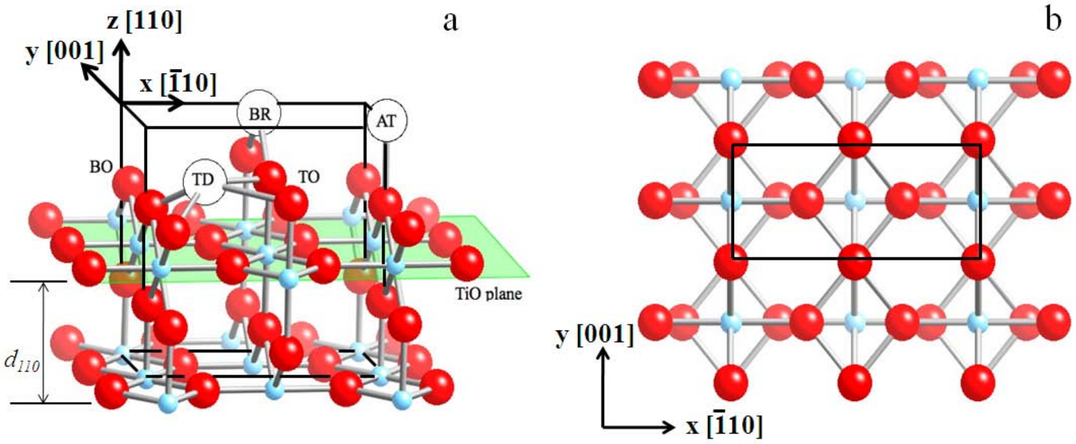

Figure 1.2 A ball-and-stick model of the (110) terminated TiO_2 structure: (a) perspective-view; (b) top-view. Oxygen atoms are in red and titanium atoms are in cyan. For convenience the non-primitive unit cell (outlined with black lines) with a c-axis along the [110] will be used as the reference to locate vanadium cation positions in XSW 3D atomic density maps. The model shows one of the possible surface terminations in which two types of oxygen atoms bind to Ti cations [bridging oxygen (BO) and terminal oxygen (TO)]. This model also represents the hydroxylated surface if the surface oxygen atoms are replaced by the hydroxyl group. Solid circles denote possible adsorption sites: atop (AT), bridge (BR), tetradentate (TD).

There are two kinds of Ti atom positions on such a surface. One is fully six-coordinated Ti, which is bonded to two BO atoms. The other is five-fold coordinated Ti atom where one longer Ti-O bond is broken. The two Ti positions are denoted as BTi (for titanium atom bonded to BO) and TTi (for titanium atom bonded to TO), respectively. As depicted in Figure 2.3, the hydroxyl-saturated α-TiO_2 (110) surface created at ambient conditions has multiple adsorption sites [21, 22]. For convenience of working with rutile (110) surface, a non-primitive tetragonal unit cell is defined, as sketched out in black in Figure 2.3, with $a = c = 6.495$ Å and $b = 2.959$ Å, the unit vector ***a***, ***b***, and ***c*** along bulk crystal [-110], [001], and [110] direction, respectively. The transformation matrix from the primitive tetragonal unit cell to the non-primitive tetragonal unit cell is: $\begin{pmatrix} -1 & 1 & 0 \\ 0 & 0 & 1 \\ 1 & 1 & 0 \end{pmatrix}$. The non-primitive tetragonal unit cell is twice the volume of a primitive tetragonal unit cell, i.e., there are four Ti atoms and eight oxygen atoms in such a unit cell. On the surface, however, there are 1, 2 and 3 oxygen atoms missing from one nonprimitive tetragonal unit cell for termination #1, #2, and #3, respectively.

Although the termination #2 with BO atoms is a stable surface in vacuum, a fraction of the BO atoms can be relatively easily removed from the surface to create the surface oxygen vacancies. However, a rutile (110) surface with BOs completely removed (termination #3 configuration) is not energetically favorable because of too high a density of dangling bonds.[23]

Traditionally, TiO_2 is mainly used in selective oxidation reactions on mixed vanadia/titania catalysts, and vanadium and vanadia/TiO_2 systems have been considered by several groups [24]. Although TiO_2 is not suitable as a structural support material, small additions of titania can modify metal-based catalysts in a profound way.[9] The so-called strong metal support interaction is, at least in part, due to encapsulation of the metal particles by a reduced TiO_X overlayer.[25] Deposition of vanadium in an oxygen ambient results in vanadium oxide that interacts only weakly with the support.[26] The Ti 2p levels remain fully oxidized, but the work function is increased.[26] When vanadium is deposited in a molecular oxygen environment (1×10^{-7} Torr) on stoichiometric TiO_2 (110), disordered vanadium oxide is formed with a composition similar to V_2O_3 or VO_2.[27] Sambi et al[28] proposed that the adsorbed V atoms occupy a well-defined atomic site that corresponded to a Ti bulk-like substitutional site within the first surface layer. There was no diffraction evidence of diffusion of the vanadium before the initial surface layer and it was suggested that the mild annealing provided the necessary energy for bulk oxygen to diffuse to the TiO_2 surface and fully oxidize the surface Ti and V atoms [28]. Sambi et al also reported that on the growth of several monolayers of epitaxial VO_2 on the TiO_2 (110) surface. The VO_2 oxide layer was prepared with successive depositions of vanadium; after each deposition step, the TiO_2 surface was annealed in an oxygen environment. This growth process was described as 'deposition under thermodynamic control', in which the post-deposition annealing process was intended to enhance the order and oxidation of the surface. It was determined that the resulting vanadium oxide layer was well-ordered and pseudomorphic to the TiO_2 (110) substrate[29, 30]. The above studies provide clues about how to prepare vanadium oxides for heterogeneous catalysis.

1.2 Substrate: Hematite (α-Fe_2O_3)

Iron oxides are one of the most abundant materials on earth[31] and exist with a large variety of phases with different stoichiometries, structures and magnetic properties[32-34]. Iron oxides are also easily synthesized in laboratory or industrial environments.[35] Because iron oxides are so prevalent in all aspects of the global system, from iron ore in the terrestrial environment to precipitates in the marine environment, it is not surprising that the study of iron oxide is an important field in geology, mineralogy, and geochemistry. However, iron oxides have an important role in other disciplines as well, such as oxidation catalysts[36], gas sensors[37], sorbents[38, 39], or in magnetic storage media as a pinning layer for spin valves[40].

Like all iron oxides, hematite consists of close packed arrays of oxygen anions in which the interstitial sites are occupied by Fe cations. In the case of hematite, the Fe and O atoms crystallize in the corundum structure (space group $R\underline{3}c$), in which the oxygen O^{2-} ions are arranged in a hexagonal close packed (hcp) array, and the interstices of the hcp array are partially filled by trivalent Fe. This arrangement forms octahedra, which consist of the central Fe^{3+} cation and the surrounding anion ligands, as shown in the depiction of the hematite hexagonal unit cell in Figure 2.3. More specifically, the Fe^{3+} cations occupy two-thirds of the sites in an ordered arrangement, where two adjacent sites in the (0001) plane are filled followed by an empty site. Because the cations are slightly larger than the octahedral sites formed by the anion close packing, the anion packing in the [0001] direction is slightly irregular and the $Fe(O)_6$ octahedra that are formed are somewhat distorted. There is also a distortion in the cation sublattice from the ideal structure, which will be briefly explained below.

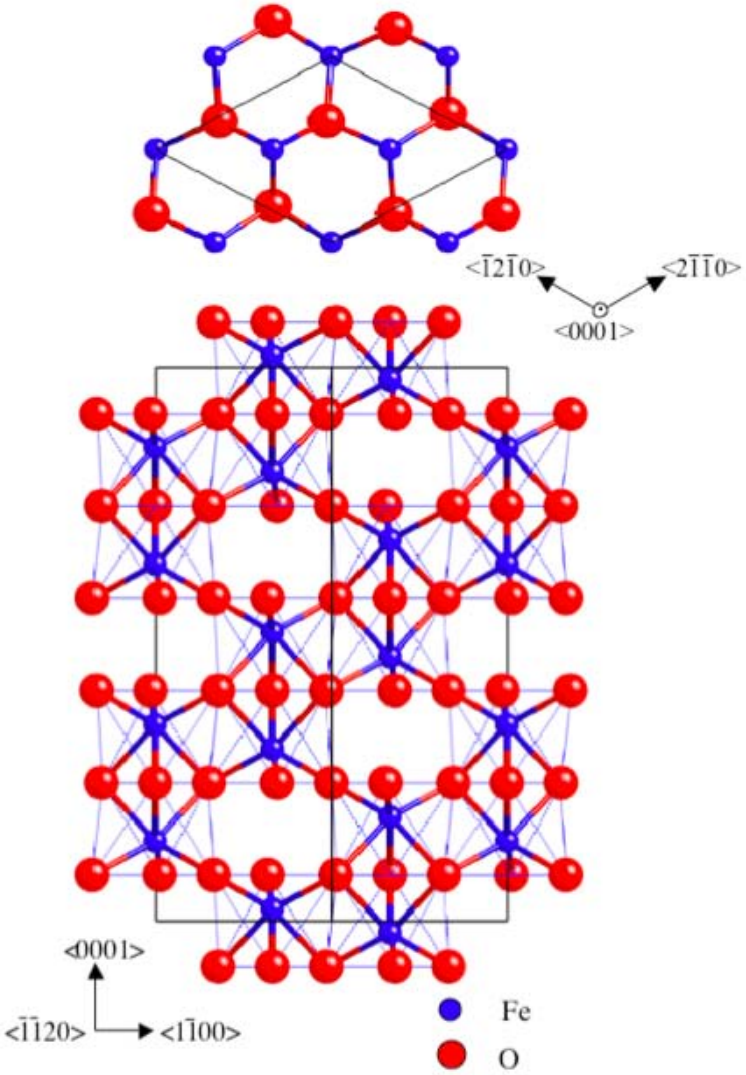

Figure 1.3 Top and side views of the α-Fe_2O_3 hexagonal unit cell. The top view represents the structure of the (0001) hematite surface terminated with a complete layer of Fe cations. The side view shows the crystal structure as seen along the <$\underline{1}$ $\underline{1}$ 2 0> direction. The octahedral formed by the arrangement of Fe and O ions are also emphasized. This figure is reproduced from Ref. [35]

Part of what distinguishes the various structures of the different iron oxides is how these octahedra are arranged with respect to each other, i.e. whether the octahedra are linked to each other by sharing corners, faces, edges, or a combination of all three. In hematite, the arrangement of vacant and occupied octahedral sites results in pairs of $Fe(O)_6$ octahedra, configured so that octahedra in adjacent planes along the [0001] direction share a single face. The aforementioned irregularities in the oxygen anion and iron cation packing arise from this face-sharing configuration. The Fe cations contained within the octahedra are shifted away from the shared face and move along the [0001] direction closer to the unshared faces in order to minimize the electrostatic repulsion between the Fe^{3+} ions. Furthermore, the distance between O anions within the shared face is only 2.669 Å while the corresponding distance for the unshared face is 3.035 Å; this disparity results in the trigonally distorted octahedra that make up the hematite structure. The face-sharing configuration is commonly described as a "Fe-O_3-Fe" triplet, which describes the stacking sequence of the iron and oxygen planes along the [0001] direction. Within the basal plane, there is also edge sharing between the octahedron unit and three of its $Fe(O)_6$ neighbors [41].

This entire atomic configuration can be described by a hexagonal unit cell with lattice constants of a = 5.038 Å and c = 13.772 Å. As demonstrated in Figure 2.3, the in-plane lattice parameter of the hexagonal unit cell corresponds to the interatomic distance between Fe cations within a single layer of the Fe bilayer. Six formula units comprise the nonprimitive hexagonal unit cell. The primitive bulk hematite structure is described with a rhombohedral unit cell, which has a lattice parameter of a_{rh} = 5.427 Å and α = 55.3°. There are two formula units per primitive rhombohedral unit cell.

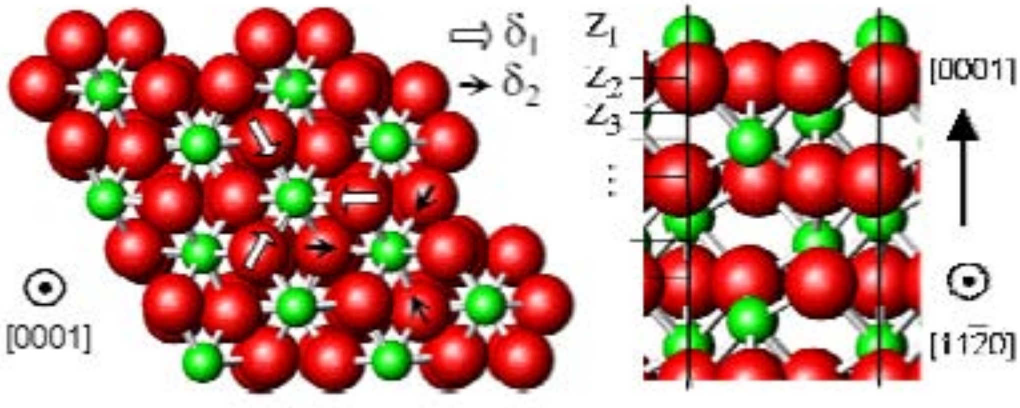

Figure 1.4 Schematic drawing of the α-Fe_2O_3 (0001) structure. Large (small) circles stand for O (Fe) atoms. Top (left) and side (right) views with symmetry elements and allowed relaxations. Radial relaxations of the O atoms are labeled δ_i and relaxations of layer I along the [0001] axis by $z_{i.}$ This figure is reproduced from Ref. [42].

The α-Fe_2O_3 (0001) surface can have many different stable terminations. The bulk structure is illustrated in Figure 2.4. However, by exposing to different conditions (i.e. oxygen annealing, ultra-high vacuum annealing, etc.), different surface structures can be formed. Theoretically, density functional theory (DFT) is used to predicted the termination structure under environmental conditions as a function of the oxygen pressure p and temperature T (defining the oxygen chemical potential μ).[42, 43] Using DFT methods[36, 43, 44], upon decreasing μ, three surface structures are predicted to appear in the following order: bulk-like oxygen-terminated O_3-Fe- (as shown before, a subscript number denotes the number of atoms in a layer in the unit cell, and the stacking from surface to bulk reads from left to right), ferryl termination in which one double bonded Fe=O group is present per surface unit cell, and finally, single and double Fe iron terminations competing with the transformation to Fe_3O_4. All of those terminations need experimental confirmation and investigation.

Experimentally, many treatments can lead to different surface terminations and some of which fall into the three different surface structures as predicted by DFT calculations above. A common surface treatment for producing a clean hematite surface is Ar^+ ion sputtering; however, Kurtz *et al.* has shown that ion sputtering can preferentially remove oxygen from the surface layers and produce a reduced surface.[45] Replacing the lost surface oxygen by annealing in an oxygen environment can fill the vacancies caused by sputtering, but the recovery of the ideal surface can be strongly dependent on the annealing conditions. One early LEED and XPS structural study of the α-Fe_2O_3 (0001) surface suggested that the sputtering process transforms part of the hematite surface into a thin layer of metallic Fe^0 that lies above a thicker reduced iron oxide layer.[45] Similar investigations have suggested that it is the annealing temperature (and not the annealing environment) that primarily governs the extent of re-oxidation of the surface overlayers. It has been proposed that the choice of annealing temperature also determines whether the re-oxidized surface region consists solely of hematite or if a magnetite (Fe_3O_4) layer is produced by the removal of oxygen anions from the underlying Fe_2O_3.[46] However, other investigations have found that after a surface layer of magnetite is formed during sputtering, annealing under an increased oxygen pressure allows the Fe_3O_4 to be reoxidized at a lower annealing temperature.[47] Finally, in an STM study, Condon *et al.* reinterpreted some of these conclusions as the result of a phenomenon called *biphase ordering*, in which islands of α-Fe_2O_3 and FeO (111) coexist on the hematite surface and form an extended superlattice.[48, 49] STM images of this unique overlayer structure are shown in Figure 2.5.

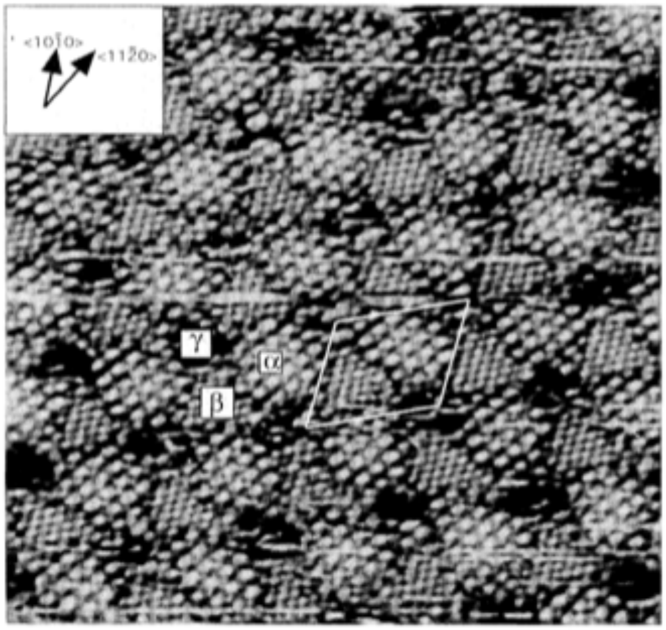

Figure 1.5 A 200 Å x 200 Å constant current (sample bias -2 V, tunneling current 1 nA) STM image of an α-Fe_2O_3 (0001) surface which shows a biphase ordering, namely α and β types of islands with holes at positions label γ. This figure is reproduced from Ref. [49].

An extensive surface X-ray diffraction (SXRD) investigation on the α-Fe_2O_3 (0001) surface encountered all these aforementioned iron oxide phases as the oxygen-deficient hematite surface was recovered to the stoichiometric (1×1) surface[50]. Unlike the electron-based surface techniques that probe only the first few atomic layers of the surface, the X-ray scattering provides structural information from both the surface and subsurface regions. It was determined that after annealing the reduced surface in a molecular oxygen environment, the uppermost surface layers can be recovered to the stoichiometric Fe_2O_3 phase, but a remnant magnetite layer remains below the recovered oxide surface. By slightly increasing the oxygen annealing temperature (from 1008K to 1018K in this particular study), the subsurface magnetite can be converted to hematite, but the previously stoichiometric surface is simultaneously transformed into the non-stoichiometric biphase ordered surface. The topmost biphase layer can finally be converted to Fe_2O_3 by annealing in an atomic oxygen environment. This elaborate surface history is a telling example of some of the complexities that can arise when preparing and characterizing the stoichiometric α-Fe_2O_3 (0001) surface.

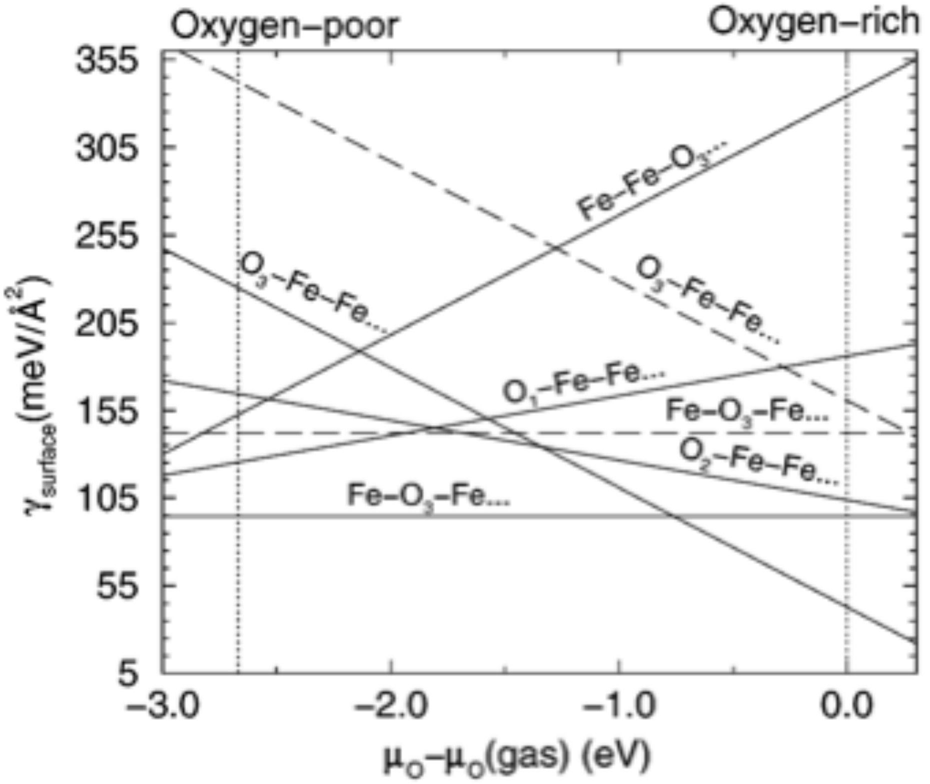

Figure 1.6 Surface energies of different Fe_2O_3 (0001) surface terminations as a function of the chemical potential per oxygen atom of molecular O_2, calculated from DFT. Solid lines show results for relaxed geometries, and dashed lines represent unrelaxed surfaces. This figure is reproduced from Ref. [36]

Furthermore, even if the stoichiometric structure can be recovered from the oxygen deficient surface using oxygen annealing, the question of what is the chemical composition of the α-Fe_2O_3 (0001) surface remains. Because of the "Fe-O_3-Fe" stacking sequence of the bulk hematite structure, it is possible that the α-Fe_2O_3 (0001) surface can consist of a terminal layer of either Fe cations or O anions. In addition, the hematite surface can be expected to undergo significant atomic relaxations, which are in part driven by the tendency of the surface cations to increase their oxygen coordination. A detailed theoretical study employing a variety of periodic slab models and computational methods found a large relaxation effect for the two outermost surface layers of a Fe-terminated α-Fe_2O_3 (0001) surface. These substantial relaxations were attributed to the reduced coordination of the surface atoms[51]. In one spin-density functional theory (DFT) study, Wang *et al.* calculated the surface energies of various α-Fe_2O_3 (0001) surface terminations as a function of the oxygen chemical potential. From the results of these calculations (which are summarized in Figure 2.6), it was determined that both a Fe-terminated (Fe-O_3-Fe) and an O-terminated (O_3-Fe-Fe) surface can be stabilized if they were accompanied with significant atomic interlayer relaxations. The presence of both surface terminations was observed using STM.[36] Another STM study[52] also observed the significant dependence of the hematite surface structure on the ambient oxygen pressure detailed in Ref.[51]. In another DFT investigation of the α-Fe_2O_3 (0001) surface, several Fe- and O-terminated hematite surfaces were explored, including an additional surface phase involving a single O atom bonded on top of a reactive surface Fe atom; this structure stabilizes as the surface is allowed to relax in an oxygen-rich environment, as shown in the calculated surface phase energy plot shown in Figure 2.7.[43]

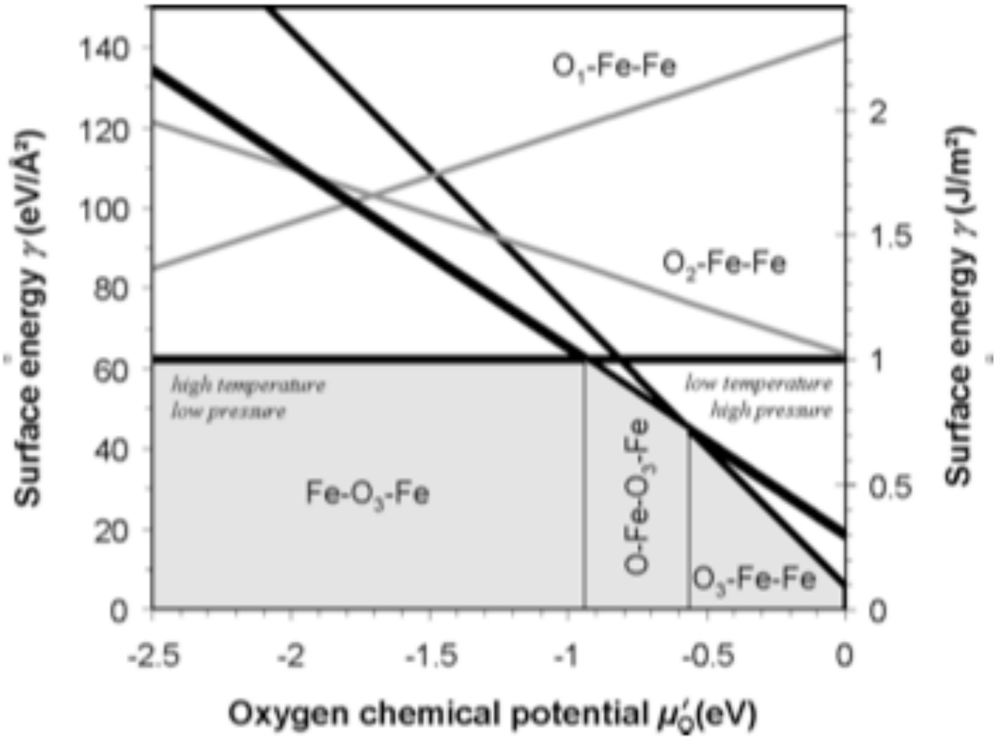

Figure 1.7 Free energy of α-Fe_2O_3 (0001) surface as a function of oxygen chemical potential. The thermodynamically stable structures are Fe-O_3-Fe, O-Fe-O_3-Fe, and O_3-Fe-Fe. This figure is reproduced from Ref. [43]

However, these results were somewhat disputed by Chambers *et al.* in a XPD and STM investigation of α-Fe_2O_3 (0001) surfaces grown by oxygen-plasma-assisted molecular beam epitaxy. This study suggested that the Fe-terminated surface is the most stable surface even under highly oxidizing conditions[53]. These experimental results were supported by an *ab initio* theoretical study, which included electron correlation effects within a density functional description. By including the strong correlation effects, it was determined that a Fe-terminated surface is the most stable surface over the allowable range of oxygen chemical potentials; the proposed surface model consists of a partially occupied Fe layer in which half of the octahedral sites are vacant[44]. An earlier X-ray photoelectron diffraction (XPD) experiment also found this particular structure to be the most stable surface phase and found no evidence of a possible O-termination[54]. The authors of this study suggested that since the partially occupied Fe termination layer fully auto-compensates the hematite surface due to charge transfer from the Fe dangling bonds to the O dangling bonds, it is not surprising that the Fe-termination surface model provided the best fit to the PED spectra.[55]

Finally, for some catalytic investigations the presence of surface point defects may be desirable, since oxygen vacancies can result in a redistribution of charge and a reduction of surface cations, which can help promote the adsorption and dissociation of foreign molecules. A surplus of cations in the form of Fe interstitials is another form of non-stoichiometry that can also contribute to the catalytic activity. Therefore, there is a need to characterize non-ideal hematite surfaces in order to more accurately model real- world catalytic processes. In a theoretical study of the defect chemistry of the α-Fe_2O_3 (0001) surface, Warschkow *et al.* found that at the hematite surface, the energy required to form an oxygen vacancy is markedly smaller than in the bulk[56]. Furthermore, the same investigation determined a lowering of some of the transition barriers to oxygen vacancy migration within the uppermost oxygen layers near the hematite surface. However, there are few experimental studies on the formation of defects and their effect on the properties of the α-Fe_2O_3 (0001) surface.

1.3 Substrate: Strontium Titanate ($SrTiO_3$)

$SrTiO_3$ belongs to the important family of perovskites and is one of the most used materials. This perovskite family is governed by the formula ABO_3. The ‘A’ cation typically consists of metal ions from the first two columns of the periodic table and ‘B’ cations occupy the site with octahedral coordination.

Single crystal strontium titanate was not discovered in a natural setting until 1984.[57] However, bulk synthetic $SrTiO_3$ crystals have been available for scientific study since the early 1950’s and $SrTiO_3$ powder was available even earlier. The most common way to grow large $SrTiO_3$ crystals is to use a modified version[58] of the Verneuil method. The growth occurs by feeding $SrTiO_3$ powder through an oxygen-hydrogen combustion blow-pipe that melts the powder. The melted $SrTiO_3$ droplets descend onto a slowly rotating pedestal. Crystals of several inches in diameter can be grown by this method. The $SrTiO_3$ substrates used in this project are mainly from three major substrate vendors: MTI Corp. (Richmond, California), Crystal GmbH (Berlin), and CrysTec GmbH (Berlin). They all use the modified Verneuil method to obtain bulk single crystals. Their crystal qualities are tested by high-resolution X-ray diffraction by comparing the measured rocking curve width with the theoretical value. High quality substrates are chosen for X-ray standing wave (XSW) measurements. The poor crystal quality is most likely due to the crystal growing via a stream of molten oxide droplets that leads to a collection of crystallites forming single crystal of mosaic structures a few nanometers in dimension.

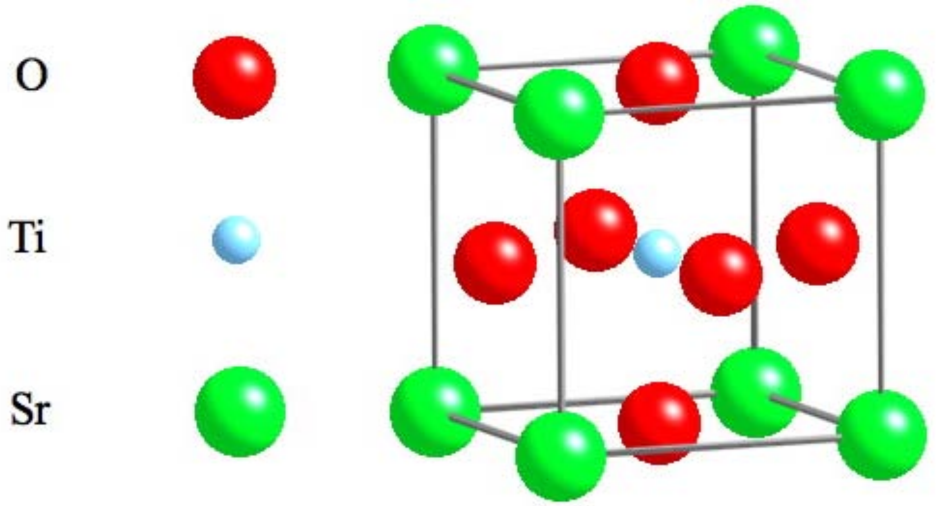

Figure 1.8 The cubic-P unit cell for $SrTiO_3$(001) with a Sr cation at the origin, O anions at the face-centered positions and Ti cation at the body-centered position.

At room temperature strontium titanate has a cubic perovskite structure (space group: Pm3m) with a room temperature lattice constant of a = 3.905 Å. Figure 2.8 shows the unit cell of $SrTiO_3$. Due to its relative simple structure for ABO_3 type materials, $SrTiO_3$ is one of the most widely studied model perovskite materials. We will use the (001) surface for which different treatments lead to a number of different surface structures and chemistries[59, 60] of interest.. Depending on the experimental environment, under oxidative conditions, many (001) surface reconstruction of $SrTiO_3$ have been achieved, such as (1×1), (2×2), (2×1), (6×2), c(4×4), c(4×2), c(6×2), (√5×√5)-R26.6°, (√13×√13)-R33.7°.[59-66] The recipes to produce these structures are sometimes unreliable and indeed one of the major challenges in the surface structure of SrTiO3 (001) is the lack of well-defined methods guaranteed to achieve a particular reconstruction.

Another important advance in the $SrTiO_3$ (001) surface preparation occurred in 1994 where a method to isolate the TiO_2 bulk termination was identified.[67] Kawasaki *et al.* showed that using buffered hydrofluoric acid (BHF), the strontium-oxygen layer could be preferentially removed, leaving behind a pristine titanium-oxygen surface. Using ion scattering spectroscopy (ISS) and AFM, Kawasaki *et al.* determined the surface termination was greater than 99% titanium - oxygen with 0.4 nm tall atomic terraces, which is the height of one unit cell of $SrTiO_3$. ISS has been used to confirm this result for a series of treatments with slight variations in buffer pH and other experimental parameters.[68-70] Prior to the BHF discovery most studies focused on spectroscopy of the surface using photoelectron and Auger electron probes. Following the Kawasaki paper, a series of structural studies cataloged a number of surface reconstructions observed with diffraction and/or scanning tunneling microscopy (STM).[59, 61-64, 70-72]

Besides the great interests provoked by the material itself, strontium titanate has also been used as the substrate to either epitaxially grow other perovskite materials or metal/metal oxides for catalytic use. Due to strontium titanate's bulk lattice constant being similar to important thin film materials, it has application in the microelectronics research field. In 1980s, group in UC Berkeley found that $SrTiO_3$ supported Pt can improve the efficiency of water splitting by a factor of 16 compared to plain $SrTiO_3$.[73] During the 1990s, the material was identified as a substrate for high-temperature superconducting film materials. $SrTiO_3$ is also used as a substrate material for multiferroic films and devices. Recent efforts have been made by Sholong group to proper strain perovskite materials on different ABO_3 type materials to achieve ferroelectric and magnetic materials.[74] Nevertheless, the result of these research efforts inspired a number of studies related to the surface structure and use of $SrTiO_3$ as a substrate material.

1.4 Preparation of the Atomic Flat Oxide Surfaces

When compared to α-Fe_2O_3(0001) and $SrTiO_3$(001) rutile α-TiO_2(110) is the most stable of the three surfaces[11] against hydrogen reduction. Thus when used as the support for catalysts, it is treated mostly as the non-reducible substrate. In contrast to α-TiO_2(110), α-Fe_2O_3(0001) can be quite easily reduced. So mostly hematite support are treated as the reducible substrate. $SrTiO_3$(001) is between the above two. In my thesis, the three substrates were used as comparison for supported metal oxides catalysis studies.

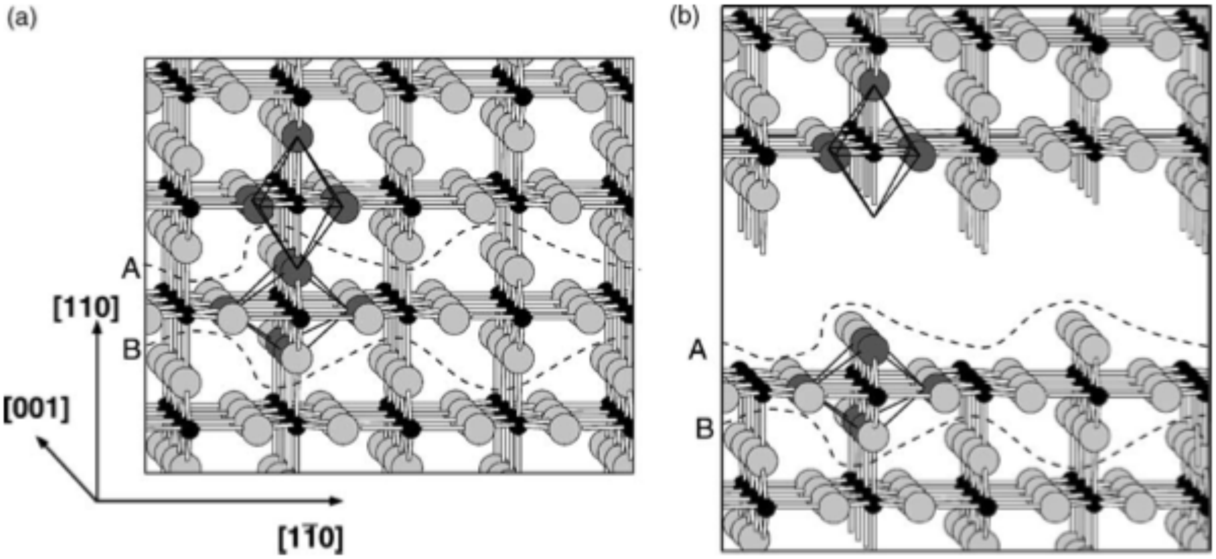

Figure 1.9 (a) Ball-and-stick model of the rutile crystal structure. The dashed line enclose a charge-neutral repeat unit without a dipole moment perpendicular to the [110]-direction, which is called a ‘type 1’ crystal plane according to literature [75]. (b) The truncated crystal is stable due to auto-compensation.[76] This figure is reproduced from Ref. [11].

For rutile, there are several surface terminations, such as α-TiO_2(110) (1 x 1) and TiO_2(100) (1 x3)[77, 78]. The α-TiO_2(110) (1 x 1) surface is one of the most studied surfaces, also very stable surface structure. The 1 x 1 unit cell is described by the rectangular outline in Fig. 2.2(b). This surface is known from experimental as well as theoretical studies. It can be obtained from bulk truncation, and its stability are predicted and confirmed by Tasker's purely electrostatic consideration[76] and LaFemina's auto-compensation criterion [75]. Figure 2.9 illustrate the 'simple' way to obtain stable (1 x 1) surface by bulk-truncation. As shown in Figure 2.9(b), this surface contains two different kinds of titanium atoms: 6-fold coordinated Ti atoms (as in the bulk) alternate with 5-fold coordinated Ti atoms with one dangling bond perpendicular to the surface. In real conditions, the (1 x 1) surface with atomically flat large terraces (up to 400 Å) can be generally obtained by sputtering and annealing at high temperature in ultra-high vacuum (UHV) condition[79], as shown in Figure 2.10. The alternating bright and dark rows indicate the (1 x 1) structure. However, annealing in oxygen condition at high temperature in UHV chamber makes the surface rougher and the surface shows three different features: rosettes, termed (1 x 2) strands and small (1 x 1) islands [79]. The morphology of the surface is affected by the oxidation condition and the history of the TiO_2 (110) sample.

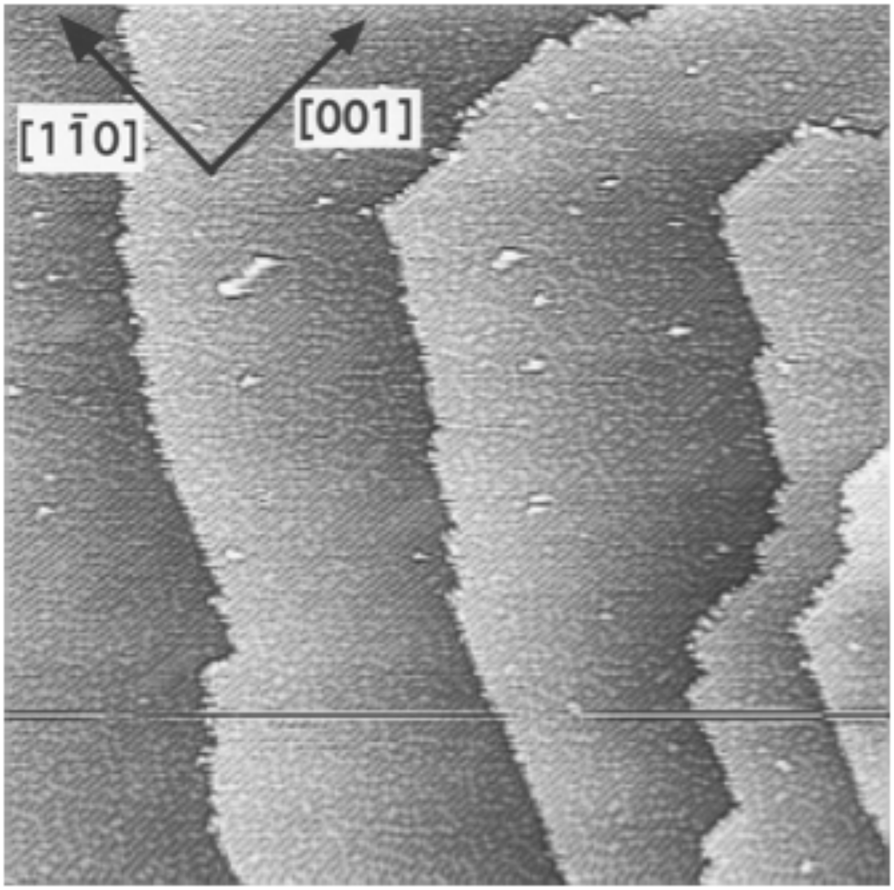

Figure 1.10 STM image of a $TiO_2(110)$ surface, which was sputtered and annealed at 920 K in ultrahigh vacuum. This figure is reproduced from Ref. [79]

Another method for creating an atomically-flat TiO_2 (110) surface is by annealing in an oxygen ambient condition at a very high temperature [21]. This is the method used in this thesis. Double side polished α-TiO_2 (110) (10 x 10 x 1 mm^3) substrates with a miscut smaller than 0.1° were obtained from commercial vendor (Crystal GmbH, Germany). Substrates were annealed in a tube furnace with flowing O_2 (~100 standard cubic centimeters per minute or sccm) at 400 °C for 0.5 h, then at 900 °C for 1 h or 4 h.[21] This process gives atomically flat surfaces with terrace steps of ~3.3 Å, measured from AFM height profile. Figure 2.11 shows the typical atomically flat surface of α-$TiO_2(110)$ imaged by AFM.

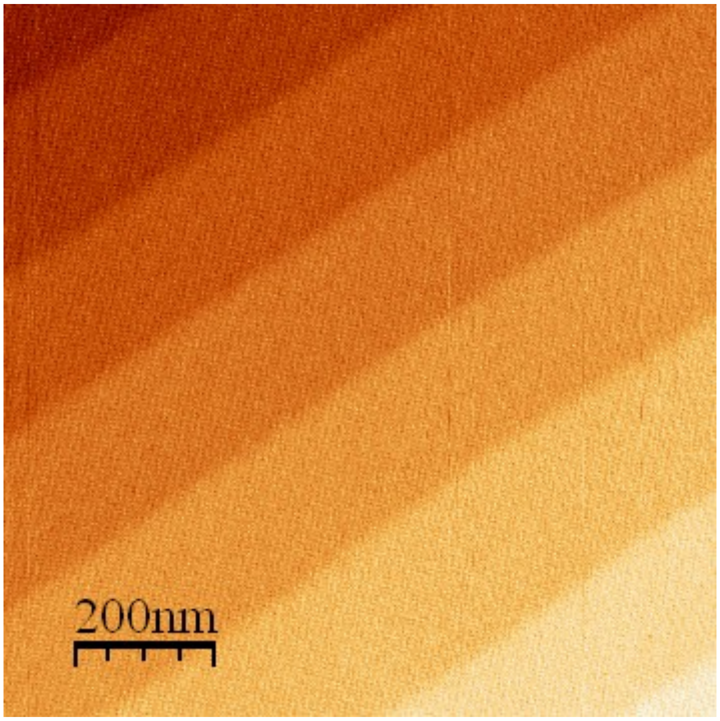

Figure 1.11 Atomically-flat terraces on α-TiO_2 (110) examined by atomic-force microscopy. The step height between terraces is ~3.3 Å, which corresponds to the (110) d-spacing.

For α-Fe_2O_3(0001), both UHV annealing and ambient annealing can be used to obtain atomically flat surfaces (as with α-TiO_2 (110)). In UHV, a pure biphase surface was obtained after cleaning by repetitive Ar^+ sputtering and oxygen annealing (760 °C with O_2 pressure at 3 x 10^{-6} Torr)[80]. However, a mixture of biphase and (√3 x √3) R30° phase was obtained if the annealing at 700 °C with O_2 pressure at 1 x 10^{-6} Torr.[80] Further investigation shows that after Ar^+ sputtering and annealing at 450 °C for 0.5 h with a stream of atomic oxygen gas (O_2 pressure at 2 x 10^{-6} Torr), a (1 x 1) low energy electron diffraction (LEED) pattern was observed. If increasing the temperature to 720 °C and annealing under oxygen flow (O_2 pressure at 1 x 10^{-5}

Torr), (2√3/3 x 2√3/3) R30° LEED pattern will be observed.[50] These give stoichiometric and atomically flat α-Fe_2O_3 (0001) surfaces. Compared to UHV annealing, ambient annealing, which was used in this thesis, is easier and can also be used to obtain atomically flat terraces. In this case, mineral α-Fe_2O_3 (0001) substrates (from Commercial Crystal Laboratories in Naples, FL) were annealed in a tube oven with flowing O_2 (~100 sccm) at 400 °C for 0.5 h, followed by 5 h at 750 °C. As shown in Figure 2.12, an atomically flat surface with 0.2 nm tall steps was observed by AFM.[81]

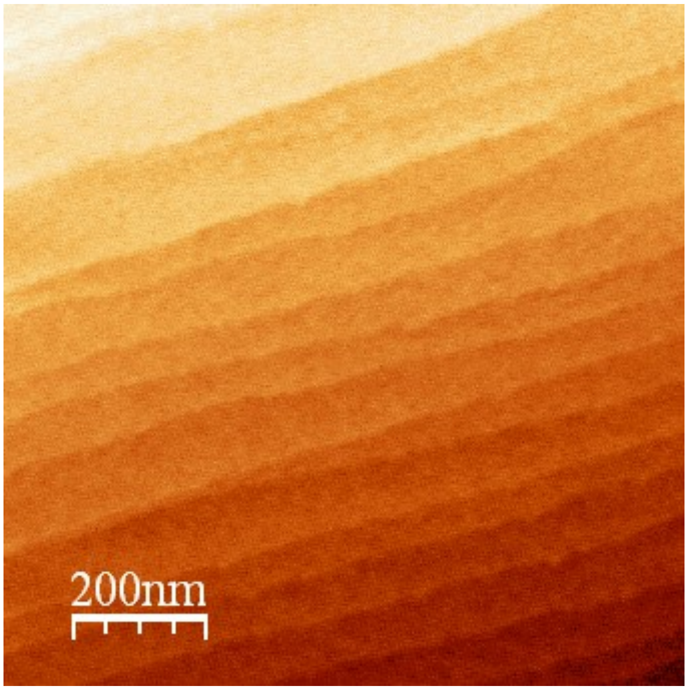

Figure 1.12 AFM image of the α-Fe_2O_3(0001) substrate surface after the two step annealing process shows the clean atomically flat terraces with 0.2 nm high steps.

For $SrTiO_3$(001), there are two basic surface terminations; TiO_2-terminated and SrO-terminated. As discussed above, the well-established surface preparation procedures[67, 82] can produce stable TiO_2-terminated surfaces. In this thesis, all work is done based on TiO_2-terminated surface, but with different surface reconstructions. Our method is to ultrasonicate $SrTiO_3$(001) substrates for 10 minutes in deionized water (18 MΩ/cm) and subsequently etch them in a buffered HF solution for approximately 30 s. The substrates were then rinsed in deionized water and dried in Ar gas. To produce atomically flat terraces terminated with titanium oxide, the substrates were loaded into a tube furnace with O_2 flow (~100 sccm) and annealed at 1050 °C for 5 hours. Figure 2.13 shows the atomic-flat $SrTiO_3$(001) surface.

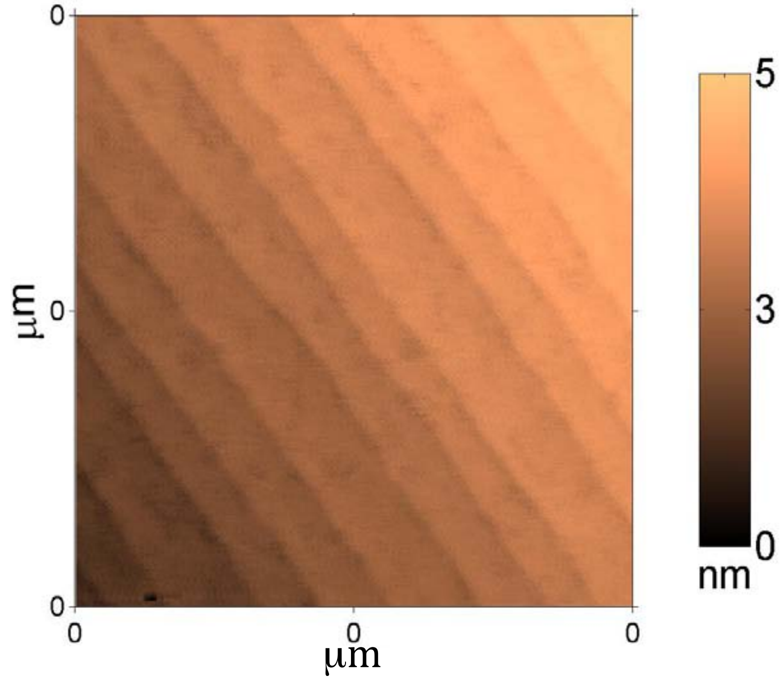

Figure 1.13 AFM image of a $SrTiO_3$(001) substrate surface after the two step annealing process shows the clean atomically flat terraces with 0.3 nm high steps.

This tube-furnace annealing procedure typically produced a (√13×√13)-R33.7° TiO_2-terminated surface.[65, 83] To obtain other surface reconstructions, further UHV annealing is necessary. In this thesis, a two-domain (2×1) TiO_2-terminated surface is obtained by annealing at 950 °C for 30 min in the UHV chamber after open air annealing.

1.5 Supported Metal and Metal Oxides Catalysts

Metals and their oxides are heavily used as catalysts for refining of petroleum, conversion of automobile exhaust, hydrogenation of carbon monoxide, hydrogenation of fats, and many other process.[84] Examples such catalysts are gold, platinum, palladium, vanadium, tungsten, chromium, titanium, and molybdenum. Figure 2.14[1] shows a summary of several transition metals in the field of metal oxide catalysis, which can also be found in open literature [85]. This figure shows the great importance of vanadium oxides in supported metal oxide catalysis. Besides vanadium, tungsten oxides also play a very important role in industrial processes, especially in selective reduction of NO_X with NH_3 when mixed with vanadium oxides[7, 86, 87]. The use of all kinds of supports (mainly metal oxides) can not only improve the catalytic properties of those metal or metal oxides, but also positively help the chemical reactions. For example, most catalyst supports have pores that allow reactants and product to be into and out of the interior volume, which provide high-area internal platforms for the catalysts and help reactions.[84] Furthermore, in the field of heterogeneous catalysis, the interface between supported catalysts and oxide substrates has been suggested as the site of catalytic activity (say, the activity occurs at the 2D region), not at the 3D islands.[88, 89]

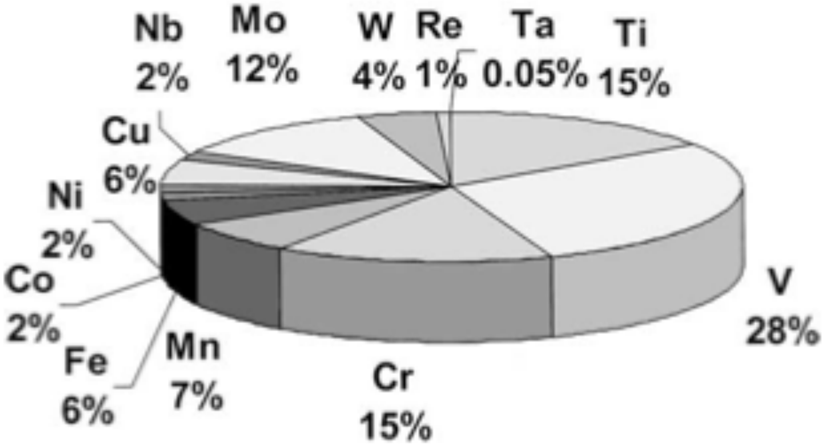

Figure 1.14 Metal and metal oxides as catalysts discussed in open literature in the period of 1967-2000. This figure is reproduced from Ref. [1]

1.5.1 Platinum

Platinum is one of the most important catalysts in the world, due to its application as a photocatalyst,[73, 90, 91] catalytic oxidation of carbon monoxide,[92] its use as an oxygen gas-sensor system, and by the fact that it is the classic strong-metal support interaction SMSI system.[11, 88]

Platinum is a face-centered-cubic (FCC) structure, which has the $Fm\underline{3}m$ space group (#225), as shown in Figure 2.15. The lattice constant for Pt , 3.922 Å, is a very close match to that of $SrTiO_3$. This is one ingredient in making it possible to grow Pt epitaxially on $SrTiO_3$ with different orientations.[93-97] Because the unit cells are in the same family with the $m\underline{3}m$ symmetry designation, the diffraction peaks of Pt are very close to those of $SrTiO_3$ .. The $SrTiO_3$ primitive unit cell has no forbidden diffraction peaks. Whereas the fcc diffraction rules apply for Pt, meaning mixed *hkl* peaks are absent. This makes it difficult to study platinum diffraction apart from $SrTiO_3$ substrate diffraction when the two materials are paired together. Due to the

~0.4 % larger lattice constant of Pt, the Pt diffraction peaks will be at slightly smaller 2θ angles. Platinum generally appears to be quite inert and refractory. It has a relatively high melting point (1780°C) and does not easily oxidize when heated in oxygen. Nevertheless, Pt will form a variety of stoichiometric oxides including PtO, PtO_2, and Pt_3O_4. Platinum is one of the most important catalytic materials used in energy technologies despite its apparent chemical inertness. Catalytic converters utilize platinum catalysts to reduce CO and NO_X emissions from automobiles. Furthermore, Pt based catalysts can be employed in re-forming and isomerization reactions to produce fuels including gasoline. Fuel cells use Pt extensively to facilitate the conversion of hydrogen and oxygen in polymer membrane architectures and in the case of solid oxide fuel cells as a high-temperature electrode material. Platinum is also used extensively in the electrolysis and photochemistry as a cathode material; it does not degrade under reaction conditions and interacts favorably with hydrogen. Therefore, Pt as either a catalyst or metal-insulator-metal heterostructure has attracted more and more attention.

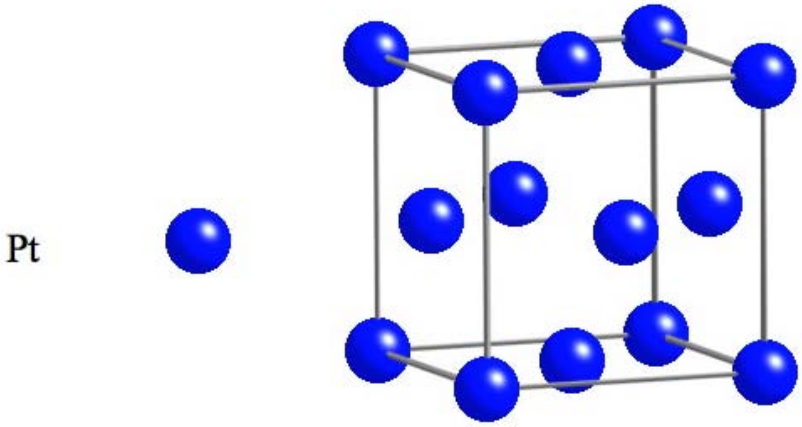

Figure 1.15 Crystal structure for Pt with lattice constant 3.922 Å and space group Fm$\underline{3}$m.

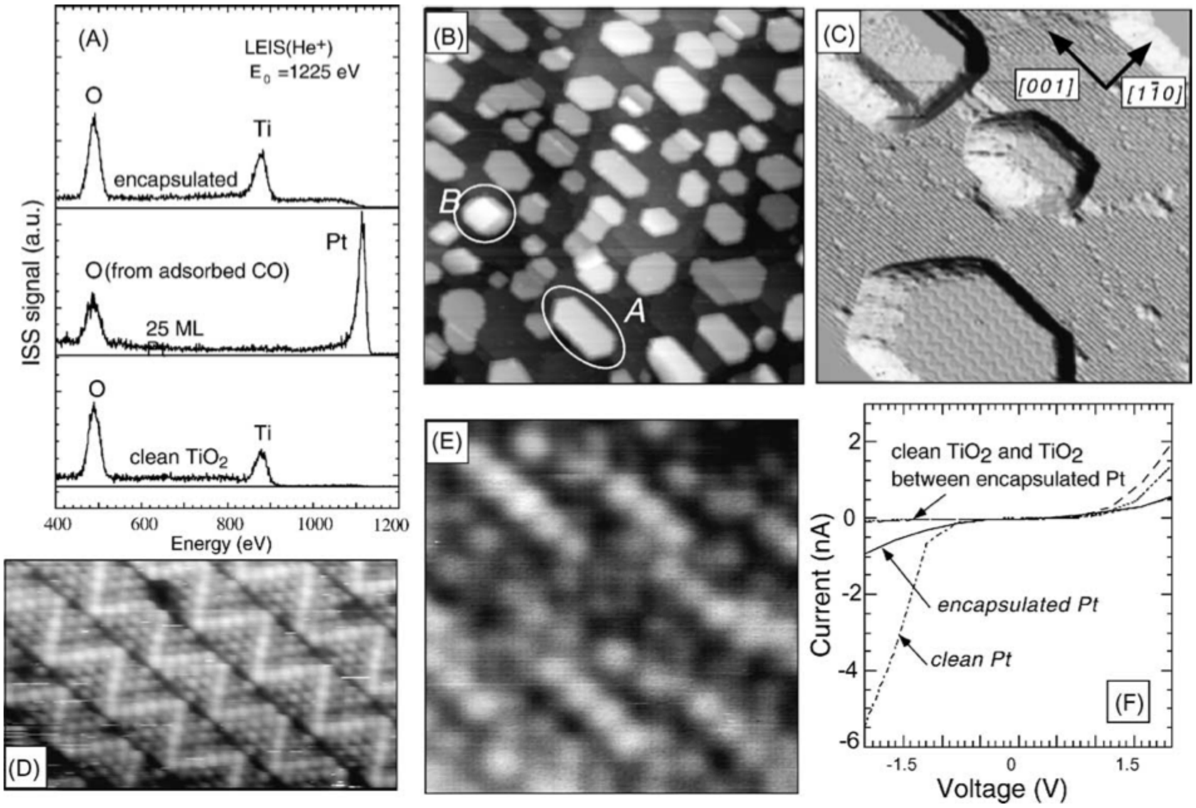

Figure 1.16 Experimental results on an SMSI model system, Pt / TiO_2(110). (A) Low-energy He ion scattering (LEIS) spectra of (bottom) the clean TiO_2(110) surface, (center) after evaporation of 25 ML Pt at room temperature, and (top) after high- temperature treatment caused encapsulation. (B)-(F) STM and STS results after the high-temperature treatment. (B) Overview (2000 Å × 2000 Å). Clusters are approximately 200 Å wide and 40 Å high. Most clusters show hexagonal shape elongated along the substrate [001] direction (type A). A few square clusters (type B) are seen. (C) Small-scale image (500 Å × 500 Å), filtered to show the structure of the encapsulation layer and the substrate. (D) Atomic-resolution image of an encapsulated hexagonal ‘type A’ cluster. (E) Atomic-resolution image of a square `type B' cluster, showing an amorphous overlayer. (F) STS of the different surfaces. This figure is reproduced from Ref. [88].

When Pt is used as a catalyst, one interesting phenomenon is discovered. It is the so-called strong-metal support interaction (SMSI). This is common for the group VIIIA metals (Fe, Co, Rh, Ir, Ni, Pd, Pt), which all show a very interesting behavior upon annealing in a reducing atmosphere that has been discussed in the catalysis literature for several decades. The acronym SMSI has been termed by Tauster[89] to account for the changes in catalytic activity when catalysts, consisting of these metals supported on TiO_2 or other reducible oxides (TaO_5, CeO_2, NbO, etc.), are reduced at elevated temperature. Adsorption of H_2 and CO is drastically reduced, but competitive hydrogenations vs. hydrogenolysis reactions are greatly favored in SMSI systems. For example, methane production from CO or CO_2 and H_2 is enhanced by three orders of magnitude.[25] Therefore the SMSI phenomenon makes it possible to tailor the selectivity of a catalyst and has caused wide-spread interest.[11]

Figure 2.16 shows an example of SMSI for 25 monolayers (ML) of Pt deposited on a $TiO_2(110)$ surface. Low-energy ion scattering experiments clearly show that UHV annealing at higher temperatures causes encapsulation (Figure 2.16(A)), and glancing-exit XPS identified the layer as highly reduced with (probably) Ti^{2+} species present.[98] The overlayer in the SMSI state was imaged successfully with STM by Dulub et al.[88], as shown Figure 2.16(B)-(E). Most clusters (type A) have a hexagonal shape elongated along the substrate [001] direction and are, on average, 40 Å high and 200 Å wide. A few have a square shape (type B). Those are smaller. A simple calculation (taking into account the deposited amount of Pt (25 ML), the surface coverage after encapsulation (40%), and the cluster height) shows that the clusters resemble “icebergs” reaching several tens of Angstroms deep into the substrate. On top of the type A clusters, striped “zigzags” are visible. On different clusters the stripes are oriented either parallel to the substrate [001] direction or rotated by ±60°. No clear preference for any rotational orientation was observed, nor a strict correlation between the directions of stripes and cluster elongations. Figure 2.16(D) is an atomically resolved image of a "type A" cluster surface. The stripes are approximately 15 Å wide and consist of bright spots arranged in a hexagonal symmetry with a distance of 3 Å. The bright zigzag rows contain either 5 or 6 atoms along the close-packed directions and separate triangular areas consisting of 10 atoms. Surfaces of type B square clusters exhibit no apparent long-range order (Figure 2.16(E)) with strings of 3-6 atoms oriented along the substrate [001] direction. The "type B" clusters are probably crystallites with their (100) face parallel to the substrate. It is conceivable that such surfaces should be found at the sides of the hexagonal, (111)-oriented "type A" clusters. STM current vs. voltage (*I-V*) curves have been taken from the clean sputter-annealed $TiO_2(110)$ surface, from $TiO_2(110)$ between encapsulated clusters, and from clusters of clean and encapsulated Pt (Figure 2.16(F)). There is almost no difference in the *I-V* curves from clean TiO_2 and from TiO_2 between encapsulated clusters, indicating that the electronic structure of the substrate is not strongly affected by the encapsulated clusters.[88]

1.5.2 Vanadium Oxides

Discovered in 1801 in Mexico by A. M. del Rio[99-101], vanadium is presently most widely used worldwide as a steel additive. From the 20th century, vanadium oxide-based catalysts have been generally used in the manufacturing of important chemicals such as sulfuric acid, in the reduction of environmental pollution, and have become arguably the most important metal used in metal oxide catalysis[5, 102]. Most catalysts based on vanadium oxide consist of a vanadium oxide phase deposited on the surface of an oxide support, such as SiO_2, TiO_2 or Al_2O_3. The oxide support is initially proposed to improve the catalytic activity of the active metal oxide phase due to a gain in surface area and mechanical strength[102, 103]. The support was considered as an inert substance that provided a high surface to carry the active metal oxide component or to improve the mechanical strength of the catalyst materials. However, during the last decades of the 20th century, catalysis research has shown that the activity and selectivity of supported metal oxide catalysts are significantly affected by the properties of the support oxide materials, which is generally known as the metal oxide-support effect, although its exact origin and mechanism of operation is still unknown. The fundamental basis for the catalytic performance of supported vanadium oxides lies in the variability in geometric and electronic structure of surface vanadium oxides.[1]

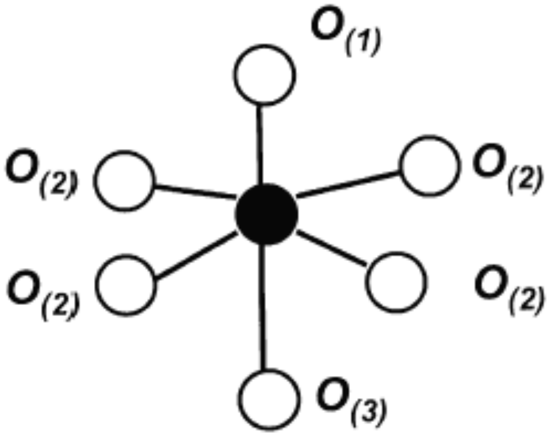

Figure 1.17 Molecular structure of V^{5+} in V_2O_5 crystals indicating three different V-O distances. This figure is reproduced from Ref. [1].

Supported vanadium oxides show different chemical and electronic properties from those found for unsupported vanadium oxide (V_2O_5), in aqueous media and in the solid state [99-101]. The principal vanadium oxides are V_2O_5, VO_2, V_2O_3 and VO, in which the formal oxidation state of vanadium changes from +5 to +2. Other more exotic vanadium oxide compounds are mixed valence oxides and can be expressed as V_nO_{2n-1}.[1] In these vanadium oxides, the configurations are complicated. Generally there are three different bonds. Taking V_2O_5 as an example, as shown in Figure 2.17, the vanadium ion is slightly displaced from the basal plane towards the apex of the pyramid, which creates a strong and short $V{=}O_{(1)}$ bond of 1.58 Å. The $V\text{-}O_{(3)}$ distance in opposite direction is much longer (2.79 Å). The four $V\text{-}O_{(2)}$ bonds to the oxygen in the basal plane have a length of 1.83 Å. For supported vanadium oxides, the configurations on the surface are more complicated, and are still not quite clear. Figure 2.18 shows the possible molecular configurations for supported vanadium oxides. References[5, 104, 105] show that the supported vanadium oxide species formed on various supports all essentially possess the same molecular structures. At low surface vanadium oxide loading the supported vanadium oxides are isolated VO_4 units, containing one terminal mono-oxo V=O bond and three bridging vanadium-oxygen-support bond with symmetry C_{3v}[1]. Results show that the V=O bond is ~1.62 Å, whereas the three V-O-support bonds each have lengths of ~1.81 Å.[1] The support oxide has some effect on the mono-oxo V=O bond length, which varies in the range from 1.60 to 1.79 Å depending on the support oxide materials.

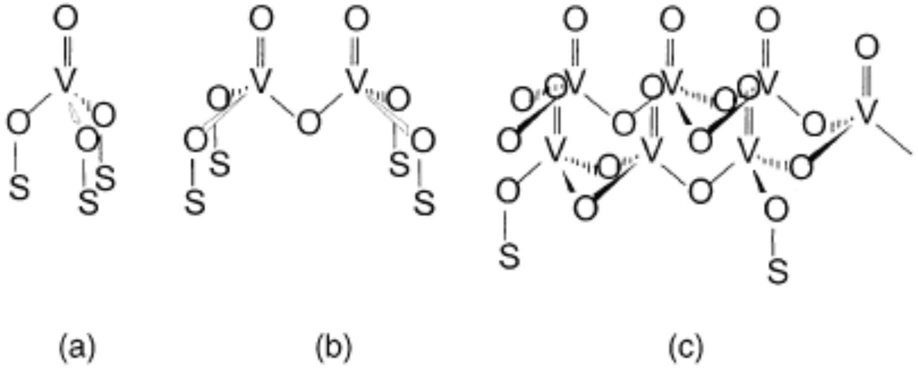

Figure 1.18 Possible molecular configurations for supported vanadium oxides (with S the support cation): (a) isolated vanadium oxide species; (b) dimeric vanadium oxide species; (c) two-dimensional vanadium oxide chains. This figure is reproduced from Ref. [1].

In the catalytic process, the reduction of supported vanadium oxide catalysts at high temperatures in the presence of, e.g. CO and H_2 may lead to the formation of a variety of oxidation states (i.e. V^{5+}, V^{4+} and V^{3+}) and coordination environments (i.e. VO_4, VO_5 and VO_6)[106]. However, not much is presently known about the quantitative distribution of the different vanadium oxide oxidation states (V^{5+}, V^{4+} and V^{3+}) and their exact coordination environment at the catalyst surface after reduction and the parameters influencing the reduction degree of supported vanadium oxides.[1] Thus, much more research efforts should be directed towards the elucidation of supported vanadium oxides under reduced conditions.

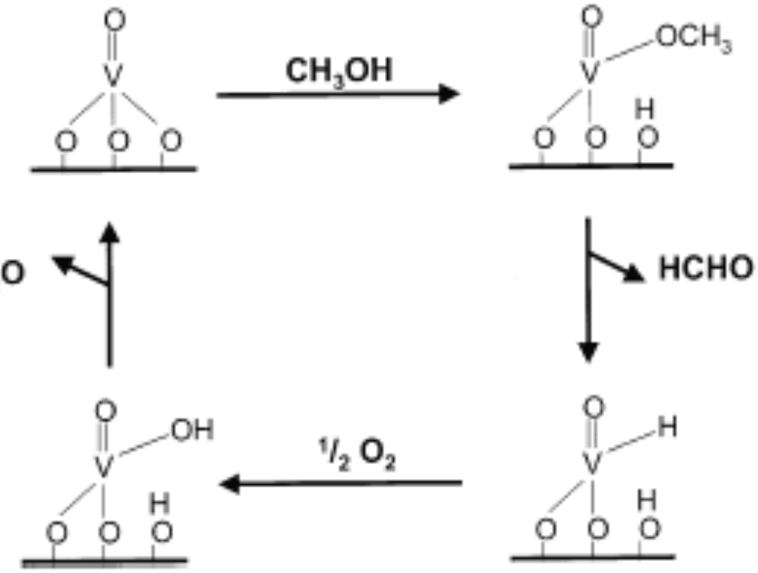

Figure 1.19 Reaction mechanism for the selective oxidation of methanol to formaldehyde over supported vanadium oxide catalysts. This figure is reproduced from Ref. [1].

Another important issue is the catalytic operation during the catalytic process. Weckhuysen and Keller[1] show a particular useful example, which is the selective oxidation of methanol to formaldehyde, because this catalytic reaction can be considered as a simple probe reaction for a number of other selective oxidation reactions.[105] And the concepts developed for the selective oxidation of methanol over supported vanadium oxide catalysts can be easily transferred to these catalytic reactions as well. The selective oxidation of methanol can be written as

$CH_3OH + O_2 \rightarrow CH_2O + H_2O$.

This reaction is usually conducted at 230 ^{o}C in a fixed-bed reactor. During the oxidation of methanol to formaldehyde, the supported vanadium oxide becomes partially reduced by the reaction environment [104, 105]. Figure 2.19 shows the possible reaction mechanism, which is a four-step process. Catalytic measurements show that the selectivity to formaldehyde is 90-99% for V/TiO_2, V/ZrO_2, V/Nb_2O_5 and V/CeO_2, whereas only a selectivity of 50% to formaldehyde was observed for V/Al_2O_3 catalysts.[107] Literature[1] suggests that the extent of reduction during methanol oxidation is rather limited and almost independent of the surface vanadium oxide loading, the specific support and the reaction temperature, meaning that the fraction of supported vanadium oxide is almost constant. It also suggests that the selective oxidation of methanol to formaldehyde over supported vanadium oxide catalysts is a uni-molecular reaction requiring only one surface vanadium oxide species, which can be referred to as the catalytically active site.

1.5.3 Tungsten Oxides

Tungsten oxides have been widely studied in details because of their application in ferroelectric, electro-optic, semiconducting properties[108] and recently in catalysis[109]. The tungsten trioxide crystal shows five phase transitions in the range of -180 to 900 °C changing from tetragonal-orthorhombic-monoclinic-triclinic-monoclinic during cooling[110, 111]. At room temperature a monoclinic (WO_3 I) and triclinic (WO_3 II) modification can be obtained. Literature[108] shows that from *ca* 467 to 680°C WO_3 exhibits orthorhombic symmetry. The structure is perovskite-like with space group *Pmnb* and $a = 7.341$ Å, $b = 7.570$ Å and $c = 7.754$ Å. The deviation from the ideal perovskite structure is characterized by a zigzag motion of the W position in the **b** and **c** directions as well as a tilt system with tilt angles around **a**. Literature [112] also shows that between *ca* -40 and 17 °C tungsten trioxide has a pseudocubic triclinic crystal structure. Its space group is $P\underline{1}$ (C^{1}_{i}), with $a = 7.309$ Å, $b = 7.522$ Å and $c = 7.678$ Å, $\alpha = 88.81°$, $\beta = 90.92°$ and $\gamma = 90.93°$, volume $V = 421.93$ Å^3, and $Z = 8$. The W atoms are off-center in the O octahedral and close to an O triangle, giving three short and three long W-O bonding distances.

As a catalyst, bulk tungsten oxide exhibits acidic functionality in *n*-heptane hydrocracking[113], olefin isomerization[114], and alcohol dehydration reactions[115]. Mixed metal oxides such as Al_2O_3-TiO_2[116], as well as supported metal oxides such as MoO_3 on Al_2O_3 or WO_3 on Al_2O_3[117-119], also display acidic properties. Commonly tungsten oxides are used as one of the mixed catalysts in vanadium-tungsten oxide systems to remove nitric oxide from flue gases of stationary sources of emission, such as power and heat plants, nitric acid factories, waste incinerators and stationary diesel engines[120-123]. NO removal in the presence of oxygen occurs via selective catalytic reduction (SCR) by ammonia, based on the reaction[124]:

$$4NO + 4NH_3 + O_2 \rightarrow 4N_2 + 6H_2O$$

Nowadays, industrial catalysts for the SCR process are based on TiO_2-supported V_2O_5-WO_3 and/or V_2O_5-MoO_3 oxides[121, 125]. V_2O_5-WO_3 / TiO_2 catalysts show significant activities for SCR in excess of oxygen already at temperatures near 420 K. Also, experiments, as shown in Figure 2.20, report the conversion of NO measured on different catalysts belonging to the V_2O_5-WO_3/TiO_2 system. It clearly appears that (i) the activity of the catalysts is increased by increasing the V loading, and (ii) the addition of WO_3 increases the activity of V_2O_5/TiO_2 [122]. In all cases it has been found that the best catalysts contain just a few less than a full “monolayer” of vanadium plus tungsten (or molybdenum) oxides over the TiO_2-anatase supports.[122]

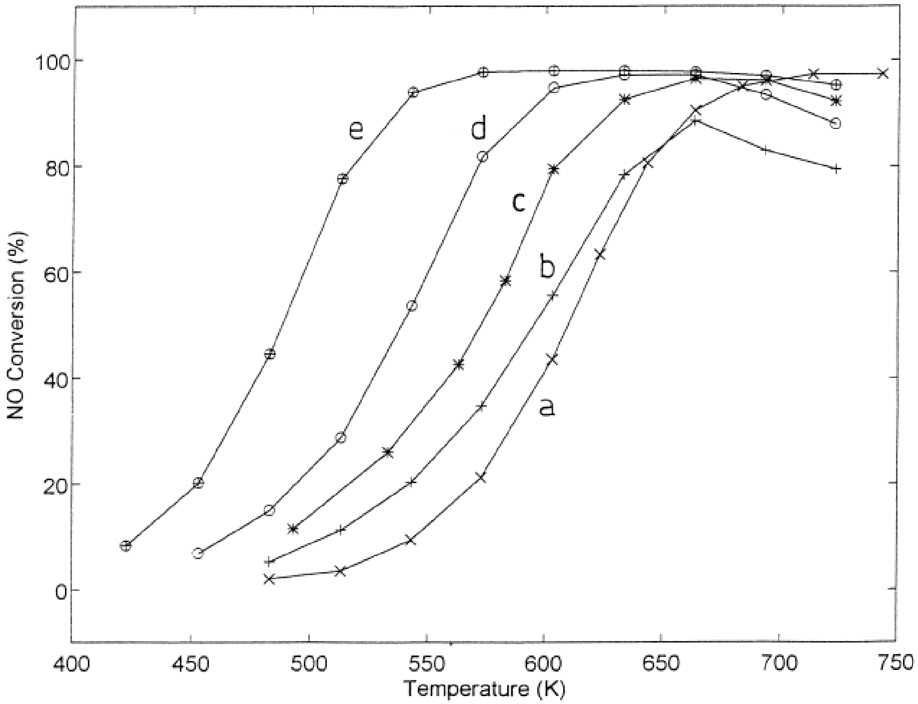

Figure 1.20 NO conversion versus temperature over: (a) WO_3 (9)/TiO_2; (b) V_2O_5 (0.78)/TiO_2; (c) V_2O_5 (1.4)/TiO_2; (d) V_2O_5 (0.78) ±WO_3 (9)/TiO_2; (e) V_2O_5 (1.4) ±WO_3 (9)/TiO_2. Experimental conditions: catalyst weight, 160 mg (60±100 mesh); P.1 atm; flow rate.60 Ncc/min; feed: He.800 ppm NH_3.800 ppm NO .1% O_2. This figure is reproduced from Ref. [125].

Many efforts have been made to grow ordered tungsten oxides on different supports. Tungsten oxide is one of those transition-metal oxides (TMO), which represent a particularly important class of catalytically active oxides. Kim[21] and Feng[81] with their collaborators have reported the growth of ordered sub-monolayer tungsten oxides on oxide single crystals. The ordered tungsten structure on α-TiO_2 (110) is shown in Figure 2.21. In these cases, atomic layer deposition (ALD) was used for controlling the growth. Oxidization-reduction reactions help forming ordered structure.

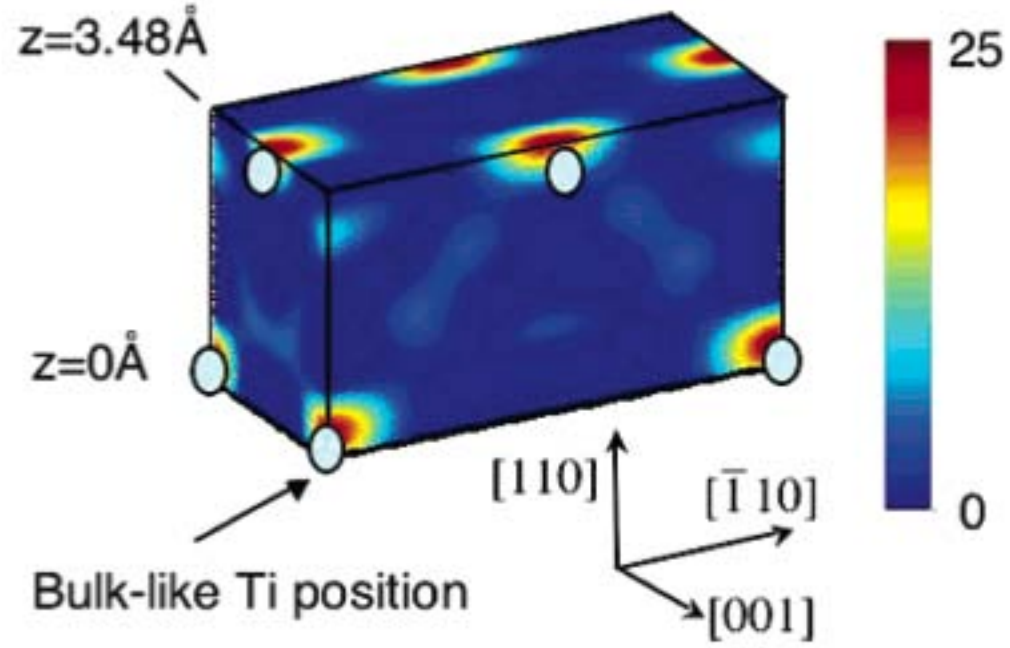

Figure 1.21 Tungsten oxides after atomic layer deposition show ordered structure by occupying the surface bulk-like Ti sites. As a point of reference open circles denoting the ideal bulk-like Ti sites are shown at heights of 0 and 3.25 Å. The hot spots are tungsten density maxima. This figure is reproduced from Ref. [21].

By directly thermal evaporating tungsten trioxide on TiO_2 (110), Bondarchuk et al[126] obtained mono-disperse cyclic $(WO_3)_3$ as shown in STM image in Figure 2.22. Furthermore, they tested those clusters' catalytic properties by dehydrating 2-propanol[127]. Their results show that the clusters provide an extremely efficient dehydration reaction channel for alcohols, which utilizes both strong Lewis acid W (VI) sites and doubly bonded oxygen tungstyl (W=O) groups. However, in their study, $(WO_3)_3$ cluster shows no support effect during reaction. This contrasts with the Bronsted acid based activity of most high surface area WO_x-based support oxide[128, 129]. This could be interesting and worth further investigation.

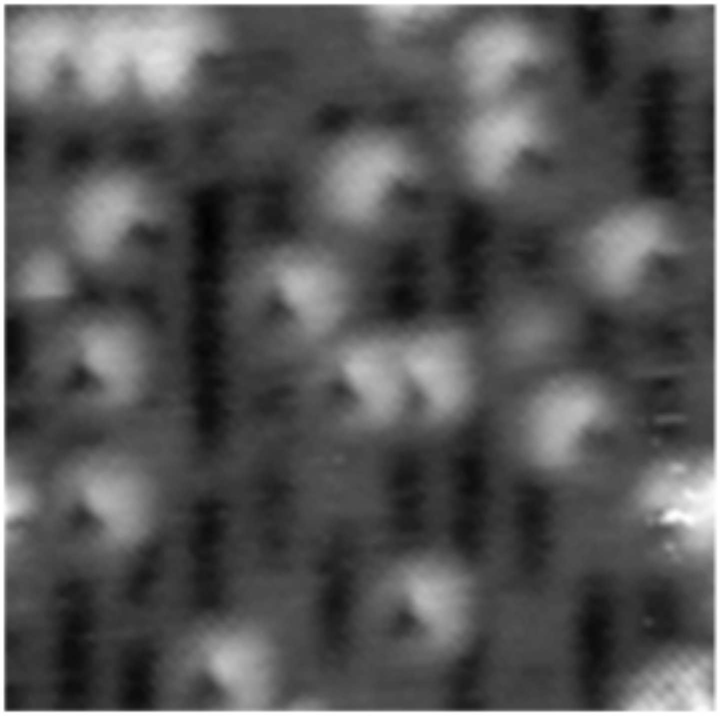

Figure 1.22 STM image exhibits strong trigonal intensity contrast, which implies the formation of $(WO_3)_3$ clusters on $TiO_2(110)$. This figure is reproduced from Ref. [126].

All of the above background information for vanadia and tungsten oxide shows that the two catalysts and their mixtures on supports are very important and of interest to the catalysis community. Further and deeper investigations are needed to understand their physical and chemical behavior during chemical reactions.

1.6 Atomic Layer Deposition (ALD)

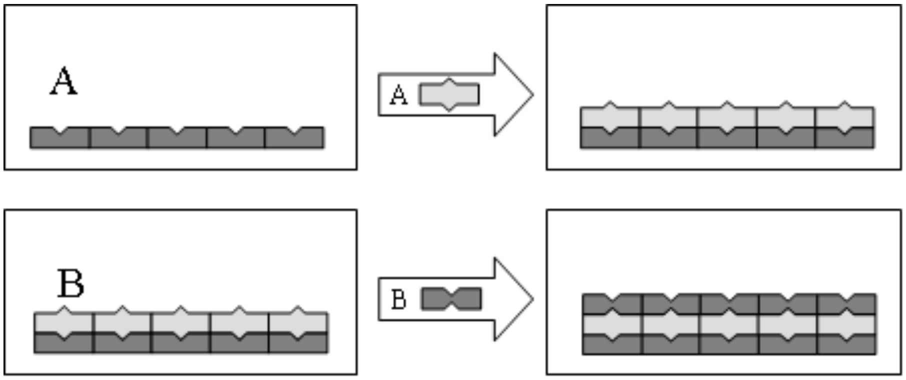

Figure 1.23 The A+B sequence required for Atomic Layer Deposition of one monolayer. The notches in the starting substrate for reaction A represent discrete reactive sites. Exposing this surface to reactant A results in the self-limiting chemisorption of a monolayer of A species. The resulting surface becomes the starting substrate for reaction B. Subsequent exposure to molecule B will cover the surface with a monolayer of B species. Consequently, one AB cycle deposits one monolayer of the compound AB and regenerates the initial substrate. By repeating the binary reaction sequence in an ABAB… fashion, films up to micrometer thickness can be deposited with atomic layer precision.

In this thesis work, Atomic layer deposition (ALD) is the main technique to grown nanoclusters or thin films on oxide single crystal surfaces. ALD is a thin film deposition technique that utilizes self-limiting surface reactions of precursor gases to deposit material in a layer-by-layer fashion[130] (as illustrated in Figure 2.23) upon completion of a precursor dosing sequence known as an ALD cycle. By repeating the binary reaction sequence in an ABAB… fashion, and using current viscous flow reactor designs, monolayer-by-monolayer growth rates as high as 1 micron/hour are possible. This alternating reaction philosophy eliminates the “line of site” or “constant exposure” requirements that make it impossible for conventional metal-organic chemical vapor deposition (MOCVD) to coat porous, high-surface-area catalyst supports. Since the deposit is conformal to the support at the atomic scale, the surface area is largely preserved. The technique has been known[131, 132] since the early 1970’s, but recently has gained more interest as the number of compounds available for deposition has greatly expanded from semiconductors to nitrides, metals, and oxides. ALD oxide compounds, such as hafnium oxide, are of particular interest to serve as state-of-the-art microelectronic gate materials. The motivation behind this and other ALD applications stems from the extreme precision in which ALD uniformly coats complex support geometries[133-135].

The precision of ALD is based on the reliance of precursors that react with the surface, but not each other. Precursor molecules typically constitute an organometallic compound and an oxidizing or reducing agent such as oxygen, hydrogen, or steam. The first precursor dose, typically the organometallic, will saturate the reactive sites on the surface through chemisorption. The ALD cycle is completed by a second precursor dose that only reacts with the adsorbed precursor species from the first dose. Usually, the second precursor liberates the remaining organic ligands on the adsorbed precursor to create a surface that is reactive to the next organometallic pulse. The classic ALD example is aluminum oxide using trimethylaluminum and steam[136]. The deposition proceeds with trimethylaluminum reacting with hydroxyl groups on the surface to liberate a methane molecule. The steam dose then liberates the remaining methyl groups to leave behind the deposited Al atoms attached to hydroxyl groups that are ready for the next trimethylaluminum dose. Steady state growth then proceeds where the ALD occurs on the Al_2O_3 film deposited in earlier cycles.

The formation of a film may not always occur in the first few ALD cycles as the process strongly depends on how efficiently a monolayer of precursor will adsorb on the surface. The efficiency of ALD in the early stages will be related to the precursor pressure, dosing time, reactivity of the surface, and the temperature. These factors combine to give a growth regime where an incomplete film forms and eventually coalesces leading to the steady state growth regime as the number of cycles increase. ALD at the early stages has not been widely studied and consequently a number of interesting opportunities arise to extend the capabilities of the technique. The key prospect related to this project is the formation of nanoparticles due to the incomplete coalescence of a film for the case of platinum. Noble metal ALD chemistries are particularly prone to the formation of nanoparticles[133, 135, 137-140]. A detailed understanding of the nucleation, growth and coalescence of the nanoparticles is needed at the nanometer length scale in order to systematically pursue the technological application of such nanoparticles from ALD.

By repeating the binary reaction sequence in an ABAB… fashion, and using current viscous flow reactor designs, monolayer-by-monolayer growth rates as high as 1 micron/hour are possible. This alternating reaction philosophy eliminates the “line of site” or “constant exposure” requirements that make it impossible for conventional metal-organic chemical vapor deposition (MOCVD) to coat porous, high-surface-area catalyst supports. Since the deposit is conformal to the support at the atomic scale, the surface area is largely preserved. Figure 2.24 shows the growth of VO_x/TiO_2 by a gas phase preparation technique[141]. Figure 2.24(b) illustrates the ALD growth used in my work.

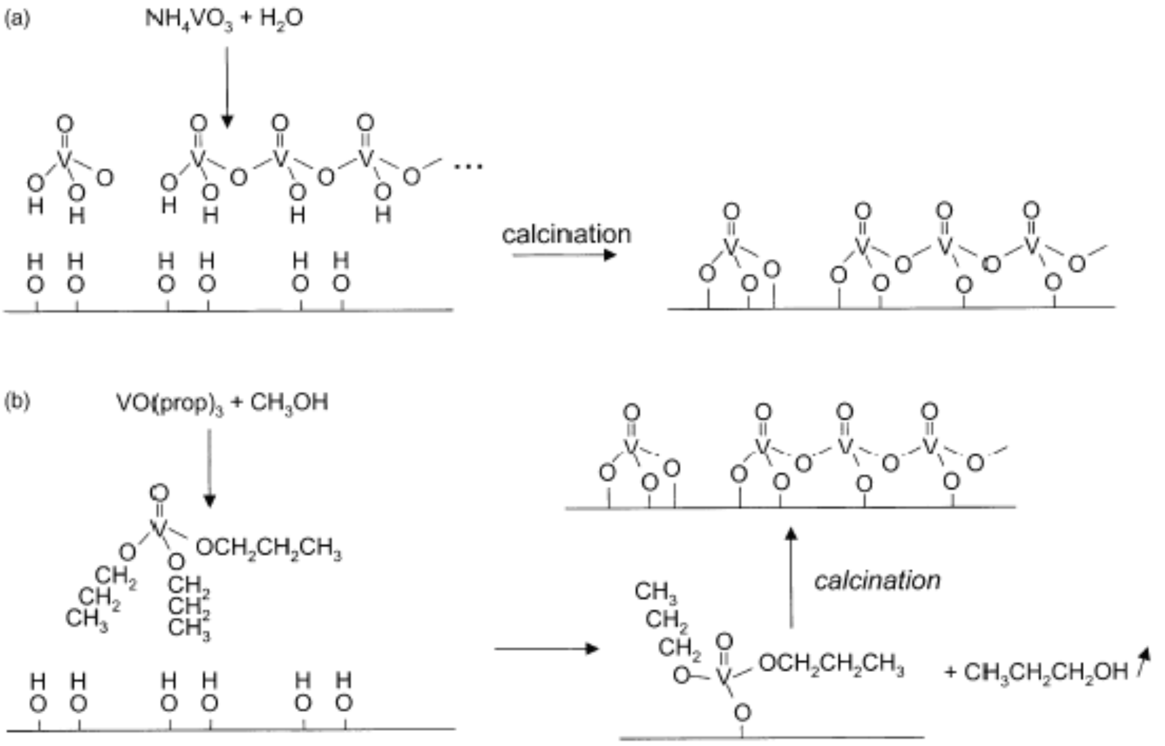

Figure 1.24 Synthesis methods for the preparation of supported vanadium oxide catalysts: (a) impregnation with an aqueous solution of NH_4VO_3, followed by calcination in oxygen and (b) impregnation with $VO(OC_3H_7)_3$ in methanol, followed by calcination in oxygen or air and release of propanol. This figure is reproduced from Ref. [1].

Chapter 2: Experimental Method and Setup

2.1 Why X-ray and Synchrotron?

X-rays, which interact weakly with matter, are ideal for probing buried interfaces or interfaces under “real” gas reaction conditions. X-ray elastic scattering is dominated by Thomson scattering from electrons in the medium. The wavelength of hard X-rays is roughly 1 Å, which is the same scale as the atom size. The resolution of the X-ray measurements can easily be achieved at < 1 Å level. Therefore X-ray based methods are good candidates for in situ probing of atomic scale structures.

Based on the photoelectric effect an X-ray can be absorbed by an atom causing an inner core electron to be emitted, leaving an ion in an excited state that decays by, the emission of a fluorescence photon or Auger electron. The spectral analysis of the energies of the emitted primary photoelectrons and secondary fluorescence photons and Auger electrons is element specific due to the distinct atomic energy levels. An X-ray carries no charge, so it does not bring or take away electrons from the sample directly, though electrons can be removed from atoms either directly through photoelectron emission or indirectly through secondary processes. Little or no net charge accumulation on the sample means that a conducting substrate is not required, which is quite important for studying oxides since they are mostly insulators.

The theory of X-ray interactions with matter has been well developed.[142, 143] Consequently, data from X-ray measurements can be quantitatively associated with the atomic structure of the sample. For example, kinematical scattering theory can often be applied for the surface X-ray scattering measurements (excluding the Bragg peaks, where the dynamical diffraction theory should be applied) because of the weak interaction with matters[143-145]. The atomic structure information can be retrieved with the direct relation between structure and measured data[146-148].

The third generation synchrotrons offer high-brilliance X-ray sources, which can be highly collimated, polarized and tunable in energy by adjusting the undulator gap.[149] The higher intensity and smaller X-ray source size make it possible to probe much weaker signals thus achieve higher resolution in the surface structure study as well as to study the dynamical processes in real-time. X-ray beam cross sections, depending on the source and optics used, are normally macroscopic sizes, which are practically larger than a few micrometers across even after being focused and/or cut down with slits. While this means, on the one hand, that no information about a single atom can be obtained, on the other hand the data are statistically averaged over a large quantity of atoms and are less sensitive to the local structure disturbance (such as defects) and thus yield the overall structure.

2.2 X-ray Standing Wave Method

2.2.1 Basic Concepts

X-ray standing wave (XSW) field can be produced by superposition of two coherently coupled X-ray beams [150-153], as shown in Figure 3.1 [23]. The XSW period D is given by

$$D = \frac{\lambda}{2\sin(2\theta/2)} = \frac{2\pi}{q}, \tag{3.1}$$

where λ is the wavelength of X-ray; $q=|\boldsymbol{Q}|$, is the amplitude of the scattering vector (or standing wave vector). $\boldsymbol{Q} = \boldsymbol{K_f} - \boldsymbol{K_0}$; $\boldsymbol{K_0}$ and $\boldsymbol{K_f}$ are the wave vectors of the two traveling waves, respectively, with the amplitudes $|\boldsymbol{K_0}| = |\boldsymbol{K_f}| = 2\pi/\lambda$; and 2θ is the angle between them. The XSW period will change when the angle 2θ changes. Since $\lambda \sim 1$ Å, it is typical to obtain an XSW period ranging from a few Angstroms (at larger values of 2θ, e.g., corresponding to single crystal Bragg diffraction) up to a few hundred Angstroms (at small values of 2θ, e.g., corresponding to total external reflection). If the relative phase between the two waves, v, changes, the XSW field will shift in space. As shown in Figure 3.1(A) and (B), upon shifting one wave with respect to another by $\lambda/2$, i.e., the relative phase between them changes from $v = 0$ to $v = \pi$, while keeping the XSW period the same, the XSW anti-node positions (marked with solid line) moves by half the d-spacing, i.e., the XSW field shifts by $D/2$. These features of the XSW field can be taken advantage of as an atomic scale probe by monitoring the photoelectric effect, such as photoelectron emission, X-ray fluorescence, and/or Auger electron emission.

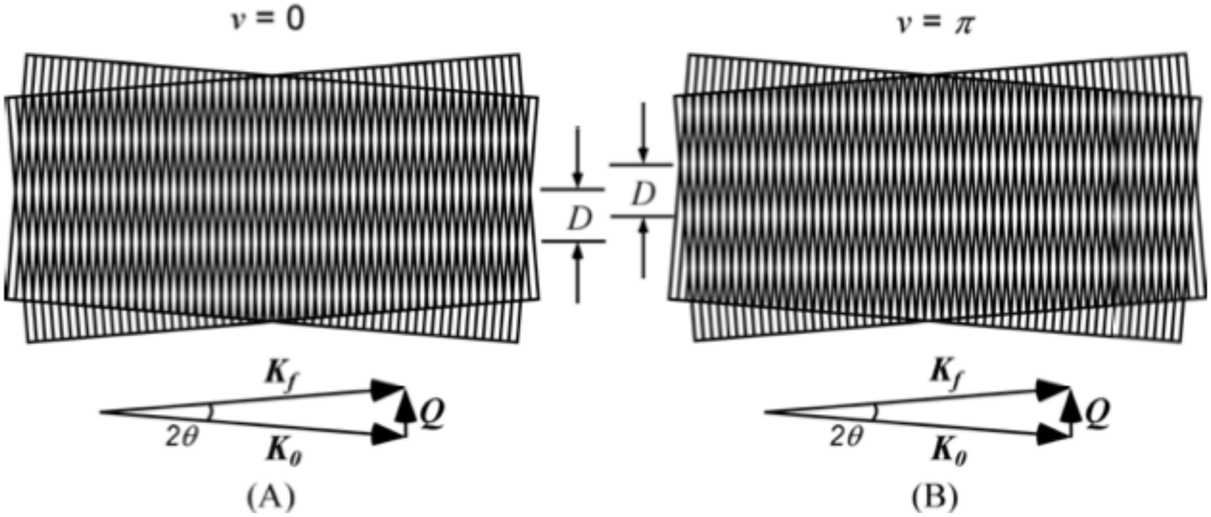

(A) (B)

Figure 2.1 XSW generated by two coherently interacted parallel X-ray beams. The XSW period is D, the wavelength is λ and two beam traveling with angle 2θ. The phases between the two plane waves, v, are (A) 0 and (B) π, respectively. This figure is reproduced from Ref. [153].

There are several ways to generate XSW fields, such as the strong Bragg reflection from a single crystal, total external reflection (TER) from a mirror surface, the strong Bragg reflection of a periodic layered synthetic microstructure, etc. In my thesis, we used single crystal Bragg diffraction to generate the XSW. At the Bragg condition, as shown in Figure 3.2, the diffracted X-rays interfere coherently with incoming X-rays to form a standing wave field in[150] and above the surface[154] of the single crystal. The XSW period matches the period of the diffraction planes. When the incident angle is scanned from the low-angle side to the high-angle side of this arc-second wide *H* (=*hkl*) Bragg condition, the relative phase of XSW field decreases by π radians. This causes the XSW antinodal planes to move by one-half of a *d* spacing (d_H) in the **–H** direction. When scanning across the rocking curve, the shift of the XSW can induce the X-ray fluorescence (XRF) modulation.

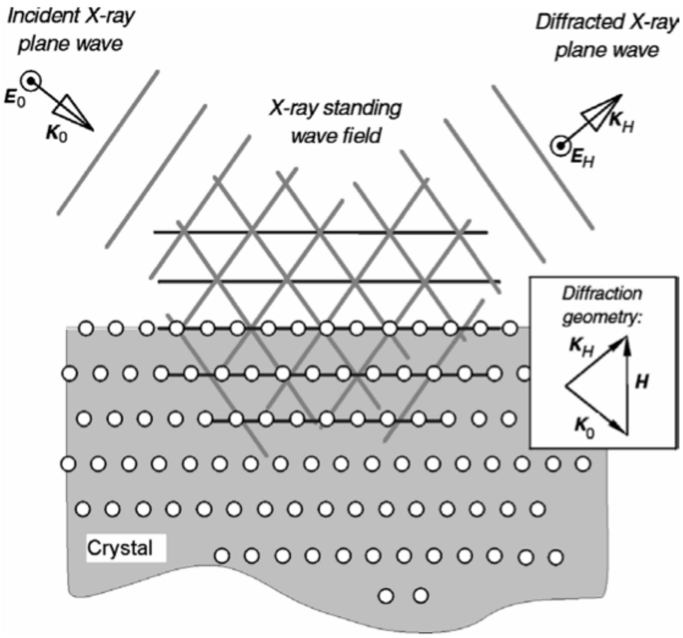

Figure 2.2 X-ray standing wave field generated at the strong Bragg condition. This figure is reproduced from Ref. [153].

In the dipole approximation the photoelectric effect cross section is proportional to the *E*-field intensity at the center of the atom. Thus the normalized fluorescence yield $Y(\theta)$ can be expressed as

$$Y(\theta) = \left[1 + R(\theta) + 2\sqrt{R(\theta)} f_H \cos\left(\nu(\theta) - 2\pi P_H\right)\right] Z(\theta), \qquad (3.2)$$

where $R(\theta) = \left| E_H(\theta) \big/ E_0 \right|^2$ is the reflectivity, $\nu(\theta)$ is the phase between the reflected and the incident X-ray planes wave, $Z(\theta)$ is the effective-thickness factor.[155] $Z(\theta) = \dfrac{\mu_0 (\sin\theta)^{-1} + \mu_f(\alpha)'}{\mu_z(\theta) + \mu_f(\alpha)}$

$\mu_z(\theta)$ is the effective absorption coefficient of the incident X-rays and $\mu_f(\alpha)$ is the effective absorption coefficient of the outgoing fluorescence X-rays from the crystal at takeoff angle, α.[153] $Z(\theta) = 1$ for atoms above the surface of the crystal. $Z(\theta) \sim 1$ at a depth much less than the extinction depth. Both $R(\theta)$ and $\nu(\theta)$ can be calculated directly from the known bulk structure using dynamic diffraction theory. f_H and P_H in this equation are coherent fraction and coherent position for the measured element, respectively. They are also the amplitude and phase of the corresponding *H*th Fourier component of the XRF-selected atom density distribution. Namely,

$$F_H = \int_{uc} \rho(r) \exp(iH \cdot r) dr = f_H \exp(2\pi i P_H). \qquad (3.3)$$

Both f_H and P_H are unitless quantities ranging between 0 and 1.

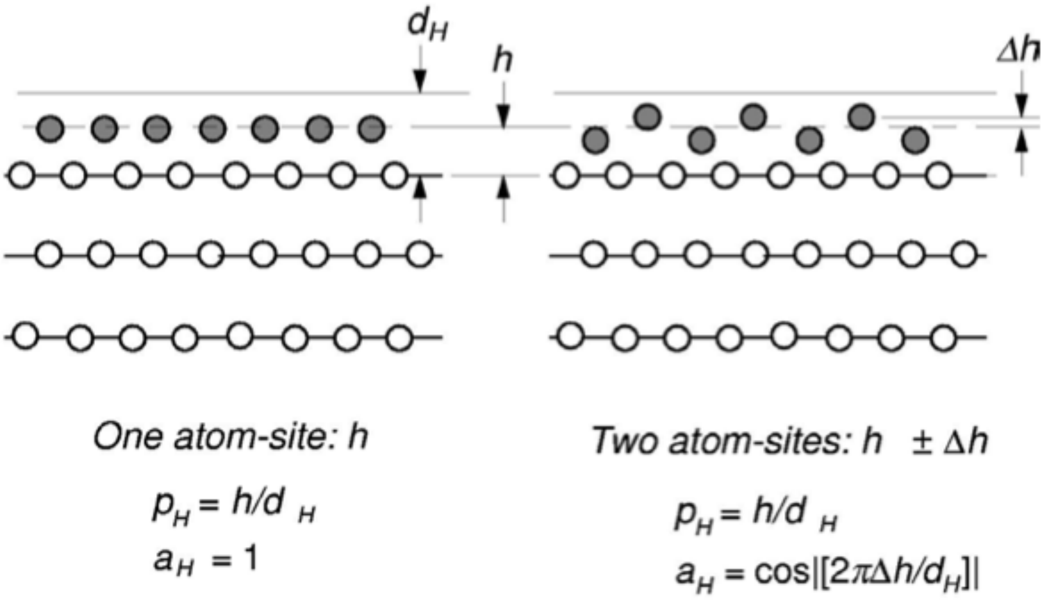

Figure 2.3 Illustration of single height adsorbed atoms (left) and double-height adsorbed atoms (right) on single crystal surface with respect to diffraction plane spacing d_H. The dark circles are adsorbed atoms. In both cases the atomic distribution has the same coherent position with respect to d_H; but different coherent fractions. This figure is reproduced from Ref. [153].

There is another way to understand the two parameters, as illustrated in Figure 3.3. The coherent fraction f_H is a measure of the spatial distribution of the fluorescent atoms, and it can be approximated as,

$$f_H = Ca_H D_H, \tag{3.4}$$

where C is the ordered fraction, a_H is the geometrical factor, and D_H is the Debye-Waller factor. All three factors range in value from 0 to 1. The ordered fraction C is the fraction of the atoms that are coherently located or are crystallographically registered with the substrate crystal lattice. If the atoms' occupation fractions for the ordered positions are c_1, c_2,..., c_N, respectively, the ordered fraction is given by

$$C = \sum_{j=1}^{N} c_j \quad . \tag{3.5}$$

Since the geometrical factor a_H is the modulus of the normalized geometrical structure factor S_H for the ordered fluorescent-selected atoms:

$$S_H = \frac{1}{C} \sum_{j=1}^{N} \left[c_j \exp\left(2\pi i \boldsymbol{H} \bullet \boldsymbol{r}_j\right) \right] , \tag{3.6}$$

Thus, the geometrical factor is the amplitude of S_H,

$$a_H = \frac{1}{C} \left| \sum_{j=1}^{N} \left[c_j \exp\left(2\pi i \boldsymbol{H} \bullet \boldsymbol{r}_j\right) \right] \right| , \tag{3.7}$$

and the coherent position is the phase of S_H,

$$P_H = \frac{1}{2\pi} Arg \left\{ \sum_{i=1}^{N} \left[c_i \exp\left(2\pi i H \bullet r_i\right) \right] \right\} . \tag{3.8}$$

Generally, Debye-Waller factor D_H can be expressed in terms of the mean-square vibrational amplitude along the ***H*** direction, $\langle u_H^2 \rangle$, as

$$D_H = \exp(-M) = \exp\left({-2\pi^2 \langle u_H^2 \rangle} \big/ {d_H^2} \right) . \tag{3.9}$$

2.2.2 XSW Direct-Space Imaging

Note in equation (3.2), by fitting the fluorescence yield, the two parameters, f_H and P_H, are model-independent quantities determined by the fit. Based on equation (3.3), if a set of f_H and P_H values is obtained from the XSW measurements, the distribution $\rho(\boldsymbol{r})$ of each fluorescent atomic species can be synthesized directly by the Fourier summation

$$\rho(\mathbf{r}) = \sum_{\mathbf{H}} f_H \exp\left[2\pi i\left(P_H - \mathbf{H}\cdot\mathbf{r}\right)\right] = 1 + 2\sum_{\substack{\mathbf{H}\neq-\mathbf{H}\\ \mathbf{H}\neq 0}} f_H \cos\left[2\pi\left(P_H - \mathbf{H}\cdot\mathbf{r}\right)\right]. \tag{3.10}$$

The above simplification to a summation of cosine terms makes use of the symmetry relationships analogous to Friedel's law: $f_{-H} = f_H$, $P_{-H} = -P_H$. It also uses $f_0 = 1$ for a normalized atom distribution. In this way, XSW method preserves the phase information, P_H. This method is unlike the simple or traditional X-ray diffraction methods, which lose the phase information. As previously derived and experimentally proven[155], the phase of the XSW is directly linked to the phase of the structure factor. This is an essential feature of the XSW method that makes it unique; namely, it does not suffer from the well known "phase problem" of X-ray diffraction. Therefore, a density map can be generated and the direct-space imaging is possible to tell the structural and distribution information of the fluorescent atoms on the surface.

Experimentally it has been demonstrated that by direct Fourier inversion (Eq. 3.10) one can obtain the real-space $\rho(\mathbf{r})$ (in the case of lattice and impurity atoms in muscovite) [156]. Unlike the traditional method for analyzing the Bragg XSW data[23], this XSW direct-space method does not require a structural model for interpretation of the lattice positions of the bulk impurity atoms or surface adatoms . From the ~0.5 Å resolution 3D model-independent image a new more complicated model should emerge that when fitted to the data should give high-resolution (± 0.02Å) adsorbate-site positions. It should be stressed that the Bragg XSW positional information is in the same absolute coordinate system as used for describing the substrate unit cell. This unit cell and its origin were previously chosen when the structure factors F_H and $F_{\overline{H}}$ were calculated from the known bulk structure using dynamic diffraction theory. By projecting the model-independent density maps onto this unit cell, the locations of the surface adsorbed atoms can be obtained and so does their distribution. Figure 3.4 shows this method. In this case, 0.74 ML vanadium oxide was deposited onto the surface of α-TiO_2(110).[157] By summing the 5 sets of measured f_H and P_H into equation (10), the vanadium atomic density map is obtained in the coordination of α-TiO_2 (110) surface unit cell, which is described in Figure 2.3. Therefore, we can identify where vanadium cations are located with respect to the substrate unit cell.

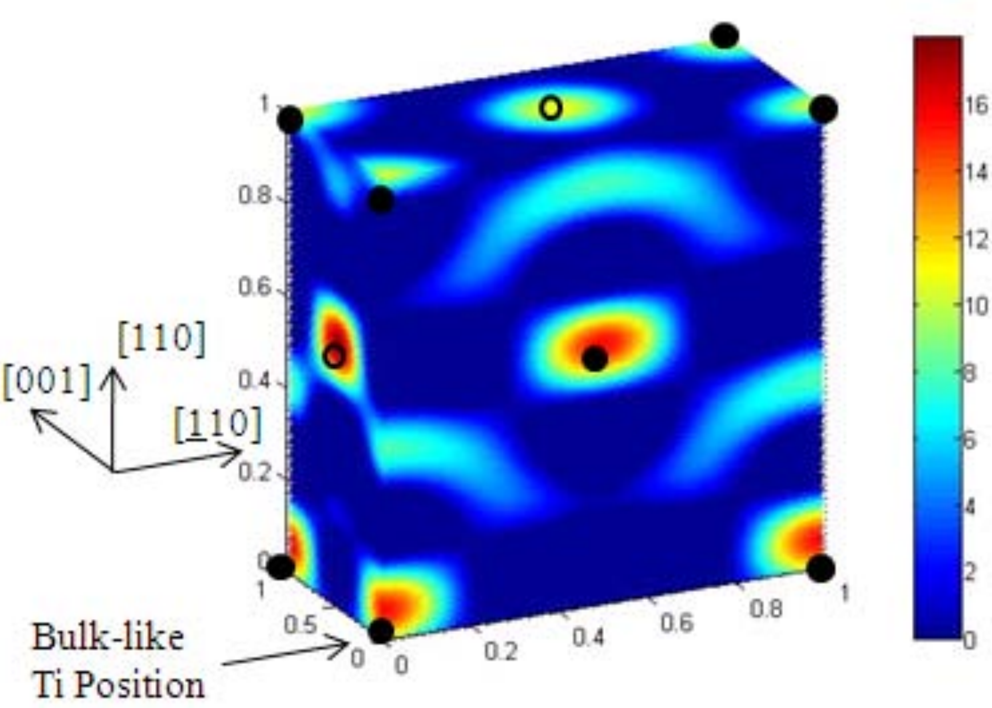

Figure 2.4 X-ray standing wave direct-space imaging by projecting the vanadium atomic density map onto the α-TiO_2 (110) surface unit cell described in Figure 2.3. The open and solid circles denote two different symmetry inequivalent bulk-like Ti sites. In this case, it is ¾ ML vanadia deposited onto rutile surface by ALD method.

2.2.3 Creating Atomic Density Maps and Global Fitting Analysis

In reality, one cannot measure infinite sets of f_H and P_H to complete the Fourier summation in equation (3.10). Thus, the resolution of this direct-space imaging will be limited to one-half of the smallest *d*-spacing that has been entered into the summation in that direction [158]. This imaging method in *3D* is especially useful for solving multi-site surface adsorbate phases. After this typically 0.5-Å-resolution model-independent analysis step, the measured f_H and P_H values can be used to refine the parameters of a structural model (suggested by the imaging method).

By using the symmetry of the single crystal, one can have more sets of f_H and P_H than what one has measured. For example, in XSW measurements of α-TiO_2 (110), measured f_H and P_H values of (020) reflection can be expected to be the same as (200). When picking symmetry equivalent *hkl*'s for a surface adatom distribution, we must preserve the fact that the symmetry is broken in the vertical direction. It should be emphasized here that choosing correct set of hkl reflections for measurements is very important. Simulations[23] show that the more reflections used, the finer the derived profile. But the simulated profiles could also reveal "false" atom locations depending on the chosen set of *hkl*'s. If a subset of reflections selected overwhelmingly presents one or more symmetry components, the same symmetries will show up in the constructed element density profile. Therefore, in practice, selecting a complete set within a limited range of reciprocal space is more important than measuring more reflections from a single subset containing the same symmetry components. Even with a few or only one reflection, the elemental distribution is clearly shown on the image. A rule of thumb is to determine the outermost *hkl* (smallest d-spacing) for which an XSW data set (with acceptable quality measuring time) can be obtained and then to measure all symmetry-inequivalent *hkl*'s within the reciprocal-space volume defined by this outermost *hkl*. Figures 3.5, 3.6, 3.7 show the stereographic projection and reciprocal space projection of hkl and their symmetry equivalents used in Fourier summation for α-TiO2(110), α-Fe_2O_3(001) and $SrTiO_3$(001), respectively.

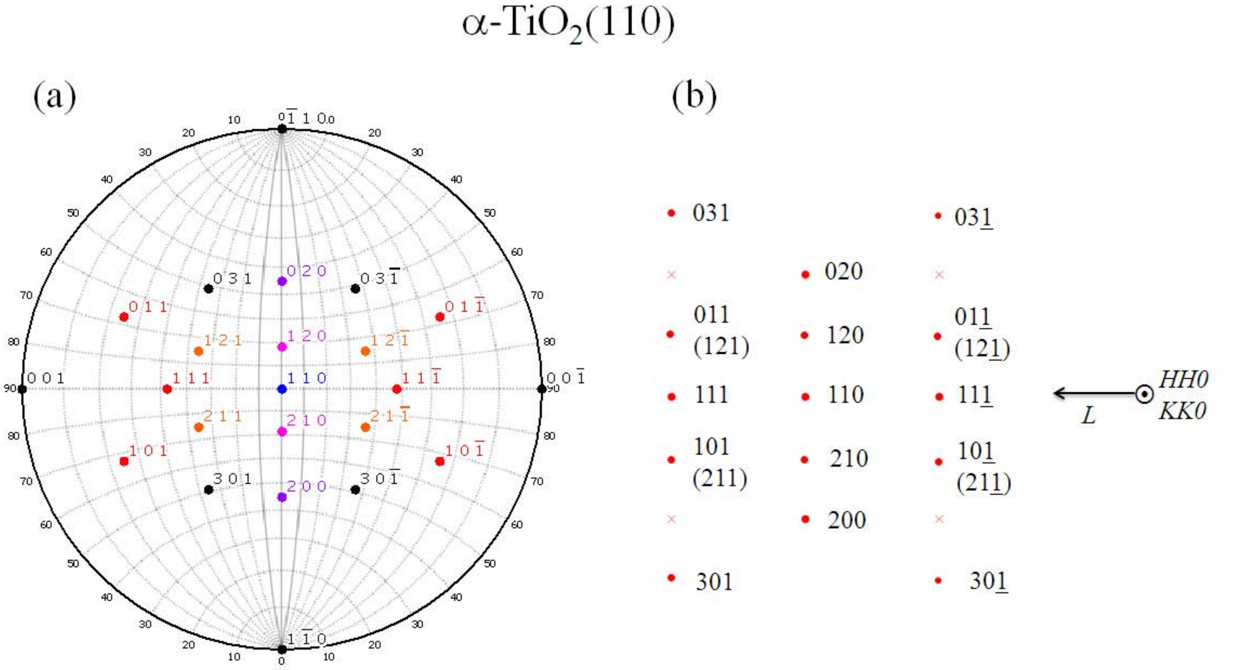

Figure 2.5 (a) The (110) stereographic projection for α-TiO_2. The *hkl* poles are referenced to the standard tetragonal-P unit cell. (b) The (110) projection of the α-TiO_2 reciprocal space lattice, only showing hkl's that were used in the Fourier summation. An hkl point listed in parenthesis is located directly above the *hkl* not in parenthesis. The set of symmetry inequivalent *hkl's* are contained in the lower-left octant.

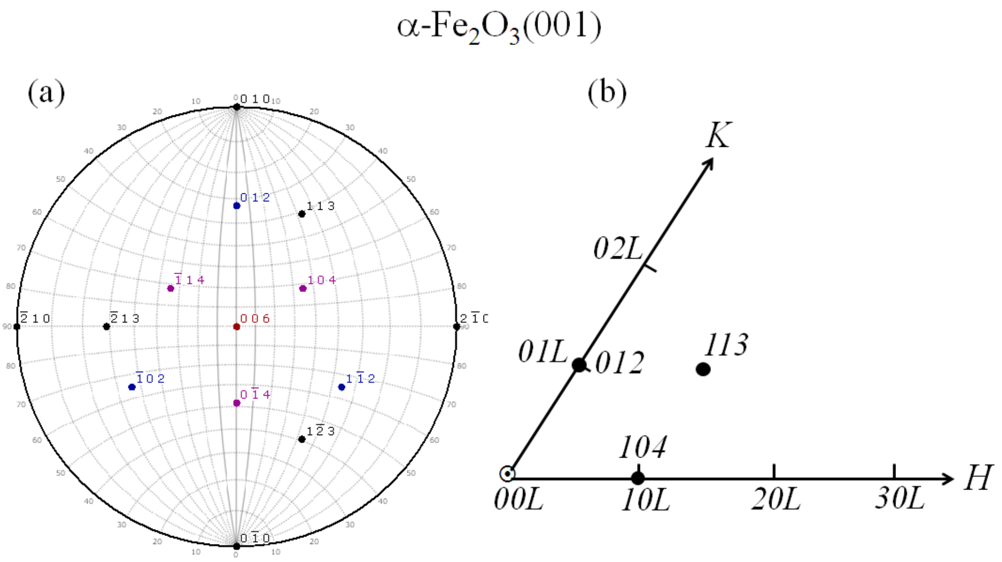

Figure 2.6 (a) The (*00l*) stereographic projection for α-Fe_2O_3. The *hkl* poles are referenced to the standard hexagonal unit cell. (b) The (*00l*) projection of the α-Fe_2O_3 reciprocal space lattice, only showing symmetry inequivalent *hkl's* that were used in the Fourier summation.

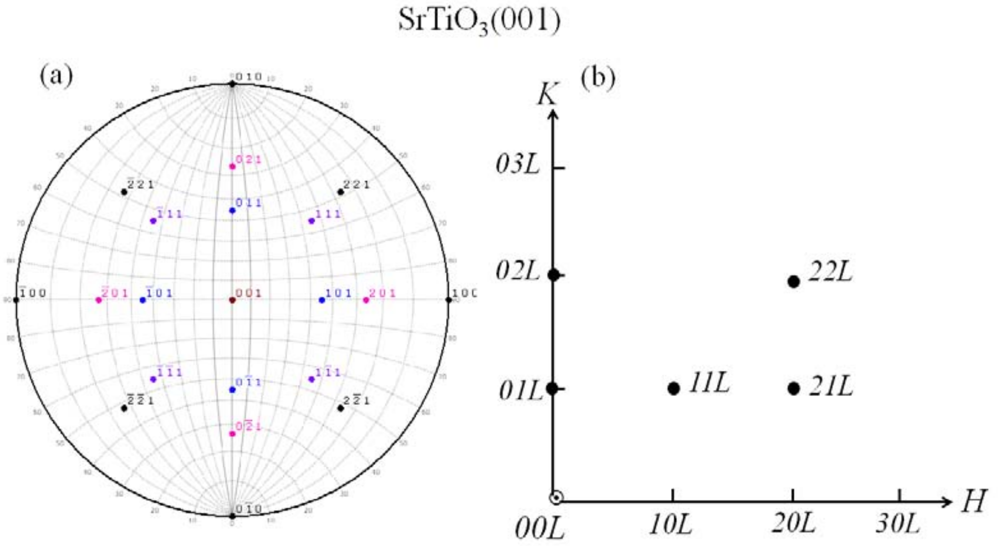

Figure 2.7 (a) The (001) stereographic projection for $SrTiO_3$. (b) The (001) projection of the $SrTiO_3$(001).reciprocal space lattice, only showing symmetry inequivalent *hkl's* that were used in the Fourier summation.

Although the direct-space imaging is model-independent and can provide useful information, the resolution in a given direction is limited to the smallest *d* spacing measured in that direction. Therefore, the subsequent step of model-dependent analysis is necessary for better understanding. With it, the resolution can be as high as 0.02 Å. Suggested by the model-independent maps, a better model can be proposed. Then a global fitting procedure helps refine those parameters to get information such as the ordered fraction of adsorbed atoms at certain sites, heights of those atoms, etc. Escuadro[35] gave one example for applying the global fitting procedure. Kim[8, 21, 159] and Feng[81] developed these procedures. Assuming the density of adsorbed atoms at certain sites, $\rho(r)$, is described by delta functions. Equation 3.3 will give

$$F_H = \int \rho(r)\exp(iH\cdot r) = f_H \exp(2\pi i P_H) = \sum_j c_j \exp(2\pi i H\cdot r_j), \qquad (3.11)$$

where index j is summed over the all possible sites on the surface, vector $\boldsymbol{r_j}$ locates the adsorbed atom at the jth site, and c_j refers to the occupation fraction at the jth site. In most cases, this assumption of delta functions is too simple. An improved approximation is to model the density of adsorbed atoms as spread out. A Gaussian distribution is better to represent the density of the atoms at certain sites. Then equation (3.11) changes to

$$F_H = f_H \exp(2\pi i P_H) = \sum_j c_j \exp\left[-2\pi^2\left(h^2\sigma_x^2 + k^2\sigma_y^2 + l^2\sigma_z^2\right)\right]\exp(2\pi i H\cdot r_j), \qquad (3.12)$$

where σ is the width of the Gaussian distribution in the x, y or z direction and accounts for dynamic and static displacements of the atoms with respect to a unit cell location. In this case, the area under this Gaussian distribution gives the occupation fraction of the adsorbed atoms at or around a certain site.

2.3 X-ray Photoelectron Spectroscopy

X-ray photoelectron spectroscopy (XPS) is a powerful surface analytical technique, which is mostly used to probe the chemical states of certain element on the surface.[160] XPS is based on the photoelectric effect. Each atom in the material has core electrons with characteristic binding energies, which is conceptually, not strictly, equal to the ionization energy of that electron. When the surface of a solid is exposed to an X-ray beam, the atoms in the sample will absorb the X-ray photon energy. If the photon energy is large enough, the core electron will then be emitted as a photoelectron. The binding energy of the core electron is given by the famous Einstein relationship:

$$E_b = h\nu - E_k - \phi, \tag{3.13}$$

where $h\nu$ is the X-ray photon energy, E_k is the kinetic energy of photoelectron, which can be measured by the energy analyzer, and ϕ is the work function induced by the analyzer (typically 4~5 eV). The work function in the measurement can be compensated artificially and then eliminated. The XPS system and working principle are illustrated in Figure 3.8[161].

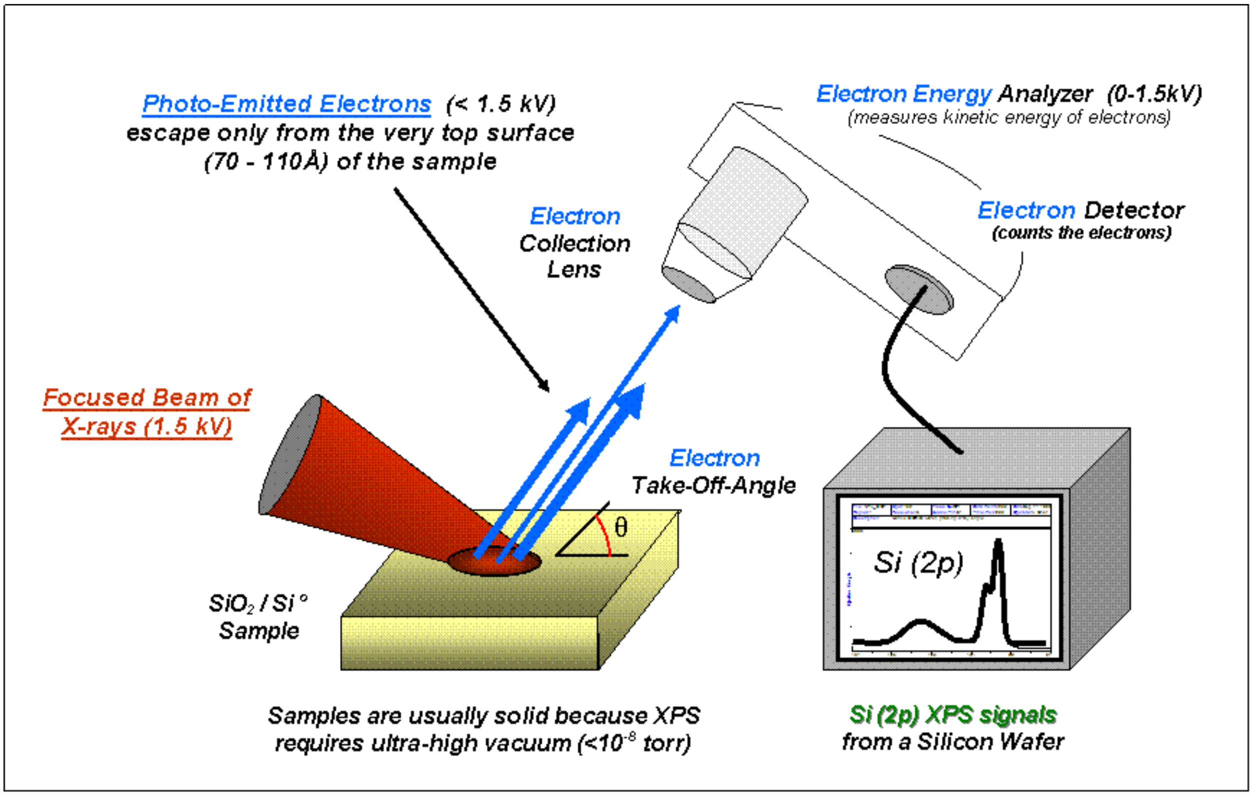

Figure 2.8 Simple illustration of monochromatic XPS system, which includes the X-ray source, electron detector and readout system (computer). This figure is reproduced from Wikipedia webpage: http://en.wikipedia.org/wiki/X-ray_photoelectron_spectroscopy

When measuring insulating samples, a positive potential zone forms on the surface because of electron emission from the sample. This reduces the kinetic energies of core electrons by amount C:

$$E_b = h\nu - \left(E_k - C\right) . \tag{3.14}$$

Consequently, this reduction of the kinetic energies of the core electron causes a shift in the XPS spectrum. In this case, an internal reference peak is needed to calibrate the binding energy. Typically the C 1s (284.8 eV) peak from the adventitious carbon-based contaminant is commonly used as the reference for calibration. Furthermore, to neutralize the surface charge during data acquisition, a low-energy electron flood gun is typically used to deliver the electrons to the sample surface. By tuning the electron flood gun, XPS peaks can be "pushed" back to the real position.

Since the binding energy of the core electron of an element is unique, like fluorescence. XPS can identify all elements, except hydrogen and helium, by measuring the binding energies of the core electrons[162]. Moreover, the binding energy is very sensitive to the chemical environments of the element. The same atom bonded to a different chemical species shows changes in the binding energy of its core electron, causing 0.1 eV to 10 eV shift of the corresponding XPS peak. This "chemical shift" can be applied to study the chemical status of element in the surface, making XPS an excellent tool for probing surface chemistry of elements. [REF] XPS is also useful for quantifying the elemental composition or their ratio in the sample, since the number of photoelectron of an element is dependent on the atomic concentration of that element in the sample. After the value of peak intensity (the peak area after background removal) is obtained, the atomic concentration of an element, C_i, can be obtained as:

$$C_i = \frac{I_i / S_i}{\sum_i I_i / S_i}, \tag{3.15}$$

where I_i is the peak intensity for element i, and S_i is the sensitivity factor for the peak i.

2.4 X-ray Absorption Fine Structure Method

X-ray absorption fine structure (XAFS) method[163] makes use of the absorption phenomena of X-rays passing through materials. XAFS measures the absorption of X-rays as a function of incident energy. The linear absorption coefficient $\mu(E) = -d\ln I/dx$, when plotting along the energy *E* (Figure 3.9), shows three general features[164]: (1) Decreasing of X-ray absorption with increasing energy. This is related to the well-understood quantum-mechanical phenomenon of X-ray absorption by atoms. (2) The presence of a sharp rise at certain energy edges. This is unique to a given absorption atom because it reflects the excitation energy of inner-shell electrons. (3) Above the edges, a series of wiggles or oscillatory structure that modulate the absorption. This feature reveals the structural information of atoms in the materials.

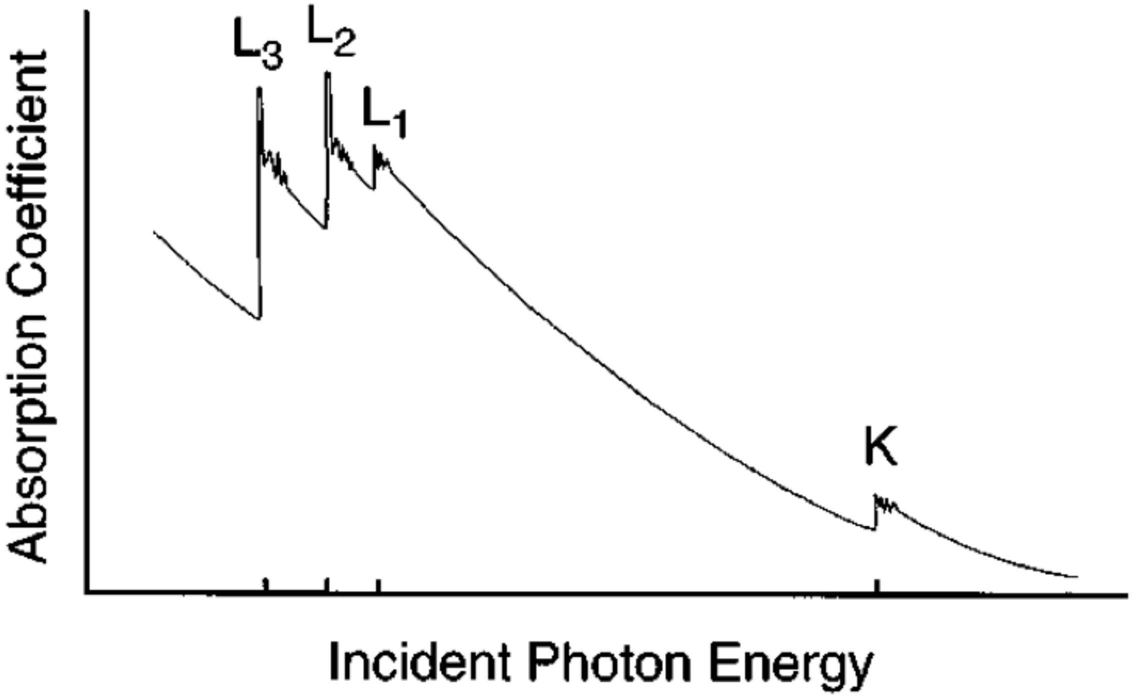

Figure 2.9 A typical X-ray absorption fine structure spectrums, in which the absorption coefficient changes as a function of incident photon energy. This figure is reproduced from Ref.[164].

XAFS includes two parts during the analysis, namely, X-ray absorption near-edge structure (XANES) and extended X-ray absorption fine structure (EXAFS). XANES gives information about chemical state and site symmetry, and EXAFS provides information about interatomic distances, R_i, coordination numbers, N_i, statistical spread (root mean square) of the distances, σ_i^2, due to thermal motion and/or static disorder, and chemical species via characteristic backscattering amplitude, $|f_i(k)|$, and phase shift, $\varphi(k)$[165]. From the XAFS spectrum, an equation can describe the intensity oscillation[163, 164]:

$$\chi(k) = \sum_i \frac{N_i(\theta)|f_i(k)|S_0^2}{kR_i^2} \sin\left[2R_i k + \varphi(k) + \frac{2}{3}C_3 k^3\right] e^{-2R_i/\lambda(k)} e^{-2\sigma_i^2 k^2}, \tag{3.16}$$

where S_0^2 is the intrinsic loss factor and $e^{-2R_i/\lambda(k)}$ is the attenuation factor due to the electron mean free path, $\lambda(k)$, which are both determined using a suitable reference materials. $e^{-2\sigma_i^2 k^2}$ is the Debye-Waller factor. The general knowledge about the surroundings of the center atoms is needed beforehand when analyzing the EXAFS data, such as the type of the atoms and its possible structure. When such information is available, by comparing/fitting the measured spectrum with the calculated spectrum from a known structure, the local structure information, such as the coordination shell position and the coordination number of the surrounding atoms can be obtained. By doing the Fourier transformation of $\chi(k)$, one obtains the pseudo-radial atomic distribution function around the absorbing atom.

Different from XSW, the XAFS method focuses on the local structure around a central atom. Therefore its requirement for materials quality is less demanding. However, similar to XSW method, XAFS is vulnerable to interference from background fluorescence signals. When a relatively large amount of the same element is found in the system, but not bound to the surface of interest as a simple adsorbate, the fluorescence of such atoms results in a substantial background, and the measured spectrum may not reflect the structure of the specifically bound atoms. Therefore care must be given to control the source of the fluorescence signal when working with ion adsorption on the single crystal surface.

Since XSW probes the adatom structure with respect to the substrate lattice, XAFS combined with XSW can give a more comprehensive picture of the structural information of materials. With the help of XPS, chemical information can be obtained as well. So all three techniques together can better understand the adsorbed catalysts supported on oxide single crystal and how they change, structurally and chemically, during chemical reactions, such as reduction-oxidization (redox) reaction primarily discussed in this thesis.

2.5 Experimental Setup

2.5.1 X-ray Surface UHV Multi-Chamber

For *in situ* MBE growth and *in situ* XSW measurements, an X-ray surface science ultra high-vacuum (UHV) multi-chamber is used. Figure 3.10 shows the chamber, which was located at the 12ID-D undulator BESSRC-CAT station at the Advanced Photon Source (APS), Argonne National Laboratory (ANL). The vacuum chamber was maintained at a base pressure 2 x 10^{-10} torr and equipped with a reverse-view low-energy electron diffraction (LEED; PHI), Auger electron spectroscopy (AES: PHI) and an electron-beam evaporator source (Omicron).

The central chamber is the characterization chamber, which is an R2-P2 design from Vacuum Generators LTD. Connected to the R2-P2 system are a load-lock chamber, a sample storage area, a surface science analysis area, a growth chamber and an X-ray chamber. The UHV system is supported by a frame that rests on three z-motion translation stages. Using stepper motors, the chamber has a range of 80 mm in the X direction (horizontal motion in the plane perpendicular to the beam) and 100 mm in the Z direction. Due to the kinematical mounts of the Z-motion stages, the entire chamber can perform a small rotation about the theta axis in the x-ray chamber; this is the mechanism used for rocking curve scans. Steps as small as 2 x 10^{-5} degrees in theta can be achieved.

The growth chamber has a Perkin-Elmer 10-320 sample manipulator that can move in X, Y, Z and chi. The manipulator is also equipped with a heater filament that can heat samples to over 1000 °C. The LEED-Auger chamber has a Perkin-Elmer 283-8550 sample manipulator capable of X-Z motion, plus a rotation. There is a gate valve between the X-ray chamber and the R2-P2 chamber. The X-ray chamber features a Perkin-Elmer 15-630 sample manipulator, which provides for X, Y and Z translation in addition to theta and chi motion. The detailed description can be found in Ref.[166].

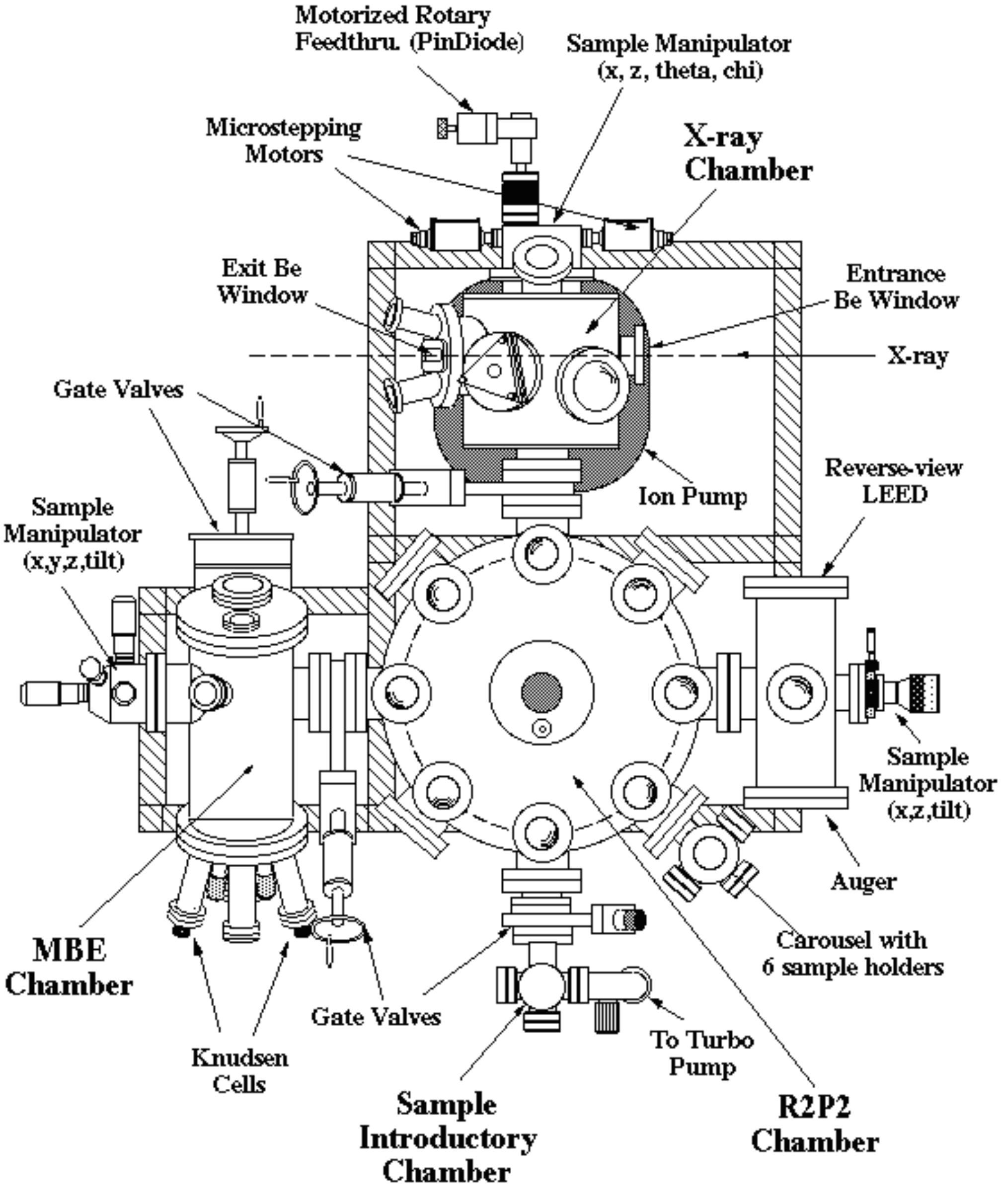

Figure 2.10 “Top-view” schematic diagram of UHV multi-chamber used at APS station 12ID-D. The Pt e-beam evaporator (not shown in this view) is below the two Knudsen cells.

2.5.2 Ex Situ XSW Setup

Figure 3.11 shows the typical XSW setup, which is used in APS Sectors 5 and 33, and was used at Sector 12 before relocation to 33. All three beamlines have a 3.3 cm period type-A undulator. Sectors 5 and 12 used a L-N_2 cooled Si(111) high-heat load monochromator. Sector 33 used a water-cooled Diamond(111) high-heat load monochromator. The horizontal mirror focusing was only in Sector 5.

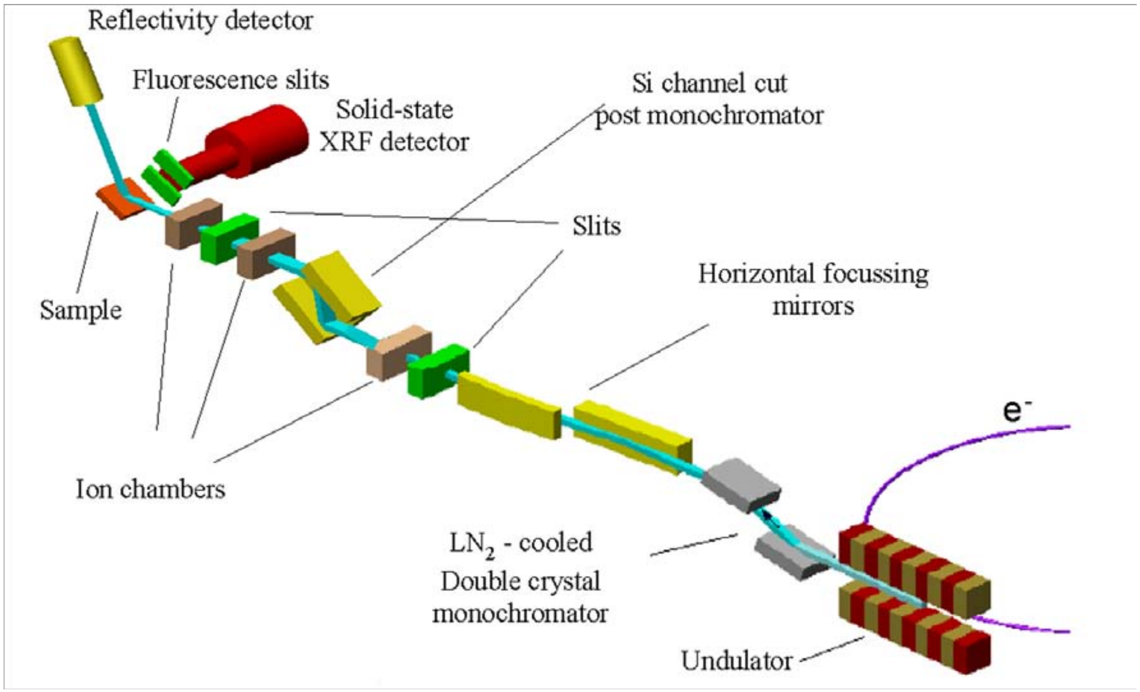

Figure 2.11 Experimental setup used for X-ray standing wave (and XRF) measurements at the APS-DND-5ID-C station. This setup is similar to the XSW setup at APS Sector 12 and Sector 33. The monochromatic beam that enters the experimental hutch is conditioned by a Si(111) or Si(220) channel cut post monochromator. Ion chambers are used to monitor the X-ray flux. The sample stage is mounted on a diffractometer. An energy-dispersive solid-state detector collects X-ray fluorescence emitted from the sample in a direction that is perpendicular to the incident beam. See Ref. [167] for further details.

Single crystal XSW experiments are carried out at the undulator stations. The incident photon energy is tuned by the undulator-gap and by the high-heat-load monochromator (HHLM).

A two-bounce Si(hhh), (hh0) or (00h) channel-cut crystal is used to create a nondispersive reflection from the sample. The rule is to match the d-spacing of the channel-cut as closely as possible to that of the sample crystal reflection being studied. By using a feedback controlled piezoelectric actuator or monochromator stabilizer (MOSTAB), the channel-cut angle is continuously adjusted with sub-microradian resolution to maintain a constant intensity ratio between incident and reflected X-ray beams. Two ion chambers are placed before and after the channel-cut crystal to read these two intensities. A third ion chamber is placed after the incident slit, which is after the channel-cut crystal. The sample is placed on a four-circle (12ID-D and 33ID-D) or a five-circle (5-IDC) diffractometer. For the collection of XSW data, two detectors are used. One is placed on the 2 theta arm for reflectivity. This can be a Cyberstar point detector or an ion chamber. On the side of the sample stage, a Vortex Si drift-diode (SDD) detector is placed for collecting X-ray fluorescence. At Sector 33ID-D, a Phi-stage adaptor is used so that the XRF detector can be placed on the adaptor and kept at a constant takeoff angle ~5° to the sample surface. In this case, the fluorescence signal from the sample substrate can be reduced when the sample is rotated to off-normal Bragg condition.

2.5.3 Be-Dome Reaction Cell for In Situ Measurements

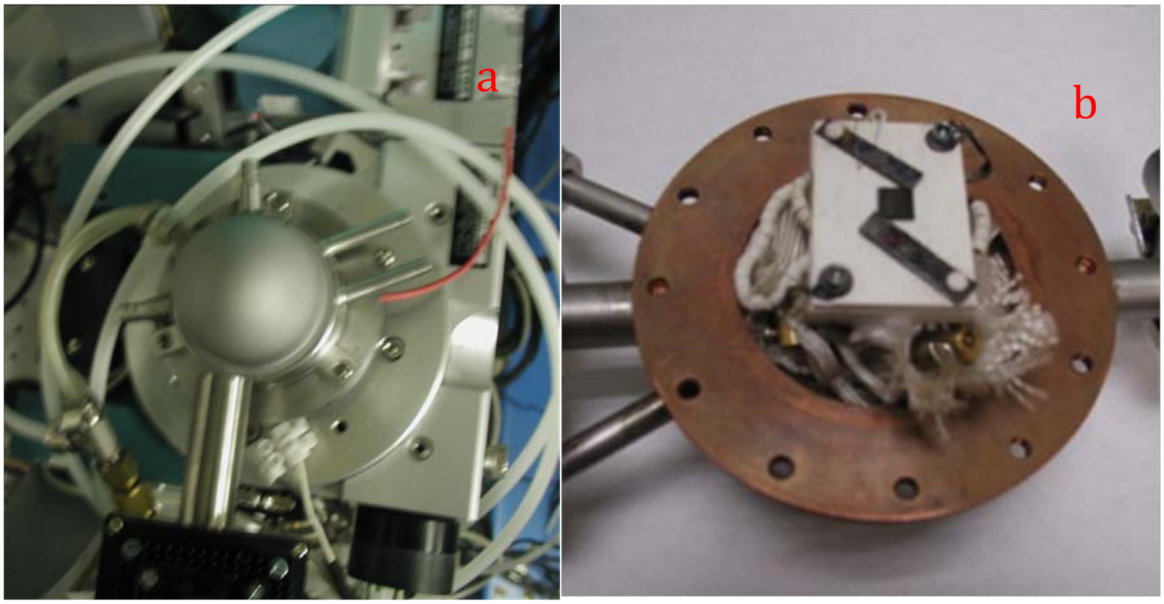

Figure 2.12 (a) A photograph showing the top view of the beryllium dome reaction chamber. The 0.25 mm thick Be hemisphere has a 25.4 mm radius, a boron-nitride interior and exterior surface coating, and is brazed to a water-cooled stainless-steal flange. Also shown in the lower-half of the picture is the XRF detector snout. (b) Inside the beryllium dome, the 5 × 5 × 1 mm^3 hematite sample is held by two stainless steel clips to a pyrolytic boron nitride heating plate (Momentive Performance Materials Quartz, Strongsville, Ohio, part no HTR1001).

For *in situ* X-ray measurements on catalysts during chemical reactions, a reaction cell is necessary. Figure 3.12 shows the Be-dome reaction cell used for in situ XSW, surface XAFS and X-ray diffraction measurement. The Be-dome reaction cell system contains a ceramic heater, a pair of stainless steel (or platinum) claps, thermal couples to detect the sample temperature, copper base with gas in/outlets, and Be-dome cap with water cooling channels. In this Be-dome, the sample can be heated up to 800 °C, the vacuum can reach 10^{-6} Torr, and H_2, O_2 and other gases can be fed through for reactions. The dimension of the Be-dome system can be found in Appendix of Ref. [168].

Chapter 3: Pt / $SrTiO_3(001)$

3.1 Pt Grown by Molecular Beam Epitaxy

3.1.1 Introduction

Dramatically enhanced catalytic activities have been observed for a variety of noble metals supported on oxide surfaces.[73, 169, 170] A prime example is Pt on $SrTiO_3$ as a photocatalyst for water splitting.[73, 169] The structure and resulting electronic properties of the Pt/$SrTiO_3$ interface are also of importance to thin-film technologies such as those used for dynamic random access memory devices.[171] Predictions of the metal/oxide interface structure, in general, would impact our understanding of numerous chemical and physical processes. However, there are very few atomic-scale studies of these buried interfaces.

One important issue of catalysis is to grow proper metal or metal oxides on different oxide supports. Oxides supported sub-monolayer (ML) metal and metal oxides have attracted many attentions due to greatly enhanced catalytic properties. Therefore, in this work, we study the early (low coverage) stages of the nucleation and growth of Pt nanoparticles on the TiO_2-terminated surface of $SrTiO_3(001)$ with a non-destructive 3D atomic imaging method that uses X-ray standing waves (XSW). And the growth method is molecular beam epitaxy (MBE).

3.1.2 Experimental Results and Discussions

Strontium titanate ($SrTiO_3$) single crystals were oriented, cut (10 x 10 x 1 mm^3) and polished parallel to the (001) by OKEN (Japan). $SrTiO_3$ (001) substrates were ultra-sonicated for 10 minutes in deionized water (18 MΩ/cm) and subsequently etched in a hydrofluoric acid buffer solution for approximately 30 s. The substrates were then rinsed in deionized water and dried in Ar gas. To produce atomically flat terraces terminated with titanium oxide [62, 82, 172], the substrates were loaded into a tube furnace with O_2 flow (~100 sccm) and annealed at 1050 °C for 5 hours.

After annealing in O_2, the substrates were mounted on a tantalum sample plate using spot-welded tantalum wire and loaded into an X-ray surface science UHV multi-chamber (See Fig. 3.7) Prior to platinum deposition, the substrates were annealed at 950 °C for 30 min in the UHV chamber using a resistive tungsten filament heater placed behind the sample. Auger analysis showed clean surfaces with negligible carbon contamination. A 1.5 mm diameter Pt rod was placed inside the e-beam evaporator to deposit Pt thin films. Platinum was deposited onto the atomically clean $SrTiO_3$ surface, which was held at 400 °C. One substrate was deposited with a 10 minute Pt and the other substrate was deposited with 2 minute Pt. After cooling to room temperature (RT) the “as deposited” (002) XSW measurement was made. The sample was then annealed to a series of increasing temperatures, cooled down to RT and given a 002 XSW measurement. The series of annealing temperatures were 0.5 h at 500°C, 1 h at 700°C, 1 h at 800 °C and 1 h at 910 °C.

LEED measurements were taken before Pt deposition, after Pt deposition and after the 910 °C annealing step. Figure 4.1 clearly shows that the two-domain 2 x 1 LEED pattern from the $SrTiO_3(001)$ surface can be seen after each of these steps; with some dimming of the half-order spots for the "as-deposited" surface.

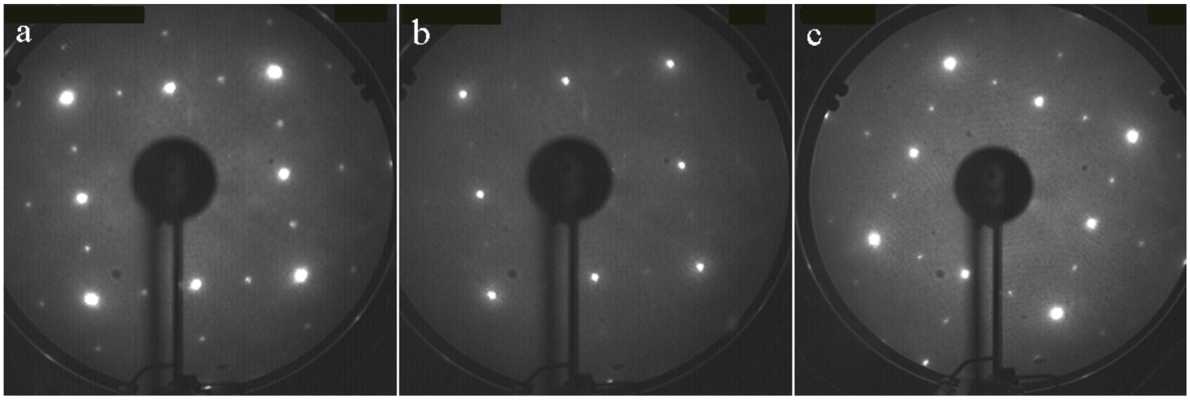

Figure 3.1 Low-energy electron diffraction (LEED) patterns for (a) clean $SrTiO_3$ (001) after UHV annealing treatment to obtain the 2-domain 2 x 1 surface reconstruction, (b) 0.60 ML Pt/ $SrTiO_3$ (001) as-deposited surface and (c) 0.60 ML Pt/ $SrTiO_3$ (001) surface after 910 °C anneal. The electron beam voltage was set at 65 V for each collected LEED pattern.

Finally, the sample was moved out of the chamber and mounted on a 4-circle diffractometer for further XSW measurements, as shown in Fig. 3.11. XSW measurements were performed at the APS undulator station 12ID-D of BESSRC-CAT. An incident photon energy of 12.50 keV was selected with a Si (111) high-heat load monochromator and conditioned further with a Si (004) channel-cut post-monochromator crystal. The incident beam slit was 20 μm high by 100 μm wide. Using this small X-ray spot it was possible to find lateral positions on the sample surface that produced reflectivity curves that reasonably matched dynamical diffraction theory predictions for a $SrTiO_3$ single crystal. A solid-state Si(Li) detector was used to collect the X-ray fluorescence (XRF) spectra. An XRF collected spectrum is shown in Fig. 4.2. The Pt coverages, 0.17 ML and 0.60 ML, were determined from a side-by-side XRF comparison to a Si implanted standard that was calibrated by Rutherford backscattering (RBS). One monolayer is defined as 6.58 atoms / nm^2.

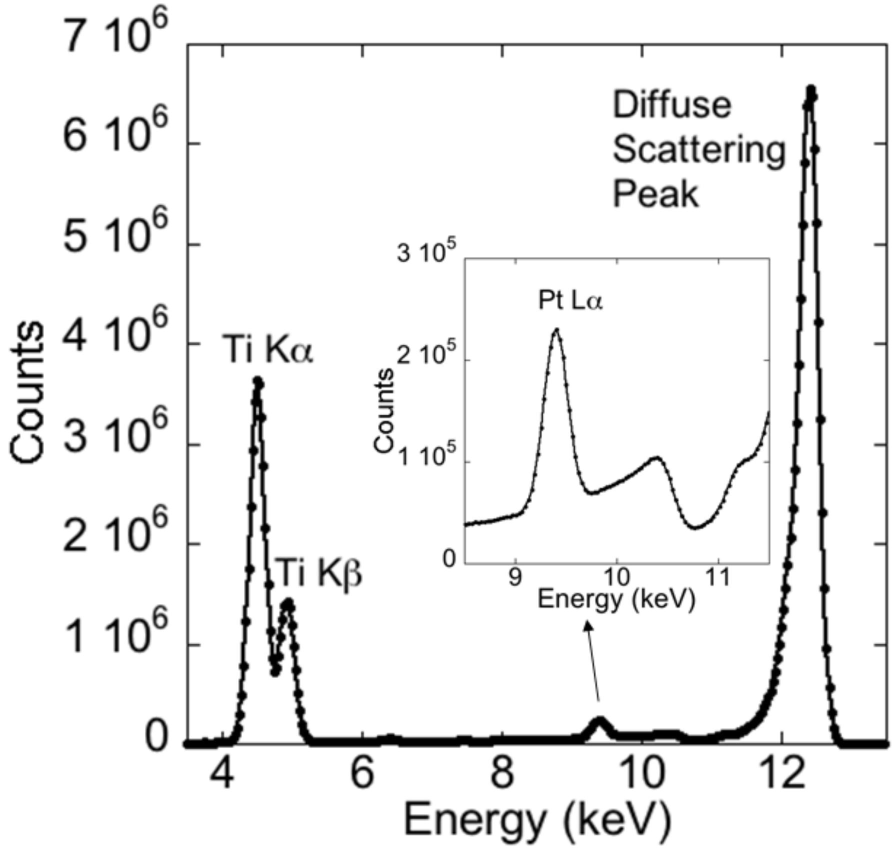

Figure 3.2 An XRF spectrum of 0.60 ML Pt/SrTiO$_3$(001) that was collected at an incident photon energy of 12.50 keV.

Figure 4.3 shows the XSW data and analysis of the 0.60 ML sample for the (*002*) SrTiO$_3$ Bragg reflection measured in the UHV condition and in open air. The XSW induced modulation of the background-subtracted and deadtime-corrected Pt Lα fluorescence yield, $Y(\theta)$, from each scan is used to determine the coherent fraction (f_H) and coherent position (P_H). This determination is based on fitting the normalized yield data for the $H = hkl$ reflection to the model independent expression for the yield[152, 153, 173],

$$Y(\theta) = [\ 1 + R(\theta) + 2\sqrt{R(\theta)}\ \ f_H \cos(v(\theta) - 2\pi P_H)\ ]\ Z(\theta), \qquad (4.1)$$

where $R(\theta)$ and $v\theta)$ are respectively the intensity and phase of the reflected plane wave relative to the incident plane wave, $Z(\theta)$ is the normalized effective thickness. $Z(\theta) = 1$ for surface atoms, such as the Pt atoms in our case. Measurements in UHV and open air give essentially the same coherent fraction and coherent position ($f_{002} = 0.33$ and $P_{002} = -0.17$ for UHV measurement and $f_{002} = 0.39$ and $P_{002} = -0.18$ for the open air measurement). This strongly indicates that the Pt on $SrTiO_3$(001) surface is stable in open-air against oxidation at RT. Therefore our *ex situ* XSW findings for the Pt atomic structures can represent the *in situ* atomic structures. Figure 4.4 shows all *ex situ* measured XSW data and analysis for the 0.60 ML sample for (*001*), (*002*), (*011*), (*022*), (*111*) and (*222*) $SrTiO_3$ Bragg reflections.

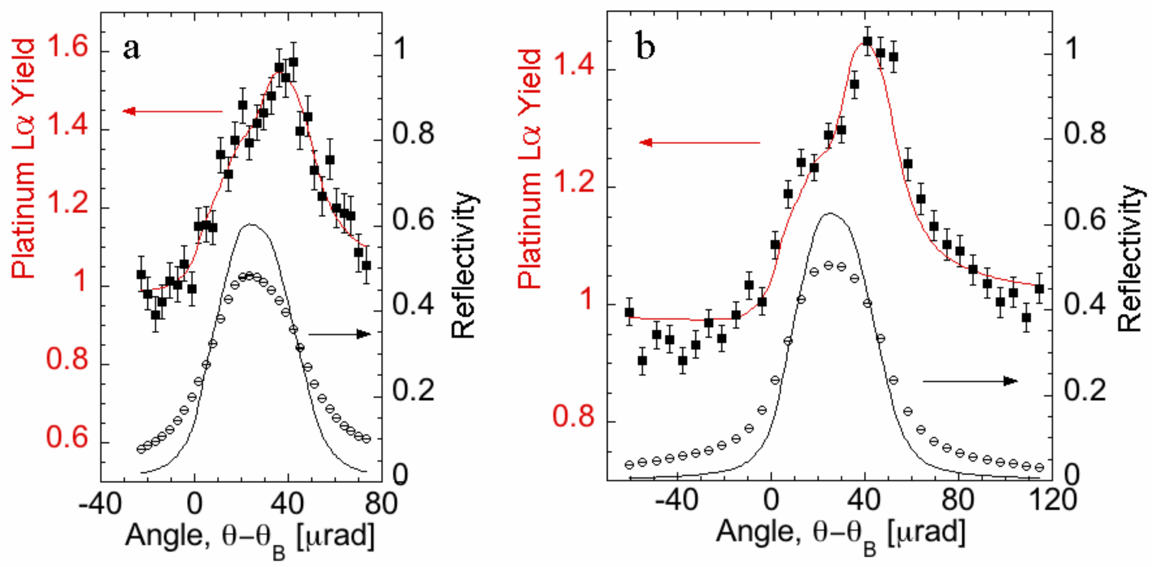

Figure 3.3 X-ray standing wave (XSW) data (markers) and fits (lines) at (002) $SrTiO_3$ Bragg reflection for 0.60 ML Pt measured at room temperature in (a) UHV after 910 °C annealing and (b) open air. Within the measured error, the measured values for the coherent fraction and position agree; indicating the stability of this surface against oxidation.

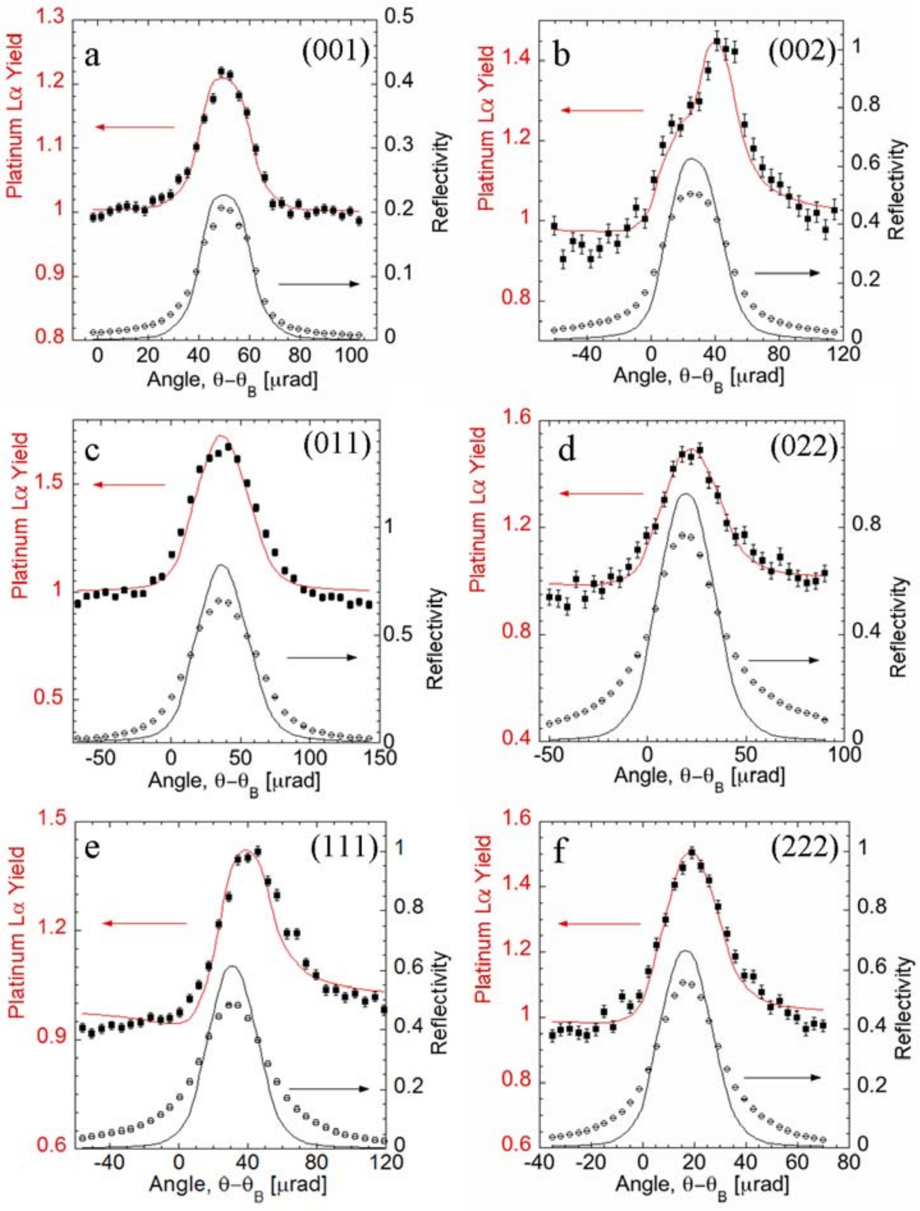

Figure 3.4 The *ex situ* XSW measurements for the 0.60 ML Pt / SrTiO$_3$(001) surface from 6 different hkl SrTiO$_3$ Bragg reflections: (a) (001), (b) (002), (c) (011), (d) (022), (e) (111) and (f) (222). Each frame shows the relative incident-angle dependence of the experimental X-ray reflectivity (open circles) and Pt Lα XRF yield (filled symbols). The solid lines correspond to dynamical diffraction theory based fits to the data. (See Refs. [152, 153, 173]) Table 4.1 shows the results of the fit of Eq. 4.1 to the yield data.

Table 3.1 For 0.60 ML Pt/SrTiO$_3$(001) case: XSW measured *hkl* Fourier amplitudes, f_H, and phases, P_H, for Pt and Ti. The calculated values for Pt are determined from the best-fit of the model described in Eq. 4.3.

	Pt measured		Pt calc		Ti measured	
hkl	f_H	P_H	f_H	P_H	f_H	P_H
001	0.07(3)	-----	0.07	0.07	0.73(3)	0.50(1)
002	0.39(3)	-0.18(2)	0.32	-0.15	0.60(3)	0.00(1)
011	0.07(3)	----	0.06	0.07	0.59(3)	0.00(1)
022	0.22(3)	-0.16(2)	0.23	-0.15	0.49(3)	0.00(1)
111	0.35(3)	-0.13(2)	0.37	-0.07	0.55(3)	0.50(1)
222	0.15(3)	-0.08(5)	0.16	-0.15	0.55(3)	0.00(1)

The Pt Lα fluorescence yields at the (*002*), (*022*), (*111*) and (*222*) Bragg reflections have asymmetrical shapes, indicating that the Pt distribution is correlated to the SrTiO$_3$ lattice. However, the fluorescence yields at (*001*) and (*011*) Bragg reflections are symmetrical and very similar to the rocking curve in peak heights and shapes; indicating that the Pt distribution has a null Fourier component for these two periodicities. Due to diffuse (incoherent) scattering, the tails of the experimental reflectivity (rocking) curve are higher than the theory for a perfect single crystal. Table 4.1 lists the entire *ex situ* measured set of f_H and P_H values of Pt and Ti for the 0.60 ML sample. The summation of these two sets of XSW measured Fourier components (and their symmetry equivalents) produce model-independent 3D maps of the Pt and Ti atomic distributions,[81, 174]

Based on the 4-fold symmetry axes and mirror planes along the c-axis for this particular substrate surface, we only need to measure the symmetry inequivalent reflections that occupy one-half of the 1st octant in reciprocal space. That would be the $SrTiO_3$ Bragg reflections with indices $\{(hkl) \mid l \geq 0 \text{ AND } h \geq 0 \text{ AND } k \geq h \text{ AND NOT } 000\}$. As an example, for the Pt atomic map we use the Pt La measured f_{022} and P_{022} values in Eq. 1 for summation terms with indices $H = 022, 202, 0\text{-}22, \text{and } \text{-}202$. For the bulk Ti atomic map there is additional symmetry that allows us to assign the Ti Kα measured f_{022} and P_{022} values to two additional in-plane terms with indices *220 and -220.* Note that even if there are local Pt domains that do not exhibit the 4-fold axes and mirror planes along the c-axis, the various *hkl* XSW measurements would exhibit this symmetry due to domain-averaging over the ~0.01 mm^2 X-ray spot.

The XSW Pt atomic map is a projection of the macroscopic Pt distribution into a single $SrTiO_3$ cubic-P unit cell. Each Pt is positioned inside this unit cell by the translation symmetry of the bulk substrate lattice. Due to substrate crystal quality and data collection time constraints, we did not collect XSW Fourier components for *hkl* reflections that had d-spacings smaller than d_{222} for the 0.6 ML and d_{022} for the 0.2 ML case. We also did not measure *hk0* –in-plane reflections due to experimental constraints. In principle these could be measured by a 3-beam variation of the XSW technique that coherently couples total external reflection with an in-plane dynamical Bragg reflection.[175]

Summation terms in Eq. 4.1 that were not part of the measured set or their symmetry equivalents are nulled out. Based on the convolution theorem this truncation of the semi-infinite summation produces a map that is convoluted with the inverse Fourier transform of the window function that extends symmetrically into all 8 quadrants of reciprocal space to cover measurements made and their symmetry equivalents. The effect of this convolution can be seen by the broadening of the peaks in Fig. 4.7(b).

Note that in this case the fcc-like Pt distribution causes fcc- forbidden Fourier components to be nulled out in our measurement. (See f_{001} and f_{011} in Table 4.1). Whereas, if the Pt distribution were bcc-like (and had a close lattice constant match to STO) the nulled out Fourier components would have been a different set; namely *001* and *111*.

Figure 4.5(a) and (c) show, respectively, the Pt and Ti 3D atomic maps for the 0.60 ML sample as referenced to the $SrTiO_3$ substrate unit cell with Sr positions at the corners of the cube. As expected the Ti shows up in the body-centered position. Due to the Fourier summation process the XSW maps have the 3D periodicity of the substrate primitive unit cell. What was not obvious from studying the values in Table I, but becomes immediately obvious by their subsequent Fourier summation, is that the Pt atoms form a face-centered-cubic (*fcc*) lattice that is registered to the substrate unit cell, namely $[001]_{\mathrm{Pt}} \parallel [001]_{\mathrm{STO}}$ and $[010]_{\mathrm{Pt}} \parallel [010]_{\mathrm{STO}}$. Furthermore, one sees that the Pt lattice is shifted vertically inward, relative to the Sr sublattice, by $\sim {}^{1}/_{10}\, a_{STO} = 0.4\ \text{Å}$.

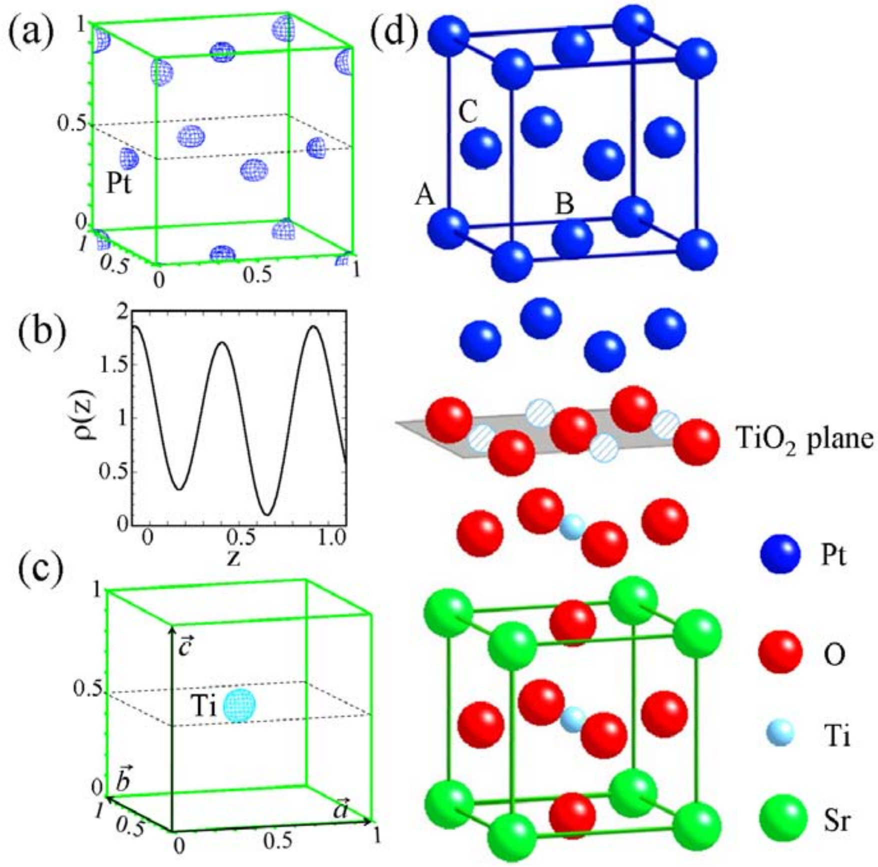

Figure 3.5 For the 0.60 ML Pt / $SrTiO_3(001)$ interface: (a) the XSW measured model-independent 3D Pt atomic map. The outlined green cubes are the $SrTiO_3$ unit cell with Sr at the corners (origin). (b) Projection of the 3D density along the c-axis to produce a 1D Pt atomic density as a function of the fractional c-axis coordinate, z, for the $SrTiO_3$ unit cell. (c) The 3D Ti atomic density map. The contour plots in (a) and (c) are at 80%. (d) Pt fcc atomic model on double-layer TiO_2 terminated $SrTiO_3(001)$ surface, where A, B and C refer to the three symmetry-inequivalent Pt sites. The striped light blue spheres in the extra TiO_2 layer represent Ti sites that are on average 50% occupied due to the 2-domain 2 × 1 reconstruction of the surface.

To better understand the Pt 3D map, a 1D projection along the *c*-axis is shown in Fig. 4.5(b). The $\Delta z = 0.25$ FWHM of the two peaks corresponds to $\frac{1}{2} d_{002}$, which is the resolution of the measurement due to truncation of the Fourier summation at *002*. The two peaks have nearly equal density (occupation) and are spaced by $\frac{1}{2} a_{STO}$. This corresponds to Pt in a nearly perfect *fcc* atomic arrangement, for which $f_{001} \sim 0$ (analogous to structure factor $F_{001} = 0$ for *fcc)*. As will be discussed later, this is different from the 0.17 ML case, where a non-zero value of f_{001} was measured.

Figure 4.5(d) shows a proposed interface atomic model for explaining the observed 0.60 ML 3D Pt density map. This is based on the 2 × 1 reconstructed double layer (DL) model,[59, 176, 177] in which one extra TiO_2 layer is added to the TiO_2 terminated $SrTiO_3(001)$ surface.

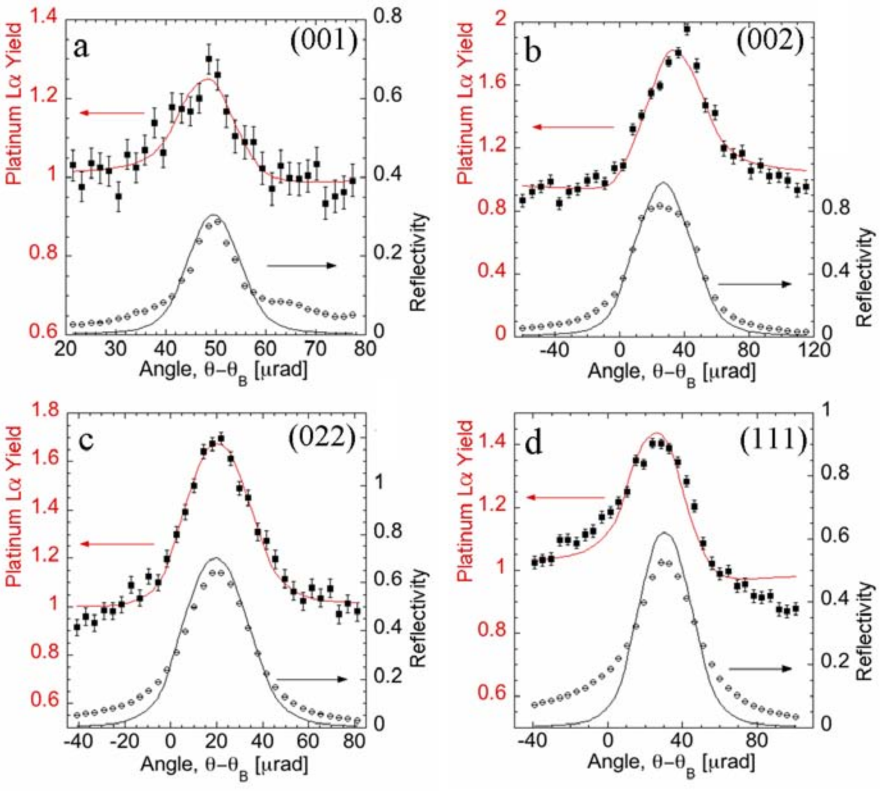

Figure 3.6 The *ex situ* XSW data (symbols) and fits (lines) for the 0.17 ML Pt / SrTiO$_3$(001) surface from 4 different *hkl* SrTiO$_3$ Bragg reflections: (a) (001), (b) (002), (c) (011), (d) (111). Table 4.2 shows the results of the fit of Eq. 4.1 to the yield data.

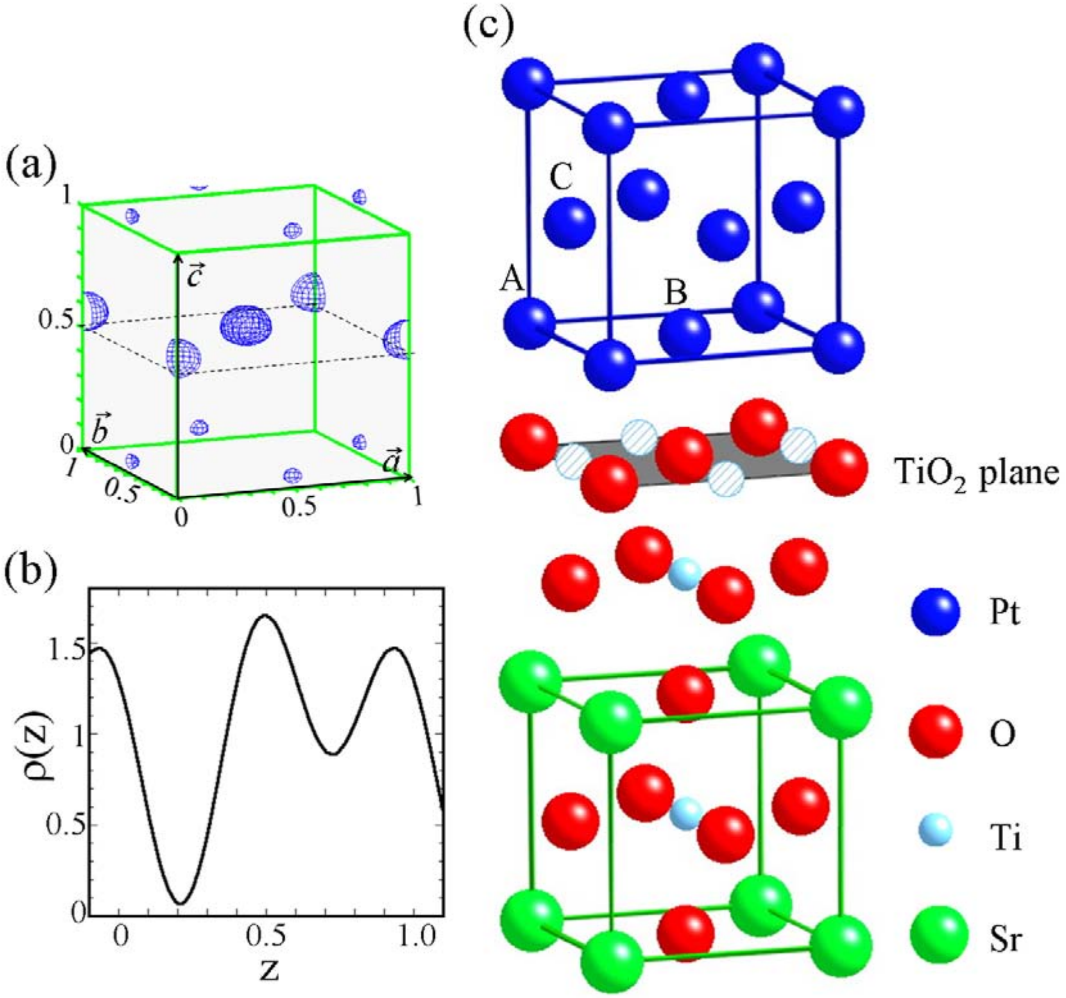

Figure 3.7 For the 0.17 ML Pt/SrTiO$_3$(001) interface: (a) 3D XSW measured Pt atomic density map. The outlined cube is the SrTiO$_3$ unit cell with Sr positions at the corners (origin). (b) Projection of 3D Pt density along c-axis. (c) Proposed atomic interface model.

The same XSW measurements were done for 0.17 ML sample in open-air condition. Figure 4.6 shows measurements at (*001*), (*002*), (*011*) and (*111*) Bragg reflections and Table 4.2 list all of the measured Fourier components. The XSW measured 3D Pt density map, Fig. 4.7(a), also shows an *fcc*-like structure, but with a vertical shift of ~ ½ a_{STO}. This is quite different from the 0.60 ML case shown in Fig. 4.5(a). Therefore, a different interface model is proposed in Fig. 4.9(c) that shows the first layer of Pt directly above the O atoms in the DL TiO_2-terminated $SrTiO_3$. The 1D projection of this Pt atomic density along the *c*-axis (Fig. 4.7(b)) shows a significant deviation from the ideal *fcc* arrangement; i.e., the two layers have a vertical spacing of $0.4a_{STO}$; rather than ½ a_{STO}. Table 4.2 list all XSW measured sets of f_H and P_H values.

Table 3.2 Summary of the XSW experimental analysis and best-fit parameters for 0.17 ML Pt / $SrTiO_3$ (001). Model independent parameters, f_H and P_H, are the measured $H = hkl$ Fourier amplitude and phase for the Pt distribution. These can be compared to the calculated f_H^C and P_H^C values determined from the best-fit of the model that is described by Eq. 4.3. Table 4.1 holds the same type of information for the 0.60 ML case.

hkl	f_H	f_H^C	P_H	P_H^C
001	0.21(3)	0.25	-0.32(3)	-0.33
002	0.26(3)	0.20	-0.03(3)	0.13
022	0.11(3)	0.20	0.15(4)	0.13
111	0.26(3)	0.33	-0.39(3)	-0.45

For this *fcc*-like Pt unit cell there are three types of symmetry-inequivalent adsorption sites on the $SrTiO_3$(001) surface: the corner site (A site), base-center site (B site) and the two symmetry equivalent side-center sites (C site). Because the surface breaks the symmetry along c-axis, the bulk fcc symmetry-equivalent B and C sites become symmetry-inequivalent. To further analyze the model-independent Pt maps in Figs. 4.6 and 4.7, several 2D plane-cuts and 1D line-cuts are used on these density maps. Figure 4.8 shows the analysis at the A site near the (0,0,0) Sr position in the STO unit cell for the 0.60 ML Pt case. Numerical analysis of the 3D distribution function around the hot spot gives the center Pt position as (0,0,-0.083). Three plane cuts ($x=0$; $y=0$; $z = -0.083$) and 3 line cuts ($x=y=0$; $x = 0$, $z = -0.083$; $y = 0$, $z = -0.083$) are used to examine the properties of the hot spot. A tetragonal box is chosen so that the Pt atomic density inside the box is greater than 1. The volume normalized atomic intensity sum in this box gives the occupation fraction of Pt at this site. Similar analyses are carried out for B and C sites for the 0.60 ML Pt case and the three sites for 0.17 ML Pt. The properties of the hot spots at each site are summarized in Table 4.3. It clearly shows that the A, B and C site occupation ratio, $I_{norm}(A) : I_{norm}(B) : I_{norm}(C)$, is 5:4:4 for the 0.60 ML Pt and 2:2:1 for the 0.17 ML Pt. The ratio would be 1:1:1 for ideal fcc. Analyses also show that that the Pt heights relative to the substrate SrO origin plane are $h_A = 7.49$ Å, $h_B = 7.41$ Å, and $h_C = 5.46$ Å for the 0.60 ML case and $h_A = 6.13$ Å, $h_B = 6.13$ Å, and $h_C = 7.65$ Å for the 0.17 ML case, as listed in Table 4.3.

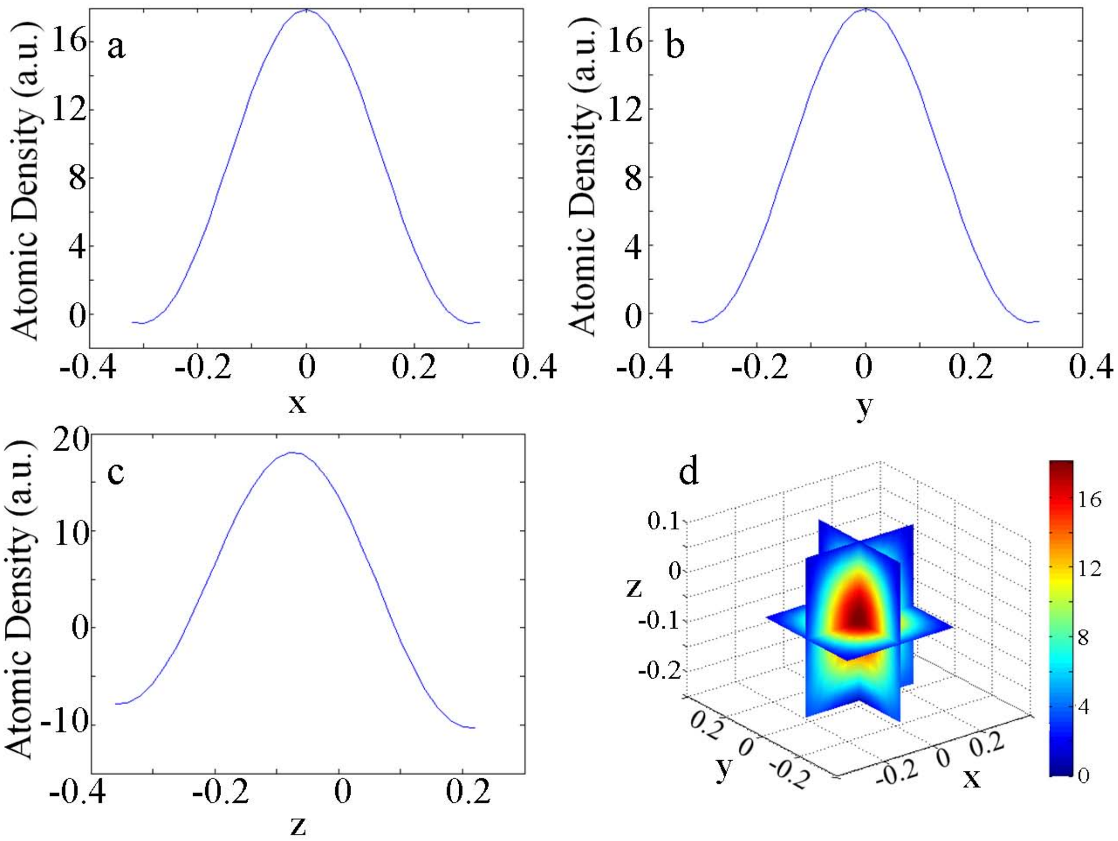

Figure 3.8 0.60 ML platinum model-independent analysis around an A site: (a-c) 1D line cuts through 3D atomic density map at (a) y=0, z=-0.083; (b) x=0, z=-0.083; (c) x=y=0; (d) orthogonal 2D plane-cuts in density map through the A site. The 3 planes are x=0, y=0 and z=-0.083.

Table 3.3 Numerical analysis of model-independent Pt atomic distribution ρ(x,y,z) around A, B and C sites for the 0.60 ML and 0.17 ML Pt/SrTiO$_3$(001) surfaces. The x, y and z ranges refer to the range of the tetragonal box chosen for the atomic density integration. The FWHM$_i$ refers to the FWHM in i (i=x, y or z) direction. h denotes the height of the three symmetry inequivalent sites to the SrO origin plan. I$_{norm}$ is the volume normalized atomic density sum in this tetragonal box.

	x-range	y-range	z-range	FWHM$_x$ (Å)	FWHM$_y$ (Å)	FWHM$_z$ (Å)	(x,y,z) Center	h (Å)	I$_{norm}$ (a.u.)
0.60 ML									
A	[-0.22, 0.22]	[-0.22, 0.22]	[-0.24, 0.08]	1.30	1.30	0.86	0, 0, -0.083	7.49	76
B	[0.26, 0.74]	[0.26, 0.74]	[-0.24, 0.06]	1.13	1.13	0.82	0.5, 0.5, -0.10	7.41	58
C	[0.26, 0.74]	[-0.24, 0.24]	[0.26, 0.56]	1.13	1.14	0.82	0.5,0,0.40	5.46	59
0.17 ML									
A	[-0.28, 0.28]	[-0.28, 0.28]	[0.38, 0.80]	1.36	1.36	1.02	0, 0, 0.571	6.13	49
B	[0.22, 0.78]	[0.22, 0.78]	[0.38, 0.80]	1.36	1.36	1.02	0.5, 0.5, 0.571	6.13	49
C	[-0.28, 0.28]	[0.22, 0.78]	[-0.12, 0.25]	1.63	1.63	0.95	0, 0.5, 0.96	7.65	25

To better quantify the Pt occupation fractions (c_X) and heights ($h_X = a_{STO}\bullet z_X$) above the bulk-like SrO plane for the three sites, we used a least-squares global fit of the proposed model to the set of measured Fourier components,

$$F_H = f_H \exp(2\pi i P_H) = \exp(-2(\pi\sigma/d_H)^2)\{c_A \exp(2\pi i \boldsymbol{H}\bullet\boldsymbol{r}_A) + c_B \exp(2\pi i \boldsymbol{H}\bullet\boldsymbol{r}_B)$$

$$+ c_C [\exp(2\pi i \boldsymbol{H}\bullet\boldsymbol{r}_{C1}) + \exp(2\pi i \boldsymbol{H}\bullet\boldsymbol{r}_{C2})]\}, \qquad (4.3)$$

where vectors $\boldsymbol{r}_A = (0,0,z_A)$, $\boldsymbol{r}_B = (½,½,z_B)$, and $\boldsymbol{r}_{C1} = (½,0, ½+z_C)$ and $\boldsymbol{r}_{C2} = (0,½, ½+z_C)$ locate the four Pt sites relative to the substrate unit cell origin and σ is the width of the isotropic Pt distribution about these sites. The best-fit determined results are $c_A = 0.16$, $c_B = c_C = 0.11$, $h_A = 7.69$ Å, $h_B = 7.44$ Å, $h_C = 5.49$ Å *and* $\sigma = 0.26$ Å, which agrees very well with the numerical analysis of the model-independent 3D map. The occupation ratio between the three sites ($c_A : c_B : c_C \sim$ 3:2:2) is reasonably close to the ratio for an ideal *fcc* arrangement (1:1:1). For 0.17 ML case, the calculated Fourier components based on the model are listed in Table 4.2 and the best-fit determined parameters are $c_A = 0.14$, $c_B =0.13$, $c_C = 0.06$, $h_A = 6.25$ Å, $h_B = 6.29$ Å, $h_C = 7.46$ Å. The model-independent and model-dependent analyses both show that the Pt occupation fraction ratio of the three sites are $c_A : c_B : c_C$ = 2:2:1; indicating that Pt atoms prefer to occupy the A and B sites. For both coverages the model-dependent analysis (that assumes 3 sites A, B and C) agrees very well with the model-independent analyses of the 3D Pt map described in Table 4.3.

To check the validity of our Pt XSW analysis, the Ti Kα signal from bulk $SrTiO_3(001)$ was also analyzed, as shown in Fig. 4.8. As shown in Fig. 4.2, these signals were collected simultaneously with the Pt signals. The analysis results are listed in Table 4.4. The XRF takeoff angle, α, relative to the sample surface is used to calculate the effective thickness, $Z(\theta)$, of the Ti Kα fluorescence signal, which includes the extinction effect [153]. The analysis results are consistent with Ti at the ½,½,½ position in a $SrTiO_3$ unit cell with Sr at the origin; demonstrating the validity of our XSW analysis for Pt.

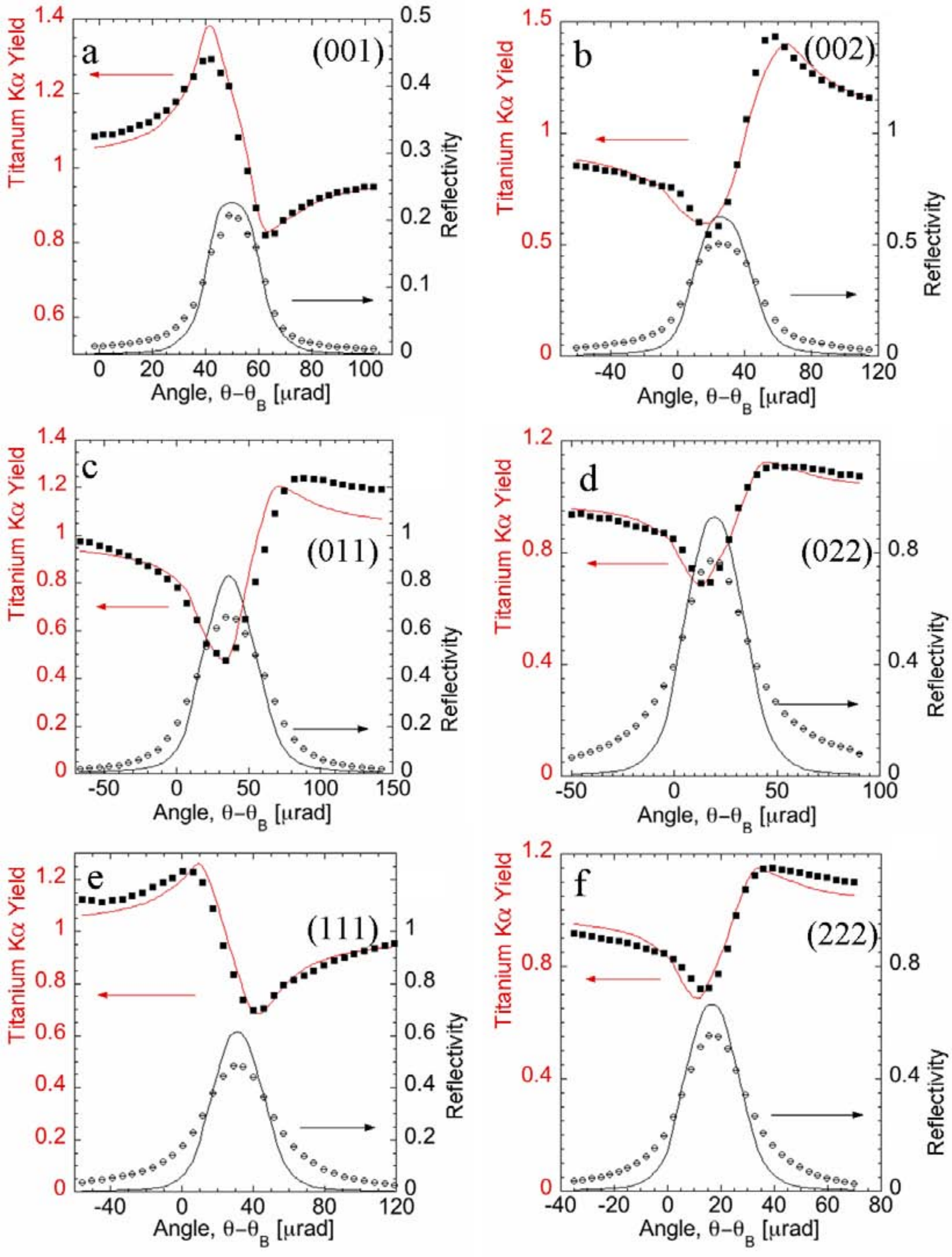

Figure 3.9 *Ex situ* XSW results of bulk Ti Kα signal for diffraction planes: (a) (001), (b) (002), (c) (011), (d) (022), (e) (111), and (f) (222) for 0.60 ML Pt/SrTiO$_3$(001). Table 4.4 shows the results from the fit of Eq. 4.1 to the yield data.

Table 3.4 XSW analysis of the bulk Ti sublattice of $SrTiO_3(001)$. The coherent fractions (f) and coherent positions (P) are experimentally determined from the modulations in Ti Kα XRF yields shown in Fig. S8. The takeoff angle (α) of the detected XRF emission relative to the surface are also listed. The P values are referenced to the Sr atom at the origin. $\exp(-M) = \exp(-2(\pi\sigma/d_H)^2)$ is the temperature Debye-Waller factor, where $\sigma = 0.12$ Å.

hkl	*001*	*002*	*011*	*022*	*111*	*222*
f	0.73(3)	0.60(3)	0.59(3)	0.49(3)	0.55(3)	0.55(3)
P	0.50(1)	0.00(1)	0.00(1)	0.00(1)	0.50(1)	0.00(1)
α (°)	8	11	48	40	40	41
$\exp(-M)$	0.98	0.92	0.96	0.85	0.94	0.78
$f/\exp(-M)$	0.74	0.65	0.61	0.58	0.59	0.71

Note that the measured Ti coherent fractions (Table 4.1 and Table 4.4) are significantly less than the ideal value of $f = \exp(-M) = \exp(-2(\pi\sigma/d_H)^2)$, the temperature Debye-Waller factor, which is near unity at room temperature. This degradation to the Ti coherent fraction is primarily due to the $SrTiO_3$ substrate not being a perfect single crystal, which leads to noticeable reduction in the coherently scattered intensity that is responsible for the XSW interference pattern, as well as part of the incident intensity being scattered incoherently. This can be seen in Figs. 4.4, 4.6, and 4.9, where the tails of the measured reflectivity (rocking curve) show a diffuse scattered intensity that is significant in comparison to the intensity calculated for perfect crystal. The XSW analysis (Eq. 4.1) of the Ti XRF yield induced by these incoherently scattered x-rays will produce a coherent fraction of $f = 0$ even if the emitting Ti atoms are correlated with the substrate. Therefore the measured incoherency (*1-f*) is due to both the uncorrelated part of the Ti atomic distribution (which should be very small) and the incoherently scattered X-rays. The Pt XRF yield is similarly affected by this X-ray incoherent scattering and therefore the measured 51% incoherency of Pt for the 0.60 ML case is primarily attributed to this effect. Likewise 61% incoherency in the 0.17 ML case.

Normally for a highly perfect single crystal substrate, such as Si or Ge, this would mean that 51% of the Pt atoms are uncorrelated with the substrate lattice. However, this is not a perfect single crystal substrate as the diffuse tails of the measured reflectivity (Figs. 4.3, 4.4, 4.6) indicate. Furthermore, the XSW analysis of the Ti Kα XRF signal from the substrate (Table 4.4) leads to Ti Fourier amplitudes that are on average 35% less than expected for the Ti sublattice in a perfect $SrTiO_3$ substrate. (It is important to note that the XSW measured Ti Fourier phases listed in Table 4.1 match their expected ideal values.) This significant degree of added incoherency to the XSW measured Pt and Ti XRF yields is primarily due to those incident photons that scatter incoherently and, therefore, do not participate in the generation of the XSW interference field. Assuming that the incoherency caused by defects affects the surface and bulk atoms in the same way, the true Pt correlation fraction can be increased from the uncorrected value of 49% to 75%. This estimates that 25% of the Pt atoms are in an uncorrelated distribution, such as Pt nanoparticles at $SrTiO_3$ surface defect sites.

By inserting the measured coherent fractions and positions of bulk Ti into Eq. 4.2, a Ti atomic density map is generated as shown in Fig. 4.9 and Fig. 4.5(c). As it should be, the Ti density maximum is located in the center of the $SrTiO_3$ cubic unit cell. This further validates our XSW analysis procedure. Other subsidiary maxima in the 3D map are due to the truncation of the Fourier summation.

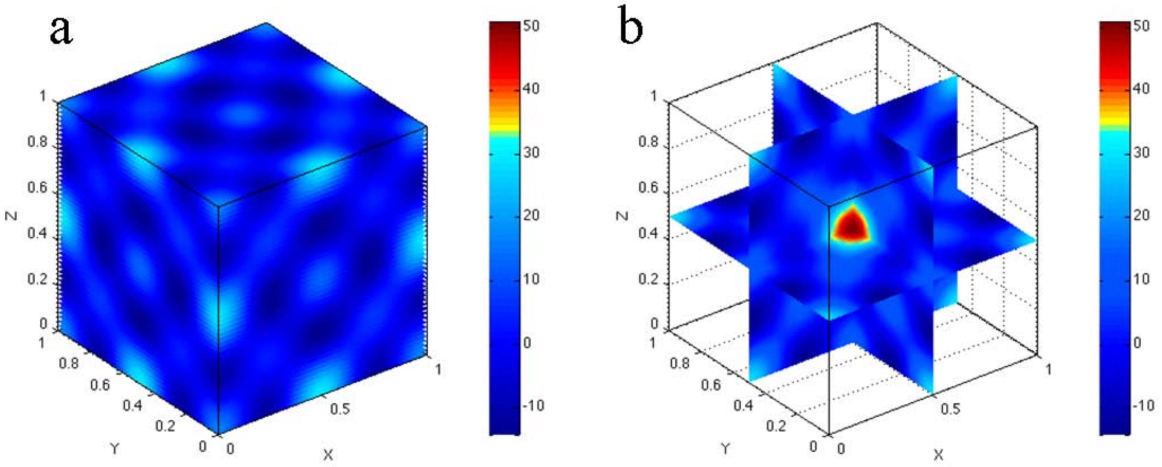

Figure 3.10 3D titanium atomic density map, (a) surface and (b) 2D plane-cuts, generated by the summation of XSW measured (*hkl*) Fourier components listed in Table 4.4 plus their symmetry equivalents. Ti atomic density maps are superimposed on the $SrTiO_3(001)$ unit cell with Sr at the origin.

Atomic-force microscopy (AFM) images were collected after the XSW measurements to understand the surface morphology of $Pt/SrTiO_3(001)$. Figure 4.11(a) and (b) show the surfaces of 0.60 ML and 0.17 ML $Pt/SrTiO_3(001)$, respectively. A Thermomicroscopes CP Research AFM operated in intermittent contact mode was used to collect surface morphology information from all surfaces discussed in this study. The silicon AFM tips (μMasch) had a nominal 10 nm radius of curvature and resonant frequency of ~75 kHz. The vertical piezo response was calibrated using standard $SrTiO_3(001)$ (d_{001} = 3.905 Å) sample. The white spots on the surfaces indicate the formation of Pt nanoclusters. The average Pt nanoclusters lateral sizes are ~30 nm and heights are 1.5 nm for 0.60 ML and 1.0 nm for 0.17 ML.

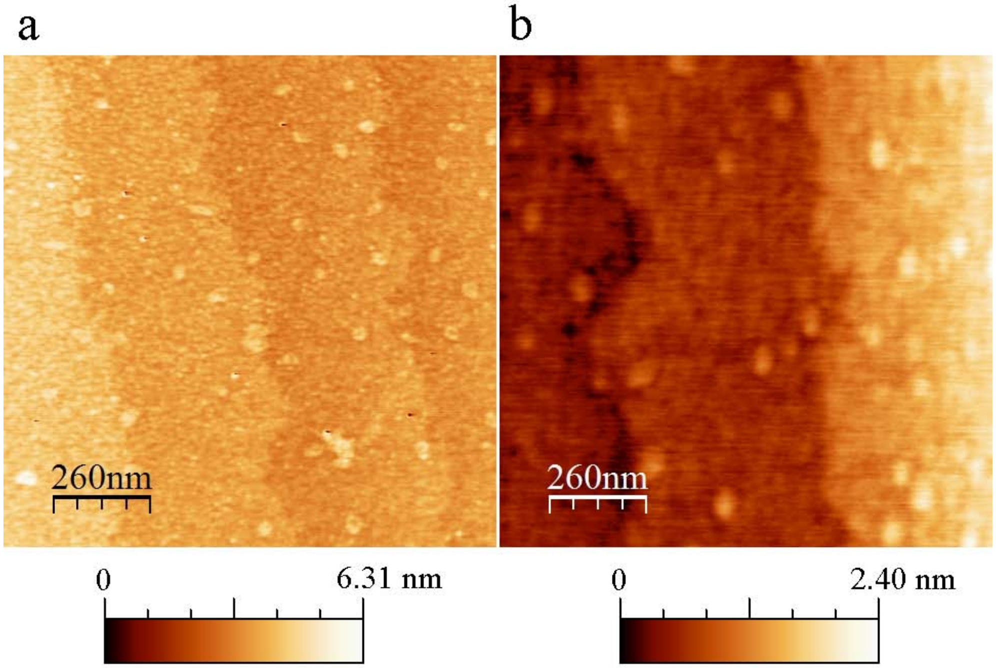

Figure 3.11 AFM images of (a) 0.60 ML and (b) 0.17 ML Pt / $SrTiO_3$ (001) surfaces show atomically flat terraces supporting nanoclusters.

The two distinct interface structures we observed for the two different Pt coverages (0.17 and 0.60 ML) can be attributed to the $SrTiO_3$(001) surface termination, Pt-support interactions and Pt-Pt interactions. Earlier experimental[59, 176] and theoretical[177, 178] studies of the bare 2x1 $SrTiO_3$(001) surface support the formation of a double-layer (DL) TiO_2-terminated surface. We found no reported theory predictions for Pt on the DL TiO_2-terminated surface. However, density functional theory (DFT) calculations for very low Pt coverages on TiO_2-terminated $SrTiO_3$(001) predict that the Pt-support interaction is stronger than the Pt-Pt interaction,[179] and Pt atoms strongly prefer to adsorb on top of the O atoms.[179, 180] The surface terminations and the strong Pt-O interaction lead to the atomic model proposed in Fig. 4.7(c). At very low coverages (e.g., 0.17 ML), the largest fraction of Pt occupy the first layer on the surface with less nucleation and growth to form second or third Pt layers that make up the AFM observed nanoclusters. Therefore, the atomic model in Fig. 4.7(c) indicates that A and B sites are most favored by Pt atoms for DL TiO_2-terminated $SrTiO_3(001)$ surface. This is consistent with our XSW analysis above, and further confirms the validity of our model and the 2x1 $SrTiO_3$ (001) surface termination.

DFT calculations by Asthagiri and Sholl[179] show that as the Pt coverage increases from 0.5 to 1 ML on the TiO_2-terminated $SrTiO_3(001)$ surface, the Pt-substrate bond is weakened due to additional Pt-Pt bonds on the surface. For 1 ML this same DFT study proposes that interface Pt atoms would prefer to bind above Ti sites on TiO_2-terminated surface to continue the *fcc*-like packing.[179] This leads to the interface structure model proposed in Fig. 4.5(d) for the 0.60 ML case, which is quite different from the 0.17 ML case. The equal occupation of the three symmetry inequivalent sites further indicates that the Pt nanoclusters seen in the AFM are primarily built from multiple layers of Pt.

3.1.3 Summary

In summary, using the XSW 3D direct imaging technique, we observed the *fcc* cube-on-cube epitaxial structure for sub-monolayer Pt grown on $SrTiO_3(001)$ surface by MBE. We experimentally show for the first time that two different interface structures of Pt are formed with different initial Pt coverages, which are further explained by the surface termination of $SrTiO_3(001)$ and the interactions of Pt-Pt and Pt-support. Our proposed atomic-scale interface models, which start with a TiO_2 double-layer $SrTiO_3(001)$ surface, indicate that at an ultra-sub-monolayer coverage (0.17 ML) Pt prefers to bond on top of the O atoms due to the strong Pt-support interaction. However, at a higher coverage (0.60 ML) taller Pt nanocrystals are formed with stronger Pt-Pt interaction, which causes the interface Pt atoms bond above Ti atoms sites. Equal occupation in the three symmetry-inequivalent sites indicates those Pt nanocrystals have more than one Pt layer locally.

3.2 Pt Grown by Atomic Layer Deposition

3.2.1 Introduction

MBE can grow thin films on atomically clean and controlled surfaces, but this requires UHV condition. Compared to MBE, atomic layer deposition (ALD) is much more convenient. As discussed in Chapter 2, ALD does not require UHV condition but very accurate control of growth can be performed. Therefore, in this part, we choose ALD as another alternative method to grow Pt from sub-ML to ML on $SrTiO_3(001)$.

Undoubtedly, metallic thin films grown on perovskite substrates are important building blocks for catalytic and electronic materials systems. This includes use as heterogeneous catalysts[73, 90], ferroelectric devices[181], giant magnetoresistance thin films[182], and tunable microwave capacitors[183]. We chose Pt / $SrTiO_3$ because Pt has high electrical conductivity and excellent thermal stability against oxidation, and $SrTiO_3$ (STO) is a model system representing a large class of oxides with the perovskite structure.[67, 176, 184] However, for this system and its technological applications, a key question is how to effectively control the properties of the metallic film, such as surface morphology (3D particles or conformal film growth),[185, 186] crystallinity, and grain size.[187]

Pt and STO have very close lattice constants, which is one of several factors affecting the crystalline properties of Pt grown on $SrTiO_3(001)$. Other factors are the TiO_2 or SrO termination of the $SrTiO_3$ surface,[96] deposition method, and annealing treatment. It is reported that pulsed laser deposition produces Pt films on $SrTiO_3(001)$ with nearly perfect cube-on-cube epitaxy for growth at 600 °C, but not at 400 °C.[93, 94] For the case of DC sputtering, pre-annealing of the $SrTiO_3(001)$ substrates strongly affects the crystalline orientation of the Pt films.[188] Electron beam lithography can create a Pt nano-array.[189] Pt nanoparticles can be formed either by self-assembly methods[190] or atomic layer deposition (ALD).[83, 137, 191] Compared with other growth methods, ALD has the advantage of applicability for uniformly coating granular and porous materials.

In an earlier study[83] we concentrated on the nucleation and growth of as-deposited (AD) ALD Pt on single crystal $SrTiO_3(001)$ surfaces as a function of number of ALD cycles in the Pt coverage range of 1 to 40 monolayers (ML). Since ALD is a low-temperature growth method, these AD surfaces are expected to be far from equilibrium. Our XSW measurements also showed that those ALD grown Pt on STO has uncorrelated structure to the substrate lattice, which is quite different from our MBE case. In this part we investigate how post-annealing is used to drive these same surfaces closer to thermal equilibrium. Platinum grown by ALD on $SrTiO_3(001)$ surfaces was studied as a function of Pt coverage and post-deposition thermal treatment. The combination of atomic-force microscopy, scanning electron microscopy, X-ray fluorescence, X-ray reflectivity, and grazing-incidence small-angle X-ray scattering reveals significant changes in the nanoscale surface morphology and crystallinity for the differently prepared films.

3.2.2 Experimental Results and Discussions

Similarly, atomic-flat surfaces need to achieve first before materials growth. Following previously established surface preparation procedures[67, 82, 83], 10 × 10 × 1 mm^3 $SrTiO_3$ (001) substrates (MTI Corp.) were solution cleaned and then dried with nitrogen gas. To obtain atomically flat TiO_2 terminated surfaces, the substrates were loaded into a tube furnace with flowing O_2 (~100 sccm) at 760 Torr and annealed at 1050 °C for 5 hours. AFM described below showed that the surfaces had flat terraces with 4 Å steps, consistent with the $SrTiO_3$ lattice constant. The $SrTiO_3$(001) substrates were then transferred to a custom ALD reactor consisting of a hot-walled stainless steel tube and a computer controlled gas manifold for precursor dosing.[192] Before Pt growth the substrates in the ALD reactor were allowed to equilibrate and outgas for 10 min at 300 °C in a flowing nitrogen environment. To grow Pt by ALD, the substrates were alternatively exposed to $MeCpPtMe_3$ (Strem Chemicals, 99.5% pure) and 400 sccm of ultrahigh purity (99.995% pure) oxygen at 300 °C carried by 360 sccm of ultrahigh purity (99.995% pure) nitrogen at a steady state pressure of ∼1 Torr.[83] A Pt ALD cycle is defined as a 10 s exposure to $MeCpPtMe_3$, a 5 s N_2 purge period, a 5 s exposure to O_2, and a final 5 s N_2 purge period. Our previous study of the as-deposited surfaces formed by 10 to 80 ALD cycles of Pt on STO[83] showed that Pt nucleates as isolated islands, the islands grow laterally with repeated Pt ALD cycles, and the islands coalesce to form a nearly continuous film after 40 cycles. After 40 cycles the constant growth rate was ~ 0.5 Å/cycle. X-ray photoelectron spectroscopy (XPS) confirmed that the platinum chemical state was metallic for these as-deposited films.[83]

Then Pt/$SrTiO_3$ samples were prepared using 10, 20, 30, 40, and 80 Pt ALD cycles. To study the Pt structural and morphological changes due to annealing, the ALD samples were studied in their as-deposited (AD) condition and after annealing (AN) in ultra-high vacuum (UHV) at 800 °C for 10 minutes.

A Thermomicroscopes CP Research AFM operated in intermittent contact mode was used to collect surface morphology information from all surfaces discussed in this study. The silicon AFM tips (μMasch) had a nominal 10 nm radius of curvature and resonant frequency of ~70 kHz. The piezo tube motion was corrected by a polynomial subtraction to the images. The vertical piezo response was calibrated using standard $SrTiO_3(001)$ (d_{001} = 3.905 Å) and $TiO_2(110)$ (d_{110} = 3.25 Å) samples.

SEM imaging was performed using a Hitachi S-4800 II cFEG SEM. The samples were imaged in the SEM without the use of conductive coatings.

The Pt coverage was measured by X-ray fluorescence (XRF) using a Zr coated rotating anode and an energy-dispersive XRF detector at the Northwestern University (NU) X-ray Facility. The 15.75 keV Zr Kα X-rays excited Pt L fluorescence without inducing Sr K fluorescence, which would have saturated the XRF detector system. The Pt Lα XRF yield from each ALD deposited film was converted into a Pt coverage by using a side-by-side comparison to a Rutherford backscattering calibrated Pt standard. For the $SrTiO_3(001)$ surface, 1 monolayer (ML) corresponds to $N_{surface}^{STO} = a_{STO}{}^{-2} = 6.558$ atoms / nm^2.

X-ray reflectivity (XRR) and reciprocal-space map data were collected with Cu Kα_1 (λ = 1.5406 Å) radiation from rotating anode-based diffractometers in the NU X-ray Facility. A Rigaku ATX-G with a parabolic multilayer followed by a Ge(111) condenser-two-bounce monochromator was used for XRR and a Huber 4-circle with a graphite sagittal focusing monochromator was used for collecting the reciprocal space maps. The reflectivity data as a function of scattering angle 2θ was background subtracted, dead time corrected, and normalized to the straight-through beam intensity. The low-angle XRR data as a function of perpendicular momentum transfer $Q = Q_Z = 4\pi\sin\theta/\lambda$ was fitted by the Motofit program, which uses a slab-model approach with Parratt's recursion formulation to perform dynamical scattering analysis.[193]

GISAXS measurements were performed at the XOR 12ID-C at the Advanced Photon Source (APS) (Argonne National Laboratory) with a 2048 × 2048 pixel MAR165 CCD detector. The incident photon energy was 11.50 keV. The sample-to-detector distance was 2 m. Samples were mounted on a two-circle diffractometer that enabled rotations to set the incident angle, α_i, and azimuthal rotation angle, ϕ, about the substrate surface normal. While samples were measured at various incident angles, GISAXS data presented in this report were collected with $\alpha_i < \alpha_C$; where $\alpha_C = 0.15°$ is the critical angle of the $SrTiO_3$ substrate. This corresponds to $Q_C = 0.032$ Å^{-1}. A silver behenate standard was used for angle calibration, and images were corrected for detector dark current via data subtraction.

Figure 4.12 and Table 4.5 present the AFM analysis illustrating the evolution of the Pt/$SrTiO_3$(001) surface morphological changes before and after the 800 °C UHV anneal. Each starting blank $SrTiO_3$(001) surface (not shown) was atomically flat with an RMS roughness of 0.1 nm. The XRF determined Pt coverage for each sample is listed in Table 4.5. We showed previously that the ALD Pt forms a uniform coating of isolated nanoparticles on the $SrTiO_3$(001) surface in the early stages of growth.[83] Consistent with this observation, terraces were still clearly seen after ALD via AFM, indicating a conformal film-like structure on the surface. The RMS roughness of the AD samples increased only slightly with the number of ALD cycles. However, after annealing, the AFM images show distinctive morphological changes for higher coverages. Figure 4.12(a) shows a 0.2 nm RMS roughness for the 0.7 ML AN sample, indicating that annealing has little effect at low Pt coverages. As more Pt is deposited, annealing has a stronger effect. As shown in Fig. 4.12(b-e), the 0.4 nm atomic steps that were preserved on the AD surfaces disappear in the images of the annealed surfaces as the Pt starts to coalesce. The Pt coalescence and average cluster size increase with Pt coverage resulting in an increased roughness.

Table 3.5 XRF determined Pt coverage (Θ_{XRF}) and AFM measured RMS roughness for the set of ALD Pt / $SrTiO_3(001)$ surfaces. AD = as-deposited surface. AN = annealed surface. Prior to ALD the AFM surface RMS roughness was 0.1 nm.

ALD cycles	(Θ_{XRF}) (ML)	AD RMS (nm)	AN RMS (nm)
10	0.7	0.21	0.16
20	11.2	0.22	0.47
30	25.1	0.31	0.97
40	35.6	0.45	1.65
80	39.8	0.91	7.57

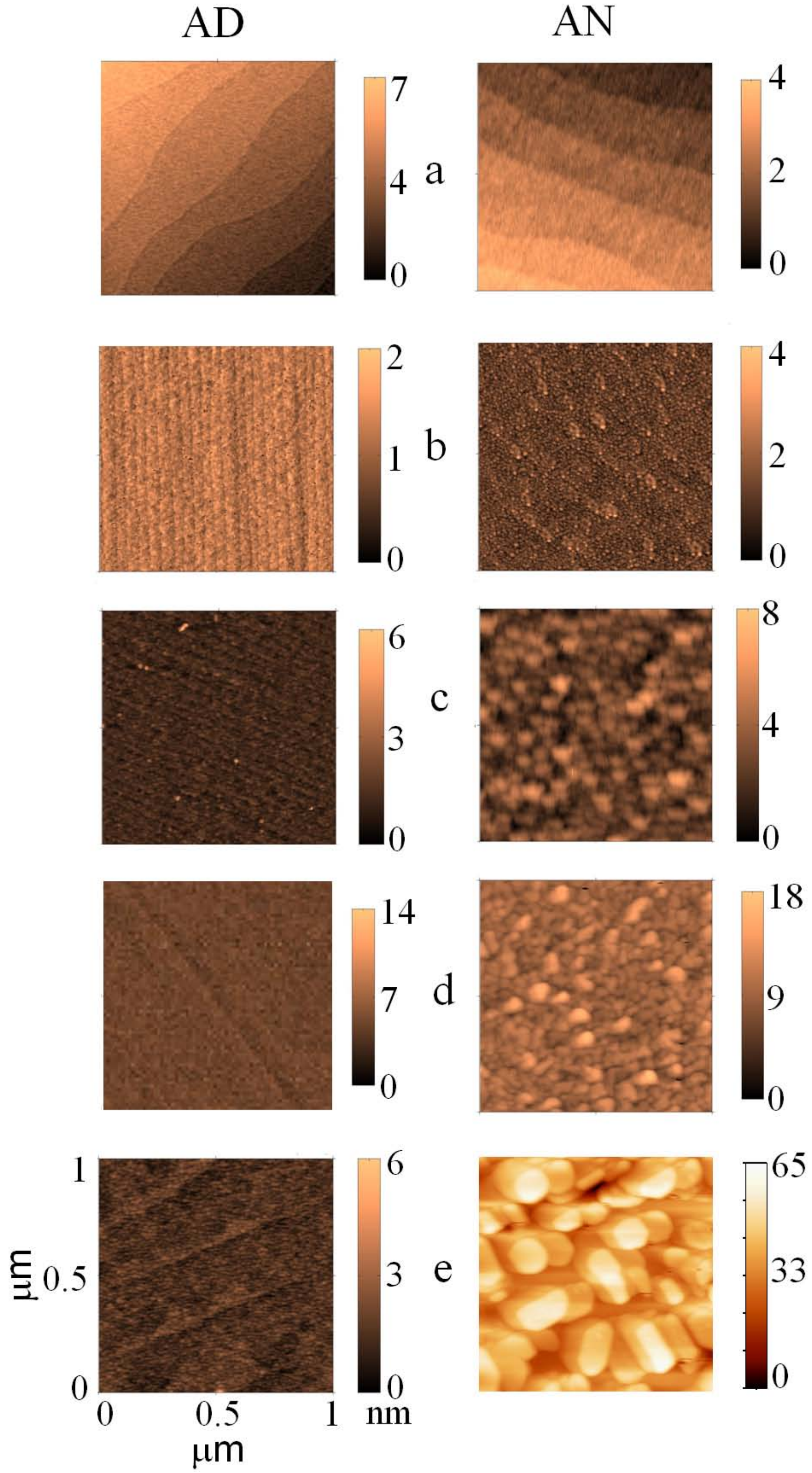
AD
AN
7
4
0
a
4
2
0
2
1
0
b
4
2
0
6
3
0
c
8
4
0
14
7
0
d
18
9
0
1
0.5
0
μm
6
3
0
e
65
33
0
0
0.5
1
nm
μm

Figure 3.12 Pairs of 1 × 1 μm^2 AFM images for ALD Pt on $SrTiO_3$(001). The left-hand column shows the images for the as-deposited (AD) surfaces. The right-hand column shows the same surfaces after annealing (AN) to 800 °C in UHV. The number of ALD cycles for each pair of images is: (a) 10, (b) 20, (c) 30, (d) 40, and (e) 80. The 0.4 nm atomic steps of the underlying $SrTiO_3$ (001) substrate are clearly seen for all AD surfaces and for the 10-cycle AN surface.

Figure 4.13 shows the SEM images of the annealed samples with 20, 40 and 80 ALD cycles. Compared to our earlier reported SEM images of similarly prepared as-deposited samples[83], the Pt nanoclusters become significantly larger after annealing. The SEM observation that the 80 cycle sample shows the most dramatic size increase effect confirms the AFM observations of Fig. 4.12 that annealing has a much stronger effect for surfaces with a higher Pt coverage. Furthermore, as seen in Fig. 4.13(c), the Pt nanoclusters of the AN 80-cycle sample show faceted edges.

To better understand the film and interfacial properties, XRR analysis was carried out as shown in Fig. 4.14 on the AD films. The results are summarized in Table 4.6. The thickness fringes in the XRR data confirm the conformal film-like structure of the AD samples. However, the XRR determined effective electron density (ρ_{film}) for each film is less than that of bulk Pt ($\rho_{\text{bulk}} = 5.164$ Å^{-3}). Table 4.6 shows that the 20-cycle sample has only 60% of the bulk Pt electron density, while the other cases have roughly 80%. The XRR fit uses a slab-model that assumes a homogenous density for the Pt layer. The laterally averaged value being less than bulk Pt density, is consistent with Pt forming a discontinuous film. The real Pt distribution could be more complicated, such as Pt islands on a fully covered Pt layer. Table 4.6 also shows that the Pt coverages determined from XRR (Θ_{XRR}) are consistent with those determined from XRF (Θ_{XRF}) in Table 4.5.

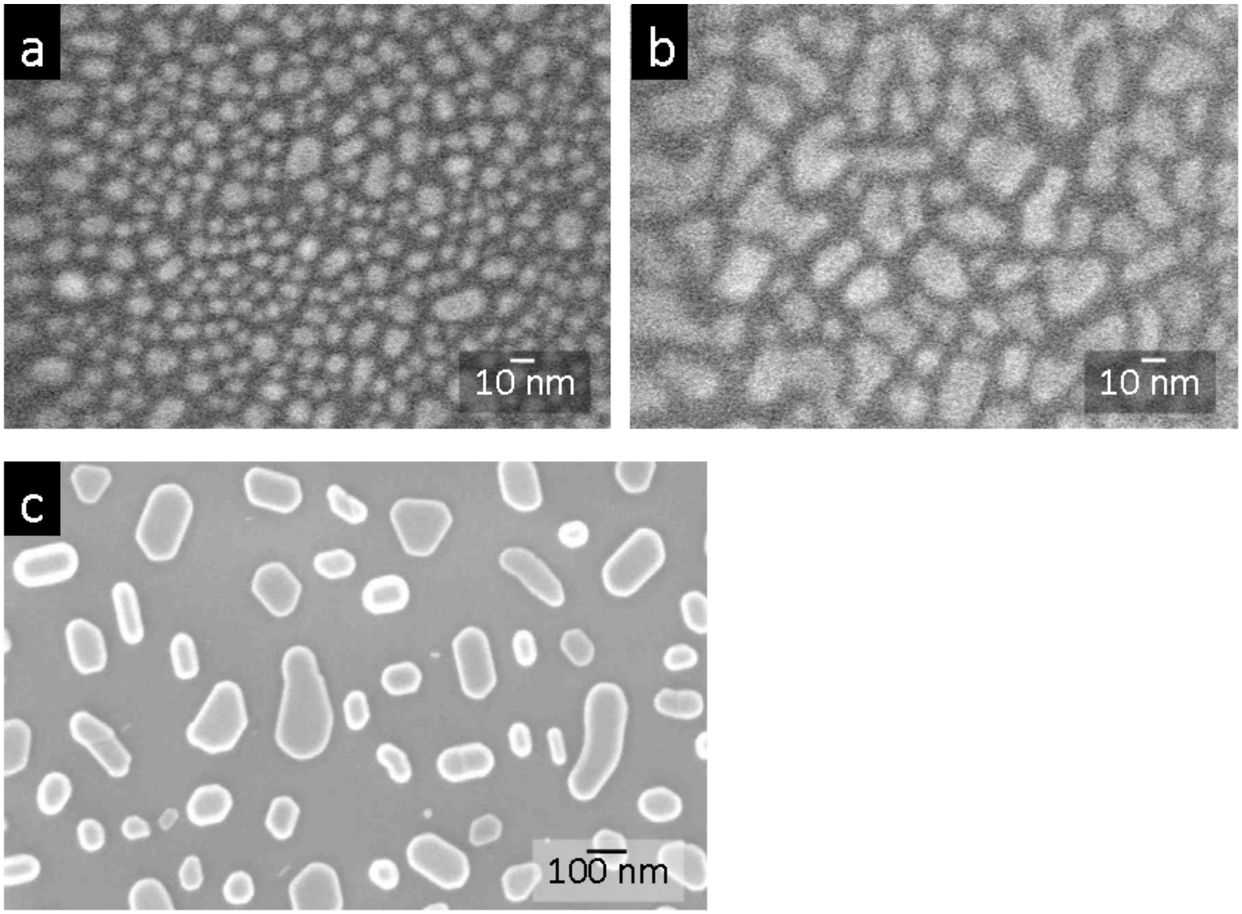

Figure 3.13 High-resolution SEM images for ALD Pt/SrTiO$_3$(001) after annealing: (a) 20 cycle, (b) 40 cycle, and (c) 80 cycle. Aggregation is greatly enhanced for the 80-cycle sample, in which faceting can be seen.

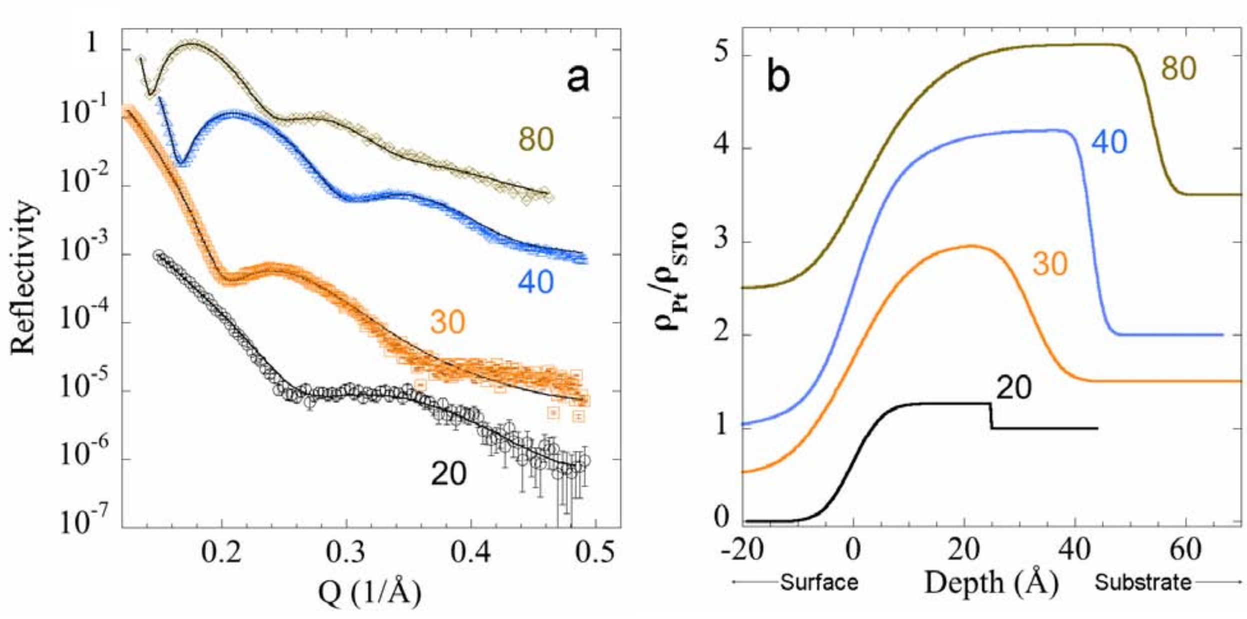

Figure 3.14 (a) X-ray reflectivity data and analyses for as-deposited (AD) ALD Pt/$SrTiO_3$(001) thin film samples. (b) The electron density profiles that were determined by the best fit of a model to each set of XRR data. Curves are offset vertically for purposes of clarity. The number next to each curve represents the number of ALD cycles. See Table 4.6 for the values of the fit determined parameters.

Typically for metals grown on oxides, there are three different growth modes, namely, 1) layer-by-layer or Frank-van der Merwe (FW) growth, 2) three-dimensional islands or Volmer-Weber (V-W) growth, and 3) intermediate case of three-dimensional islands on layered films or Stranski-Krastanov (S-K) growth.[2, 194] Our XRR analysis of the AD ALD Pt films is consistent with the S-K and/or V-W growth mode with 2D discontinuous films instead of 3D islands. This is also confirmed from images taken by AFM (Fig. 4.13) and SEM in previous studies[83]. At low temperature (300 °C in ALD) a “2D-island” mode[195] can dominate and consequently 2D films can be observed.

Table 3.6 Summary of XRR data analyses shown in Fig. 4.15 for the as-deposited ALD Pt / SrTiO$_3$(001) interfaces: Pt film thickness (t), film electron density relative to bulk Pt ($\rho_{film}/\rho_{\mathrm{bulk}}$), and XRR determined Pt coverage $\Theta_{XRR} = \frac{\rho_{film}}{\rho^{Pt}_{bulk}} N^{Pt}_{bulk} \frac{t_{film}}{N^{STO}_{surface}}$, where $N^{Pt}_{bulk} = 4a^{-3}_{Pt} = 66.20\ nm^{-3}$ and $N^{STO}_{surface} = a^{-2}_{STO} = 6.558\ nm^{-2}$.

ALD cycles	t (nm)	$\rho_{film}/\rho_{\mathrm{bulk}}$	Θ_{XRR} (ML)
20	2.3 ± 0.2	0.56 ± 0.19	13 ± 5
30	3.2 ± 0.1	0.79 ± 0.11	25 ± 4
40	4.3 ± 0.1	0.85 ± 0.04	37 ± 2
80	5.4 ± 0.2	0.79 ± 0.09	43 ± 5

For all these AD samples, no Pt Bragg peaks were observed at higher Q, indicating these AD films have crystal domains with sizes below the ~ 10 nm detectable limit for our rotating-anode X-ray source with single crystal substrates. [See Fig. 4.15(b)] Note that for 1 to 5 ALD Pt cycles on single crystal STO nanocubes with {001} faces that the AD Pt formed fcc nanocrystals[191] with cube-on-cube epitaxy[196]. For these powder samples, with a much larger effective surface area, synchrotron-based XRD measurements observed high-Q diffraction peaks with widths corresponding to domain sizes between 1 and 3 nm.

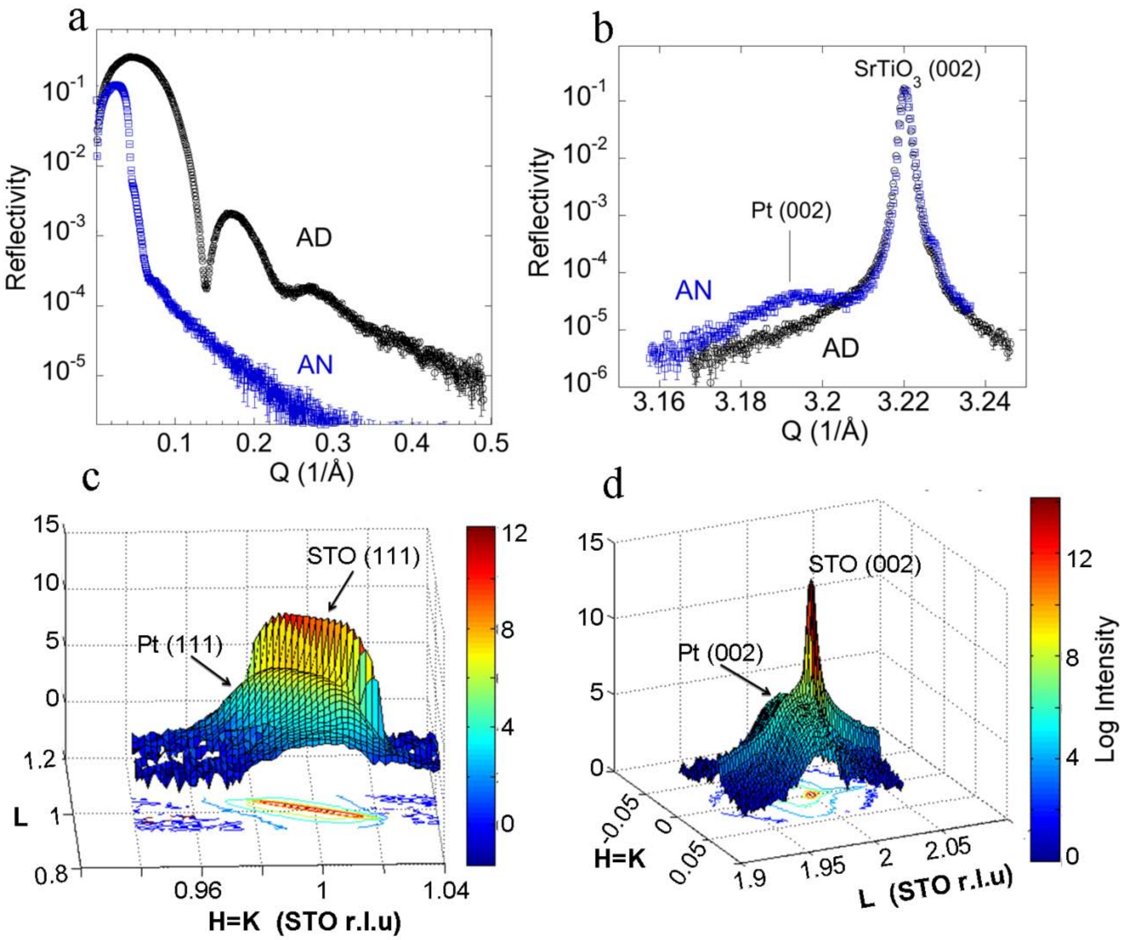

Figure 3.15 For 80-cycles ALD Pt/SrTiO$_3$(001) sample: (a) Low-Q and (b) high-Q XRR data for AD (black circles) and AN (blue square) conditions. Reciprocal space maps and contour plots using SrTiO$_3$ (STO) reciprocal lattice units (r.l.u.) in the vicinity of (c) (111) and (d) (002). Note that in (a) the critical angle for bulk-like SrTiO$_3$ and Pt correspond to $Q_C = 0.032$ and 0.084 Å^{-1}, respectively.

After UHV annealing, the low-Q reflectivity for each of these samples shows a significant change that becomes more dramatic as the Pt coverage increases. Figure 4.15(a) shows the reflectivity change for the 80-cycle sample before and after annealing. At lower Q, no thickness fringes were observed, indicating that the conformal film feature was lost. However at higher $Q = Q_Z$, as shown in Fig. 4.15(b), a Pt (002) peak appears. This indicates that the annealing-induced clusters seen in Fig. 4.12(e) by AFM and in Fig. 4.13(c) by SEM are Pt ordered nanocrystals with preferred (001) orientation along the surface normal direction. Annealing further breaks up the already discontinuous microstructural film causing it to aggregate (coarsen) into larger more separated clusters, as seen in Fig. 4.12 and Fig. 4.13. Figure 4.15(c) and (d) are reciprocal space maps surrounding the $SrTiO_3$ (111) and (002), respectively. This shows strain-relaxed Pt with $[111]_{Pt} \parallel [111]_{STO}$ and $[001]_{Pt} \parallel [001]_{STO}$, indicating that Pt nanocrystals have a cube-on-cube epitaxial structure on $SrTiO_3(001)$ after annealing. Analysis of the Pt (002) and (111) Bragg peaks both show a bulk-like lattice of $a = 3.92$ Å with peak widths (corrected for the 0.007 Å^{-1} instrument resolution) of $\Delta Q_z = 0.043$ Å^{-1} and $\Delta Q_{xy} = 0.036$ Å^{-1} corresponding to Pt nanocrystal domain sizes of 14 nm in the vertical and 16 nm in the horizontal directions, respectively. Note that this Pt (002) Bragg peak was below the detection limit for similar radial scans of the other annealed ALD samples. As seen in the AFM and SEM images, Pt nanocluster sizes change dramatically from low coverages to higher coverages. The typically larger nanocluster seen by AFM and SEM contain smaller ordered crystal domains as measured by high-Q XRR. As the Pt coverage increases, the sizes of both nanoclusters and the ordered crystal domains increase after annealing.

To further understand the morphological changes, GISAXS measurements were carried out for the 10, 20, 30, and 40 ALD-cycle samples in the AD and AN states. As a representative example, Fig. 4.16 shows the GISAXS data for the 10-cycle sample before Pt deposition, after deposition, and after annealing. Fig. 4.16(a) shows the expected scattering from an atomically flat surface where the majority of the intensity remains in the specular direction and is blocked by the beamstop. In contrast, Figs. 4.16(b) and (c) show the characteristic scattering of closely-spaced polydispersed particles that are monolayered; with a broad peak along the in-plane (Q_{xy}) direction and with a monotonically decaying intensity along the vertical (Q_z) direction. Comparing Figs. 4.16(b) and (c), the scattered intensity condenses around the origin. This indicates very small, closely-spaced particles coalescing into larger particles that are spaced farther apart. Using the analysis in our previous work,[83] the horizontal and vertical line cuts of intensity were extracted from the CCD images and fit using the distorted wave Born approximation[197, 198] (DWBA) framework for a cylinder form factor and the local monodisperse approximation[197, 199] (LMA) with 1D paracrystal model[197] for an interference function representing the interparticle spacing distribution. Figure 4.17 shows the vertical line cut of the data and fits, and Table 4.7 lists the analysis results for each sample. For the 10-cycle sample, there is no significant size or shape change before and after annealing. This is consistent with AFM analysis, and the GISAXS result suggests the formation of Pt nanoparticles. For samples with 20 - 40 ALD cycles after annealing, the in-plane nanocrystal size, *R*, changes dramatically, while the out-of-the-plane height, *H*, changes slightly. The in-plane nanocrystal size is consistent with that measured by SEM. This indicates that annealing mainly affects the lateral structure of the Pt. However, for the 80-cycle sample, XRR analysis shows that the film thickness is 5.4 nm before annealing as compared to a post-annealing 14 nm vertical domain size, which can be considered as the lower limit of the cluster height. This indicates that Pt aggregates much more strongly in the vertical direction under thermal treatment for the higher coverage sample.

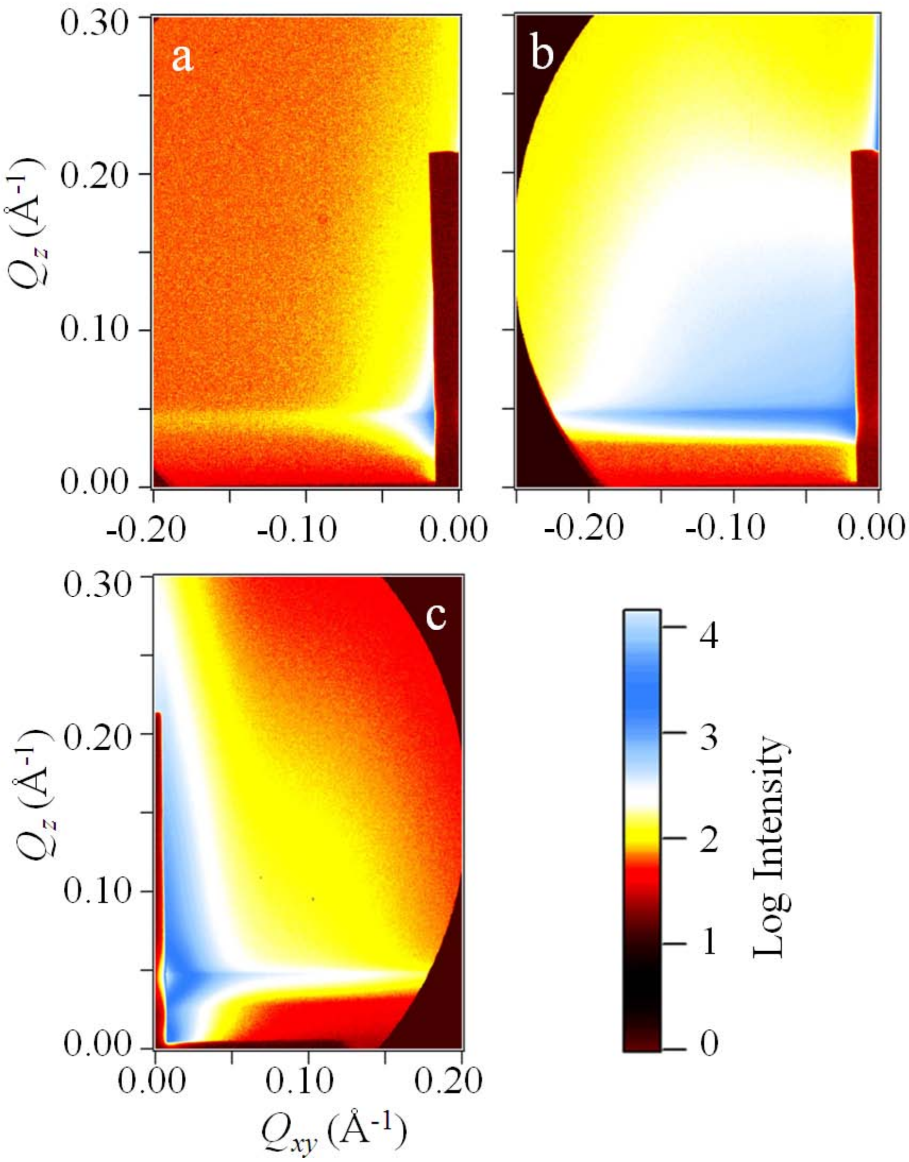

Figure 3.16 GISAXS data for (a) blank atomically-flat $SrTiO_3$ (001) surface, (b) 10 ALD cycles Pt as-deposited and (c) 10 ALD cycles Pt after 800 °C UHV annealing.

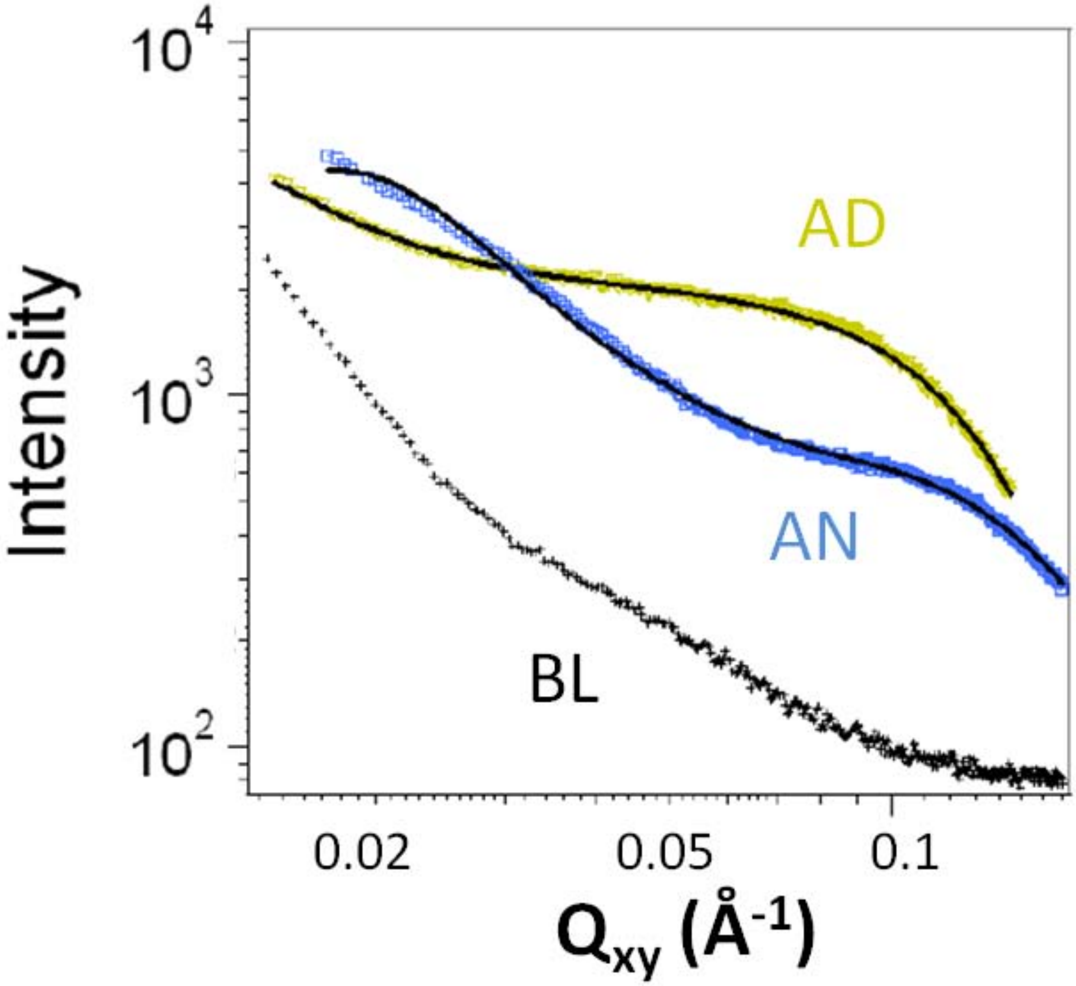

Figure 3.17 GISAXS horizontal line cut data and fits for blank (BL) $SrTiO_3$, Pt 10 cycles ALD as deposited (AD), and after annealing (AN). The individual curves are vertically offset for clarity. The line cuts are taken at $Q_Z = 0.04$ Å^{-1}. The values of the fit determined parameters are listed in Table 4.7.

Table 3.7 GISAXS fitting and analysis results for as-deposited (AD) and annealed (AN) ALD Pt/$SrTiO_3$(001) samples. In this case, the particle model is taken to be a cylinder of radius, R, and height, H, with a center-to-center interparticle spacing, *D*. The parameter, σ, gives the distribution width of the respective parameter.

ALD cycles	R (nm)	σ_R (nm)	H (nm)	σ_H (nm)	D (nm)	σ_D (nm)
AD						
10	1.1	0.1	1.2	0.3	2.2	0.8
20	2.1	0.5	2.3	0.6	6.3	1.3
30	3.1	0.7	3.0	0.8	9.0	2.1
40	3.5	0.9	3.8	1.0	9.0	2.5
AN						
10	1.2	0.1	1.0	0.1	2.6	0.7
20	3.4	0.9	3.3	0.4	9.9	0.3
30	6.9	2.6	4.1	0.6	21.4	0.7
40	9.0	3.0	4.3	0.7	37.8	0.7

The GISAXS observed annealing effects are most dramatic in the higher coverage 80 ALD cycle case shown in Fig. 4.18; where evidence of long-range orientational ordering and faceting of the Pt nanocrystals can be seen. These images are part of a set of GISAXS patterns collected at 2° intervals in azimuthal angle ϕ over a range of 180°. Figure 4.18(a) was taken with the incident beam approximately along $SrTiO_3$ [100] direction; whereas Fig. 4.18(b) was along the [110]. This rotation shows a change in the intensity pattern consistent with scattering from nanoparticle crystallographic facets.[197] In this case, a scattering lobe is directed at an angle of ~55° from the specular direction and is four-fold symmetric about the surface normal rotation axis. This would indicate {111} facets for Pt nanoparticles with cube-on-cube epitaxy. Furthermore, the Pt nanoparticles in this case possess a high degree of long-range orientational ordering as GISAXS measures the ensemble average of nanoparticle orientation. Similar in-plane investigations for the cases of ALD cycles less than 80 yielded no such evidence of faceting and/or long-range orientational ordering. The four-fold symmetric GISAXS intensity about the surface normal indicates a pyramidal or truncated pyramidal nanocrystal morphology with {111} facets.[197] The SEM image in Fig. 4.13(c) shows a morphology in which the nanocrystals appear to be faceted and exhibit an in-plane directional edge pattern that is not simply 4-fold symmetric. This seeming discrepancy between GISAXS and SEM could be due to the fact that many of the nanoparticles as observed by SEM are elongated and stretch at regular angles across the surface; while GISAXS senses the ensemble averaged structure. However, for lower Pt coverage, i.e. ALD cycle less than 40, no faceting of the Pt nanocrystals was observed. These results indicate that the UHV annealing has stronger effects on high coverage Pt and therefore a structural correlation between the platinum and strontium titanate can be observed.

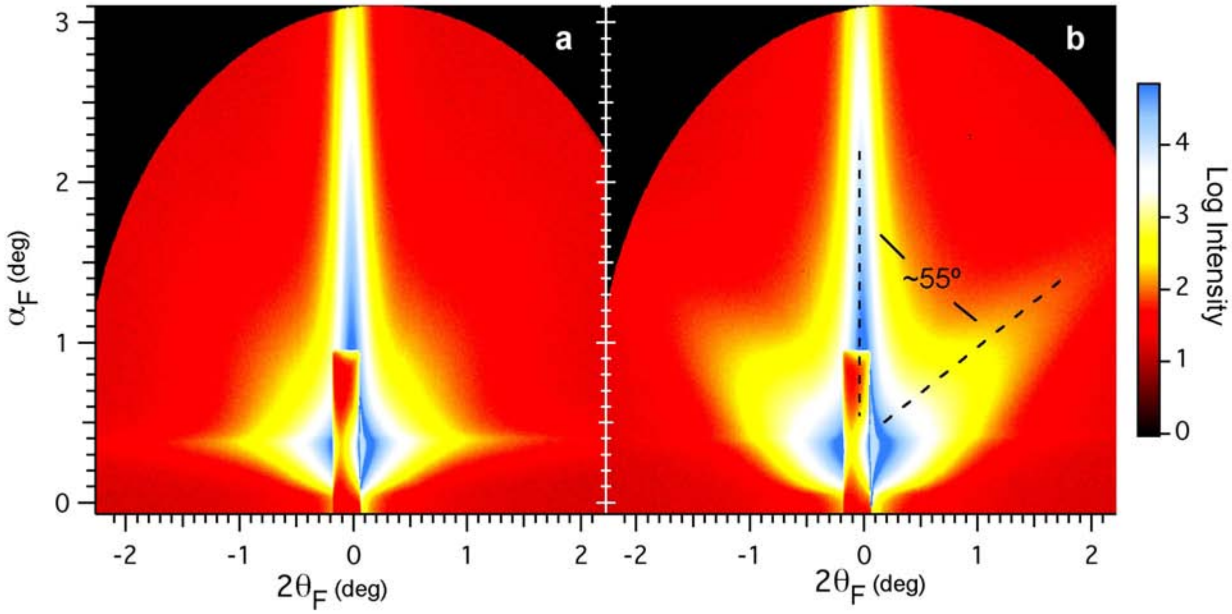

Figure 3.18 GISAXS data showing faceting and long-range orientational ordering of the Pt nanocrystals for the annealed 80 ALD cycle case. The data is given as a function of scattering angles α_F and $2\theta_F$ for simplicity. Pattern (a) was collected with the incident beam approximately along the $SrTiO_3$ [100] direction; while (b) was taken along the [110] direction. The intensity lobe in (b) is indicative of scattering off the {111} facet for a Pt nanocrystal with cube-on-cube epitaxy.

These various annealing effects of Pt with different coverages can be attributed to surface diffusion, interfacial energy, and surface energy anisotropy of noble metals (including platinum, gold and palladium) on oxide surfaces. The typical thermodynamic preference of metal/ceramic systems is to leave exposed substrate surface and form 3D island-like morphologies.[13] However, at low temperatures island growth cannot be reached. Therefore a “quasi-2D” or “2D-island” growth mode[195] dominates and flat metal films can be gown[200, 201]. This would be consistent with the discontinuous films (2D-islands) we observed for the AD Pt films grown at 300°C. When annealed at a higher temperature (800 °C), Pt adatoms gain sufficient kinetic energy to diffuse on the surface, causing the formation of nanoclusters. The strong temperature dependent effect of Pt surface diffusion coefficient in cm^2/s is described by an empirical relationship given by Gjostein,[202]

$$D_s(T) = 0.014\exp\left(-\frac{13T_m}{R_cT}\right), \tag{4.4}$$

where T and T_m are the substrate temperature and Pt melting point in °K, and R_c =1.99 cal mol^{-1} K^{-1} is the gas constant,. This surface diffusion coefficient at 800 °C is $5.8x10^{-8}$ cm^2/s, much greater than that at 300 °C, $1.2x10^{-12}$ cm^2/s. For sub-monolayer coverages, Pt on $SrTiO_3(001)$ surfaces exists as widely separated nanoparticles, which under thermal treatment may come together without sintering to form nanoclusters.[83] It is also possible that under UHV annealing these widely distributed Pt nanoparticles are encapsulated by the substrate titanium oxide layers,[88] prohibiting Pt mobility at high temperature. Therefore in this sub-monolayer case after annealing, no significant surface structural changes were observed by GISAXS, which is most sensitive to small nanoparticles. However, as the Pt coverages increase, high surface diffusion and limited surface area cause Pt to come together. In another view, encapsulation of Pt nanoparticles by the substrate cannot compete with Pt coalescence, also resulting in the formation of nanoclusters.

In addition to surface diffusion, the interfacial energy and the surface energy anisotropy, or the difference between the surface energies of competing metal film orientations, also play important roles in determining the surface morphology and Pt nanocluster orientations. Generally speaking, epitaxial orientation minimizes the surface and interface energy.[96] Growth of (001)-

orientated fcc metals on oxides is challenging because close-packed {111} planes have the lowest relative surface energy, γ.[203, 204] From powder diffraction studies of 20 to 110 nm thick platinum films grown via ALD on amorphous substrates, {111} texture was strongly preferred.[137] To achieve (001)-orientated films, this energetic preference must be overcome by a favorable interfacial relationship between the ceramic and the metal (001) orientation. Furthermore, since Pt has low oxygen affinities, for growth temperature $T < 600$ °C, various crystal orientations can be expected.[94] When these samples were annealed at 800 °C, the AD ALD Pt with discontinuous film structures started to coalesce, forming 3D islands, as observed in AFM and SEM. This aggregation can be understood as an Ostwald ripening process, which is also observed for other noble metals grown on oxides, such as Ag/TiO_2(110)[205], Au/TiO_2(110)[206] and Au/FeO(111)[207]. In our case, discrete Pt nanoparticles formed at sub-monolayer are not measurably affected by annealing, showing some thermodynamic stabilization. However, when the sample coverages is in excess of several ML, formation of large nanoclusters is the dominant trend, although some very small nanoclusters are still visible, as seen by SEM. This bimodal size distribution[205, 206] of Pt nanoclusters is the evidence for Ostwald ripening, which is observed as some clusters increase in size while other clusters shrink.

The formation of (001)-orientated epitaxial nanocrystals at a higher Pt coverage can be explained by the temperature dependence of Pt surface anisotropy, $\gamma(001)/\gamma(111)$. At high temperature (800 °C in our case), the Pt surface energy anisotropy is lowered and the energetic preference to {111} planes thus becomes lower, while the film/substrate interfacial energy is unaffected.[93] This will promote the epitaxial (001) orientation of Pt on $SrTiO_3$(001). On the other hand, fast surface diffusion at high temperature means that atoms can most easily locate their preferred crystalline orientation.[94] In our ALD Pt samples, only the higher coverage sample, 80 ALD cycles, achieved detectable epitaxy. This is because the initial Pt grain size and the initial degree of surface coverage are also primary factors in determining the epitaxial growth, as shown elsewhere[208]. Monte Carlo simulations show that high initial Pt coverages result in the growth of the epitaxial grain sizes and can eventually evolve to an epitaxial thin film, while low initial Pt coverage can only result in a final polycrystalline microstructure.[208] This is consistent with our observation. For coverages lower than 40 ML, some Pt epitaxial grains may form, but not sufficiently enough to form larger ordered nanocrystal domains above our ~10 nm detectable limit. When the Pt coverage is sufficiently high, as with the 80 ALD cycle case, Pt aggregates more in the vertical direction during the annealing process, and eventually results in the formation of strain-relaxed Pt nanocrystals with cube-on-cube epitaxial structure. The formation of the faceted Pt nanocrystals is complicated. As shown in the Pt/Al_2O_3(0001) case[95], faceting was observed at some critical thickness by AFM. Several factors can affect this formation, such as surface and edge diffusion[209], elastic interaction[210] and substrate interaction[211]. Due to various defect sites and different substrate terminating atoms, the surface energy can vary by up to 30%.[212] For a particular initial film thickness, Pt surface can exhibit various diffusivity, leading to a wide range of geometric shapes.[95] In our case, the coupling and competition of above factors result in Pt {111} faceting.

3.2.3 Summary

In this part, we studied the thermally-induced nanoscale nucleation and structural changes of Pt on $SrTiO_3(001)$ synthesized by ALD with 20 to 80 growth cycles. Combined AFM, SEM, XRF, XRR, reciprocal-space map, and GISAXS measurements show that Pt exhibits different structural and surface morphological changes after annealing that depend on the initial as-deposited Pt coverage in the range of 1 to 40 ML. This is attributed to the surface diffusion, interfacial energy, and surface energy anisotropy of noble metals on oxide surfaces. Annealing has no significant effect on widely separated Pt nanoparticle formed at sub-monolayer coverages, while it causes aggregation for Pt films formed at coverages exceeding several monolayers. This effect becomes stronger for thicker Pt (i.e. more than 40 ALD cycles) that changes from a film with no observable texture to {111} faceted nanocrystals with cube-on-cube epitaxy. This thermal-induced aggregation and crystallization with respect to the substrate lattice should motivate future studies for the nucleation of noble metals grown by atomic-layer deposition.

Chapter 4: ALD Grown WO_X / α-Fe_2O_3 (0001)

4.1 Introduction

Metal oxide monolayers or clusters anchored to an oxide support are important catalysts for industrial processes.[1] Typically a catalyst as a monolayer (ML) exhibits greater activity than as a thicker film.[5] More importantly, predictability for the interface structure of the supported oxide would have an enormous impact upon our understanding of numerous chemical processes, since the structure of the catalyst will affect chemical reactions, as for example in the proposed case of NO decomposition.[124]

For various chemical reactions, reduction-oxidization (redox) is a basic one. During the redox reactions, the catalysts (e.g. Pt, V, W) go through the chemical states changes cycle to assist the reaction. 300 °C ~ 500 °C is a typical temperature range for redox reaction with catalysts participation. While redox induced chemical shifts in XPS for catalytically active cations are well known[213], there are (to our knowledge) no predictions or measurements that clearly show redox induced cation migration from one surface symmetry site to another. Therefore, in this part, we choose WO_X / α-Fe_2O_3(0001) as a model system to study how W cations change, structurally and chemically, in the redox reaction. In this case, α-Fe_2O_3(0001) is a reducible oxide support, which can further help W in the reaction.

4.2 Experimental Results and Discussions

Hematite (α-Fe_2O_3) mineral single crystals were oriented, cut and polished parallel to the (0001) by Commercial Crystal Laboratories (Naples, FL). Hematite adopts the corundum crystal structure (space group R-3c) with a = 5.038 Å and c = 13.772 Å.[214]

The c-face hematite substrate was annealed in a tube oven with flowing O_2 (~100 sccm) at 400 °C for 0.5 h, followed by 5h at 750 °C. Prior to ALD, the substrate was immersed in ultrapure water (resistivity > 10^{18} Ω cm^{-1}) for 1 h at 90 °C to hydroxylate the surface. Next, the substrate was rinsed in 10% HCL, followed by an ultrapure water rinse, and then blown-dry with nitrogen. The substrate was then loaded into an ALD reactor[192], where it was heated to 200 °C under ultrahigh-purity nitrogen flow at 360 sccm at a pressure of 1 Torr for 1 h, and then cleaned using flowing ozone. The sub-monolayer tungsten oxide layer was grown at 200 °C by sequentially exposing the substrate to Si_2H_6 and WF_6 at 10 Torr for 10 minutes each.

Silicon AFM tips with a nominal 10 nm radius of curvature and cantilever resonant frequency of 70 kHz were used with the JEOL-JSPM-5200 scanning probe microscope at the NIFTI facility of NUANCE Center at Northwestern University. The AFM image in Figure 5.1(a) of the annealed α-Fe_2O_3 (0001) substrate surface shows large atomically flat terraces separated by atomic steps. This is the starting point for WO_X ALD. Figure 5.1(b) shows the surface morphology after the ALD and redox reaction. Clear terraces indicate that no significant changes have occurred to the hematite surface morphology, i.e., the ALD process is conformal.

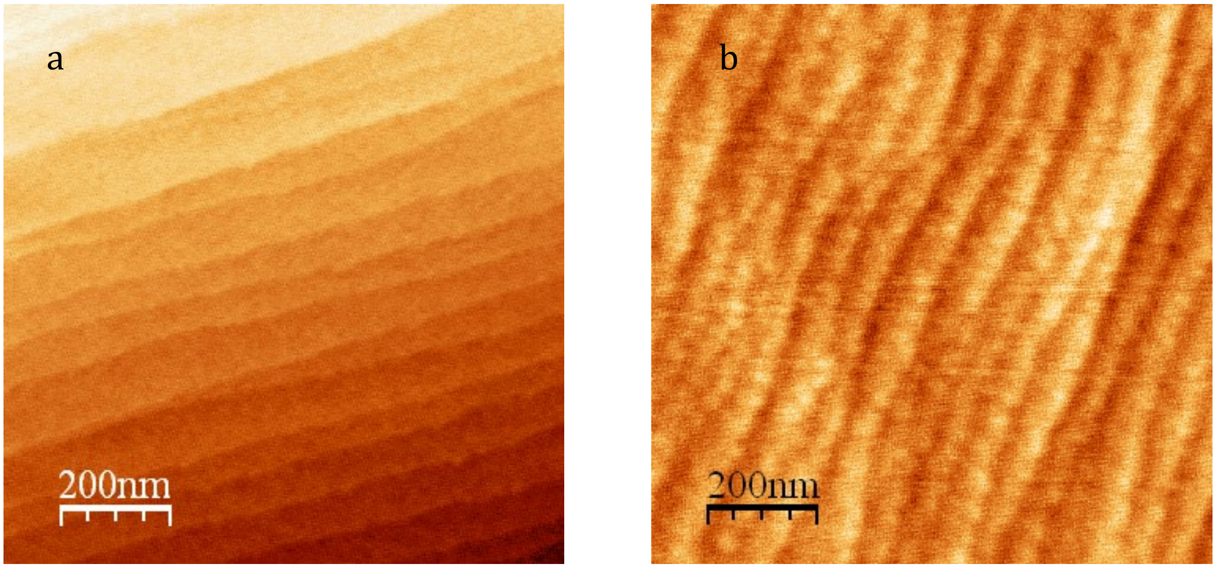

Figure 4.1 AFM images of the α-Fe_2O_3 (0001) substrate surface: (a) substrate after the two step annealing process shows the clean atomically flat terraces with 0.2 nm tall steps. (b) after ALD deposition and redox reaction, terraces are still clearly observed, indicating that the ALD process is conformal to the surface.

Figure 5.2 shows the X-ray photoelectron spectra (XPS) taken from the sample at the as-deposited (AD), oxidized (Ox) and reduced (Re) states. The Ox and Re surfaces were prepared by annealing at 350 °C in pure O_2 and 2% H_2 in Helium, respectively. These spectra were collected at the Keck II facility of NUANCE with an Omicron ESCA probe using Al Kα as the monochromatic X-ray source. A low-energy electron flood gun was used to compensate for XPS induced surface charging effects. Carbon 1s (284.8 eV) was used as reference to calibrate the XP spectra. Fig. 5.2(a) shows the W $4f_{7/2}$ and $4f_{5/2}$ doublet peaks. The identical spin-orbital separation (2.1 eV) was used to fit doublet peaks.[21] The dots are experimental data; the blue lines are W^{5+} (binding energy (BE): 34.5 eV and 36.6 eV) doublet peaks; the red lines are W^{6+}

(BE: 35.5 eV and 37.6 eV) doublet peaks; and the dashed black lines are total fit results. Fig. 5.2(b) shows the Fe 2p peaks and Fig. 5.2(c) shows survey scan across the F 1s region. XPS measurements of Fe 2p peaks show no change for AD, Ox and Re states, indicating that the Fe at the hematite surface are not changing their chemical state during the redox reaction. The survey scans across the F 1s region show that fluorine existed only in the AD state. (Fluorine originated from the WF_6 molecules used in the ALD process.) The 350 °C oxidation step completely removed the fluorine. Based on our XPS data we calculate[162] that there are on average 1.6 fluorine atoms for each tungsten atom; indicating that a varying number of fluorine are bonded to tungsten cations in AD state.

After the ALD growth, the sample was removed from the ALD reactor and placed inside a beryllium dome reaction chamber, which was mounted on a diffractometer for *in situ* XSW measurements. For the X-ray standing wave (XSW) measurements, an incident photon energy of 13.00 keV was selected with a Si (111) monochromator and collimated further with either Si (111) or (220) postmonochromator channel-cut crystals. The XSW data was collected at DuPont-Northwestern-Dow Collaborative Access Team (DND-CAT) 5ID-C of the Advanced Photon Source (APS).[167] The experimental setup can be found in Fig. 3.11. The X-ray beam size is selected by the entrance slits before hitting the sample. To do *in situ* measurements, a beryllium dome reaction chamber was mounted on a diffractometer, as shown in Figure 3.12. A Vortex silicon drift diode (SDD) detector was used to collect the X-ray fluorescence. A tungsten coverage of 0.31 ML was determined from a side-by-side comparison to a Rutherford backscattering spectroscopy (RBS) calibrated standard. One monolayer is defined as the area density of Fe ions in the hematite (0001) surface, or 9.1 atoms / nm^2.

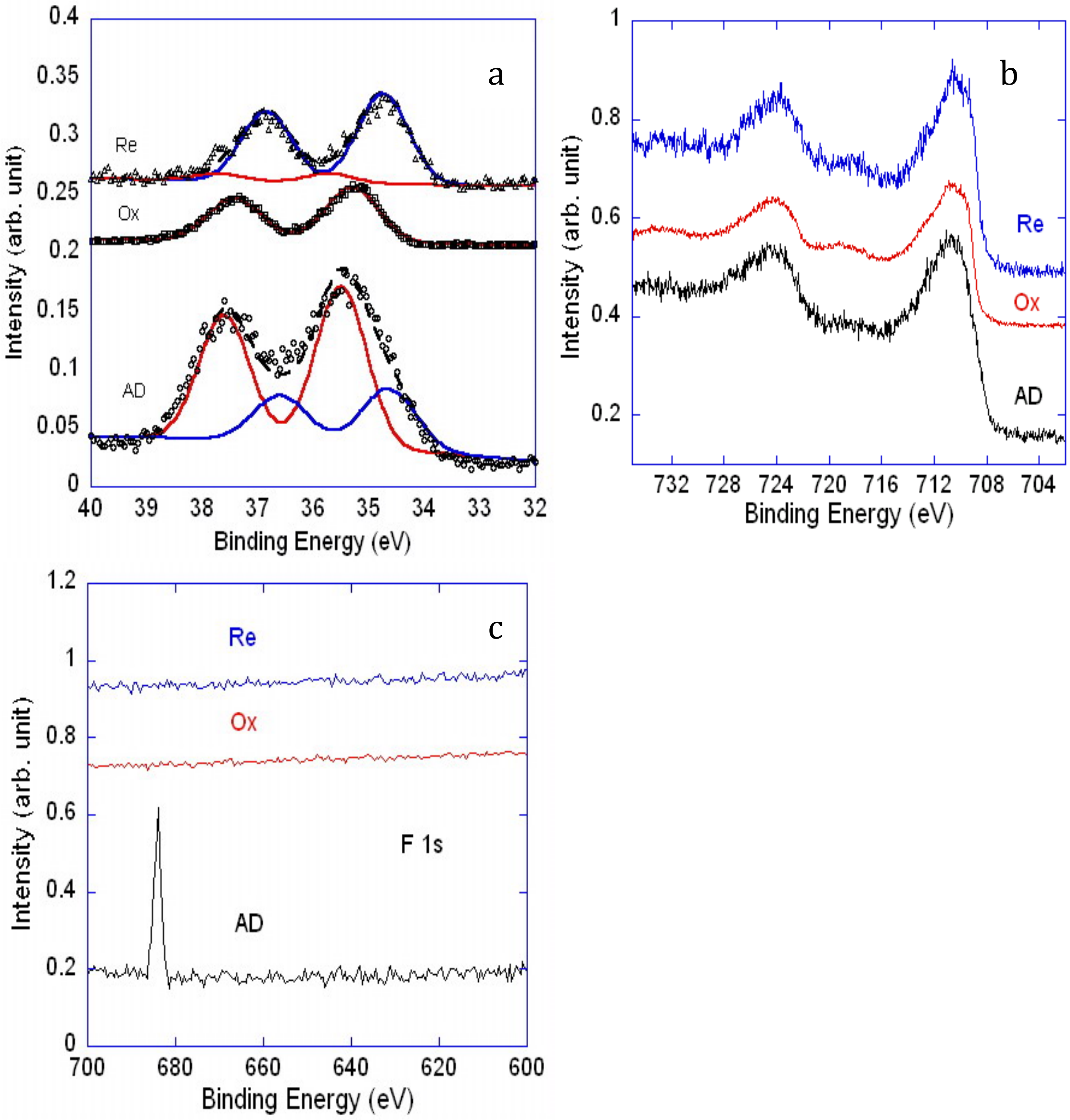

Figure 4.2 X-ray photoelectron spectra of the 1/3 ML WO_X / α-Fe2O3 (0001) interfacial structure at the AD, Ox and Re states with an electron takeoff angle of 45° (AD) and 10° (Ox and Re) from the sample surface: (a) W 4f doublet peaks. The black dashed-line is the best fit to the data based on weighted contributions from the W^{6+} (red line) and W^{5+} (blue line). AD is 70% W^{6+} and 30% W^{5+}, Ox is 100% W^{6+}, and Re is 10% W^{6+} and 90% W^{5+}. (b) Fe 2p peaks and (c) survey scan across F 1s region. The XP spectra are displaced vertically in the order of processing.

For *in situ* XSW measurements, the cell was purged with ultrahigh-purity oxygen flow (~100 sccm) at room temperature for 10 min prior to oxidization. Then continuously with oxygen flow, the temperature was increased to 180 °C for 20 minute to dehydrate the sample; followed by oxidization at 350 °C for 30 minutes. A series of reduction reactions were then performed with a flow (~100 sccm) of 2% hydrogen balanced by 98% helium: at 240 °C for 5 min, 300 °C for 10 min, 350 °C for 15 min and then 30 min. To check the reversibility of the redox reaction, a second oxidization, 30 min at 350 °C with ~100 sccm oxygen flow, was done after the reduction. Before any treatment and after each reaction, XSW measurements were carried out at room temperature in the beryllium-dome at a vacuum level held by a diaphragm roughing pump.

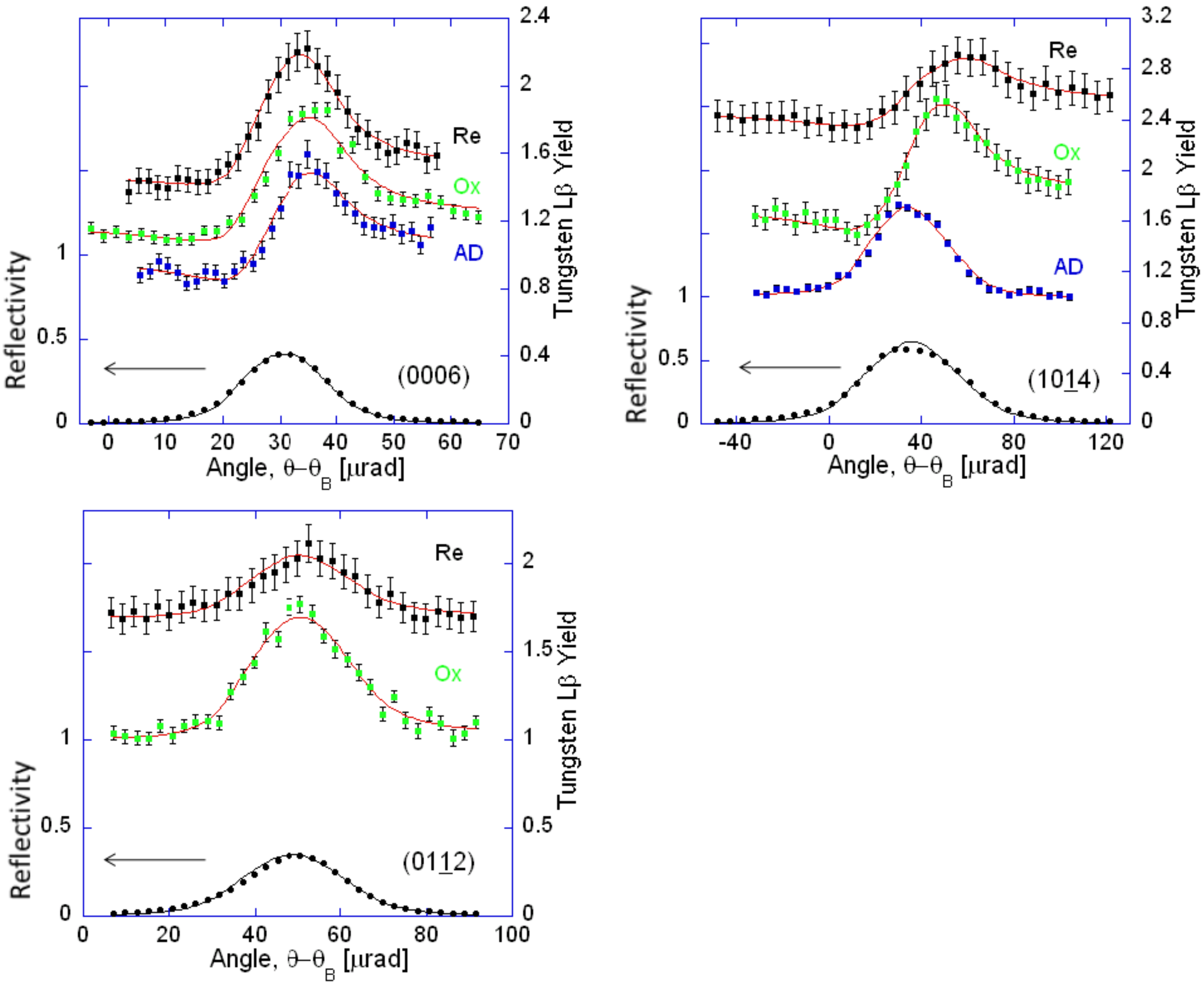

Figure 4.3 XSW results for the (0006) normal reflection, (10$\underline{1}$4) off-normal reflection and (01$\underline{1}$2) off-normal reflection of hematite for the as-deposited (AD), oxidized (Ox) and reduced (Re) ALD tungsten oxides. In the lower section of each frame is shown the measured and dynamical diffraction theory fitted reflectivity cures for each reflection. The upper section of each frame shows the W Lβ XRF data and theory (Eq. 4.1) fitted yields for each state. The XRF yields are given vertical offsets for clarity.

Table 4.1 Summary of the *in situ* XSW experimental analysis after the AD, Ox, Re, and Ox2 surface treatments of the 1/3 ML W / α-Fe_2O_3 (0001) interface. Model independent parameters, f_H and P_H, are the measured $H = hkil$ Fourier amplitudes and phases for the W distribution. These can be compared to the calculated f_H^C and P_H^C values determined from the best-fit of the model that is described by Eq. 2 with best-fit parameters listed in Table 5.2.

	(0006)				(10$\underline{1}$4)				(01$\underline{1}$2)			
	f_H	f_H^C	P_H	P_H^C	f_H	f_H^C	P_H	P_H^C	f_H	f_H^C	P_H	P_H^C
AD	0.50(1)	---	-0.01(1)	---	0.06(1)	---	---	---				
Ox	0.53(2)	0.62	0.08(1)	0.18	0.58(1)	0.65	0.45(1)	0.45	0.28(3)	0.67	-0.28(1)	-0.28
Re	0.46(2)	0.44	0.11(1)	0.02	0.61(1)	0.60	0.38(1)	0.49	0.13(2)	0.17	0.33(2)	0.55
Ox2	0.47(1)	0.59	0.11(1)	0.16	0.63(3)	0.62	0.44(1)	0.44	0.55(2)	0.65	-0.22(1)	-0.28

Figure 5.3 shows the XSW data for the sample at each redox processing step. Each angular scan is through a selected hematite *H = (hkil)* Bragg reflection. The XSW W L fluorescence data and analysis for the AD, Ox and Re surfaces show striking differences. The XSW induced modulation of the background-subtracted and deadtime-corrected W Lβ_1 fluorescence yield from each scan is used to determine the coherent fraction (f_H) and coherent position (P_H). This determination is based on fitting the normalized yield data to the model independent expression for the yield,[152, 153] based on Eq. 4.1. The measured f_H and P_H values, as listed in Table 5.1, show that the W atomic distribution for the AD surface is vertically correlated to the substrate lattice, but laterally uncorrelated; while the Ox and Re surfaces are 3-dimensionally correlated. The Ox and Re W Fourier components are similar in the (0006) normal direction, but significantly different in the two off-normal directions. This indicates lateral

differences in the W distribution. Furthermore, Ox2 gives almost the same f_H and P_H as Ox, indicating reversibility of this redox reaction.

The XSW measured values for f_H and P_H, which are also the Fourier amplitudes and phases for the W distribution, are then used in Eq. (1) to generate the 3D direct-space image of the W distribution with respect to the hematite unit cell. 2D cuts through the W maps are shown in Fig. 5.4. For the α-Fe_2O_3 (0001) surface, there are two symmetry inequivalent Fe sites, A and B, above the topmost oxygen layer. These are symmetrically equivalent to the two Fe occupied octahedral sites in the bulk. The A site is located closer to its underlying oxygen trimer than the B site. The 3D W maps show that for the Ox surface, W^{6+} cations take only B sites, while in the reduced state, tungsten cations take both A and B sites.

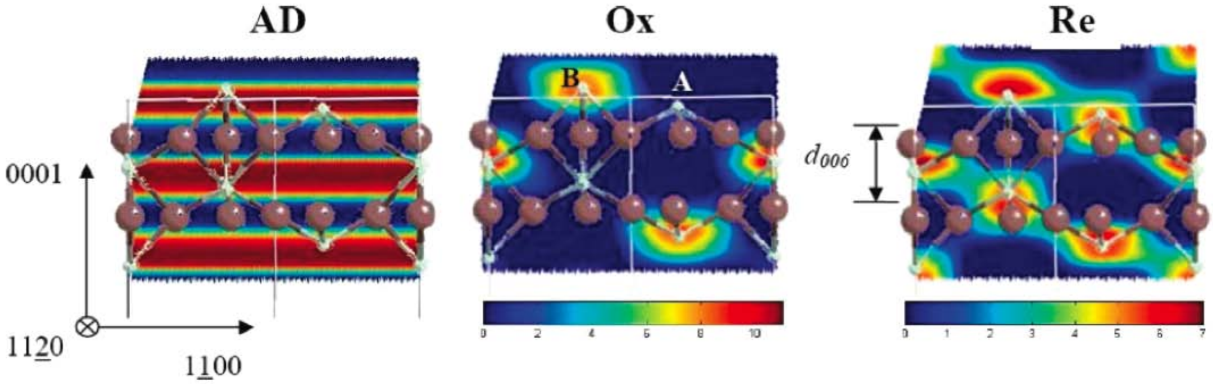

Figure 4.4 (11$\underline{2}$0) 2D cuts through the XSW measured 3D tungsten atomic density maps for the AD, Ox and Re WO_X / α-Fe_2O_3 (0001) interface and projections of the α-Fe_2O_3 ball-and-stick model. The small white balls represent Fe cations and the larger brown balls are O-anions. The map for the Ox surface is recovered after a second oxidization.

To obtain the local structure surrounding the tungsten cations on hematite, *ex situ* X-ray absorption fine structure (XAFS) measurements were carried out on the oxidized (Ox) sample and a set of W standards. After oxygen oxidation at 350 °C, the Ox WO_X / α-Fe_2O_3 (0001) sample was placed on the sample stage of DND 5BM-D station at the APS. A 13-element solid state detector was used to collect the W L fluorescence signal while the Si(111) monochromator scanned the incident X-ray photon energy through the W L_2 absorption edge. WO_3 and WO_2 powder samples were used as reference materials for comparison, and tungsten metal standard foil was used for energy calibration of the monochromator. Powder samples were spread uniformly onto Scotch tape, which was then folded a few times, yielding edge steps slightly less than unit. The bulk spectra were recorded in transmission mode.

Figure 5.5(a) compares the normalized W L_2 edge X-ray absorption near edge spectra (XANES) of the Ox sample, bulk WO_2 and WO_3. It clearly shows that the L_2 edge structure of the Ox sample is dominated by a strong white line peak that closely matches that of WO_3. The splitting of the white lines due to t_g and e_g states is a signature of W^{6+}.[215] The differences in the peak widths and the small feature (arrow) are likely due to bulk effects (or lack of) and the detailed differences in the local structural configurations. The first derivatives of the XANES (Fig. 5.5(b)) indicate that the edge energies for the Ox sample and WO_3 powder are practically aligned, and 1.5 eV higher than that of WO_2 powder, further supporting the W^{6+} assignment.

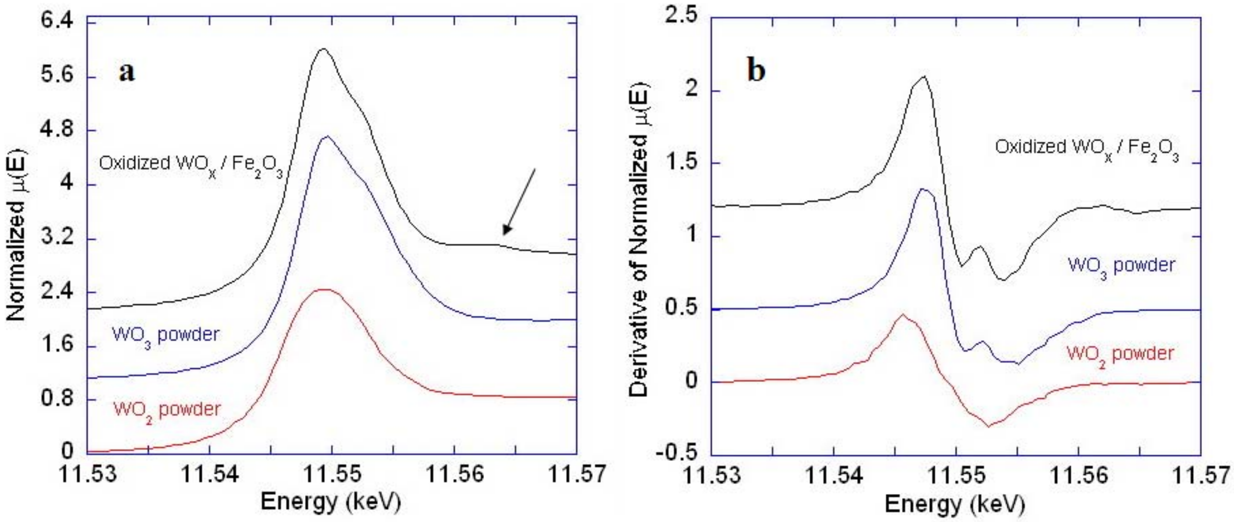

Figure 4.5 X-ray absorption near edge spectra from the Ox sample, and powder samples of polycrystalline WO_2 and WO_3. (a) Normalized μ(E) versus incident photon energy and (b) the first derivative of the normalized μ(E) versus energy.

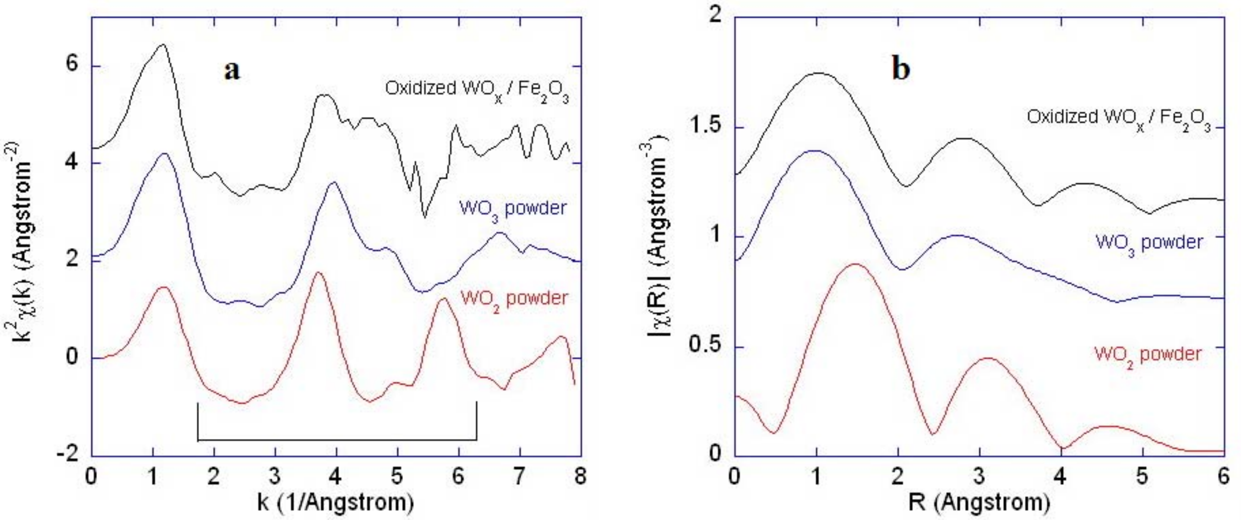

Figure 4.6 (a) Extended X-ray absorption fine structure (EXAFS) spectra of the Ox sample, powder samples of polycrystalline WO_2 and WO_3, and (b) the Fourier transform of the EXAFS spectra over the k range indicated at the bottom of (a).

Figure 5.6(a) compares the EXAFS spectra of the Ox sample, and powder samples of WO_2 and WO_3. The Ox sample spectrum has a larger statistical scatter in its signals due to its inherently lower concentration. However, the Ox sample compares very favorably to the bulk WO_3, suggesting a similar local structure around W^{6+} in the Ox sample. The Fig. 5.6(b) Fourier transforms of the EXAFS spectra in the k range indicated by the dark line in Fig. 5.6(a) also shows the similarity between the sample and WO_3. Therefore, it is very likely that W^{6+} ions are coordinated by 6 oxygen ions, in an arrangement somewhat different than that of a WO_3 crystal.

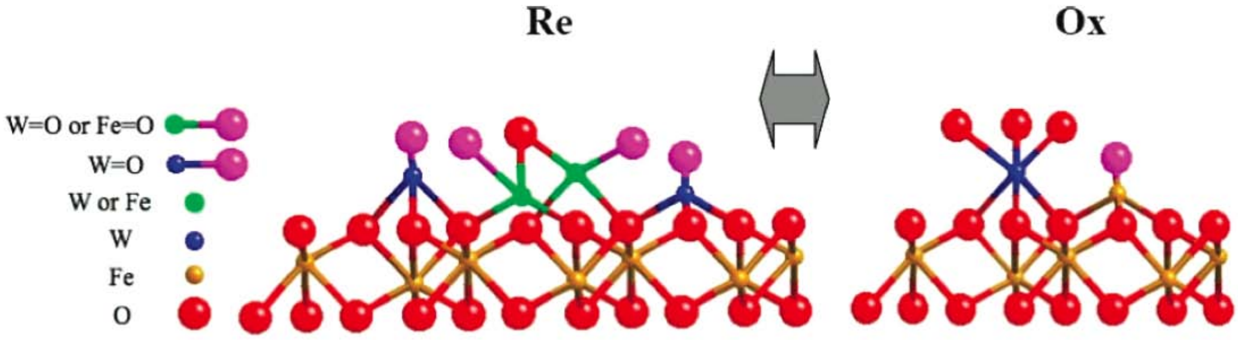

Figure 4.7 Proposed models for the fully reduced (Re) and oxidized (Ox) WO_X / α-$Fe_2O_3(0001)$ interfaces that are consistent with the XSW measured W atomic maps and the 5+ and 6+ oxidation states found by XPS.

With the confinement from XAFS, Fig. 5.7 shows our proposed models for explaining the above observations. These models are partially based on our earlier study of VO_X / α-Fe_2O_3 (0001).[8] For the Ox surface, our model shows W in the Fe B-site as measured by XSW and proposes a local structure similar to the WO_3 tetragonal crystal structure, which is composed of six W-O bonds with some distortion. This local structure is based on our XAFS measurements of the Ox sample in comparison to a standard WO_3 powder sample. (Figs. 5.6 and 5.7) The reduced state is more complex since the XSW map shows W^{5+} cations in both A and B sites. Fig. 5.7 illustrates a few possible structures: isolated WO_4 in either A or B sites, with one W=O bond above the surface and three W-O-substrate bonds; or a dimer structure as proposed in Ref.[8], with W replacing V.

To quantify the W occupation fractions (c_X) and heights (z_X) for sites A and B in the Ox, Re and Ox2 states, we use a least-squares global fit of a model to the set of measured Fourier components for the W atomic distribution:

$$F_H = f_H \exp(2\pi i P_H) = c_A \exp\left[\frac{2\pi i(2h+k+3lz_A)}{3}\right] + c_B \exp\left[\frac{2\pi i(h+2k+3lz_A)}{3}\right]. \qquad (5.1)$$

The parameters from the best fits, which are listed in the Table 5.2, quantitatively show the movement of W cations during redox reactions. In this table $c_A + c_B \sim 0.7$, indicating that 70% of the total W are ordered in both redox states. The remaining W atoms are measured to be in an uncorrelated distribution relative to the substrate lattice. Since AFM and grazing incident small angle X-ray scattering (at APS 12ID-C) showed no evidence for nanocluster formation, the uncorrelated W cations are most likely associated with hematite surface defect sites and step-edges. Table 5.2 also shows that in the Ox state, all ordered W cations are at B sites. However, the reduction causes half of those ordered W to migrate from B sites to A sites. Ox2 moves all W in A sites back to B sites. The W heights in either A or B sites are close to the original bulk-like Fe heights of 0.85 and 1.45 Å, respectively.

Table 4.2 Best fit parameters for W adsorption geometry model, where c_X and z_X are the W occupation fraction and heights for the X = A and B sites. *z* = 0 is at the bulk-like oxygen plane. As a comparison Fe in bulk-like α-Fe_2O_3 has z_A = 0.85 Å and z_B = 1.45 Å.

Surface	c_A	c_B	z_A (Å)	z_B (Å)
Ox	0.04(1)	0.64(1)	--	1.58(2)
Re	0.31(1)	0.36(1)	0.88(3)	1.46(2)
Ox2	0.05(7)	0.61(8)	--	1.54(7)

Based on information above, we can now propose explanations for the AD, Ox, and Re structures and the dynamics that occur in transition between these states. Assume that the bare hematite (0001) surface is Fe=O terminated with B-sites unoccupied and A-sites occupied by Fe in an O-Fe-O_3-Fe••• configuration as predicted by DFT[43, 44] and observed by STM[216]. (This configuration can be seen in Fig. 5.7 on the far right-hand-side.) XPS (Fig. 5.2(c)) indicated that there were, on average, 1.6 fluorine atoms per W atom on the AD surface and that F completely desorbed in the redox process. This residual fluorine from the WF_6 precursor can explain the lateral disorder. If W have varying numbers of fluorines in the AD state instead of all bonded with oxygen (as in Ox and Re states), the W lateral position of the W will shift away from the missing oxygen preventing lateral correlation. Oxidation removed all fluorines and moved W^{6+} cations to the unoccupied B-sites. Oxygen bonded tungstens are locked in B sites and the thermodynamics is evidently such that W^{6+} cations do not exchange with Fe cations in A sites. In the Re state, the top oxygen of the O-Fe-O_3-Fe••• substrate surface could be removed by 2% H_2 to form an Fe-O_3-Fe••• surface. However, the transition from Fe-O_3-Fe to O-Fe-O_3-Fe is very easy[14]. Thus in the Re state, the substrate surface is also O-Fe-O_3-Fe•••. XPS indirectly demonstrates this by showing no change of Fe spectra between the Re and Ox state. Furthermore, W^{5+} is more or less like Fe in surface terminated Fe=O and our XSW measurements indicate that a fraction of the W^{5+} replace Fe in A sites, (and perhaps some Fe can migrate to B sites). This causes the migration of W from B sites to A sites. Thus W^{5+} cations equally occupy both A and B sites in the Re state. Re-oxidization returns W^{6+} to the previous structure in the Ox state.

4.3 Summary

In summary, using the first XSW case study of ALD grown, $^1/_3$ ML WO_X on α-Fe_2O_3 (0001), we demonstrate redox driven cation dynamics for a catalyst on an oxide support. *In situ* XSW atomic imaging shows that: 1) 70% of the W atoms are correlated to the hematite lattice, 2) the reduced surface has W cations equally occupying the A and B Fe sites, and 3) oxidation moves W cations in A-sites to B-sites, with redox reversibility. *Ex situ* XPS shows that the W cations are in 5+ and 6+ oxidation states for the respective reduced and oxidized surfaces. Reversibility was observed in this redox process, which demonstrates its relevance for catalytic applications.

Chapter 5: ALD Grown VO_X / α-TiO_2 (110)

5.1 Introduction

We have discussed the redox-driven cations dynamics for WO_X / α-Fe_2O_3(0001), which shows quite interesting results. In this chapter, we will focus on vanadium, which is an even more popular catalyst. Our group has studied vanadium deposited on α-Fe_2O_3(0001) by MBE.[8] Vanadium is a active catalysts and α-Fe_2O_3(0001) is a reducible substrate, which can help supported metal or oxides during chemical reactions. TiO_2 is not so reducible compared to α-Fe_2O_3(0001). We are interested to see how vanadium perform if we combine active catalyst, V, with non-reducible substrate, α-TiO_2(110).

Vanadium oxide monolayers (ML) or clusters deposited on oxide surfaces are widely used in various chemical reactions[1, 7] that include applications such as gas sensors.[2] TiO_2 is one of the most studied supports.[105, 217] In supported vanadia catalysts, a phenomenon known as monolayer catalysis has been reported.[5] Here a sub-ML metal-oxide film supported by an appropriate oxide displays greater catalytic activity when compared to the thicker multilayer film. This would indicate that the supporting oxide plays a significant role in ML catalysis. In many cases, the catalytic activity of vanadia has an oxidation state dependency and the existence of V in the +5 oxidation state is crucial for catalytic reactions.[3, 4] Of those chemical reactions, oxidization-reduction (redox) is a common yet very important reaction for supported vanadia catalysts. Redox-induced transformations for catalysts on oxides surfaces,[81, 218, 219] including vanadium species at the TiO_2 and other surfaces[8] have been reported.

During redox reactions, the fundamental basis for the catalytic performances of supported vanadia lies in the variability in geometric and electronic structure of surface vanadium oxides.[1] If the surface structure of vanadia could be predicted, this would have an enormous impact upon our understanding of numerous chemical processes. From previous experiments, a general consensus for the atomic scale structure of supported vanadium oxide is that it exists as an isolated or polymerized VO_4 unit.[7] Therefore, in this Chapter, we will follow the similar methodology as the Chapter 5 to do a atomic-scale study of sub-ML (0.74 ML) vanadium cation positions with respect to the support and the corresponding sensitivity to the oxidation-reduction cycle.

5.2 Experimental Results and Discussions

Rutile (α-TiO_2) single crystals were oriented, cut (10 x 10 x 1 mm^3) and polished parallel to the (110) by Crystal GmbH (Berlin, Germany) with miscut < 0.1°. Rutile α-TiO_2 has a tetragonal crystal structure (space group: $P4_2/mnm$) with a room temperature lattice constant of $a = b = 4.594$ Å and $c = 2.959$ Å.

For convenience of working with the α-TiO_2(110) surface, a non-primitive tetragonal surface unit cell is defined. Fig. 6.1 shows the conventional primitive unit cell (blue dashed lines) with basis vectors ***a, b*** and ***c*** and the non-primitive surface unit cell (dark black lines) with basis vectors ***A***, ***B*** and ***C***, which have lengths $|\mathbf{A}| = |\mathbf{C}| = 6.495$ *Å* and $|\mathbf{B}| = 2.959$ *Å*. The transformation from the primitive tetragonal unit cell to the non-primitive tetragonal unit cell is

$$\begin{pmatrix}\mathbf{A}\\ \mathbf{B}\\ \mathbf{C}\end{pmatrix} = \begin{pmatrix}-1 & 1 & 0\\ 0 & 0 & 1\\ 1 & 1 & 0\end{pmatrix}\begin{pmatrix}\mathbf{a}\\ \mathbf{b}\\ \mathbf{c}\end{pmatrix}.$$

Throughout the text of this thesis, we will refer to the *hkl values* of the primitive unit cell for rutile.

α-TiO_2 (110) substrates were first annealed in a tube furnace with flowing O_2 (~100 sccm) at 400 °C for 0.5 h, then at 900 °C for 1 h. Prior to ALD, the substrates were immersed in ultrapure water (resistivity > 10^{18} Ω cm^{-1}) for 1 h at 90 °C to hydroxylate the surface. The substrates were then rinsed with 10% HCL, followed by an ultrapure water rinse, and then blown-dry with nitrogen. The substrates were then loaded into the ALD reactor[192] and heated to 300 °C under ultrahigh-purity nitrogen flow at 360 sccm at a pressure of 1 Torr for 1 h and then cleaned *in situ* with flowing ozone. For sub-ML vanadia growth, the substrates were exposed first to vanadyl oxytriisopropoxide, $VO_4(C_3H_7)_3$ (VOTP), at a partial pressure of 0.05 Torr for 2 s, followed by a nitrogen purge for 5 s. The substrates were then exposed to hydrogen peroxide at a partial pressure of 0.2 Torr for 2 s, followed by a nitrogen purge for 5 s. This process is defined as one ALD cycle for the V growth. Our X-ray fluorescence measurement later shows the coverage of this VO_X / α-TiO_2 is ¾ ML.

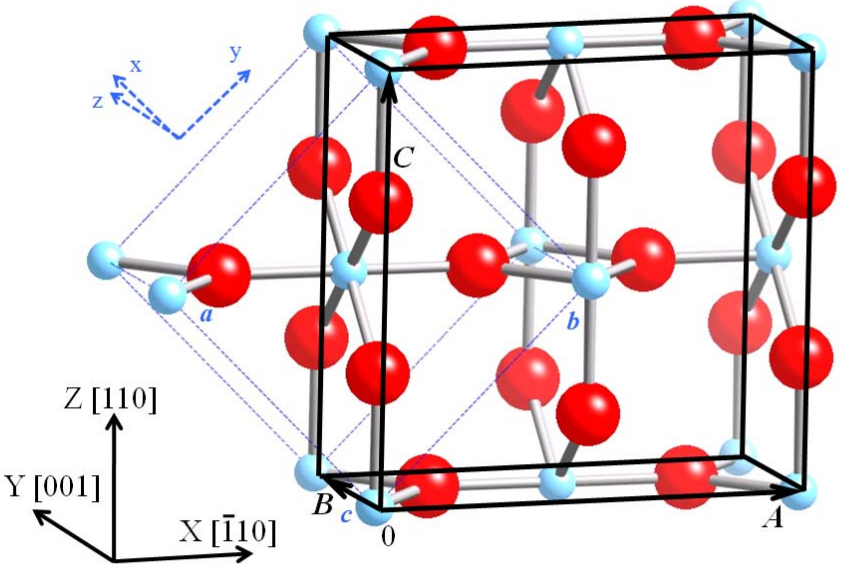

Figure 5.1 Rutile TiO_2(110) primitive unit cell (blue dashed lines) and non-primitive surface unit cell (dark black lines). Oxygen atoms are in red and Ti atoms in light blue.

XPS were taken from the sample at the as-deposited (AD), oxidized (Ox), reduced (Re) and re-oxidized (Ox2) conditions. These XP spectra were collected at the Keck II facility of NUANCE at Northwestern University with an Omicron ESCA probe using monochromatic Al Kα X-rays. A low-energy electron flood gun was used to compensate the XPS induced surface charging effects. Carbon 1s (284.8 eV) was used as the reference to calibrate the XP spectra. To obtain the Ox surface, the sample was placed in a quartz tube furnace. Oxygen was first purged for 10 min. With the continuous oxygen flow, temperature was increased to 180 °C to dehydrate the surface for 10 min and then 350 °C for 30 min to oxidize the surface. After cooling down to room temperature (RT) in oxygen condition, the sample was immediately transferred to an ultra-high vacuum (UHV) system for XPS and then outside for ambient atomic-force microscopy (AFM) measurements described later. To reduce the surface, the sample was transferred back to the furnace. Followed by a 10 min 5% hydrogen (balanced with nitrogen) purge, the sample was annealed at 350 °C for 30 min. After cooling down to RT in hydrogen condition, the sample was transferred out of the furnace for the same XPS and AFM measurements. The Ox2 surface was obtained as the Ox surface.

Figure 6.2 shows the XP spectra from the surface at the AD, Ox and Re states. We used the data processing and assignment methods described elsewhere for fitting the XPS peaks.[8, 159, 220] As seen in Fig. 6.2 for the AD and Ox states, the V $2p_{3/2}$ binding energy (BE) is 517.2 eV and the binding energy difference (BED) between the O 1s and V $2p_{3/2}$ is 12.8 eV. This indicates that V is V^{5+} for the AD and Ox states. However, in the Re state, the V $2p_{3/2}$ peak becomes broader, indicating the coexistence of multiple chemical states. Detailed analysis in Fig. 6.2 shows that V in the Re state is 25 % V^{3+} (BED: 14.6 eV) and 75 % V^{5+}. The coexistence of V^{3+} and V^{5+} has similarly been reported for V on silica and alumina[221, 222], which like titania are also non-reducible substrates. Hence a partial reduction of V^{5+} to V^{3+} in an ambient condition can be expected. Furthermore, XPS of the Ox2 surface (not shown) is identical to the Ox, indicating reversibility of vanadia in this redox reaction.

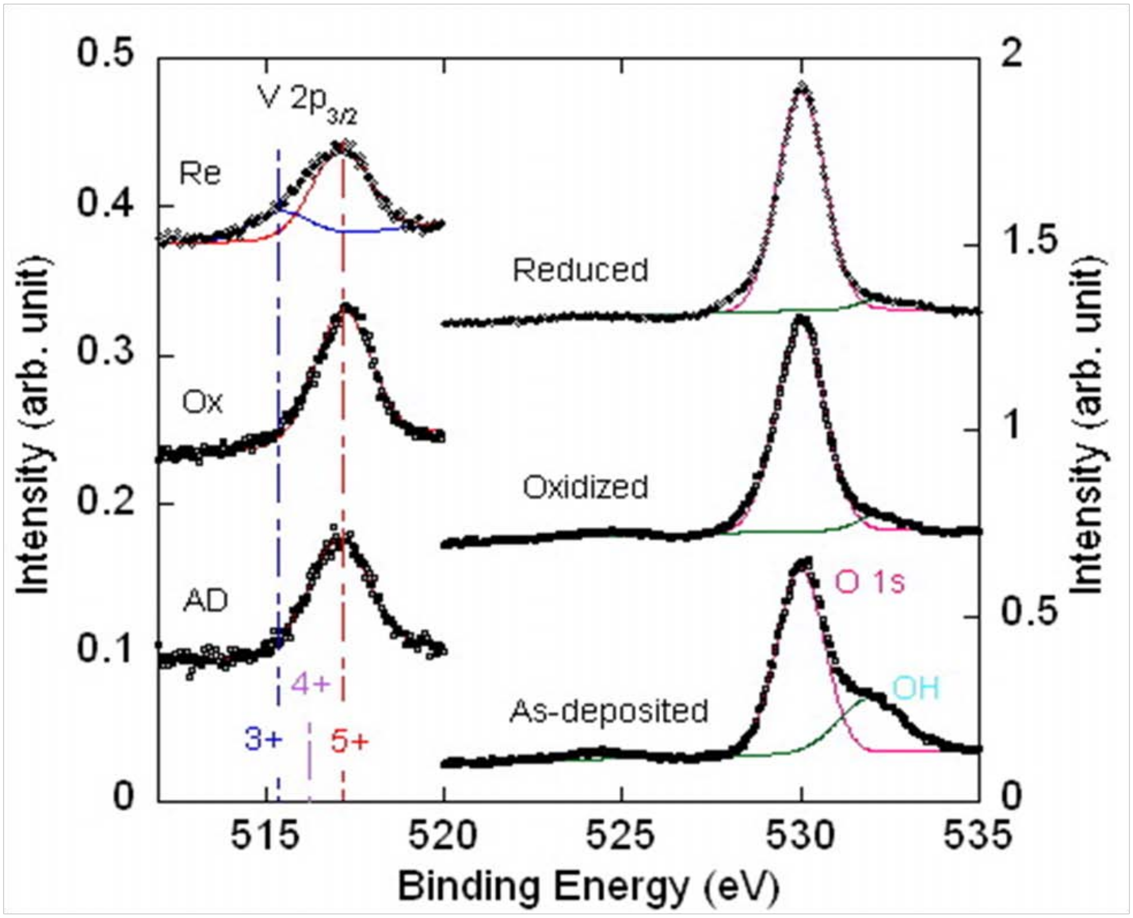

Figure 5.2 XP spectra of the as-deposited (AD), oxidized (Ox) and reduced (Re) 3/4 ML VO_X / α-TiO_2 (110) surfaces with a 45° electron emission angle. The V $2p_{3/2}$ peak fitting indicates that V is totally converted to the V^{5+} oxidation state for the AD and Ox surfaces, but split 25% V^{3+} : 75% V^{5+} for the Re surface. Re-oxidization (Ox2) returned all vanadium cations back to V^{5+} (not shown). Also shown are the O 1s and chemically shifted OH peaks for the AD, Ox and Re surfaces. The measured chemical shifts for the 3+, 4+ and 5+ V peaks (see vertical dashed lines) are improved in reliability by referencing the respective binding energy differences (BED) relative to the O 1s peak.

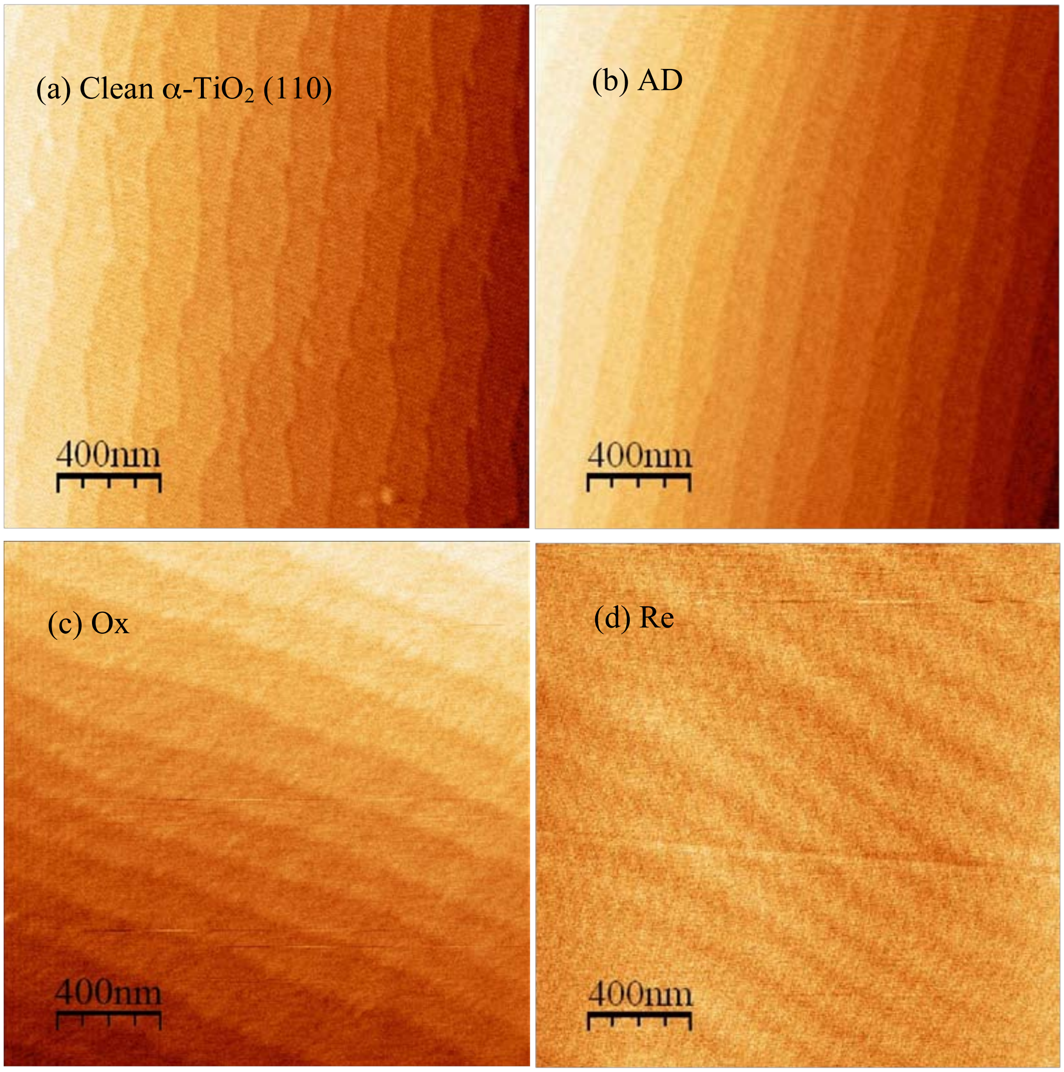

Figure 5.3 AFM images of the α-TiO_2 (110) substrate surface: (a) after the two-step annealing process AFM shows clean atomically flat terraces with 0.3 nm steps; (b) after ALD deposition (AD), (c) After Oxidization (Ox) and (d) reduction (Re), clear terraces were still found, indicating no significant change of the rutile surface.

AFM images were collected in association with each XPS measurement in order to link the chemical state changes with surface morphology changes for the VO_X layer. Silicon AFM tips with a nominal 10 nm radius of curvature and cantilever resonant frequency of 200 kHz were used with a JOEL-JSPM-5200 scanning probe microscope at the NIFTI facility of NUANCE. Fig. 6.3(a) shows the annealed blank a-TiO_2(110) substrate surface with flat terraces separated by atomic steps. This is the starting point for VO_X ALD. Fig. 6.3(b-d) show that the atomic terraces are preserved after ALD growth and each redox step. Clear terraces at each process indicate that no significant changes have occurred to the rutile surface morphology, i.e., the ALD process is conformal.

X-ray fluorescence (XRF) and X-ray standing wave (XSW) measurements were performed at the Advanced Photon Source (APS) undulator station 33ID-D. An incident photon energy of 7.00 keV was selected with a diamond high-heat load monochromator and conditioned further with either Si (111) or (220) channel-cut post-monochromator crystals. A 50 mm^2 Vortex silicon drift diode (SDD) detector was used to collect the XRF spectra. Fig. 6.4 shows a typical XRF spectrum. In this case, a 1.5 ML VO_x / α-TiO_2(110) sample was placed on a 4-circle diffractometer. The SDD detector was placed 40 mm away from the center of the sample. Four 50 mm thick aluminum foils were placed in front of the detector to attenuate the strong Ti K fluorescence signal. The spectrum is dominated by Ti Kα (4.51 keV) and Kβ (4.93 keV) signals. The V Kα (4.95 keV) peak is buried under the Ti Kβ. A small V Kβ (5.43 keV) peak appears on the tail of the Ti Kβ peak (Fig. 6.4 inset) and is used for the XSW measurements. For *in situ* XSW measurements, oxidization-reduction reactions were carried out in a beryllium-dome reaction cell, as shown in Figure 3.9 and described elsewhere.[81] Before oxidation the cell was purged with ultrahigh-purity oxygen (~100 sccm) for 10 min. Then with continuous oxygen flow the temperature was increased to 180 °C for 20 min to dehydrate the sample. This was followed by oxidization at 350 °C for 30 min. The reduction reaction was carried out with a flow (~100 sccm) of 2% hydrogen balanced by 98% helium at 350 °C for 30 min. After the oxidization and reduction reaction steps, the sample was cooled down to 25 °C in the flowing gas, the reaction cell was evacuated by a diaphragm roughing pump, and then XSW measurements were performed at several different *hkl* substrate Bragg reflections.

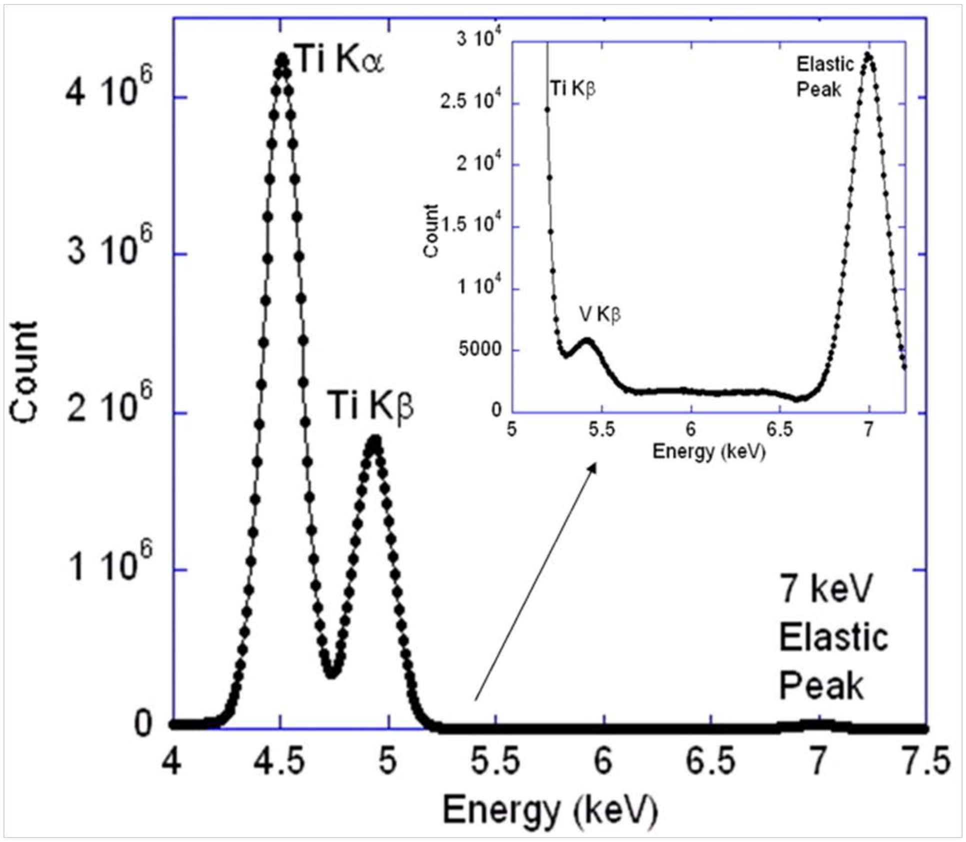

Figure 5.4 An XRF spectrum of 1.5 ML VO_X / α-TiO_2 (110) that was collected at an incident photon energy of 7.00 keV and filtered by a 200 mm thick Al attenuator.

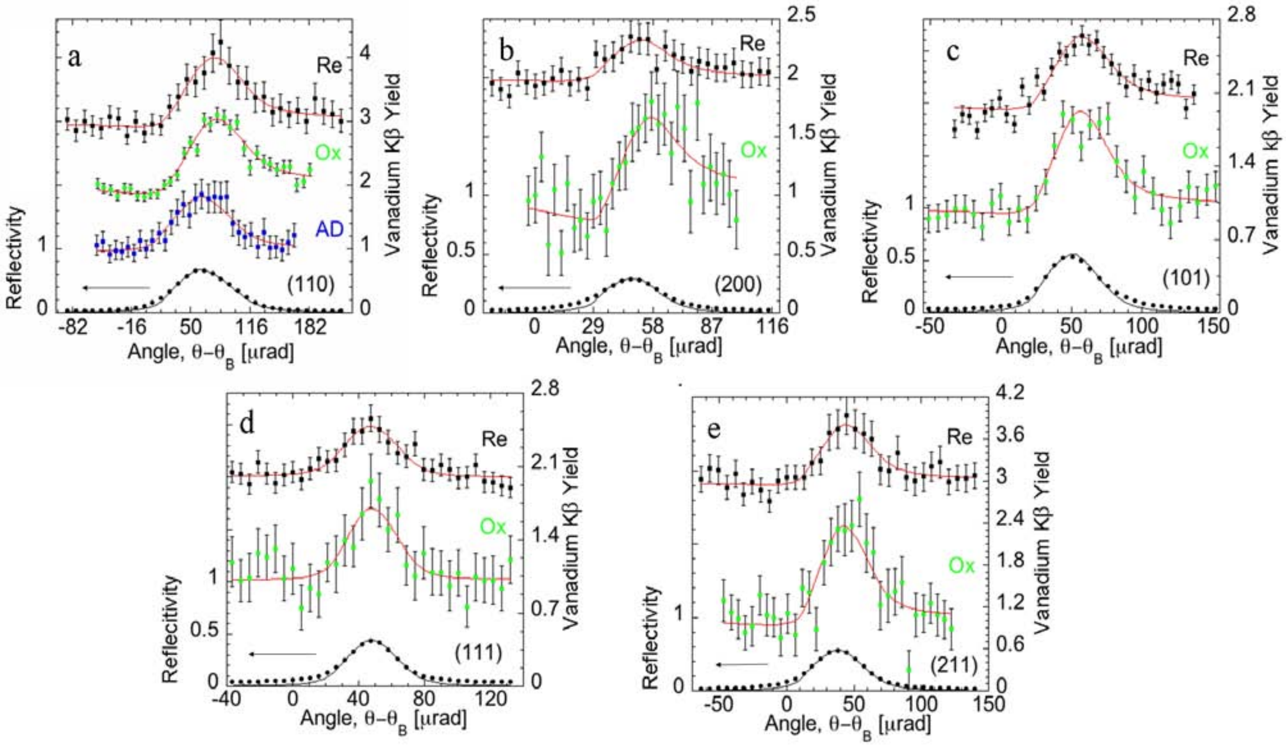

Figure 5.5 XSW results of (a) (110) normal direction, (b) (200), (c) (101), (d) (111) and (e) (211) off-normal directions of α-TiO_2(110) for as-deposited (AD), oxidized (Ox) and reduced (Re) ALD vanadium oxides. The fluorescence spectra are displaced vertically in the order of processing AD, Ox and Re. The left-side axis is the reflectivity and the right-side axis is normalized vanadium Kβ yield. Table 6.1 shows the results of the fit of Eq. 4.1 to the yield data.

Figure 6.5 shows the XSW data and analysis for the (*110*), (*200*), (*101*), (*111*) and (*211*) α-TiO_2 Bragg reflections for the AD, Ox and Re states. The XSW induced modulation of the background-subtracted and deadtime-corrected V Kβ fluorescence yield, $Y(\theta)$, from each scan is used to determine the coherent fraction (f_H) and coherent position (P_H). This determination is based on fitting the normalized yield data for the $H=hkl$ reflection to the model independent expression for the yield[152, 153], as shown in Eq. 4.1. The shapes of the (*110*) V fluorescence yields (Fig. 6.5(a)) change from symmetrical in the AD condition to more asymmetrical in Ox and Re conditions; indicating that the V atomic distribution relative to the (*110*) planes changes from uncorrelated to partially correlated. Fig. 6.5(b-d) also show changes in the fluorescence yields from the Ox to Re state, indicating different V atomic distributions for these two cases.

Table 5.1 Summary of the XSW experimental results from the as-deposited (AD), oxidized (Ox), and reduced (Re) surface treatments of the 0.74 ML VO_X / α-TiO_2 (110) Surface. f_{meas} and P_{meas} are experimentally measured coherent fractions and coherent positions, respectively. f_{calc} and P_{calc} are calculated from the best-fit model described by Eq. 6.1. The P values are referenced to an origin that coincides with a bulk Ti atom at the AT site.

hkl	AD		Ox				Re			
	f_{meas}	P_{meas}	f_{meas}	f_{calc}	P_{meas}	P_{calc}	f_{meas}	f_{calc}	P_{meas}	P_{calc}
110	0.18(7)	0.11(8)	0.45(3)	0.47	0.07(1)	0.09	0.35(8)	0.27	0.09(4)	0.09
101	--	--	0.43(7)	0.49	0.16(3)	0.04	0.28(4)	0.27	0.08(3)	0.05
200	--	--	0.8(1)	0.47	0.09(3)	0.09	0.18(7)	0.27	0.01(8)	0.01
111	--	--	0.3(2)	0.17	-0.26(7)	-0.28	0.1(1)	0.00	--	--
211	--	--	0.7(2)	0.45	0.19(3)	0.13	0.3(1)	0.27	0.12(6)	0.14

The XSW data and analysis for the different *hkl* reflections (Fig. 6.6 and Table 6.1) show differences that indicate different structures for each step of the redox reaction (AD, Ox and Re). Note that our f_H and P_H measured values for the Re state match well with the earlier reported (110) and (101) back-reflection XSW results[223] for V^{3+} cations. This earlier UHV case, which vapor deposited V, used XSW induced XPS to find V^{3+} and V^0 on the surface in different geometries.

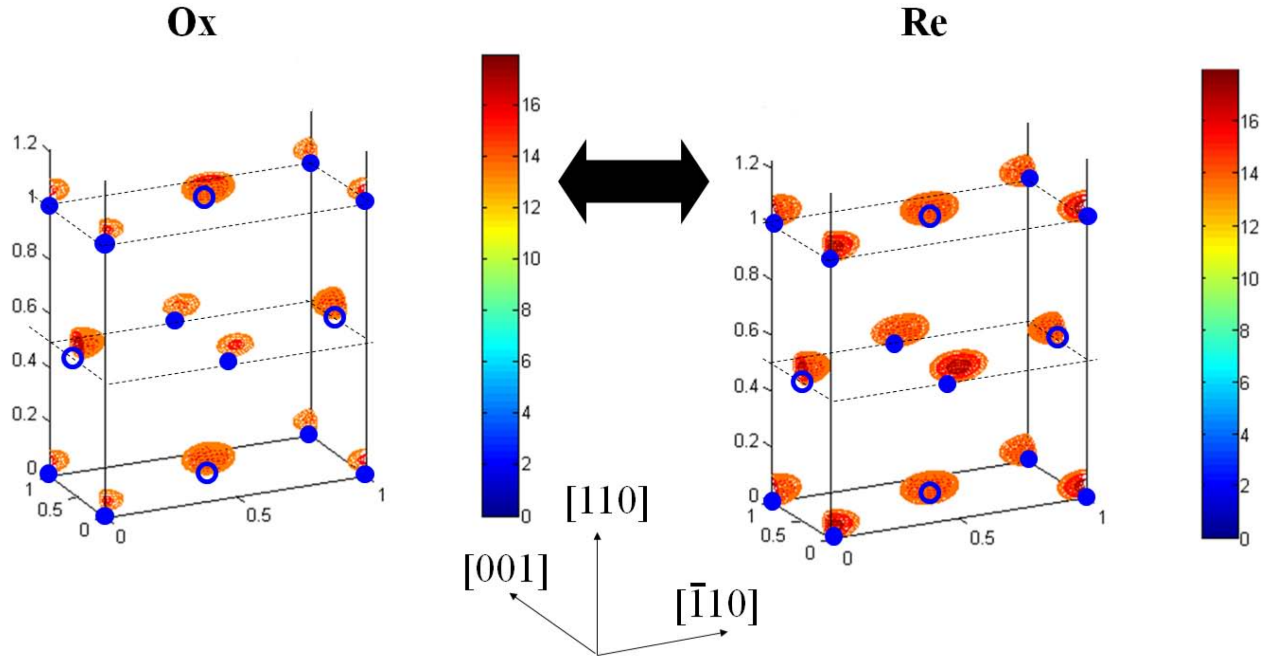

Figure 5.6 3D vanadium atomic density maps generated by the summation of several XSW measured (*hkl*) Fourier components for the oxidized (Ox) and reduced (Re) surfaces. These model-independent V atomic density maps are superimposed on the same rutile (110) surface unit cell illustrated in Fig. 2.2. As a point of reference open and filled circles denote the two Ti symmetry inequivalent sites in the ideal bulk-like structure with (110) Ti planes at heights of 0, 3.25 and 6.50 Å.

Inserting the Table 6.1 XSW measured f_H and P_H values into Eq. 4.2 generates the model-independent 3D V atomic density maps that are shown in Fig. 6.6 for the Ox and Re surfaces. These 3D maps are referenced to the same TiO_2 (110) unit cell that is outlined with black lines in

Figs. 2.2 and 6.6. Due to the Fourier summation process the XSW map has the 3D periodicity of the substrate tetragonal primitive unit cell. There are two symmetry inequivalent Ti sites denoted by the solid and open blue circles in Fig. 6.6. These are the atop (AT) and bridge (BR) respective sites shown in Fig. 2.2.[21] As can be seen, our measurement has the maxima in the V density laterally aligned with these two Ti sites with a slight outward vertical offset in the [110] direction.

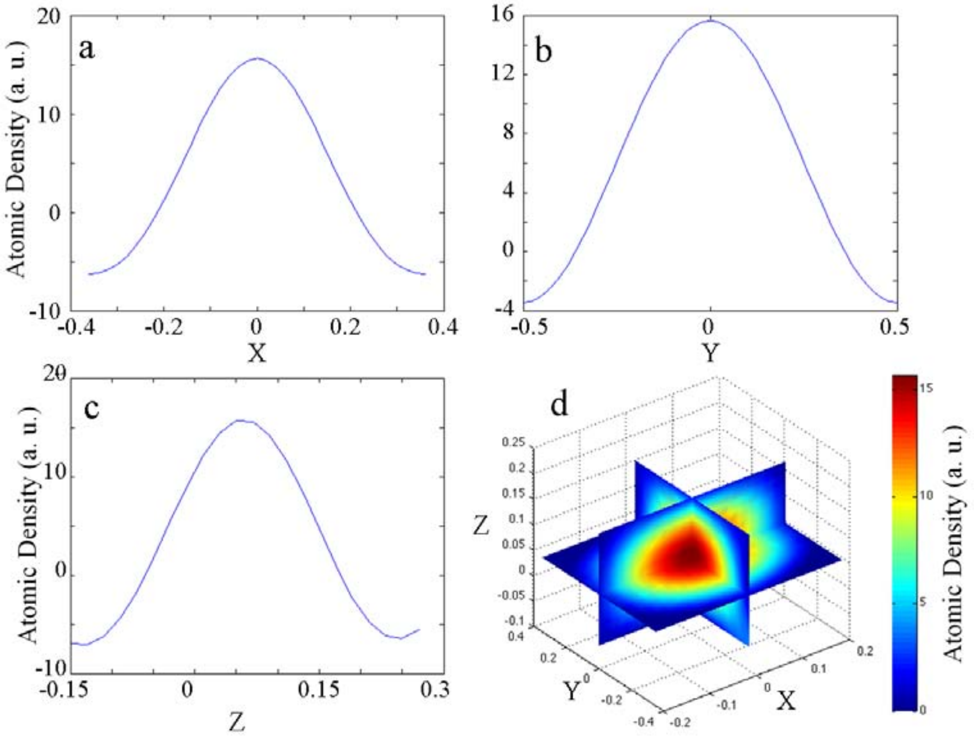

Figure 5.7 Vanadium model-independent analysis around an AT site: (a-c) 1D line cuts through 3D atomic density map in (a) YZ plane at Y=0, Z=0.54; (b) XZ plane at X=0, Z=0.54; (c) XY plane at X=Z=0; (d) orthogonal 2D plane-cuts through density map around AT site for planes of X=0, Y=0 and Z=0.54.

Table 5.2 Numerical analysis of model-independent V atomic distribution ρ(X,Y,Z) around AT and BR sites for the Ox and Re states. The X, Y and Z ranges refer to the range of the tetragonal box chosen for the atomic density integration. The FWHM$_i$ refers to the full width at half maximum in i (i=X, Y or Z) direction. I$_{norm}$ is the volume normalized atomic density sum in this tetragonal box.

	X-range	Y-range	Z-range	FWHM$_x$ (Å)	FWHM$_y$ (Å)	FWHM$_z$ (Å)	Center	I$_{norm}$ (a.u.)
Ox								
AT	[-0.2, 0.2]	[-0.35, 0.35]	[-0.06, 0.18]	1.76	1.33	0.98	0, 0, 0.054	462723
BR	[0.3, 0.7]	[0.19, 0.81]	[-0.04, 0.18]	1.89	1.24	0.98	0.5, 0.5, 0.068	604989
Re								
AT	[-0.25, 0.25]	[-0.25, 0.25]	[-0.17, 0.25]	2.15	1.18	1.04	0, 0, 0.047	337142
BR	[0.25, 0.75]	[0.25, 0.75]	[-0.17, 0.25]	2.15	1.18	1.04	0.5, 0.5, 0.047	337142

To further analyze the Fig. 6.6 model-independent V maps, several 2D plane-cuts and 1D line-cuts are used. Fig. 6.7 shows the analysis around the AT site at (0,0,0) for V in the Ox state. Numerical analysis of the 3D distribution function around the hot spot gives the center position (0,0,0.54). Three plane cuts (x=0; y=0; z=0.54) and 3 line cuts (x=y=0; x=0, z=0.54; y=0, z=0.54) are used to examine the properties of the hot spot. A tetragonal box is chosen so that the V atomic density inside the box is greater than 1. The volume normalized atomic intensity sum in this box gives the occupation fraction of V at this site. Similar analyses are carried out for BR site in the Ox state and the two sites in the Re state. The properties of the hot spots at each site are summarized in Table 6.2. It clearly shows that the BR to AT occupation ratio, I$_{norm}$(BR) /

I_{norm}(AT), is 4:3 for the Ox state but 1:1 for the Re state. This analysis also shows that in the Ox state the V heights above the TiO plane are 3.69 Å and 3.60 Å for BR and AT sites, respectively, while in the Re state, both sites have the same height, 3.56 Å.

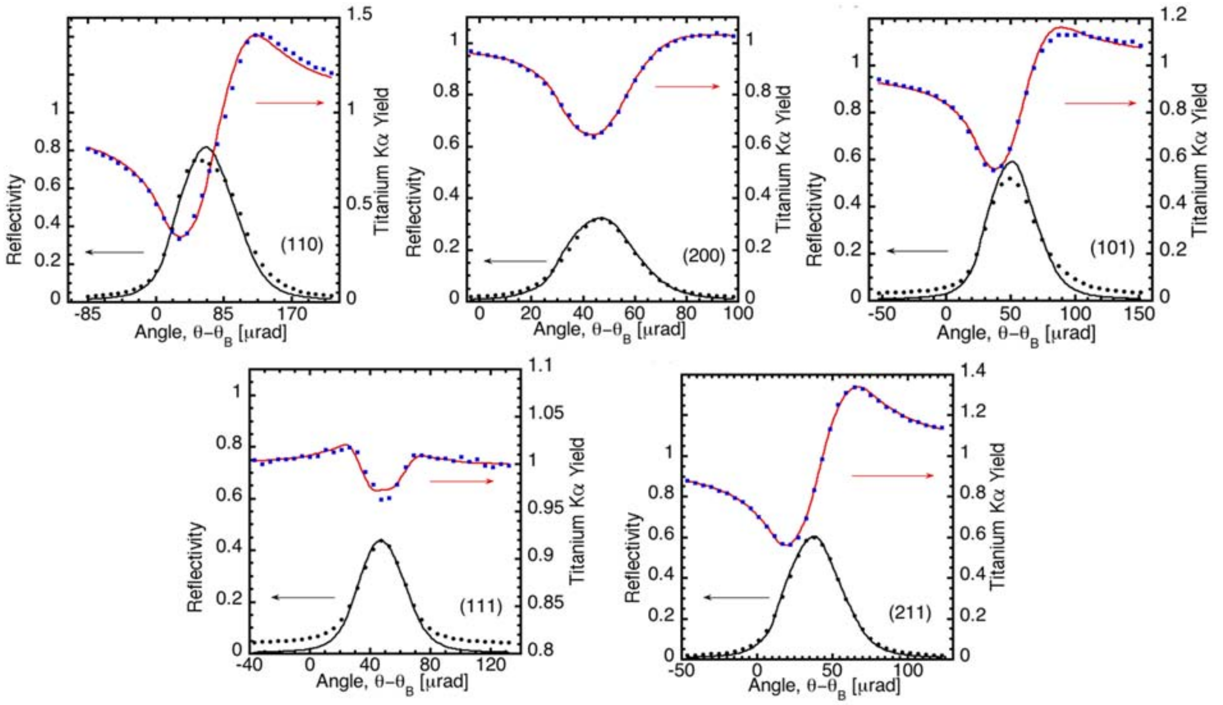

Figure 5.8 XSW results of bulk Ti Kα signal for diffraction planes (110) normal direction, (101), (200), (111), and (211) off-normal directions for sample at oxidized state. Table 6.3 shows the results from the fit of Eq. 4.1 to the yield data.

Table 5.3 XSW analysis of the bulk Ti sublattice of α-TiO$_2$ (110). The coherent fractions (*f*) and coherent positions (*P*) are experimentally determined from the modulations in Ti Kα XRF yields shown in Fig. 6.4. The takeoff angles (α) of the detected XRF emission relative to the surface are also listed. The P values are referenced to an origin that coincides with a bulk Ti atom at the AT site. As expected the AT and BR sites are perfectly in-phase with each other for each hkl; with the exception of the 111 oxygen-only reflection.

hkl	*110*	*101*	*200*	*111*	*211*
f	1.00(1)	0.87(1)	0.81(1)	0.06(1)	0.89(1)
P	0.00(1)	0.00(1)	0.00(1)	--	0.00(1)
α (°)	4.2	6.5	49	8	7

To check the validity of our V XSW analysis, the Ti Kα signal from bulk α-TiO$_2$ was also analyzed, as shown in Fig. 6.8. These signals were collected simultaneously with the V signals. The analysis results are listed in Table 6.3. Note that the XRF takeoff angle, a, refers to the angle between the detector center and the sample surface. It is used for calculating the effective attenuation of the Ti Kα fluorescence signal, which includes the extinction effect described by the variable effective thickness $Z(\theta)$.[224] Results show that for the (*110*), (*101*), (*200*) and (*211*) planes, the coherent positions are $P_H = 0$ and the coherent fractions are approaching unity as expected. Note that our analyzed value of $f_{111} = 0$ is expected because the (*111*) reflection is an oxygen-only reflection as the (*111*) is a forbidden reflection for the body-centered Ti sublattice. Analysis results are consistent with Ti structure in bulk α-TiO$_2$(110), demonstrating the validity of our XSW analysis for vanadium. By inserting the measured coherent fractions and positions of bulk Ti into Eq. 4.2, a Ti atomic density map is generated as shown in Fig. 6.9. It shows that those hot spots are right on the bulk-like Ti sites, which further validates our XSW analysis procedure.

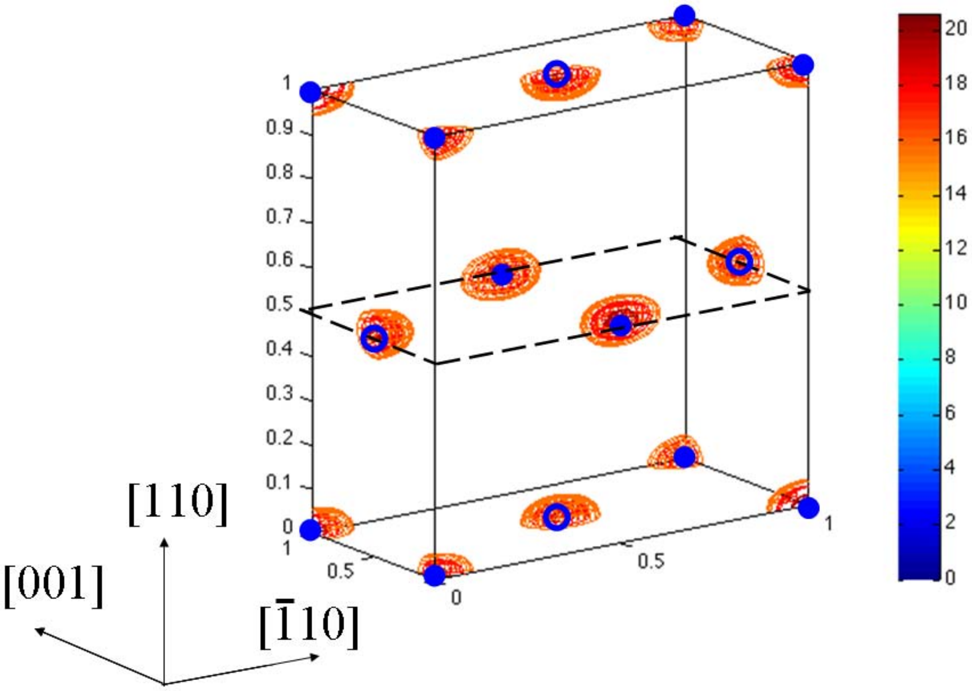

Figure 5.9 3D titanium atomic density map generated by the summation of XSW measured (*hkl*) Fourier components listed in Table 6.3 plus their symmetry equivalents. Ti atomic density maps are superimposed on the same rutile (110) surface unit cell illustrated in Fig. 2.2. As a point of reference open and filled circles denote the two Ti symmetry inequivalent sites in the ideal bulk-like structure with (110) Ti planes at heights of 0, 3.25 and 6.50 Å.

To quantify the structural parameters associated with these two adsorption sites we performed a least-squares global fit of each condition to the measured set of f_H and P_H values. The H^{th} Fourier component for the V atomic distribution is then described as,

$$F_H = f_H \exp(2\pi i P_H) = c_{AT} \exp(2\pi i H \cdot r_{AT}) + c_{BR} \exp(2\pi i H \cdot r_{BR}), \quad (6.1)$$

where c_X denotes the V occupation fraction at the AT and BR sites with positions $\boldsymbol{r}_{AT} = (0,0,z_{AT})$ and $\boldsymbol{r}_{BR} = (½,½,z_{BR})$ locating the V heights, z_X, above the TiO plane. Table 6.4, which lists the best-fit determined results for V occupation fractions and adsorption heights, shows that the calculated V heights at the AT and BR sites from this model-dependent analysis are consistent with the model-independent analysis described above. As an additional consistency check, Table 1 lists the calculated values, f_{cal} and P_{cal}, that would have been observed if V occupied sites as dictated by this best-fit model. From Table 6.4 we see that V atoms have an ordered fraction (or correlated fraction) of 49% ($c_{AT} + c_{BR} = 0.49$) in the oxidized state and 28% in the reduced state. The remaining V atoms are measured to be in an uncorrelated distribution relative to the substrate lattice. This could be VO_X nanoparticles or V in surface defect sites. The Table 6.4 calculated values also show that in the oxidized state, the BR to AT occupation ratio is 3:2, which is reasonably consistent with the XSW model-independent results (4:3) discussed above. Reduction creates a 1:1 ratio and causes one-half of the BR-site V cations to become uncorrelated with the substrate lattice, while the fraction of V occupying AT sites is slightly reduced. The 2nd oxidization reverses the process. Thus the V cations are directly shown to have redox reaction reversibility in both their chemical states and surface bonding sites.

Table 5.4 XSW determined best fit model parameters from Eq. 6.1 for the V occupation fractions, c_X, and heights, z_X, above the bulk TiO (110) plane. For comparison, Ti in bulk α-TiO$_2$ has $z_{BR} = z_{AT} = 3.25$ Å. The V correlated fraction ($\Sigma c = c_{BR} + c_{AT}$) is also listed.

Surface	c_{BR}	c_{AT}	Σc	z_{BR} (Å)	z_{AT} (Å)
Ox	0.30(7)	0.19(5)	0.49(9)	3.65(9)	3.35(6)
Re	0.14(1)	0.14(1)	0.28(1)	3.54(1)	3.54(1)

To better understand the structure of V on top of α-TiO$_2$(110), density functional theory calculations are carried out from our collaborators. Density functional theory with GGA PW91[225] functional as implemented in the VASP code[226, 227] has been used for theoretical modeling. The core electrons were described by the projector augmented wave method[228, 229]. A plane wave basis set with cutoff of 264 eV was used. Monkhorst-Pack grids[230] were used to sample Brillouin zone. The geometries were optimized using conjugated gradient method in all systems until the forces on all relaxed atoms are under 0.05 eV/Å. Using these parameters, the topmost Ti height, d_{110}, was calculated to be 3.23 Å, less than 1% shorter than the experimentally measured 3.25Å. The stoichiometric rutile surface slab consisting of 3 TiO$_2$ tri-layers was used. For supported vanadia submonolayer optimizations, the bottom TiO$_2$ tri-layers were kept frozen while the rest were allowed to relax. To investigate the stabilities of possible supported vanadia structures that have stoichiometric VO$_X$ submonolayers, we use the binding energies defined by:

$$\Delta E = \frac{E_{TiO_2+V_{2n}O_{5n}} - E_{TiO_2}}{n}, \tag{6.2}$$

where $E_{TiO_2+V_{2n}O_{5n}}$ and E_{TiO_2} are energies of the rutile (110) with vanadia submonolayer and rutile (110) surface slab alone, respectively, and n is the number of V_2O_5 units in the structure.

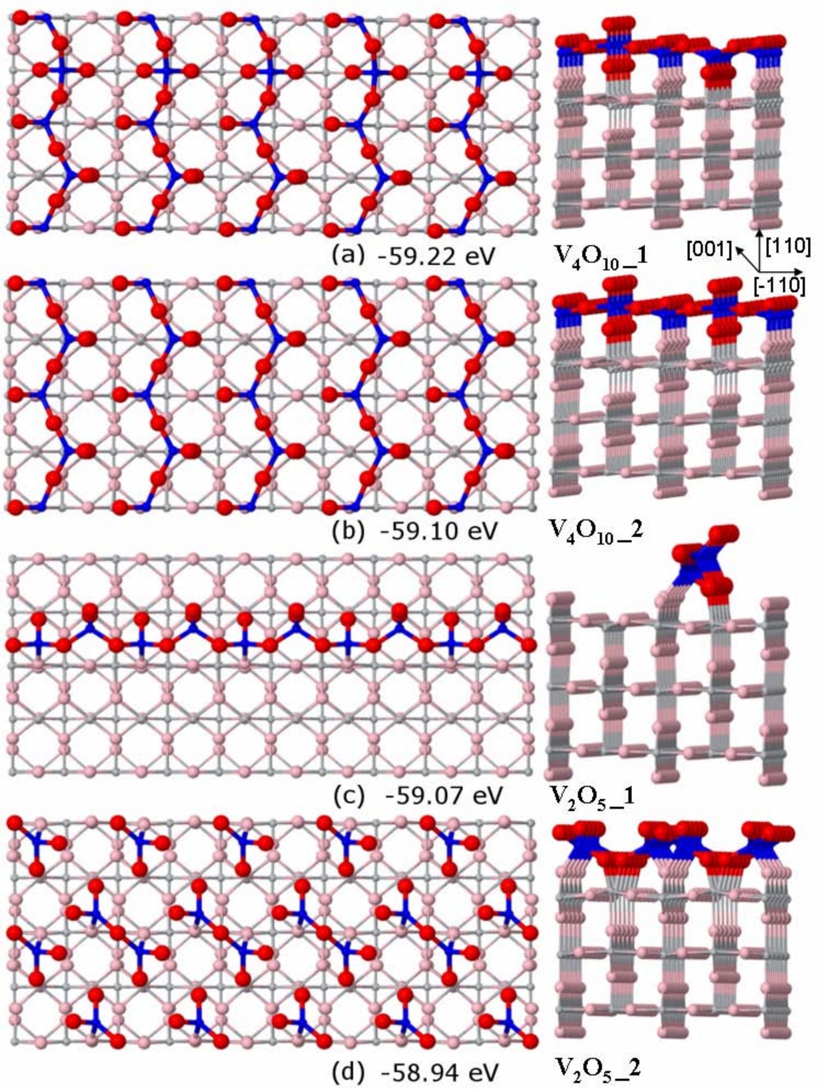

(a) -59.22 eV V_4O_{10}_1

(b) -59.10 eV V_4O_{10}_2

(c) -59.07 eV V_2O_5_1

(d) -58.94 eV V_2O_5_2

Figure 5.10 Structures of stoichiometric and stable vanadia submonolayer. The corresponding binding energies calculated using Eq. 6.2 are also reported along with each structure. Color code: gray and pink: titanium and oxygen atoms, respectively of rutile support; blue and red: vanadium and oxygen atoms, respectively, of the supported submonolayer.

In our DFT calculations, the vanadium to oxygen atom ratios in the submonolayer structures were set up to be as close to as 2:5 as possible since the XPS measurement has suggested a fully oxidized vanadia submonolayer with +5 vanadium charge and the rutile support was not reduced at the experimental conditions. We have investigated structures with various vanadia submonolayer distributions, surface coverages and alignments relative to the rutile (110) lattice, as shown in Fig. 6.10. For the non-stoichiometric vanadia submonolayer structures that we have calculated, a comparison of the relative stabilities requires knowledge of chemical potentials of the species due to different ratios of vanadium to oxygen atoms in the systems. Thus, we simply eliminated the structures that do not fit the experimental measurement and will not report those structures here. Based on DFT calculations, we propose coherent part of the oxidized and reduced structures shown in Figure 6.11. Each vanadium atom in these structures has a terminal vanadyl bond as well as three V-O single bonds, very similar to the bonding features of the V atoms in V_2O_5 bulk as well as in other supported V_2O_5 sub-ML structures. The reduced structure has a "herringbone" pattern that is continuous along the [-1 1 0] direction and it is the most stable among all the stoichiometric structures we have investigated. Therefore, it is expected that such structure would "survive" under the reduction condition. The ratio of numbers of AT to BR sites ($c_{\mathrm{AT}} : c_{\mathrm{BR}}$) occupied by vanadium atoms in this structure is 1:1 and the total correlated fraction is 0.25. The average heights of AT and BR vanadium are 3.5 and 3.3 Å, respectively, relative to the calculated atom positions in the bulk TiO_2 (110) plane. These are all in good agreement with the best-fit parameters shown in Table 6.4, as well as the coherent fractions and coherent positions measured experimentally and calculated using best-fit model

(See Table 6.5 for a detailed comparison). In addition, the simulated density map based on this structure is very similar to that obtained from the measurement.

The 6-membered (vanadium) ring oxidized structure shown in Figure 6.10(a) was constructed by adding more atoms to the stable herringbone structure based on the fact that the oxidized structure has more coherent atoms than the reduced structure (see Table 6.4). These additional atoms are not part of the continuous herringbone; therefore, this part of the structure is less stable and can easily be reduced under the reduction condition. Once reduced, these atoms become more "mobile" and this mobility should lead to the incoherence of these vanadium atoms as those not shown in the reduced model in Figure 6.10(b). The ratio of numbers of AT to BR sites ($c_{\mathrm{AT}} : c_{\mathrm{BR}}$) occupied by vanadium atoms in the oxidized model is 3:4 and the total correlated fraction is 0.44. The average heights of AT and BR vanadium are 3.8 and 3.3 Å, respectively, relative to the calculated bulk TiO_2 plane. These results also agree well with the measured and best-fit model parameters (Table 6.4 and 6.5). The stoichiometry of the structure is V_7O_{17}, corresponding to an average of +4.85 formal charge on vanadium atoms instead of fully oxidized +5 charge deduced from the XPS measurements. Despite the small deviation in charge state of vanadium atoms, the model is still valid within the accuracy of the XPS measurement and peak fitting.

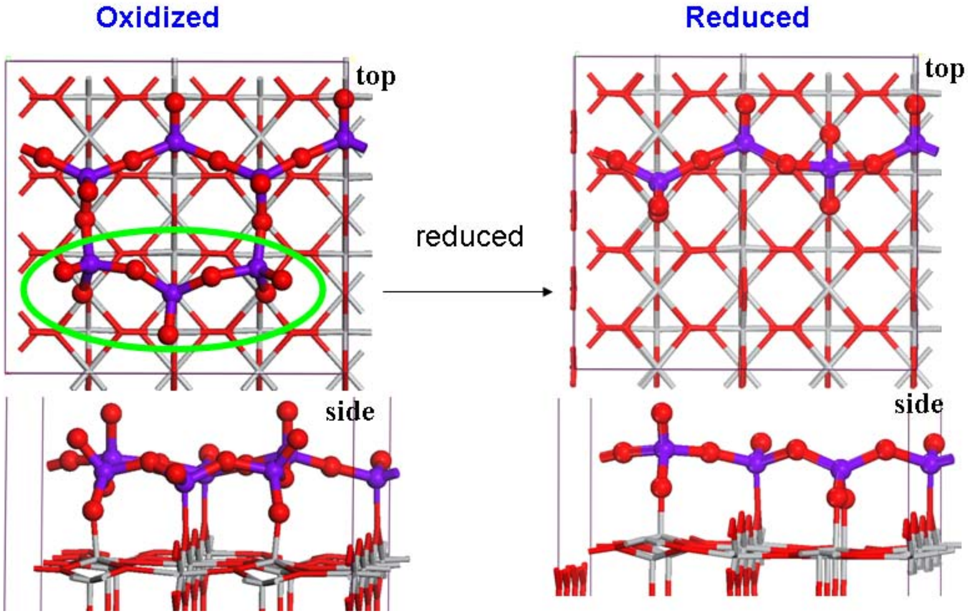

Figure 5.11 Top and side views of the proposed DFT-optimized oxidized and reduced models on rutile (110) surface. The green circle highlighted part in the oxidized state is “mobile” and is not detected by XSW in the reduced state.

Table 5.5 Summary of the XSW experimental results, model-dependent analysis and simulation results from DFT for the oxidized (Ox), and reduced (Re) surface treatments of the ¾ ML VO_X / α-TiO_2 (110) Surface. The oxidized and reduced models from DFT are descripted in Fig. 6.10

hkl	Oxidized						Reduced					
	f_{meas}	f_{calc}	f_{DFT}	P_{meas}	P_{calc}	P_{DFT}	f_{meas}	f_{calc}	f_{DFT}	P_{meas}	P_{calc}	P_{DFT}
110	0.45(3)	0.47	0.45	0.07(1)	0.09	0.12	0.35(8)	0.27	0.35	0.09(4)	0.09	0.03
101	0.43(7)	0.49	0.43	0.16(3)	0.04	0.06	0.28(4)	0.27	0.26	0.08(3)	0.05	0.01
200	0.8(1)	0.47	0.21	0.09(3)	0.09	0.10	0.18(7)	0.27	0.04	0.01(8)	0.01	-0.09
111	0.3(2)	0.17	0.27	-0.26(7)	-0.28	-0.17	0.1(1)	0.00	0.04	--	--	--
211	0.7(2)	0.45	0.29	0.19(3)	0.13	0.17	0.3(1)	0.27	0.24	0.12(6)	0.14	0.03

5.3 Summary

For ¾ ML ALD grown VO_X on α-$TiO_2(110)$, we demonstrate at ambient conditions the redox-driven cation dynamics for a catalyst on an oxide support. XPS shows that oxidation causes all 0.74(5) ML of the V to be in the 5+ state and that reduction causes 0.19(3) ML of the V cations to be converted from 5+ to 3+. In situ XSW analysis of the oxidized (Ox) surface shows that 0.36(7) ML of the vanadium occupy bridge (BR) or atop (AT) rutile(110) surface sites with a 3:2 ratio and that 0.38(7) ML of V are uncorrelated to the substrate lattice. XSW also shows that reduction causes 0.12(1) ML of the BR-site V and 0.04(1) ML of AT-site V to become uncorrelated, resulting in an equal 1:1 BR to AT site occupation ratio. Reversibility was observed in this process, demonstrating its relevance to catalytic applications. Since we have established that the same number (0.2 ML) of V cations are structurally and chemically transformed, we can conclude that the uncorrelated-to-correlated transferred V play an important role in this redox reversible cycle. By comparing DFT calculations with measured V chemical bonding configurations, we predicted the surface oxygen configurations, which are inaccessible to the XSW measurements. DFT calculations show that vanadyl oxygen is removed when V^{5+} is reduced to V^{3+}, indicating that terminal V=O is related to the catalytic performance of vanadia. These findings will help understand the redox-induced chemical bonding changes of the catalysts and the role of the supporting oxides in catalytic reactions.

Chapter 6: ALD Grown WO_X / α-$TiO_2(110)$

6.1 Introduction

Another interesting combination between catalysts and oxides substrates is the combination between catalyst WO_X and the non-reducible substrate, α-TiO_2(110). Kim et al[21] from our group have studied the ALD grown sub-monolayer (sub-ML) WO_X on α-TiO_2(110). Although no chemical or structural dynamics have been observed for W in reactions, stable and atomic-scale structural information has been obtained by XSW. The total W coverage was 0.38 ML and the ordered fraction was 0.74. This study showed that W cations occupy the AT and BR sites with occupation fraction $c_{AT} : c_{BR} \sim 1:2$. Figure 2.21 shows the W atomic density map projected on to the α-TiO_2(110) surface unit cell.

The reason for the inert behavior of sub-ML WO_X/α-TiO_2(110) could be due to the strong interaction of sub-ML W with the substrate. If W coverage is increased to ML, the interaction between W and rutile substrate could be weakened and consequentially the redox-induced dynamics would be expected. Therefore, in this Chapter, a ML WO_X is deposited on α-TiO_2(110) surface by ALD. Following the similar experimental procedures as we used for WO_X/α-Fe_2O_3(0001) and VO_X/α-TiO_2(110), we investigated the redox-induced behaviors of ML WO_X/α-TiO_2(110).

6.2 Experimental Results and Discussions

Polished rutile α-TiO_2(110) (10 × 10 × 1 mm^3) (Crystal GmbH, Germany) substrates were solution cleaned and O_2 annealed by following the similar surface preparation methods in Chapter 7 to obtain atomic-flat surface. For ALD growth, the substrates were exposed to Si_2H_6 at 10 Torr for 10 min, followed by 10 min exposure to WF_6 at 10 torr. Following each exposure, the reactor was evacuated to below 0.05 torr and subsequently purged with ultrahigh-purity nitrogen for 5 min. The process of exposure to Si_2H_6, purging with nitrogen, exposure to WF_6, and finally purging with nitrogen defined herein as one W ALD cycle. To obtain ML W coverage, 2 ALD cycles of W were deposited. The W coverage is determined to be 1.0 ML a side-by-side XRF comparison with a standard sample calibrated by Rutherford backscattering.

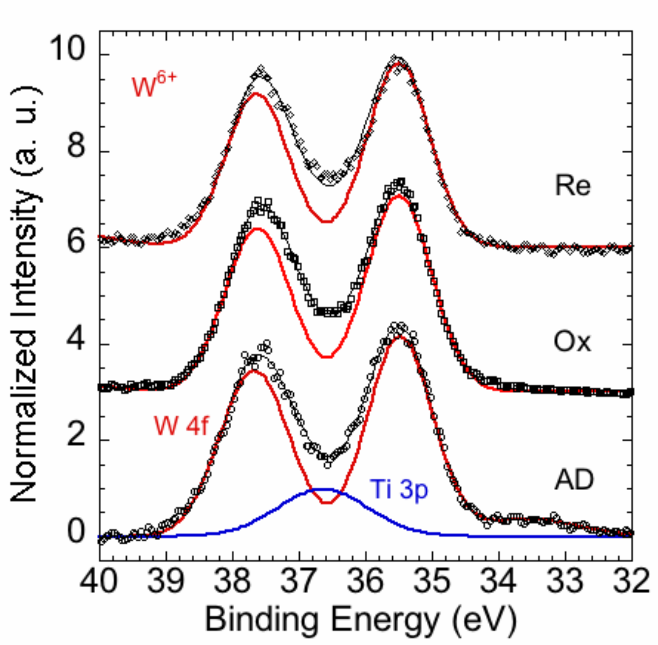

Figure 6.1 W 4f XP spectra of 1.0 ML WO_X / α-TiO_2 (110) in as-deposited (AD), oxidized (Ox), and reduced (Re) states with a 45° electron emission angle. No chemical state change of W is observed. This is also what was observed for the 0.38 ML case,[21]

XP spectra were taken from the sample at the as-deposited (AD), oxidized (Ox), and reduced (Re) conditions. Figure 7.1 shows the XPS analysis of W in each redox processing step. The chemical states of W are determined according to W 4f binding energies.[21, 213, 231] No change is observed, indicating W is inert during the redox reaction.

AFM images were taken for the the blank α-TiO_2(110) surface, the surfaces at AD and after redox reactions. Conformal W films were observed after ALD growth (Figure 7.2(b)), but nanoparticles were observed after redox reactions. This is different from sub-ML catalysts on oxides, in which conformal films were preserved through all reactions.[21]

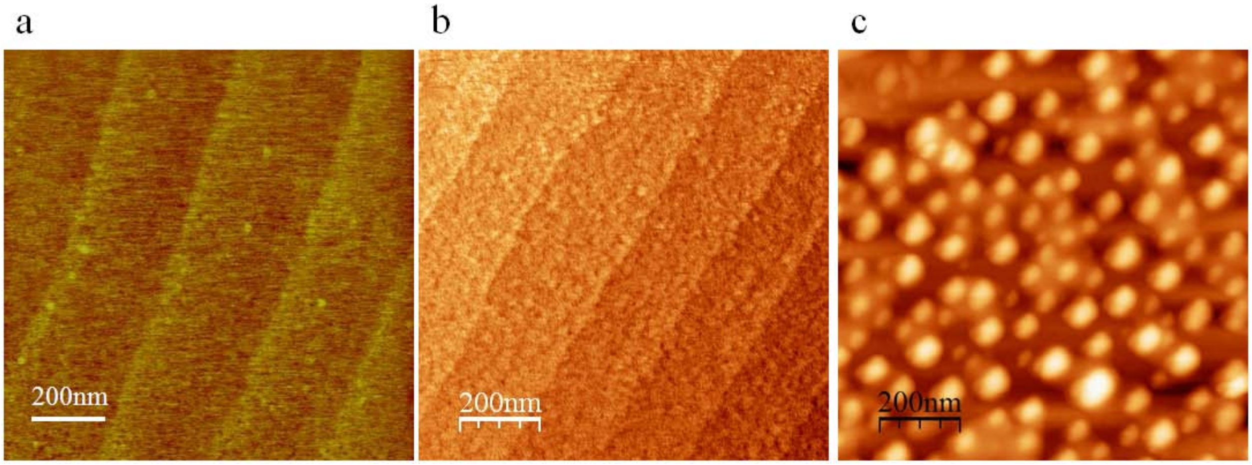

Figure 6.2 AFM images of the TiO_2 (110) substrate surface. (a) The blank substrate surface after 2-step annealing shows atomically flat terraces. (b) After ALD growth of 1.0 ML tungsten oxide, the flat atomic terraces can still be observed clearly. (c) The same surface after two redox reaction cycles shows the formation of nanoparticles.

For the XSW measurements, the sample was placed on a ceramic heating stage inside a beryllium dome gas reaction cell that was mounted on a four-circle diffractometer at the Advanced Photon Source (APS) 33ID-D station. An incident photon energy of 13 keV was selected with a diamond (111) monochromator and collimated further with either Si (111) or (220) channel-cut postmonochromator crystals. A Vortex EM silicon drift diode (SDD) detector was used to collect X-ray fluorescence. The Ox and Re surfaces were achieved by annealing at 400 °C for ½ h in O_2 and 2% H_2 in helium at 760 Torr, respectively. Figure 7.3 shows the XSW data for 7 different (*hkl*) planes. Table 7.1 lists a set of measured f_H and P_H values derived from data shown in Figure 7.3 when the surface is at the Re condition. The same sets of f_H and P_H values were obtained for the Ox and 2nd oxidized (Ox2) condition. These values match reasonably well for the surface at Ox, Re and Ox2 conditions, indicating that W is very stable in the redox reaction and has no structural change.

Table 6.1 XSW measured *hkl* Fourier amplitudes, f_H, and phases, P_H, for 1.0 ML WO_X/α-$TiO_2(110)$. The calculated values f_H^C and P_H^C are determined from the best fit of the model described in Eq. 6.1.

hkl	*110*	*101*	*200*	*111*	*211*	*210*	*220*
f_H	0.42(1)	0.45(2)	0.39(2)	0.07(3)	0.32(2)	0.06(2)	0.36(1)
f_H^C	0.41	0.41	0.41	0.06	0.41	0.06	0.41
P_H	0.10(1)	0.02(1)	0.02(1)	--	0.04(1)	-0.39(7)	0.04(1)
P_H^C	0.03	0.02	0.03	--	0.05	-0.39	0.06

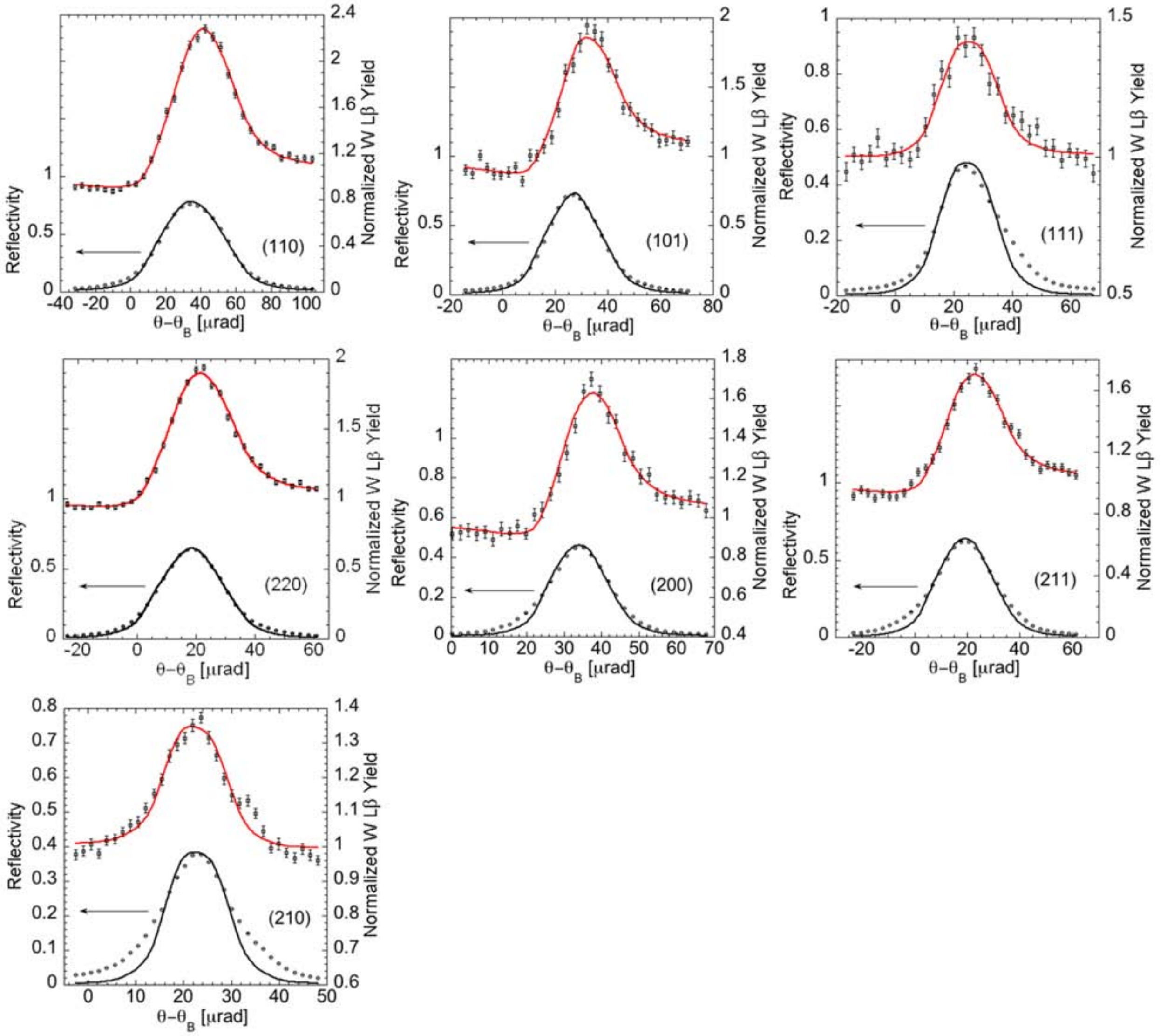

Figure 6.3 The *in situ* XSW measurements for the 1.0 ML WO_X / α-TiO_2(110) surface in the reduced (Re) condition from 7 different *hkl* TiO_2 Bragg reflections: (*110*), (*101*), (*111*), (*220*), (*200*), (*211*) and (*210*). Each frame shows the relative incident-angle dependence of the experimental X-ray reflectivity (open circles) and W Lβ. XRF yield (open squares). The solid lines correspond to dynamical diffraction theory-based fits to the data. (See Refs. [152, 153, 173])

By inserting the measured f_H and P_H values of Table 7.1 into Eq. 3.10, a W atomic density map is obtained as shown in Figure 7.4. This density map is similar to one shown previously for 0.38 ML WO_X/ α-TiO_2(110)[21]. After performing a least-squares global fit of the model described in Eq. 6.1, the best-fit determined results are listed in Table 7.2, which also lists the results of our pervious study of 0.38 ML WO_X/ α-TiO_2(110) as comparison. This further confirms that the W coverage is not the factor to affect the W structural and chemical behavior during redox reaction for WO_X/ α-TiO_2(110) case.

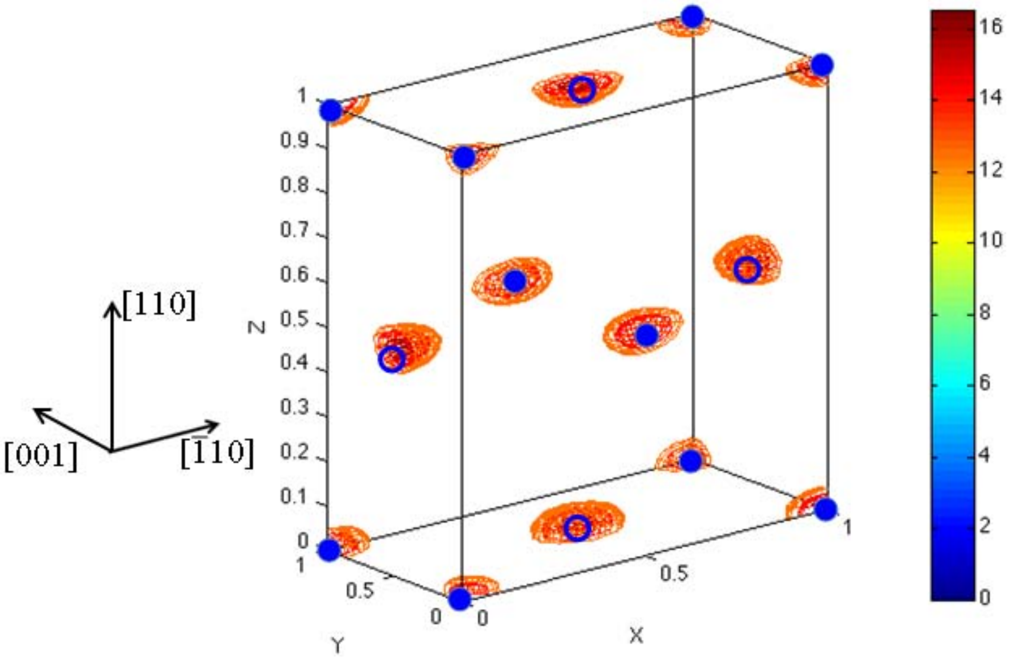

Figure 6.4 W atomic density maps of 1.0 ML WO_X/α-TiO_2(110). The rectangular outline is that of an α-TiO_2(110) surface unit cell, for reference. As a point of reference blue circles denoting the ideal bulk-like Ti sites are also shown at heights of 0, 3.25 and 6.50 Å.

Table 6.2 Least-squares fit model parameters determined from XSW data and Eq. 2 for the W occupation fractions, c_X, and heights, z_X , above the bulk TiO (110) plane for 1.0 ML and 0.38 ML[21] WO_X / α-TiO_2 (110), respectively. For comparison, Ti in bulk α-TiO_2 has $z_{BR} = z_{AT} =$ 3.25 Å. The W correlated fraction ($\Sigma c = c_{BR} + c_{AT}$) is also listed.

Surface	c_{BR}	c_{AT}	Σc	z_{BR} (Å)	z_{AT} (Å)
1.0 ML	0.23(3)	0.18(3)	0.41(4)	3.31(3)	3.29(6)
0.38 ML	0.48(8)	0.26(7)	0.74(7)	3.60(8)	3.28(8)

6.3 Summary

For 1.0 ML WO_X / α-TiO_2(110), we used XSW combined with XPS to study the structural and chemical states change of W during redox reactions. Compared with our early study of 0.38 ML WO_X / α-TiO_2(110), similar W behavior was observed, namely W occupying both AT and BR sites on α-TiO_2(110) surface and staying unchanged structurally and chemically under redox. However, with ML coverage, W surface morphology changes from a conformal-film after ALD growth to nanoparticles after redox reactions. This is different from sub-ML case, where W keeps the conformal-film morphology. This provides important information for our mixed VO_X-WO_X / α-TiO_2(110) studies.

Chapter 7: ALD Grown VO_X / WO_X / α-TiO_2 (110)

7.1 Introduction

As an extension study of the model catalysis system, mixed catalysts are chosen. Previously we have studies monolayer (ML) and sub-ML VO_X supported on α-TiO_2(110)[157, 232], and ML and sub-ML WO_X supported on α-TiO_2(110)[21]. Therefore, naturally we consider the mixed VO_X and WO_X catalysts on top of α-TiO_2(110). Another reason to choose VO_X/WO_X/α-TiO_2 is because this mixed catalyst has been widely used in industrial for selective catalytic reduction (SCR) of automotive and industrial NO_X emissions.[86, 124] With help of our studies on unmixed catalysts, we should be able to find out whether V and W behavior similarly as they are unmixed or synergistically on α-TiO_2(110) surface. In this chapter, we focus on two kinds of mixed catalysts, namely, sub-ML VO_X mixed with ML WO_X and ML VO_X mixed with sub-ML WO_X. As shown in the later discussion, quite distinct structural and chemical behaviors are observed.

7.2 Experimental Results and Discussions

Polished rutile α-$TiO_2(110)$ ($10 \times 10 \times 1$ mm^3) substrates were purchased from Crystal GmbH (Germany). To obtain an atomically flat surface, these substrates were loaded into a tube furnace with flowing O_2 (~100 sccm) and annealed at 400 °C for 30 min, then 900 °C for 60 min. Prior to ALD, substrates were immersed in ultrapure water (resistivity > 10^{18} W cm^{-1}) for 60 min at 90 °C to hydroxylate the surface. Substrates were then rinsed with 10% HCl, then ultrapure water, and blown dry with nitrogen. The substrates were heated to 300 °C under ultrahigh-purity nitrogen flow at 360 sccm at a pressure of 1 torr for 60 min, then cleaned *in situ* with flowing ozone. In the ALD reactor, tungsten oxide was deposited first, followed by vanadium oxide. With the sample temperature at 200 °C, the W ALD process began with 10 min exposure of the substrate to Si_2H_6 at 10 torr, followed by 10 min exposure to WF_6 at 10 torr. Following each exposure, the reactor was evacuated to below 0.05 torr and subsequently purged with ultrahigh-purity nitrogen for 5 min. The process of exposure to Si_2H_6, purging with nitrogen, exposure to WF_6, and finally purging with nitrogen defined herein as one W ALD cycle. Similarly, for one V ALD cycle, substrates were exposed first to vanadium oxytriisopropoxide at a partial pressure of 0.05 torr for 2 seconds, followed by a nitrogen purge for 5 seconds. The ALD coated a-$TiO_2(110)$ substrates were then exposed to H_2O_2 at a partial pressure of 0.2 torr for 2 seconds, followed by a nitrogen purge for 5 seconds. For one set of samples, the substrates were ALD coated with 2 W cycles, followed by 1 V cycle, and for the other set, the substrates were coated with 1 W cycle and then 2 V cycles.

The surface morphology of α-TiO_2 (110) was examined by AFM after the oxygen annealing treatment, after the ALD growth, and after the redox reactions. Silicon AFM tips with a nominal 10 nm radius of curvature and cantilever resonant frequencies of 200 kHz were used with a JEOL-JSPM-5200 scanning probe microscope.

After ALD growth, the samples were removed from the reactor and mounted on a 5-circle diffractometer for the XSW and X-ray fluorescence (XRF) analysis at the Advanced Photon Source (APS) 5ID-C station. The incident photon energy was set at 7 keV for observing V K XRF and 13 keV for W L XRF by a Si (111) monochromator and collimated further with either Si (111) or (220) channel-cut postmonochromator crystals. A Vortex EM silicon drift diode (SDD) detector was used to collect X-ray fluorescence spectra. The V and W coverages were determined by XRF comparison to a calibrated standard sample. For the 2 cycles of W followed by 1 cycle V, the W and V coverages were 1.2 ML and 0.7 ML, respectively; this sample will be referred to as sub-VW. For the 1 cycle W followed by 2 cycles V, the W and V coverages were 0.6 ML and 1.1 ML, respectively. This sample will be referred to as ML-VW. To facilitate surface chemical reactions, the samples were placed on a ceramic heating stage inside a beryllium dome gas reaction cell that was mounted on the diffractometer. The oxidized and reduced surfaces were prepared by annealing at 400 °C for ½ h in O_2 and 2% H_2 in helium at 760 torr, respectively. *In situ* XSW analysis[152, 153, 173] was used to measure the V and W atomic-density maps[156, 233, 234] relative to the rutile substrate lattice after each of these processing steps, namely, as-deposited (AD) → oxidized (Ox) → reduced (Re) → re-oxidized (Ox2). When scanning in angle through a selected substrate $H = hkl$ Bragg reflection, we observed an XSW induced modulation of the V Kβ or W Lβ fluorescence yields that were analyzed to determine the Fourier amplitude (f_H, or coherent fraction) and phase (P_H, or coherent position) for the separate atomic densities of V and W.

XP spectra were taken for the samples at the AD, Ox, Re and Ox2 conditions. These spectra were collected with an Omicron ESCA probe using monochromated Al Kα X-rays. A low-energy electron flood gun was used to compensate the XPS induced surface charging effects. Carbon 1s (284.8 eV) was used as the reference to calibrate the XP spectra.

To check the surface stability of the mixed catalysts against ambient condition, the Ox → Re → Ox2 XSW measurements for the same sets of samples were repeated after at least one month. During the interval these samples were kept in dry box in ambient condition. The same atomic density maps for Ox → Re → Ox2 redox cycles were observed, indicating that the V and W atomic structures are stable in ambient condition and *ex situ* XPS and AFM can be associated with *in situ* XSW measurements.

Figure 8.1(a) and (b) show the AFM images of α-TiO_2(110) substrate surfaces before and after ALD deposition, respectively. The large atomically flat terraces are separated by atomic steps of 3.3 Å, which is the *d*-spacing of α-TiO_2(110). The before and after similarity of these AFM images indicates conformal VO_X and WO_X film formation by ALD. In contrast Fig. 8.1(c), which is an AFM image of the same surface after the redox reactions, shows the formation of nanoparticles. Fig. 8.1(b) and (c) are for the sub-VW case, but similar images of the surface morphology were seen for the ML-VW case, as shown in Fig. 8.2.

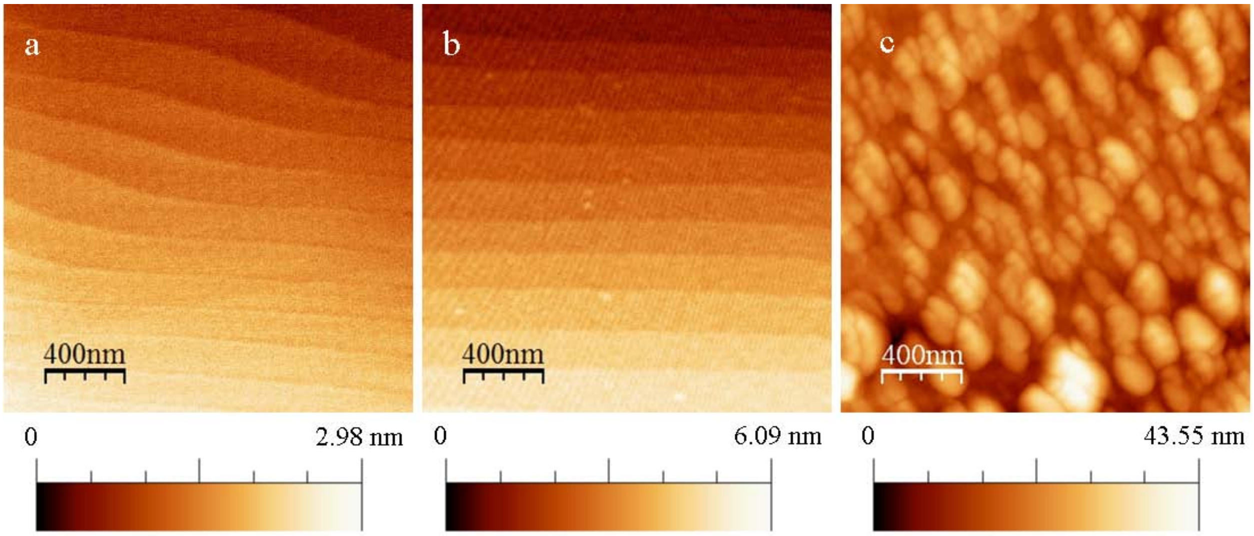

Figure 7.1 Atomic-force microscopy images of the TiO_2 (110) substrate surface. (a) The blank substrate surface after 2-step annealing shows atomically flat terraces with a 3.3 Å vertical step size. (b) After ALD growth of 0.7 ML vanadia on top of 1.2 ML tungsten oxide, the flat atomic terraces can still be observed clearly. (c) The same surface after two redox reaction cycles shows the formation of nanoparticles.

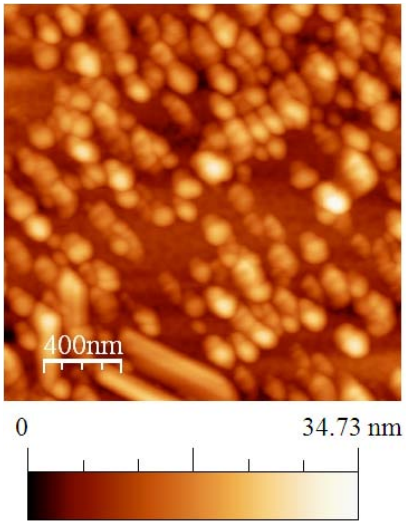

Figure 7.2 Atomic-force microscopy images of the surface of 1.1 ML vanadia on top of 0.6 ML tungsten oxide on α-TiO_2(110) after redox reaction.

Table 7.1 XPS measured chemical states changes for sub-VW (0.7 ML VO_X mixed with 1.2 ML WO_X) and ML-VW (1.1 ML VO_X mixed with 0.6 ML WO_X) surfaces during redox reaction cycles.

Surface	**Ox**idized		**Re**duced			
Chemical states	6+	5+	6+	5+	4+	3+
Sub-VW						
0.7 ML V		100%		44%		56%
1.2 ML W	100%		54%	35%	11%	
ML-VW						
1.1 ML V		100%		67%	33%	
0.6 ML W	100%		100%			

Figure 8.3 and Table 8.1 show the XPS analysis for the two cases at each redox processing step. The spectra of V and W for Ox2 (not shown) are the same as for Ox, indicating redox reversibility of the chemical state of the surface cations. The assignment of oxidation states for V and W are based on previously determined V $2p_{3/2}$ and W 4f binding energies (BE)[21, 213, 220, 231] and the binding energy difference (BED)[220] of V $2p_{3/2}$ to O 1s that are listed in Table 8.2. For the oxidized surfaces in both the sub-VW and ML-VW cases V and W are fully (100 %) oxidized to V^{5+} and W^{6+}, respectively. However, as can be seen in Table 8.1, the Re surfaces are different mixtures of V and W chemical states for the two cases. Namely, for the sub-VW case 56% of V is reduced to V^{3+} and W is reduced to 35% W^{5+} and 11% W^{4+}. For the ML-VW case 33% of V is reduced to V^{4+} and W is not reduced at all. This is different from our previous studies of 0.38 ML[21] and 1.0 ML WO_X/α-$TiO_2(110)$, which show no structural and chemical state changes are observed.

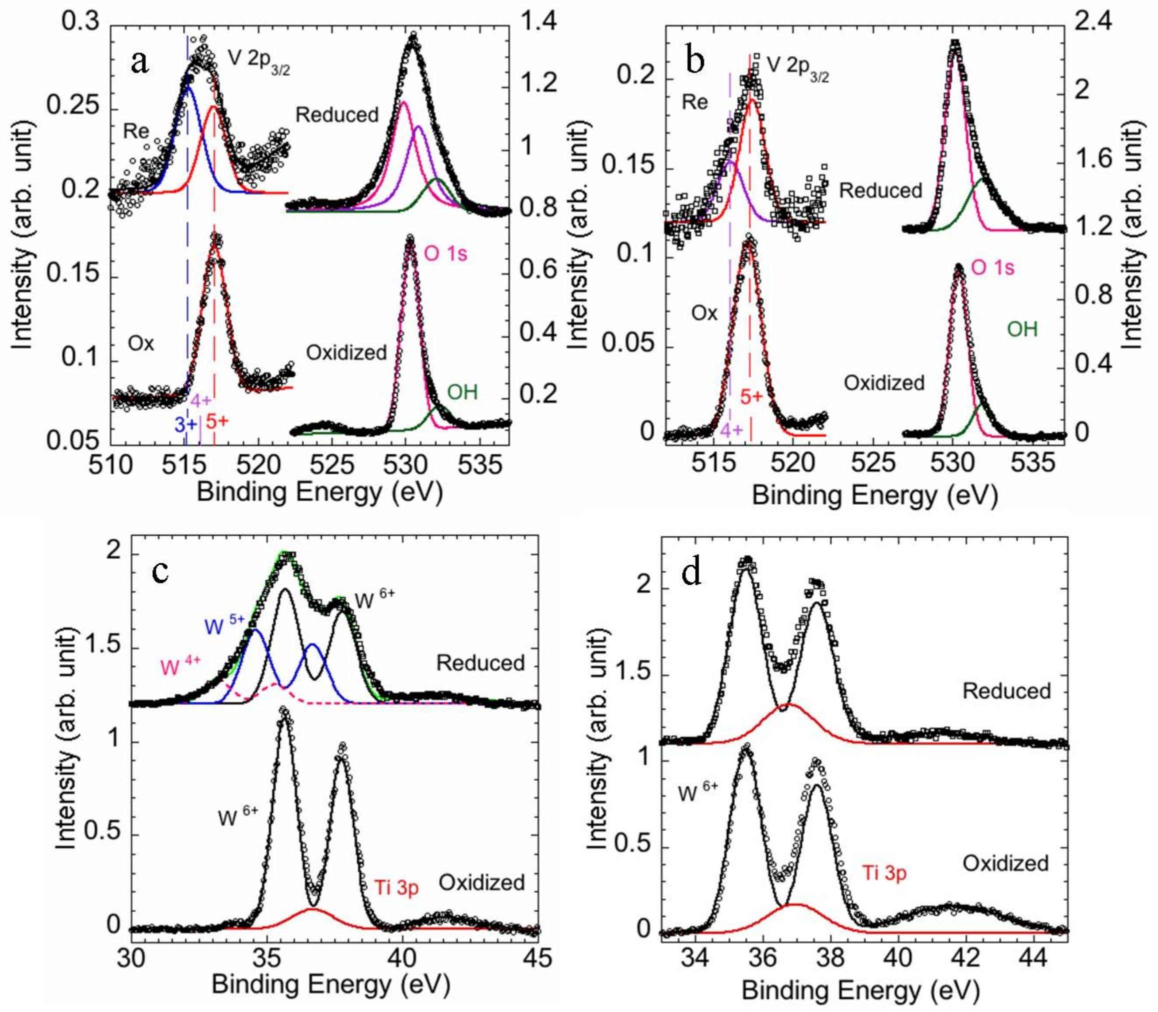

Figure 7.3 XP spectra of VO_X / WO_X / α-TiO_2 (110) mixed catalysts in oxidized (Ox) and reduced (Re) states. Regions of XP spectra showing (a and b) V $2p_{3/2}$ and O 1s peaks, (c and d) W $4f_{7/2}$ and $4f_{5/2}$ doublet peaks and Ti 3p peak, (a and c) sub-VW case of 0.7 ML VO_X / 1.2 ML WO_X / α-TiO_2 (110), and (b and d) ML-VW case of 1.1 ML VO_X / 0.6 ML WO_X / α-TiO_2 (110). XPS was collected at a 45° electron emission angle. The peak fit results are listed in Table 7.1.

Table 7.2 The values of V $2p_{3/2}$ and $4f_{7/2}$ binding Energy (BE) and the binding energy difference (BED) of V $2p_{3/2}$ to O 1s.

Element	V $2p_{3/2}$[220]			$4f_{7/2}$[21, 213, 231]		
Chemical states	+5	+4	+3	+6	+5	+4
BE (eV)	517.2	516.3	515.6	35.6	34.5	33.1
BED (eV)	12.9	13.8	14.6	---	---	---

Based on the W XPS for the sub-VW case, the average O/W ratio of WO_X in the Re state is $X = 2.7$. Note that the O 1s peak is broader in the Re state as compared to the Ox state, suggesting that O exhibits a variety of chemical states that do not correspond to stoichiometric WO_3.[231] Therefore, we consider three contributions with distinct chemical shifts to the O 1s peak, which listed in order of increasing BE would be: 1) VO_X, TiO_2 and stoichiometric WO_3 (with W^{6+} cation centers), 2) sub-stoichiometric WO_X (with a mixture of W^{5+} and W^{4+}), and 3) hydroxyl groups.

The chemical state changes of sub-ML and ML V in mixed catalysts during redox reactions are consistent with our previous studies of pure VO_X (without WO_X) grown by ALD on α-TiO_2(110). Namely for pure VO_X, the sub-ML V oxidation state changes from V^{5+} in the Ox state to a mix of V^{3+} and V^{5+} in the Re state[157], and the ML V changed from V^{5+} in the Ox state to V^{4+} in the Re state.[232] Also our previous study of pure sub-ML[21] and ML WO_X showed no chemical state change from W^{6+} in the redox reaction, which makes it different the chemical state changes observed in the present study for W in sub-VW.

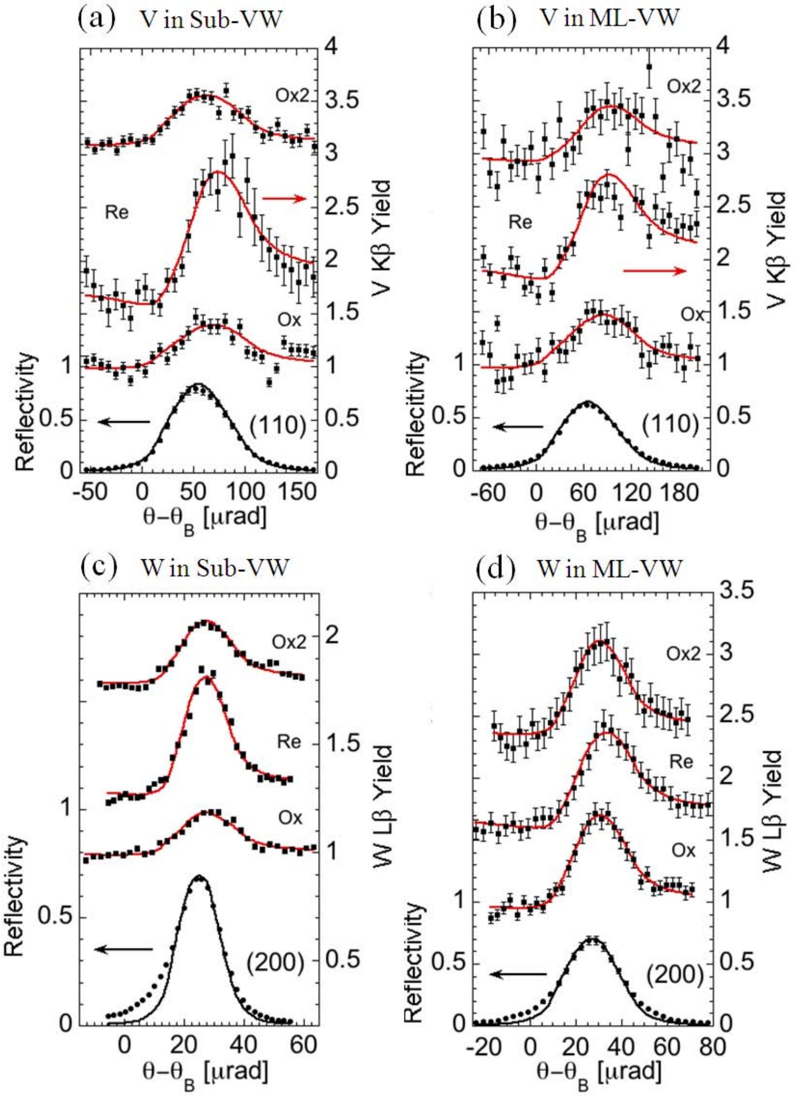

Figure 7.4 XSW data of two mixed catalyst samples for the (110) surface normal and (200) off-normal directions showing vanadium and tungsten structural changes for the oxidized (Ox), reduced (Re), and re-oxidized (Ox2) stages of a redox reaction cycle. Results for Ox2 match well with those for Ox, indicating that structural changes are reversible. Sub-VW denotes the sample with 0.7 ML vanadia on top of 1.2 ML tungsten oxide, and ML-VW denotes the sample with 1.1 ML vanadia on top of 0.6 ML tungsten oxide. V structural changes for (a) Sub-VW sample; (b) ML-VW sample; W structural changes for (c) Sub-VW sample; (d) ML sample.

Figure 8.4 shows a representative set of *in situ* XSW data and analysis after the Ox, Re, and Ox2 steps for the sub-VW and ML-VW cases. The Ox→ Re→ Ox2 reversible change in the V XSW data for both cases is consistent with reversible redox-induced V atom distribution changes; likewise, for W in the sub-VW case. For W in the ML-VW case, no change in the W structural distribution is observed, which is consistent with no changes observed in the W XPS measured chemical state. The XSW measured Fourier amplitudes and phases (Tables 8.3 and 8.4) are then summed up to create model-independent V and W density maps. Figs. 8.5 and 8.6 show the XSW atomic density maps of V and W of the ML-VW and sub-VW at the Ox and Re states, respectively. Since W in ML-VW does not undergo structural changes during redox reactions, there is only one W density map shown in Fig. 8.5. These density maps are projected into the α-TiO_2(110) surface unit cell,[21, 157, 232] and the "hot spots" in the maps are the V or W density maxima, indicating the occupation fraction of this element at this site. In this unit cell, there are two symmetry-inequivalent Ti sites, namely atop (AT) and bridging (BR) sites,[21, 157, 232] which are depicted as solid (AT) and open (BR) blue circles, respectively. It is easy to see that V and W cations in sub-VW case prefer the BR adsorption sites on the rutile (110) surface, while V and W cations in the ML-VW case are distributed equally between AT and BR sites. It is also worth noting that the W density map of the 0.7 ML WO_X in the ML-VW mixed catalyst is the same as those of sub-ML[21] and ML W (see Supporting Information) on α-TiO_2(110) surfaces in our previous studies. These differences suggest that the proper mixing of V and W can affect the structural properties of both V and W in reactions, which may result in different catalytic performance.

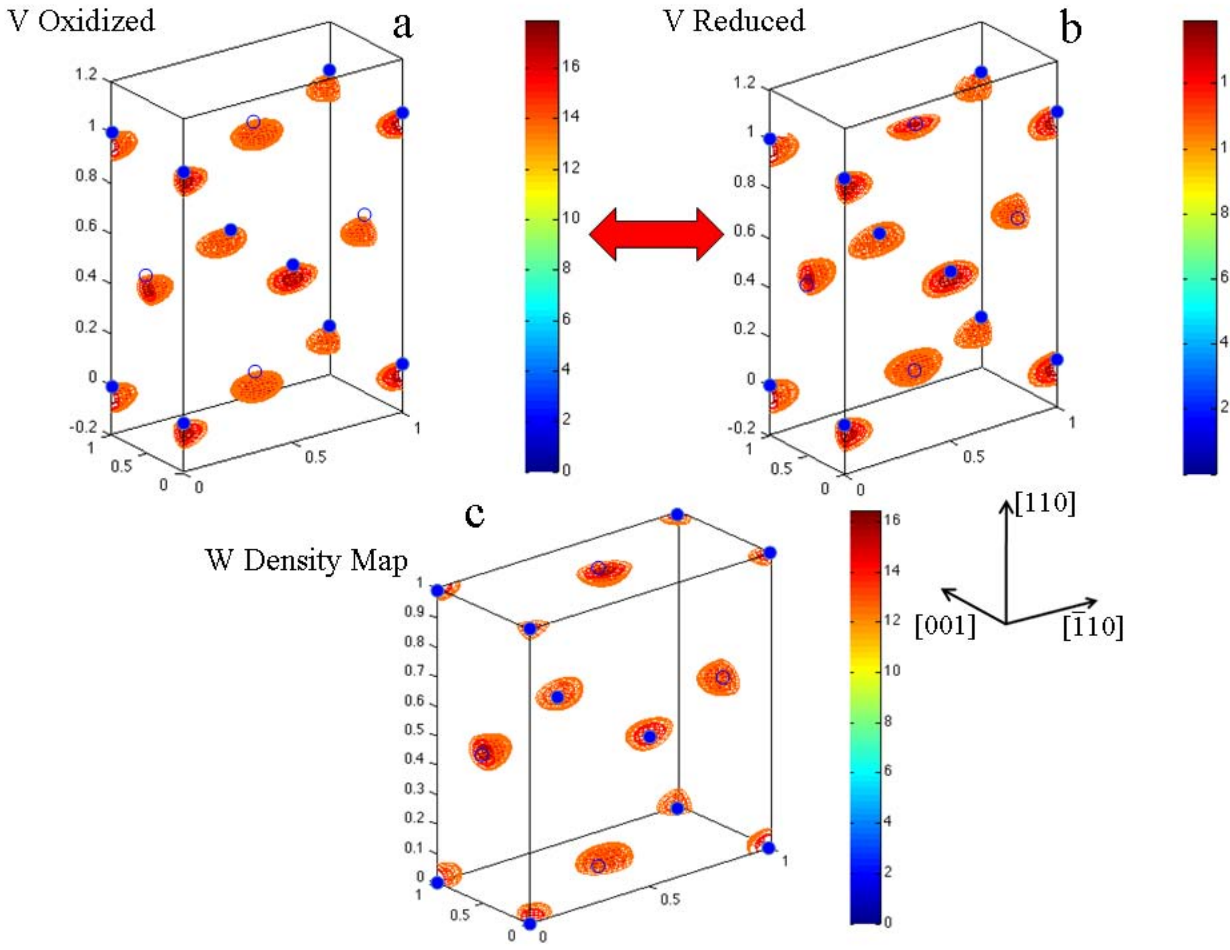

Figure 7.5 Atomic density maps of 1.1 ML vanadia on top of 0.6 ML tungsten oxide deposited on α-TiO_2 (110). Each map is projected onto the α-TiO_2 unit cell, where symmetry-inequivalent AT (filled blue circles) and BR (open blue circles) bulk-like Ti sites are shown. (a) - (b) the vanadium cations' density maps plotted in the surface unit cell reference; (c) is the tungsten cations' density map.

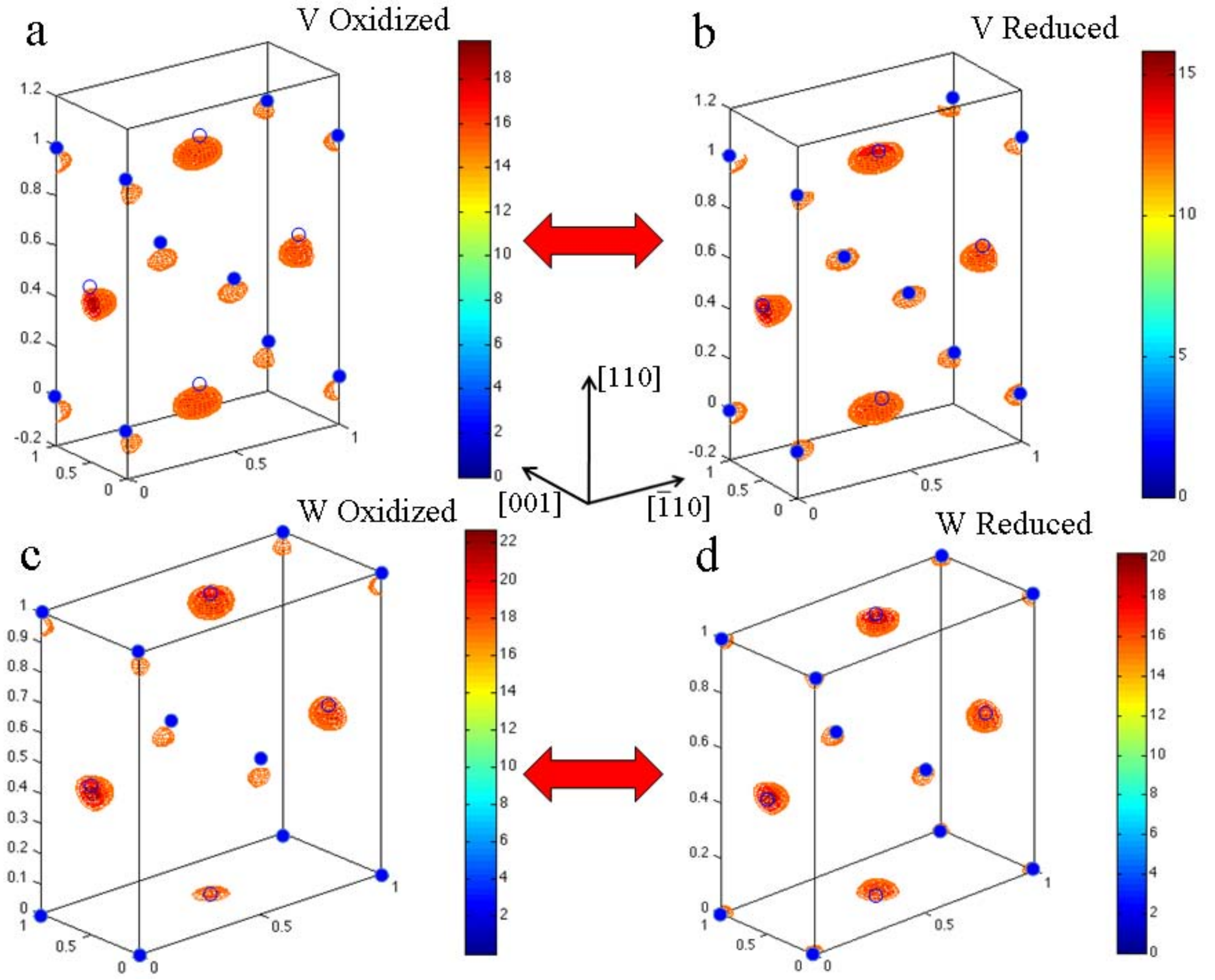

Figure 7.6 Atomic density maps of 0.7 ML vanadia on top of 1.2 ML tungsten oxide deposited on α-TiO$_2$ (110). (a) – (b) the vanadium cations' density maps plotted in the surface unit cell reference; (c) – (d) the tungsten cations' density maps. Bulk-like Ti sites are shown as blue circles, in the same scheme as used in Figure 7.5.

Table 7.3 Summary of XSW experimental results from the oxidized (Ox), reduced (Re), and re-oxidized (Ox2) surface treatments of the VO_X (0.7 ML) / WO_X (1.2 ML) / α-TiO_2 (110) sample. f_H and P_H are experimentally measured coherent fractions and coherent positions, respectively, and f_H^C and P_H^C and least-square determined best fit values. The top part of the table is the summary for V results and the lower part of the table is the summary for W results.

hkl		*110*	*101*	*200*	*111*	*211*	*210*	*220*	*301*
V									
Ox	f_H	0.30(1)	0.46(1)	0.30(6)	0.2(1)	0.31(5)			
	f_H^C	0.33	0.45	0.33	0.42	0.22			
	P_H	0.84(1)	0.95(1)	0.86(3)	0.28(6)	0.79(2)			
	P_H^C	0.83	0.91	0.83	0.45	0.72			
Re	f_H	0.60(5)	0.42(8)	0.27(6)	0.32(8)	0.36(6)			
	f_H^C	0.42	0.42	0.42	0.29	0.41			
	P_H	0.04(2)	0.01(4)	0.88(3)	0.30(4)	0.81(3)			
	P_H^C	0.93	0.96	0.83	0.41	0.90			
Ox2	f_H	0.24(2)	0.43(7)						
	f_H^C	0.27	0.41						
	P_H	0.84(1)	0.88(3)						
	P_H^C	0.86	0.92						
W									
Ox	f_H	0.30(1)	0.24(1)	0.36(1)					
	f_H^C	0.29	0.31	0.29					
	P_H	0.02(1)	0.89(1)	0.81(1)					
	P_H^C	0.93	0.97	0.93					
Re	f_H	0.21(1)	0.22(1)	0.32(1)	0.30(2)	0.16(1)	0.16(1)	0.08(2)	0.13(1)
	f_H^C	0.23	0.23	0.23	0.09	0.23	0.10	0.22	0.23
	P_H	0.97(1)	0.91(1)	0.99(1)	0.28(1)	0.96(1)	0.68(1)	0.07(4)	0.02(2)
	P_H^C	0.97	0.99	0.97	0.43	0.96	0.40	0.94	0.96
Ox2	f_H	0.25(1)	0.28(1)	0.31(1)	0.16(1)	0.18(1)	0.14(1)	0.09(1)	0.14(1)
	f_H^C	0.23	0.25	0.23	0.15	0.20	0.19	0.16	0.20
	P_H	0.96(1)	0.85(1)	0.90(1)	0.39(1)	0.94(1)	0.63(1)	0.85(1)	0.88(1)
	P_H^C	0.91	0.96	0.92	0.53	0.88	0.51	0.85	0.88

Table 7.4 Summary of the XSW experimental results from the oxidized (Ox), reduced (Re), and re-oxidized (Ox2) surface treatments of the VO_X (1.1 ML) / WO_X (0.6 ML) / α-TiO_2 (110) sample. The top part of the table is the summary for V results and the lower part of the table is the summary for W results.

hkl		*110*	*101*	*200*	*111*	*211*
V						
Ox	f_H	0.29(4)	0.18(5)	0.27(4)		
	f_H^C	0.26	0.26	0.26		
	P_H	0.86(2)	0.92(4)	0.78(2)		
	P_H^C	0.82	0.91	0.82		
Re	f_H	0.53(7)	0.62(9)	0.1(1)	0.7(2)	0.3 (1)
	f_H^C	0.45	0.61	0.45	0.48	0.22
	P_H	0.01(3)	0.03(3)	0.9 (3)	0.72(3)	0.90(6)
	P_H^C	0.96	0.98	0.96	0.72	0.96
Ox2	f_H	0.38(7)	0.39(9)		0.4(2)	0.48(9)
	f_H^C	0.43	0.43		0.04	0.43
	P_H	0.9(3)	0.87(3)		0.02(9)	0.87(3)
	P_H^C	0.89	0.95		0.01	0.84
W						
Ox	f_H	0.45(1)	0.28(1)	0.43(2)	0.06(2)	0.31(2)
	f_H^C	0.42	0.43	0.42	0.11	0.40
	P_H	0.04(1)	0.05(1)	0.90(1)	0.45(7)	0.07(1)
	P_H^C	0.04	0.02	0.04	0.37	0.06
Re	f_H	0.46(1)	0.44(1)	0.54(3)	0.11(3)	0.45(3)
	f_H^C	0.45	0.46	0.45	0.09	0.44
	P_H	0.03(1)	0.00(1)	0.01(1)	0.38(4)	0.12(1)
	P_H^C	0.05	0.02	0.05	0.37	0.07
Ox2	f_H	0.25(1)	0.26(2)			
	f_H^C	0.26	0.26			
	P_H	0.03(1)	0.04(1)			
	P_H^C	0.04	0.02			

Table 7.5 Least-squares fit model parameters determined from XSW data and Eq. 7.1 for the V and W occupation fractions, c_X, and heights, z_X, above the bulk TiO (110) plane for VO_X (0.7 ML) / WO_X (1.2 ML) / α-TiO_2 (110). For comparison, Ti in bulk α-TiO_2 has $z_{BR} = z_{AT} = 3.25$ Å. The V correlated fraction ($\Sigma c = c_{BR} + c_{AT}$) is also listed.

Surface	c_{BR}	c_{AT}	Σc	z_{BR} (Å)	z_{AT} (Å)
0.7 ML V					
Ox	0.35(3)	0.14(3)	0.49(4)	3.09(3)	2.60(6)
Re	0.35(4)	0.07(4)	0.42(6)	3.12(3)	3.22(9)
1.2 ML W					
Ox	0.18(1)	0.08(1)	0.26(1)	2.93(1)	3.20(1)
Re	0.16(1)	0.07(1)	0.23(1)	3.19(1)	3.25(1)

Table 7.6 Least-squares fit model parameters determined from XSW data and Eq. 7.1 for the V and W occupation fractions, c_X, and heights, z_X, above the bulk TiO (110) plane for VO_X (1.1 ML) / WO_X (0.6 ML) / α-TiO_2 (110). For comparison, Ti in bulk α-TiO_2 has $z_{BR} = z_{AT} = 3.25$ Å. The V correlated fraction ($\Sigma c = c_{BR} + c_{AT}$) is also listed.

Surface	c_{BR}	c_{AT}	Σc	z_{BR} (Å)	z_{AT} (Å)
1.1 ML V					
Ox	0.20(8)	0.23(9)	0.43(9)	3.06(7)	3.09(6)
Re	0.32(5)	0.34(5)	0.66(7)	3.43(4)	2.99(4)
0.6 ML W					
Ox	0.24(2)	0.19(2)	0.43(3)	3.26(2)	3.38(2)
Re	0.25(1)	0.21(1)	0.46(1)	3.29(2)	3.37(2)

To further refine the structural parameters associated with these two adsorption sites, we performed a least-squares global fit of each condition to the measured set of f_H and P_H values. The H^{th} Fourier component for the V atomic distribution is then described as,

$$F_H = f_H \exp\left(2\pi i P_H\right) = c_{AT} \exp\left(2\pi i \mathbf{H}\cdot\mathbf{r}_{AT}\right) + c_{BR} \exp\left(2\pi i \mathbf{H}\cdot\mathbf{r}_{BR}\right), \qquad (8.1)$$

where c_X denotes the V or W cations' occupation fraction at the AT and BR sites with positions $\mathbf{r}_{AT}$= (0,0,z_{AT}) and $\mathbf{r}_{BR}$= (½,½,z_{BR}), with z_X denoting the cations' heights in the (110) direction above the TiO plane. Tables 8.5 and 8.6 list the best-fit determined results of the cations' occupation fractions and adsorption heights for sub-VW and ML-VW samples, respectively. As an additional consistency check, the measured Fourier components (Tables 8.3 and 8.4) are compared with the calculated values, f_H^C and P_H^C, that would have been observed if V occupied sites as dictated by this best-fit model. Furthermore, Tables 8.5 and 8.6 show that the correlated fractions, $\Sigma c = c_{BR} + c_{AT}$, are constants for V and W in sub-VW case, and W in ML-VW case, respectively, indicating the correlated elements stay the same in redox reaction. The remaining cations are uncorrelated to the substrate lattice, distributed in defect sites or contained in the nanoparticles observed on the surface after redox processing.

Only ML V in the ML-VW case shows a significant change for the correlated fraction, indicating that some uncorrelated cations become correlated to the substrate lattice upon changing from the Ox state to the Re state. This is consistent with our previous study of 2.0 ML VO_X on α-TiO_2(110), in which V cations go through a redox-reversible coherent-incoherent (or correlated –uncorrelated) transformation, concurrent with the V chemical shift from 5+ to 4+.[26] In the discussion that follows, we consider the atomic distribution examined by the XSW atomic map to be partitioned into a correlated and uncorrelated part. From Eq. 8.1 we would define the uncorrelated part to be one in which the Fourier amplitudes $f_H = 0$ for all $H = hkl$, except $H = 0$. It is not surprising that the correlated fraction of the sub-ML W in ML-VW case stays the same in a redox reaction because no change in the W chemical state is observed. However, for the sub-VW case, the correlated fractions for both V and W are unchanged, while XPS shows that redox causes a significant fraction of both cations to undergo a chemical-state change. This implies that the correlated V and W atoms may not participate in the chemical state changes in redox reactions for this case. It is those uncorrelated cations that go through reversible chemical state changes. Note that the correlated fraction for V from the model-dependent analysis of the sub-VW case, ~ 0.45, matches well with the 0.44 fraction of the unchanged V^{5+} in the Re state from the XPS measurement. This strongly suggests that uncorrelated cations play a significant role in the redox reaction in this case. The reversible structural changes for those correlated V and W can be seen from the height changes at AT and BR sites on the rutile surface. The model-dependent global fits show that both V and W in the sub-VW case have significant adsorption height changes when they go through the redox processes. This indicates that uncorrelated cations affect the structure of the nearby correlated V and W cations when the reversible chemical state changes happen. The uncorrelated cations may be mixed with correlated V and W nanocrystals in larger nanoparticles, as shown from the AFM image in Fig. 8.1(c). Therefore reversible structural and chemical states changes are both observed.

In Table 8.5 the XSW global fit shows that the correlated fraction of W in the sub-VW case is 0.25, or 0.3 ML. This is the same as the amount of correlated W in ML-VW case, 0.6 ML×0.45 = 0.3 ML, as shown in Table 8.6. This matches very well with the coverage of correlated W in our previous study[26] of 0.38 ML WO_X / α-TiO_2. This indicates that for ALD-grown W on rutile, the correlated W amount is a constant, and these correlated W do not go through chemical state changes. The comparison between the three cases shows that a redox reaction cycle at 400 °C does not induce changes in W chemical states if only W is deposited on rutile. However, combining proper amount of V with W can yield a surface capable of redox-induced chemical state changes.

Previous studies of vanadia, tungsten oxide or V-W mixtures supported on TiO_2 powder have shown that V is much more catalytically active than W during various chemical reactions.[235-237] With additional W added to V, the catalytic activity is improved.[87, 238] This is consistent with our findings: Rutile α-TiO_2(110)-supported unmixed W is not reducible while W is reducible when ML W is mixed with sub-ML V. It is believed that a synergetic effect is brought by the additional W to V.[236, 238] Bertinchamps et al. further show that the synergy between V and W is attributed to the additional Brønsted acid sites brought by the promoter, W.[238] Therefore, an enhancement of performance is observed for the mixed catalysts over their constituents. Previous studies[87, 238] also show that the best performance of V-W mixed catalysts is achieved when the atomic concentration ratio of W to V is greater than 1. This is consistent with our findings as well: W is reducible when the W : V ratio is about 2:1, while W has no chemical state changes for the opposite ratio. Our model-dependent analysis shows that for either mixed catalysts or W alone, there is a certain amount of correlated W (~0.3 ML), which does not change during the redox reaction. It is the uncorrelated W (or V) that responds to the redox reaction chemically (and structurally, for ML V). This is also supported by the studies of V-W mixed catalysts supported on TiO_2 powder. X-ray diffraction measurements combined with reactivity experiments[87, 238] indicate that crystalline WO_X brings very small improvement to the catalytic performance. The improvement of the catalyst activity parallels the increase in W loading under the condition that these W are still present as non-crystalline.[236] In our mixed catalyst cases, the crystallinity ratio of W is much higher in ML-VW than that in sub-VW. Therefore, higher catalytic performance of sub-VW can be expected, which shows that W is reducible. W is generally catalytically inactive and thermodynamically stable in the temperature range of our redox reaction, 400 °C, so it is not surprising that no chemical state changes of W in ML-VW are observed.

7.3 Summary

For α-TiO_2(110) supported VO_X-WO_X mixed catalysts, two cases were investigated: 0.7 ML VO_X mixed with 1.2 ML WO_X (sub-VW), and 1.1 ML VO_X mixed with 0.6 ML WO_X (ML-VW). AFM shows that vanadia and tungsten oxide exist as nanoparticles on the surface after undergoing a redox reaction cycle. XSW analysis shows that these large nanoparticles are composed of nanocrystals, which are correlated to the underlying α-TiO_2, and small uncorrelated nanoparticles that play an important role during the redox reactions. XPS combined with XSW further indicates that uncorrelated V and W in sub-VW and uncorrelated V in ML-VW go through chemical state changes for the sub-VW case. Except for V in ML-VW showing an uncorrelated-correlated structural transformation, no dramatic structural changes for W in ML-VW, and V and W in sub-VW, are observed. However, the dynamics of uncorrelated V and W in a redox reaction cycle affect nearby correlated V and W, causing variation in their adsorption heights. Redox reversibility was observed in this process, demonstrating its relevance to catalytic applications. Compared with previous studies of TiO_2 single crystal- and powder-supported WO_X, additional W added to V in our cases shows some enhanced catalytic performance, which is consistent with results from powder-supported mixed catalysts. This is due to the additional Brønsted acid sites provided by the promoter, W, and thus the synergy between V and W is formed. Our studies also show that the mixed catalysts show enhanced chemical state shifts as the amount of additional W increases. This enhancement is attributed to the increase in the ratio of uncorrelated to correlated W. This study demonstrates the importance of structurally uncorrelated cations in chemical reactions, which will further help to understand the redox-induced chemical bonding changes of the catalysts and the role of the supporting oxides in catalytic reactions.

Chapter 8: Correlating Single-Crystal Surface Studies to Catalysis Properties Studies of Powders

8.1 Introduction

Single crystal studies descripted in preceding Chapters are well suited to give clear structural and chemical information for well-defined surfaces. However, single crystal surfaces are not suitable for catalytic reaction tests due to low surface areas. For this, it is necessary to use polycrystalline powders with high surface areas for catalytic property tests. XSW combined with XPS can be used to probe the surface structural and chemical information of catalysts on single crystals during reactions, while reactivity and selectivity of chemical reactions on catalysts can be studied by traditional catalytic tests on powders. The question remains is how we can correlate our single crystal surface measurements with catalytic property tests on powder samples. Our strategy here is to use XPS on both single crystals and powders to demonstrate their similar catalytic performance.

8.2 Cyclohexane ODH on Rutile Supported Vanadia

Previously the redox-driven cation dynamics of sub-ML[157] and ML[232] VO_X/α-$TiO_2(110)$ have been observed. V with different coverages showed distinct structural and chemical reversible changes. Therefore, rutile supported vanadia can be an ideal system to correlate the single crystal structural studies with powder catalytic studies. For this purpose, cyclohexane oxidative dehydrogenation (ODH) was performed on 1.5 ML VO_X/α-$TiO_2(110)$. The ODH processes on single crystal supported vanadia were separated into two parts: oxidization of vanadia by oxygen and reduction of vanadia by cyclohexane. *In situ* XSW and *ex situ* XPS were combined together to study the atomic-scale structural and chemical state changes of V. Furthermore, cyclohexane ODH were carried out on rutile powder supported ML vanadia. The reactivity and selectivity were tested.

In this study, atomic-flat surfaces of α-$TiO_2(110)$ were prepared using the 2-step annealing method mentioned before. For V ALD growth, substrates were exposed first to vanadium oxytriisopropoxide (VOTP) at a partial pressure of 0.05 torr for 2 seconds, followed by a nitrogen purge for 5 seconds. The ALD coated α-$TiO_2(110)$ substrates were then exposed to H_2O_2 at a partial pressure of 0.2 torr for 2 seconds, followed by a nitrogen purge for 5 seconds. This process is defined as one ALD cycle. For single crystal α-TiO_2 (110), 2 ALD cycle of vanadia were deposited. For powder rutile substrate, 3 ALD cycles of vanadia were deposited. To make sure the ML V was obtained for powder samples, the exposure time to VOTP during ALD growth is increased to 30 s instead of 2 s.

For XSW measurement, the single crystal sample was mounted on a 5-circle diffractometer at the APS 5ID-C station. The incident photon energy was set at 7 keV for observing V K XRF by a Si (111) monochromator and collimated further with either Si (111) or (220) channel-cut postmonochromator crystals. A Vortex EM silicon drift diode (SDD) detector was used to collect X-ray fluorescence spectra. The V coverage was determined to be 1.5 ML by XRF comparison to a calibrated standard sample. To facilitate surface chemical reactions, the samples were placed on a ceramic heating stage inside a beryllium dome gas reaction cell that was mounted on the diffractometer. The oxidized and reduced surfaces were prepared by annealing at 400 °C for ½ h in O_2 and cyclohexane carried by helium through a bubbler at 760 torr, respectively. *In situ* XSW analysis[152, 153, 173] was used to measure the V atomic-density maps[156, 233, 234] relative to the rutile substrate lattice after each of these processing steps, namely, oxidized (Ox) → reduced (Re) → re-oxidized (Ox2).

XP spectra were taken for the samples at the Ox, Re and Ox2 conditions. These spectra were collected with an Omicron ESCA probe using monochromated Al Kα X-rays. A low-energy electron flood gun was used to compensate the XPS induced surface charging effects. Carbon 1s (284.8 eV) was used as the reference to calibrate the XP spectra.

Figure 9.1 shows the XSW and XPS data analysis for 1.5 ML $VO_X/\alpha\text{-}TiO_2(110)$ at each reaction step, respectively. The uncorrelated-correlated structural changes concurrent with $V^{5+} \leftrightarrow V^{4+}$ chemical state changes are consistent with our previous study of 2 ML $VO_X/\alpha\text{-}TiO_2(110)$[232], but for the latter case H_2 is used as the reductant.

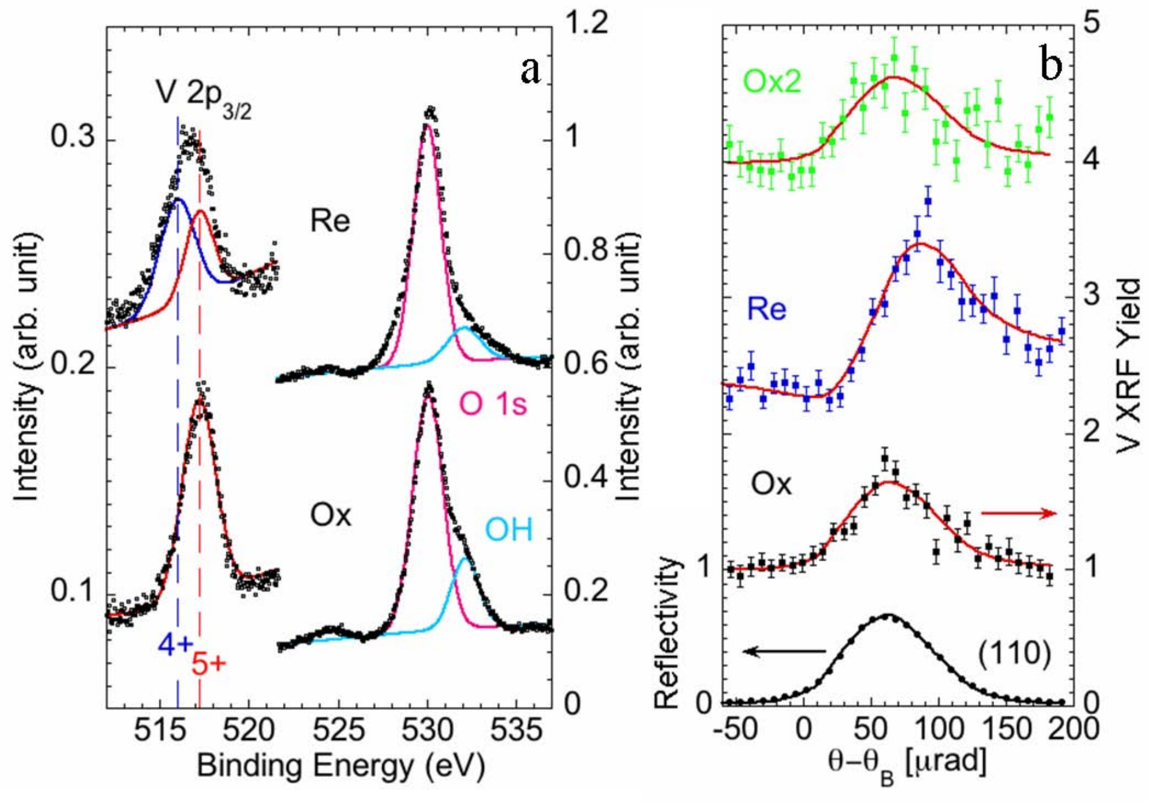

Figure 8.1 (a) XPS and (b) XSW (110) surface normal direction data analysis of 1.5 ML VO_X/α-$TiO_2(110)$, showing vanadium structural and chemical state changes for the oxidized (Ox), reduced (Re), and re-oxidized (Ox2) stages of a redox reaction cycle.

The V structure at Re state was further studied by XSW. Several off-normal *hkl* diffraction planes were measured as shown in Figure 9.2. These asymmetric V fluorescence shape indicates that V forms correlated structure to the substrate α-$TiO_2(110)$ lattice. By inserting measured Fourier components (f_H and P_H) into Eq. 3.10, a V atomic-density map of the Re state is created as shown in Figure 9.3. This Re structure as well as the redox-induced correlated-uncorrelated transformation further confirms the consistence with 2 ML VO_X/α-$TiO_2(110)$[232], indicating cyclohexane has the similar effort on V cations.

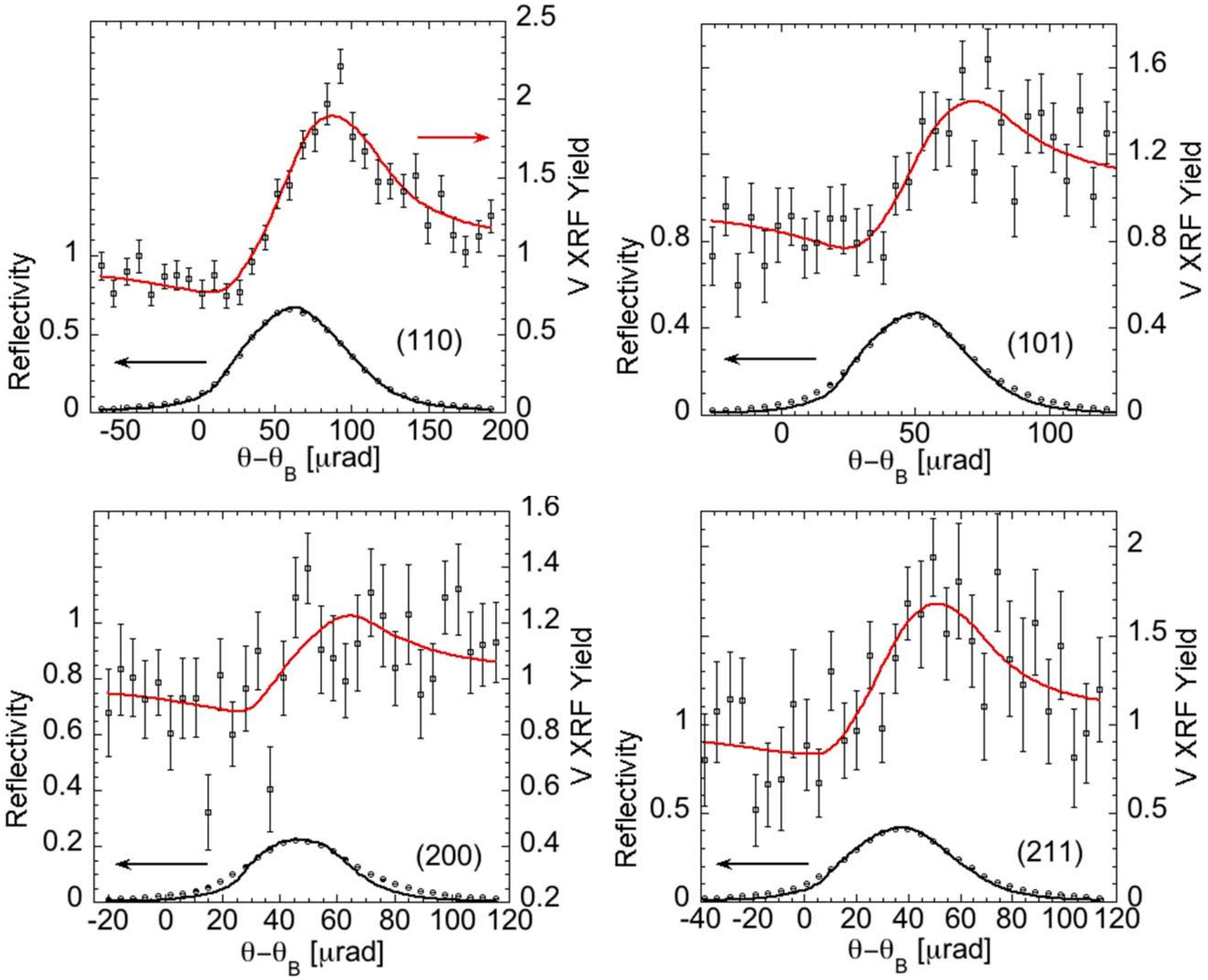

Figure 8.2 XSW data analysis for reduced 1.5 ML VO_X/α-TiO_2(110) at (110), (101), (200) and (211) diffraction planes. The asymmetric shape of V fluorescence indicates that V is correlated to substrate lattice.

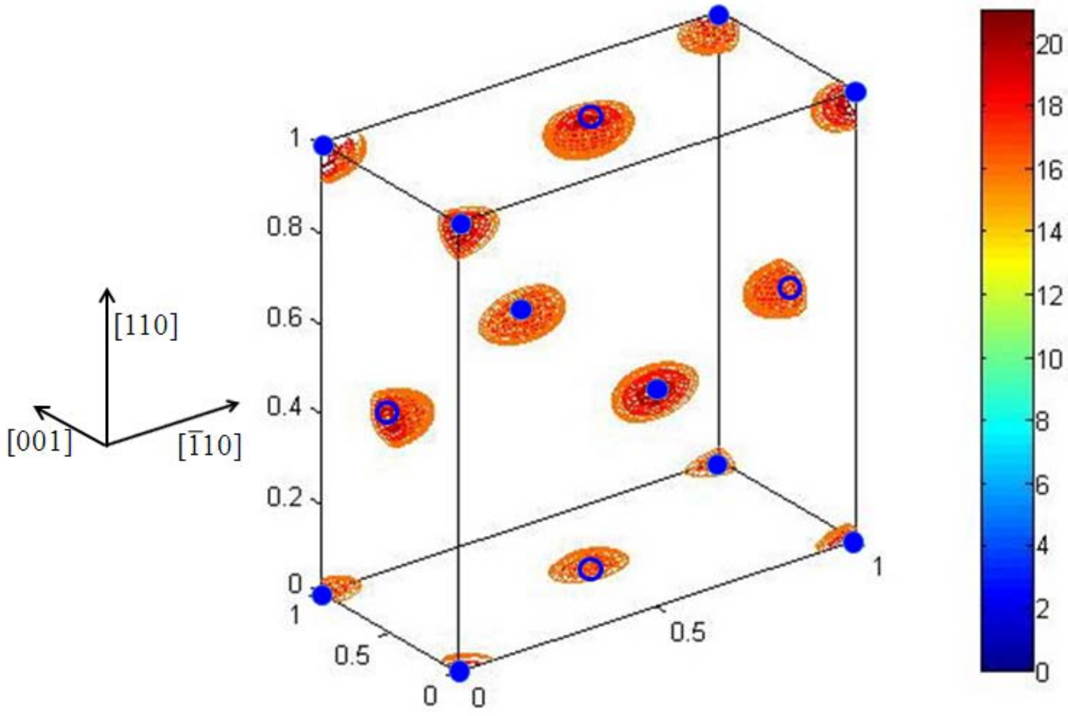

Figure 8.3 V atomic-density map at reduced condition. The open and solid circle denote two symmetry inequivalent sites, AT and BR sites, on α-TiO_2(110) surface.

Figure 9.4(a) and (b) show the AFM images of α-TiO_2(110) substrate surfaces before and after ALD deposition, respectively. The large atomically flat terraces are separated by atomic steps of 3.3 Å. Similar terraces were observed after ALD growth indicates the conformal growth of 1.5 ML vanadia. In contrast Fig. 9.4(c), which is an AFM image of the same surface after the redox reactions, shows the formation of nanoparticles. The existence of V nanoparticles is further confirmed by SEM images, as shown in Figure 9.5. This is similar to 1.0 ML WO_X/α-TiO_2(110) and indicates that if catalyst coverage is higher than one ML, nanoparticles are observed after redox reactions.

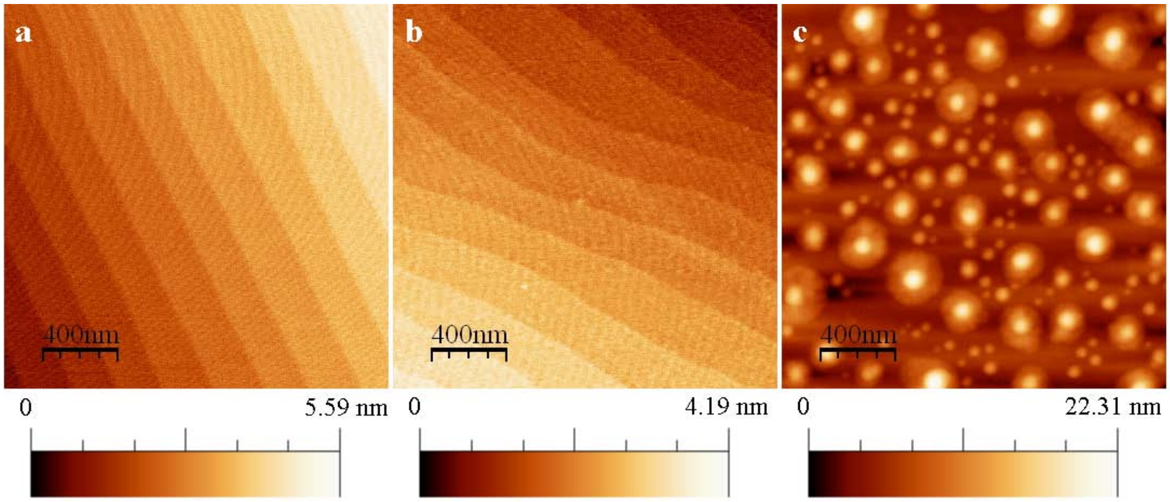

Figure 8.4 Atomic-force microscopy images of the TiO_2 (110) substrate surface. (a) The blank substrate surface after 2-step annealing with atomically flat terraces. (b) After ALD growth of 1.5 ML vanadia, the flat atomic terraces can still be observed clearly. (c) The same surface after two redox reaction cycles shows the formation of nanoparticles.

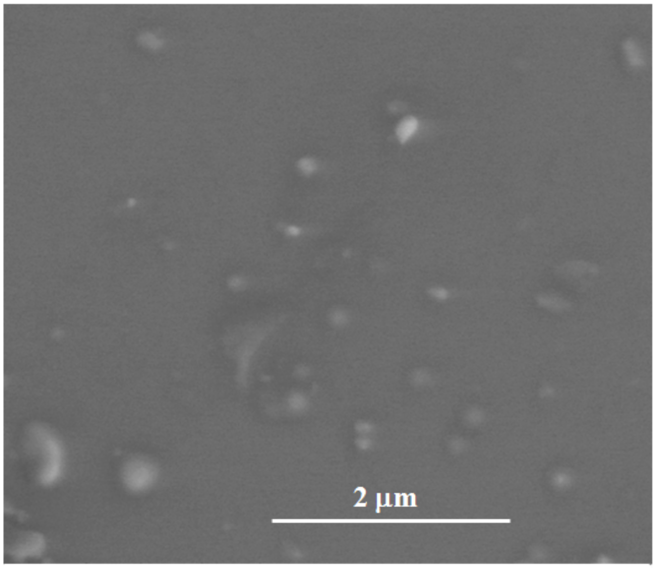

Figure 8.5 SEM images of 1.5 ML $VO_X/\alpha\text{-}TiO_2(110)$ after redox reactions. Nanoparticles are clearly seen.

To associate these atomic-structural and chemical state changes with V catalytic properties, cyclohexane ODH tests were carried out on vanadia supported by rutile powder. To make sure powder supported vanadia has the same catalytic performance as single crystal supported vanadia, XPS was used to demonstrate the similarities. Figure 9.6(a) shows the XPS analysis for 1.5 ML VO_X/α-TiO_2(110) and Figure 9.6(b) shows the XPS analysis for vanadia on rutile powder. The similarity of V^{5+} ←→V^{4+} chemical state changes for both cases indicates that vanadia performs similarly in cyclohexane ODH reaction regardless the substrate types.

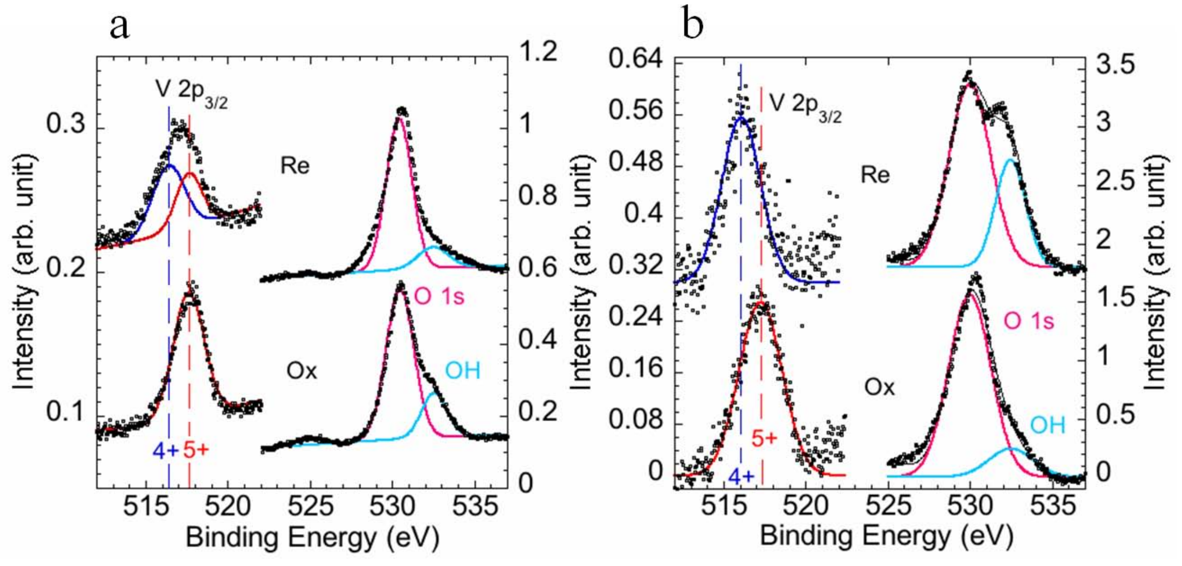

Figure 8.6 XPS of (a) single crystal a-TiO2(110) supported 1.5 ML vanadia, and (b) powder rutile supported 3 ALD cycle (30 s) vanadia at oxidized (Ox) and reduced (Re) condition. The Re surface is obtained by cyclohexane reduction.

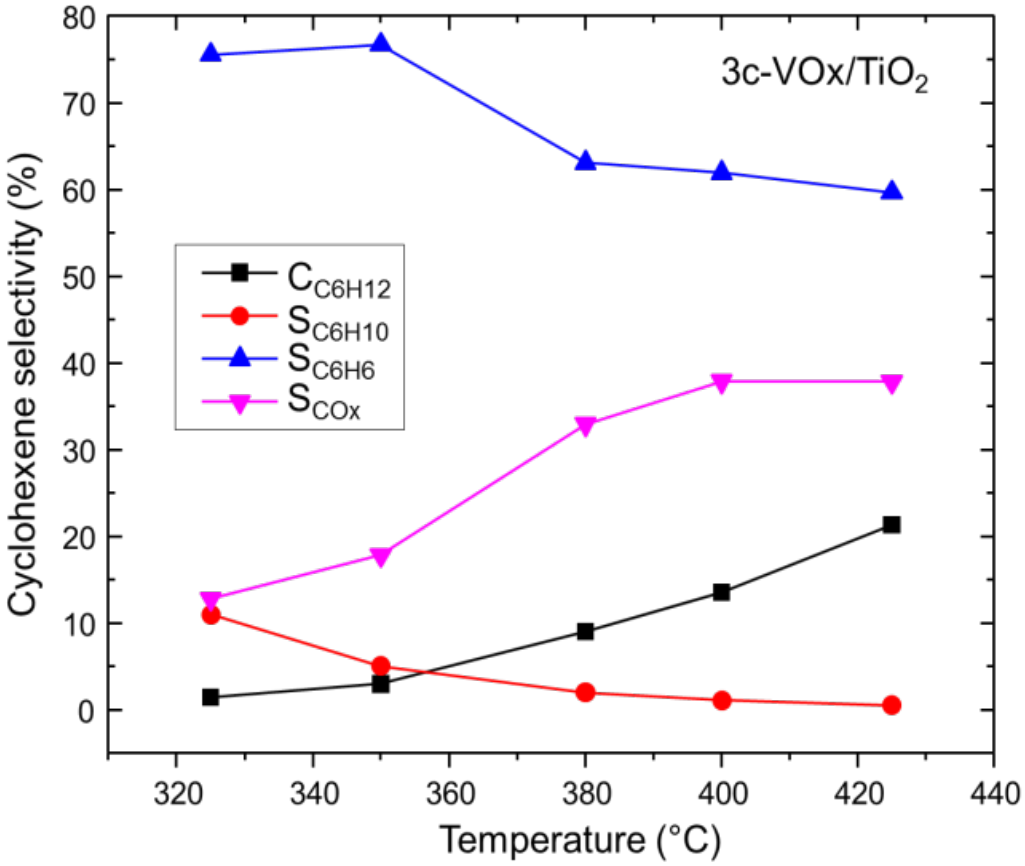

Figure 8.7 Cyclohexene selectivity as a function of reaction temperature of 3-ALD-cycle coated vanadia on rutile powder.

For cyclohexane ODH tests on powder vanadia, cyclohexane was delivered from a cyclohexane bubbler by Argon gas. The reaction was carried out at the temperature range of 325 to 425 °C. 50 mg of catalysts was used and diluted by 200 mg of SiC to avoid the hot spots during reaction. Based on the calculations and the standard we have, the flow rate of cyclohexane, oxygen, and argon was 0.22, 0.44 and 19.34 sccm. Cyclohexane to oxygen ratio was 1:2. Figure 9.7 shows our preliminary results of the cyclohexene selectivity as a function of reaction temperature. This test shows that the main product of cyclohexane ODH is benzene, and the selectivity for cyclohexene is quite low. Further tests are being carried out and the atomic-scale structure changes will be associated with vanadia selectivity.

8.3 Summary

For rutile supported ML vanadia, the structural and chemical studies of vanadia on single crystal α-TiO_2(110) have been correlated with catalytic reaction studies on rutile powder supported vanadia. During the redox reaction, V change from uncorrelated structure in oxidized (Ox) condition to rutile-like structure in reduced (Re) condition by using cyclohexane as the reductant, while V chemical states change from V^{5+} in Ox to V^{4+} in Re. The cyclohexane selectivity and reactivity on vanadia powders have been tested on rutile powder supported vanadia. The future step is to associate the selectivity and reactivity of vanadia to its atomic-scale structural changes.

Chapter 9: Summary and Outlook

9.1 Thesis Summary

This thesis work has focused on the studies of oxide supported catalysts from growth to redox-reaction induced dynamics. We studied unmixed catalysts (vanadium and tungsten) on different oxide substrates, reducible oxide α-Fe_2O_3(0001) and non-reducible oxide α-TiO_2(110), and mixed catalysts.

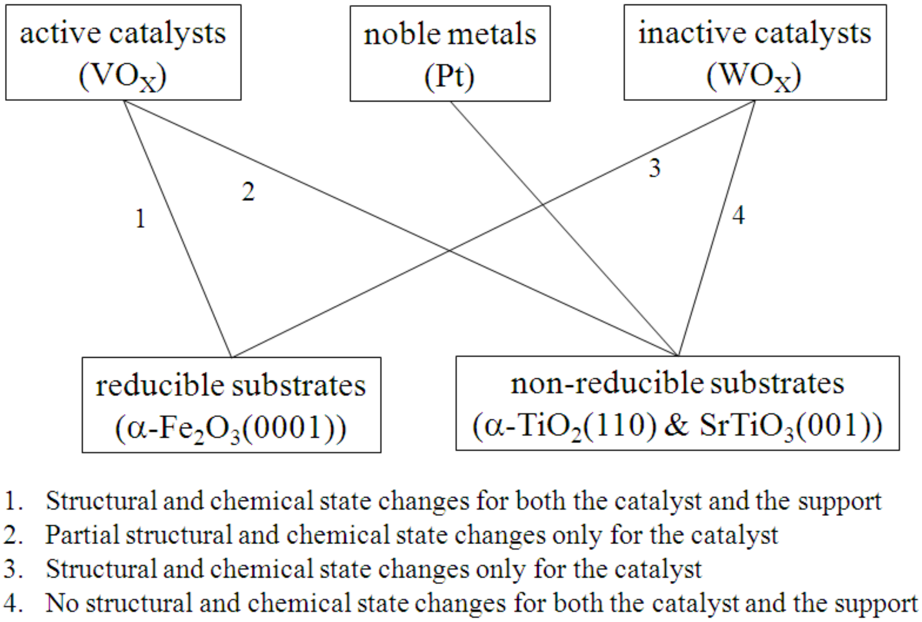

Figure 9.1 Predictions for several combinations between the catalyst and the substrate from works in this thesis.

Our previous studies[21] shows that inert catalyst supported on non-reducible substrates, such as WO_X/α-TiO_2(110), have no redox-induced cation dynamics. However, in this thesis, when a inert catalyst is supported on a reducible substrate, WO_X/α-Fe_2O_3(0001), or an active catalyst is supported on a non-reducible substrate, VO_X/α-TiO_2(110), we show that reversible structural and chemical state changes in redox reactions have been observed for both cases. This indicates that proper combination of a catalyst with a support can boost their catalytic performance in reactions. Similarly, when W is mixed with V, different ratio of W to V show distinct reversible structural and chemical state changes in reactions. This demonstrates that there is a synergistic effect when proper amount of W is mixed with V. These are summarized in Figure 10.1, which is added our predictions for the structural and chemical states changes of several possible combinations between the catalyst and the support as shown in Figure 1.2.

In this thesis, various X-ray techniques are used as *in situ* probes, and imaging methods like AFM and SEM are used for complementary surface investigations. For single crystals supported catalysts, X-ray standing wave (XSW) is a unique and powerful technique to directly image the surface catalysts' density distribution and structure at atomic-scale. XSW is very suitable to study monolayer (ML) and sub-ML metal and/or metal oxides on single crystal substrates. As shown in MBE grown sub-ML Pt on $SrTiO_3$(001) case, XSW can accurately determine the Pt lattice shift relative to substrate $SrTiO_3$ unit cell at different Pt coverage. Furthermore, by studying the added incoherent-scattering effect on a known distribution, namely, Ti sublattice in $SrTiO_3$ substrate, XSW can be used to estimate the effect of the same effect on the unknown Pt distribution. Therefore, we extend the studies from perfect single crystal to imperfect crystal substrates.

Since X-ray is nondestructive for catalysts and has weak interaction with materials, XSW is demonstrated to be an excellent *in situ* technique to study catalysts' surface dynamics induced by redox-reaction, as shown in WO_X/α-Fe_2O_3(0001) and VO_X/α-TiO_2(110) case. By combining

XPS and XAFS, atomic-models can be proposed to explain in details how these catalysts respond to reactions. With help from DFT calculations, a direct comparison between XSW density maps and DFT models can be used to identify the most possible catalysts' distribution. DFT calculations can also propose the oxygen configuration and bonding geometries, which cannot be detected by XSW.

Besides XSW, GISAXS is another powerful tool to study uncorrelated nanoparticles catalysts distributed on oxides surfaces. As shown in ALD grown Pt nanoparticles on $SrTiO_3(001)$ surfaces, GISAXS is used not only to determine the Pt nanoparticles size and shapes before and after thermal treatment, but also to detect Pt nanocrystal morphologies. These interesting observations are confirmed by AFM and SEM complementary studies.

Although XSW and GISAXS are very useful for studying correlated and uncorrelated catalysts on single crystal substrates, it is difficult to study powder supported catalysts, which have wider application in industrial. Therefore, XAFS is applied to *in situ* study vanadia supported on hematite powders, as demonstrated in the last chapter. Atomic models besides XAFS are proposed to explain reaction-induced structure and chemical state changes.

Overall, in this thesis, we show how to study catalysts' structure and chemical state information by combining several *in situ* and *ex situ* methods. XSW and GISAXS are very powerful to study catalysts supported on single crystals, while XAFS is suitable to study powder supported catalysts. With combination of XPS, AFM and SEM, comprehensive information can be obtained to show how catalysts respond to reaction chemically and structurally.

9.2 Outlook

9.2.1 Chemical- and Element-Specific in situ Methods for Oxides Supported Catalysts Studies

Although our XSW-XPS is powerful to study cations' dynamics during reactions, we cannot obtain structural information from low Z element, such as O. Furthermore, our current XSW method, which monitors the element-specific XRF signal while scanning through a Bragg reflection, is not capable in distinguishing separate maps for a cation with multiple chemical states. For example, in ¾ ML $VO_X/\alpha\text{-}TiO_2(110)$, XPS shows V^{3+} and V^{5+} coexist in the reduced condition, but XRF cannot distinguish the two kinds of V. Therefore, a new characterization strategy needs to be developed for future advanced studies, namely chemical- and element-specific *in situ* method.

The solution can be the normal incident XSW, which replaces the X-ray fluorescence detector by a XPS hemisphere analyzer. Both chemical states and structures of any element, in principle, can be *in situ* monitored by this technique. Normal incident XSW scan in energy instead of angular range like the XSW in our case. This can be used to study imperfect crystal substrates. Currently National Synchrotron Light Source (NSLS) and European Synchrotron Radiation Facility (ESRF) have the proper instrument for normal incident XSW experiment. At APS the X-ray Interfacial Science (XIS) facility is under construction, which combines MBE growth chamber, *in situ* XSW and XPS hemisphere analyzer. Chemical- and element-specific *in situ* XSW-XPS can be carried out.

9.2.2 Chemical- and Element-Specific in situ Studies for Powder Supported Catalysts

This thesis mainly discusses catalysts supported on single crystals. However, in industrials, the most used catalysts are powders, which cannot be studied by XSW. To extend the model catalysis study, *in situ* studies of catalysts supported on powder supported catalysts are necessary. Using X-ray absorption spectroscopy (XAS) to *in situ* study such catalysts is a future direction. XAS can provide both chemical- and element-specific information. For example, X-ray Absorption Near Edge Structure (XANES) gives chemical state information and Extended X-ray Absorption Fine Structure (EXAFS) gives local structure and binding coordination information of a certain element.

Using XAS to study powder materials is not new. But for the current catalysts study, if catalytic property tests can be combined with *in situ* XAS study of such catalysts, a structure-reactivity/selectivity/activity property will be obtained. This will provide a tremendous impact on catalysis community.

Reference:

[1] B. M. Weckhuysen, and D. E. Keller, Catalysis Today **78**, 25 (2003).

[2] V. E. Henrich, and P. A. Cox, *The Surface Science of Metal Oxides* (Cambridge University Press, 1996).

[3] Q. G. Wang, and R. J. Madix, Surface Science **496**, 51 (2002).

[4] G. S. Wong, M. R. Concepcion, and J. M. Vohs, Surface Science **526**, 211 (2003).

[5] G. C. Bond, and S. F. Tahir, Applied Catalysis **71**, 1 (1991).

[6] N. Magg, J. B. Giorgi, T. Schroeder, M. Baumer, and H. J. Freund, Journal of Physical Chemistry B **106**, 8756 (2002).

[7] I. E. Wachs, Catalysis Today **100**, 79 (2005).

[8] C. Y. Kim, A. A. Escuadro, P. C. Stair, and M. J. Bedzyk, Journal of Physical Chemistry C **111**, 1874 (2007).

[9] U. Diebold, Applied Physics a-Materials Science & Processing **76**, 681 (2003).

[10] F. A. Grant, Reviews of Modern Physics **31**, 646 (1959).

[11] U. Diebold, Surface Science Reports **48**, 53 (2003).

[12] G. V. Samsonov, *The Oxide Handbook* (IFI/Plenum Data Corporation, New York, NY, 1982).

[13] B. Hird, R. A. Armstrong, and J. A. Seel, Surface Review and Letters **5**, 309 (1998).

[14] R. E. Tanner, M. R. Castell, and G. A. D. Briggs, Surface Science **413**, 672 (1998).

[15] M. Ramamoorthy, D. Vanderbilt, and R. D. Kingsmith, Physical Review B **49**, 16721 (1994).

[16] D. Vogtenhuber, R. Podloucky, A. Neckel, S. G. Steinemann, and A. J. Freeman, Physical Review B **49**, 2099 (1994).

[17] S. P. Bates, G. Kresse, and M. J. Gillan, Surface Science **385**, 386 (1997).

[18] P. K. Schelling, N. Yu, and J. W. Halley, Physical Review B **58**, 1279 (1998).

[19] G. Charlton, P. B. Howes, C. L. Nicklin, P. Steadman, J. S. G. Taylor, C. A. Muryn, . . . G. Thornton, Physical Review Letters **78**, 495 (1997).

[20] E. Asari, T. Suzuki, H. Kawanowa, J. Ahn, W. Hayami, T. Aizawa, and R. Souda, Physical Review B **61**, 5679 (2000).

[21] C. Y. Kim, J. W. Elam, M. J. Pellin, D. K. Goswami, S. T. Christensen, M. C. Hersam, . . . M. J. Bedzyk, Journal of Physical Chemistry B **110**, 12616 (2006).

[22] S. Agnoli, C. Castellarin-Cudia, M. Sambi, S. Surnev, M. G. Ramsey, G. Granozzi, and F. P. Netzer, Surface Science **546**, 117 (2003).

[23] Z. Zhang, in *Materials Science and Engineering* (Northwestern University, Evanston, 2004), p. 282.

[24] J. Biener, J. Wang, and R. J. Madix, Surface Science **442**, 47 (1999).

[25] G. L. Haller, and D. E. Resasco, Adv Catal **36**, 173 (1989).

[26] J. Biener, M. Baumer, and R. J. Madix, Surface Science **432**, 178 (1999).

[27] Z. M. Zhang, and V. E. Henrich, Surface Science **277**, 263 (1992).

[28] M. Sambi, G. Sangiovanni, G. Granozzi, and F. Parmigiani, Physical Review B **54**, 13464 (1996).

[29] M. Sambi, G. Sangiovanni, G. Granozzi, and F. Parmigiani, Physical Review B **55**, 7850 (1997).

[30] M. Sambi, M. Della Negra, and G. Granozzi, Thin Solid Films **400**, 26 (2001).

[31] H. T. Dinh, J. Kuever, M. Mussmann, A. W. Hassel, M. Stratmann, and F. Widdel, Nature **427**, 829 (2004).

[32] P. Kuiper, B. G. Searle, P. Rudolf, L. H. Tjeng, and C. T. Chen, Physical Review Letters **70**, 1549 (1993).

[33] R. Pentcheva, F. Wendler, H. L. Meyerheim, W. Moritz, N. Jedrecy, and M. Scheffler, Physical Review Letters **94** (2005).

[34] Z. Zhang, and S. Satpathy, Physical Review B **44**, 13319 (1991).

[35] A. A. Escuadro, in *Materials Science and Engineering* (Northwestern University, Evanston, 2005), p. 215.

[36] X. G. Wang, W. Weiss, S. K. Shaikhutdinov, M. Ritter, M. Petersen, F. Wagner, . . . M. Scheffler, Physical Review Letters **81**, 1038 (1998).

[37] M. Ivanovskaya, D. Kotsikau, G. Faglia, P. Nelli, and S. Irkaev, Sensor Actuat B-Chem **93**, 422 (2003).

[38] T. Kendelewicz, P. Liu, C. S. Doyle, G. E. Brown, E. J. Nelson, and S. A. Chambers, Surface Science **424**, 219 (1999).

[39] B. V. Reddy, and S. N. Khanna, Physical Review Letters **83**, 3170 (1999).

[40] C. Frandsen, and S. Morup, Physical Review Letters **94** (2005).

[41] R. M. Cornell, and U. Schwertmann, *The iron oxides: structure, properties, reactions, occurrences, and uses.* (Weinheim: Wiley-VCH, 2003).

[42] A. Barbier, A. Stierle, N. Kasper, M. J. Guittet, and J. Jupille, Physical Review B **75** (2007).

[43] W. Bergermayer, H. Schweiger, and E. Wimmer, Physical Review B **69** (2004).

[44] A. Rohrbach, J. Hafner, and G. Kresse, Physical Review B **70** (2004).

[45] R. L. Kurtz, and V. E. Henrich, Surface Science **129**, 345 (1983).

[46] R. J. Lad, and V. E. Henrich, Surface Science **193**, 81 (1988).

[47] M. Pollak, M. Gautier, N. Thromat, S. Gota, W. C. Mackrodt, and V. R. Saunders, Nuclear Instruments & Methods in Physics Research Section B-Beam Interactions with Materials and Atoms **97**, 383 (1995).

[48] N. G. Condon, F. M. Leibsle, A. R. Lennie, P. W. Murray, T. M. Parker, D. J. Vaughan, and G. Thornton, Surface Science **397**, 278 (1998).

[49] N. G. Condon, F. M. Leibsle, A. R. Lennie, P. W. Murray, D. J. Vaughan, and G. Thornton, Physical Review Letters **75**, 1961 (1995).

[50] C. Y. Kim, A. A. Escuadro, M. J. Bedzyk, L. Liu, and P. C. Stair, Surface Science **572**, 239 (2004).

[51] F. Alvarez-Ramirez, J. M. Martinez-Magadan, J. R. B. Gomes, and F. Illas, Surface Science **558**, 4 (2004).

[52] S. K. Shaikhutdinov, and W. Weiss, Surface Science **432**, L627 (1999).

[53] S. A. Chambers, and S. I. Yi, Surface Science **439**, L785 (1999).

[54] S. Thevuthasan, Y. J. Kim, S. I. Yi, S. A. Chambers, J. Morais, R. Denecke, . . . G. E. Brown, Surface Science **425**, 276 (1999).

[55] M. D. Pashley, Physical Review B **40**, 10481 (1989).

[56] O. Warschkow, D. E. Ellis, J. H. Hwang, N. Mansourian-Hadavi, and T. O. Mason, J Am Ceram Soc **85**, 213 (2002).

[57] P. J. Dunn, G. Y. Chao, M. Fleischer, J. A. Ferraiolo, R. H. Langley, A. Pabst, and J. A. Zilczer, American Mineralogist **70**, 214 (1985).

[58] L. Merker, and L. E. Lynd, edited by U. S. P. Office1953).

[59] N. Erdman, K. R. Poeppelmeier, M. Asta, O. Warschkow, D. E. Ellis, and L. D. Marks, Nature **419**, 55 (2002).

[60] R. Herger, P. R. Willmott, O. Bunk, C. M. Schlepuetz, B. D. Patterson, and B. Delley, Physical Review Letters **98**, 076102 (2007).

[61] N. Erdman, O. Warschkow, M. Asta, K. R. Poeppelmeier, D. E. Ellis, and L. D. Marks, Journal of the American Chemical Society **125**, 10050 (2003).

[62] Q. D. Jiang, and J. Zegenhagen, Surface Science **425**, 343 (1999).

[63] T. Kubo, and H. Nozoye, Physical Review Letters **86**, 1801 (2001).

[64] M. Naito, and H. Sato, Physica C **229**, 1 (1994).

[65] S. T. Christensen, B. Lee, Z. Feng, M. C. Hersam, and M. J. Bedzyk, Applied Surface Science **256**, 423 (2009).

[66] F. Silly, D. T. Newell, and M. R. Castell, Surface Science **600**, L219 (2006).

[67] M. Kawasaki, K. Takahashi, T. Maeda, R. Tsuchiya, M. Shinohara, O. Ishiyama, . . . H. Koinuma, Science **266**, 1540 (1994).

[68] M. Yoshimoto, T. Maeda, K. Shimozono, H. Koinuma, M. Shinohara, O. Ishiyama, and F. Ohtani, Applied Physics Letters **65**, 3197 (1994).

[69] O. Ishiyama, T. Nishihara, S. Hayashi, M. Shinohara, M. Yoshimoto, T. Ohnishi, . . . J. Saraie, Applied Surface Science **121**, 163 (1997).

[70] T. Nishimura, A. Ikeda, H. Namba, T. Morishita, and Y. Kido, Surface Science **421**, 273 (1999).

[71] N. Erdman, and L. D. Marks, Surface Science **526**, 107 (2003).

[72] M. R. Castell, Surface Science **505**, 1 (2002).

[73] R. G. Carr, and G. A. Somorjai, Nature **290**, 576 (1981).

[74] J. H. Lee, L. Fang, E. Vlahos, X. L. Ke, Y. W. Jung, L. F. Kourkoutis, . . . D. G. Schlom, Nature **466**, 954 (2010).

[75] J. P. Lafemina, Critical Reviews in Surface Chemistry **3** (1994).

[76] N. Barberan, P. W. Tasker, and A. M. Stoneham, J Phys C Solid State **12**, 3827 (1979).

[77] P. Zschack, in *Materials Science and Engineering* (Northwestern University, Evanston, 1989).

[78] J. A. Enterkin, K. R. Poeppelmeier, and L. D. Marks, Nano Lett **11**, 993 (2011).

[79] M. Li, W. Hebenstreit, L. Gross, U. Diebold, M. A. Henderson, D. R. Jennison, . . . M. P. Sears, Surface Science **437**, 173 (1999).

[80] C. Y. Kim, M. J. Bedzyk, E. J. Nelson, J. C. Woicik, and L. E. Berman, Physical Review B **66** (2002).

[81] Z. Feng, C.-Y. Kim, J. W. Elam, Q. Ma, Z. Zhang, and M. Bedzyk, Journal of the American Chemical Society **131**, 18200 (2009).

[82] G. Koster, G. Rijnders, D. H. A. Blank, and H. Rogalla, Physica C **339**, 215 (2000).

[83] S. T. Christensen, J. W. Elam, B. Lee, Z. Feng, M. J. Bedzyk, and M. C. Hersam, Chemistry of Materials **21**, 516 (2009).

[84] B. C. Gates, Chemical Reviews **95**, 511 (1995).

[85] B. M. Weckhuysen, P. Van Der Voort, and G. Gatana, *Spectroscopy of Transition Metal Ions on Surfaces* (Leuven University Press, 2000).

[86] J. Banas, M. Najbar, and V. Tomasic, Catalysis Today **137**, 267 (2008).

[87] C. Schmitt, L. Giebeler, R. Schierholz, S. Endres, C. Fasel, H. Vogel, and H. Fuess, Z. Phys. Chem. **221**, 1525 (2007).

[88] O. Dulub, W. Hebenstreit, and U. Diebold, Physical Review Letters **84**, 3646 (2000).

[89] S. J. Tauster, S. C. Fung, and R. L. Garten, Journal of the American Chemical Society **100**, 170 (1978).

[90] M. Kitano, and M. Hara, Journal of Materials Chemistry **20**, 627 (2010).

[91] A. Kudo, and Y. Miseki, Chemical Society Reviews **38**, 253 (2009).

[92] S. Royer, and D. Duprez, Chemcatchem **3**, 24 (2011).

[93] A. J. Francis, Y. Cao, and P. A. Salvador, Thin Solid Films **496**, 317 (2006).

[94] A. J. Francis, and P. A. Salvador, Journal of Materials Research **22**, 89 (2006).

[95] D. Aurongzeb, Journal of Applied Physics **102** (2007).

[96] A. D. Polli, T. Wagner, T. Gemming, and M. Ruhle, Surface Science **448**, 279 (2000).

[97] J. Son, J. Cagnon, and S. Stemmer, Journal of Applied Physics **106**, 043525 (2009).

[98] F. Pesty, H. P. Steinruck, and T. E. Madey, Surface Science **339**, 83 (1995).

[99] R. J. H. Clark, *The Chemistry of Titanium and Vanadium* (Elsevier, Amsterdam, 1968).

[100] F. A. Cotton, and G. Wilkinson, *Advanced Inorganic Chemistry* (John Wiley & Sons Inc; , 1988), p. 1488.

[101] N. N. Greenwood, and A. Earnshaw, *Chemistry of the Elements* (Pergamon Press, Oxford, 1984).

[102] B. GrzybowskaSwierkosz, and F. Trifiro, Applied Catalysis a-General **157**, 1 (1997).

[103] C. N. Satterfield, *Heterogeneous Catalysis in Practice* (McGraw-Hill, New York, 1980).

[104] B. M. Weckhuysen, and I. E. Wachs, in *Handbook of Surfaces and Interfaces of Materials*, edited by H. S. Nalwa (Academic Press, San Diego, 2001).

[105] I. E. Wachs, and B. M. Weckhuysen, Applied Catalysis a-General **157**, 67 (1997).

[106] E. Harlin, (Helsinki University of Technology, Helsinki, 2001).

[107] G. Deo, and I. E. Wachs, Journal of Catalysis **146**, 323 (1994).

[108] E. Salje, Acta Crystallogr B **33**, 574 (1977).

[109] S. L. Soled, G. B. Mcvicker, L. L. Murrell, L. G. Sherman, N. C. Dispenziere, S. L. Hsu, and D. Waldman, Journal of Catalysis **111**, 286 (1988).

[110] E. Salje, and K. Viswanathan, Acta Crystallogr A **A 31**, 356 (1975).

[111] S. Tanisaki, Journal of the Physical Society of Japan **15**, 566 (1960).

[112] R. Diehl, G. Brandt, and E. Salje, Acta Crystallogr B **34**, 1105 (1978).

[113] E. Ogata, K. Y., and N. Ohta, Journal of Catalysis **29**, 296 (1979).

[114] H. Hattori, N. Asada, and K. Tanabe, Bulletin of the Chemical Society of Japan **51**, 1704 (1978).

[115] B. H. Davis, Journal of Catalysis **55**, 158 (1978).

[116] K. Shibata, T. Kiyoura, J. Kitagawa, T. Sumiyoshi, and K. Tanabe, Bulletin of the Chemical Society of Japan **46**, 408 (1973).

[117] W. Suarez, J. A. Dumesic, and C. G. Hill, Journal of Catalysis **94**, 408 (1985).

[118] K. Segawa, and W. K. Hall, Journal of Catalysis **76**, 133 (1982).

[119] T. Yamaguchi, Y. Tanaka, and K. Tanabe, Journal of Catalysis **65**, 442 (1980).

[120] H. Bosch, and F. Janssen, Catalysis Today **2**, 369 (1988).

[121] P. Forzatti, and L. Lietti, Heterogen Chem Rev **3**, 33 (1996).

[122] G. Busca, L. Lietti, G. Ramis, and F. Berti, Applied Catalysis B-Environmental **18**, 1 (1998).

[123] J. G. Cohn, D. R. Steele, and H. C. Andersen, USA, 1961).

[124] J. Banas, V. Tomasic, A. Weselucha-Birczynska, and M. Najbar, Catalysis Today **119**, 199 (2007).

[125] S. C. Wood, Chemical Engineering Progress **90**, 47 (1994).

[126] O. Bondarchuk, X. Huang, J. Kim, B. D. Kay, L. S. Wang, J. M. White, and Z. Dohnalek, Angewandte Chemie-International Edition **45**, 4786 (2006).

[127] Y. K. Kim, R. Rousseau, B. D. Kay, J. M. White, and Z. Dohnalek, Journal of the American Chemical Society **130**, 5059 (2008).

[128] C. D. Baertsch, K. T. Komala, Y. H. Chua, and E. Iglesia, Journal of Catalysis **205**, 44 (2002).

[129] K. D. Chen, A. T. Bell, and E. Iglesia, Journal of Catalysis **209**, 35 (2002).

[130] S. M. George, A. W. Ott, and J. W. Klaus, Journal of Physical Chemistry **100**, 13121 (1996).

[131] M. Ritala, Applied Surface Science **112**, 223 (1997).

[132] T. Suntola, Thin Solid Films **216**, 84 (1992).

[133] J. S. King, A. Wittstock, J. Biener, S. O. Kucheyev, Y. M. Wang, T. F. Baumann, . . . S. F. Bent, Nano Lett **8**, 2405 (2008).

[134] J. W. Elam, J. A. Libera, M. J. Pellin, A. V. Zinovev, J. P. Greene, and J. A. Nolen, Applied Physics Letters **89** (2006).

[135] A. Johansson, J. Lu, J. O. Carlsson, and M. Boman, Journal of Applied Physics **96**, 5189 (2004).

[136] A. W. Ott, J. W. Klaus, J. M. Johnson, and S. M. George, Thin Solid Films **292**, 135 (1997).

[137] T. Aaltonen, M. Ritala, T. Sajavaara, J. Keinonen, and M. Leskela, Chemistry of Materials **15**, 1924 (2003).

[138] T. Aaltonen, M. Ritala, Y. L. Tung, Y. Chi, K. Arstila, K. Meinander, and M. Leskela, Journal of Materials Research **19**, 3353 (2004).

[139] Y. Zhu, K. A. Dunn, and A. E. Kaloyeros, Journal of Materials Research **22**, 1292 (2007).

[140] J. W. Elam, A. Zinovev, C. Y. Han, H. H. Wang, U. Welp, J. N. Hryn, and M. J. Pellin, Thin Solid Films **515**, 1664 (2006).

[141] J. Keranen, A. Auroux, S. Ek, and L. Niinisto, Applied Catalysis a-General **228**, 213 (2002).

[142] J. A. Enterkin, W. Setthapun, J. W. Elam, S. T. Christensen, F. A. Rabuffetti, L. D. Marks, . . . C. L. Marshall, Acs Catal **1**, 629 (2011).

[143] B. D. Cullity, *Elements of X-ray Diffraction* (Prentice Hall, 2001).

[144] B. E. Warren, *X-ray Diffraction* (Dover Publications, 1990).

[145] L. H. Schwartz, and J. B. Cohen, *Diffraction from Materials* (Springer-Verlag, Berlin; New York, 1987).

[146] R. W. James, *The Optical Principle of the Diffraction of X-rays* (Ox Bow Press, Woodbridge, Connecticut, 1982).

[147] R. Feidenhans'L, Surface Science Reports **10**, 105 (1989).

[148] I. K. Robinson, in *Handbook on Synchrotron Radiation*, edited by G. Brown, and D. E. Moncton (Elsevier Science Publishers B. V., North Holland, 1991).

[149] D. M. Mills, *Third-Generation Hard X-Ray Synchrotron Radiation Sources: Source Properties, Optics, and Experimental Techniques* (Wiley-Interscience, 2002), p. 406.

[150] B. W. Batterman, Physical Review Letters **22**, 703 (1969).

[151] J. A. Golovchenko, J. R. Patel, D. R. Kaplan, P. L. Cowan, and M. J. Bedzyk, Physical Review Letters **49**, 560 (1982).

[152] J. Zegenhagen, Surface Science Reports **18**, 199 (1993).

[153] M. J. Bedzyk, and L. Cheng, Reviews in Mineralogy and Geochemistry **49**, 221 (2002).

[154] P. L. Cowan, S. Brennan, T. Jach, M. J. Bedzyk, and G. Materlik, Physical Review Letters **57**, 2399 (1986).

[155] M. J. Bedzyk, and G. Materlik, Physical Review B **32**, 6456 (1985).

[156] L. Cheng, P. Fenter, M. J. Bedzyk, and N. C. Sturchio, Physical Review Letters **90**, 255503 (2003).

[157] Z. Feng, L. Chen, C.-Y. Kim, Z. Zhang, J. W. Elam, L. A. Curtiss, . . . M. J. Bedzyk, unpublished (2011).

[158] M. J. Bedzyk, in *Encyclopedia of Condensed Matter Physics*, edited by F. Bassani, G. J. Liedl, and P. Wyder (Elsevier, Oxford, 2005), pp. 330.

[159] C. Y. Kim, J. A. Klug, P. C. Stair, and M. J. Bedzyk, Journal of Physical Chemistry C **113**, 1406 (2009).

[160] C. Y. Song, R. Bergstrom, D. Ramunno-Johnson, H. D. Jiang, D. Paterson, M. D. de Jonge, . . . J. W. Miao, Physical Review Letters **100**, 025504 (2008).

[161] *See Wikipedia webpage:* http://en.wikipedia.org/wiki/X-ray_photoelectron_spectroscopy.

[162] D. J. O'connor, B. A. Sexton, and R. S. C. Smart, *Surface Analysis Method in Materials Science* (Springer-Verlag, Heidelberg, 1992).

[163] E. A. Stern, in *X-ray Absorption-Principles, Applications, Techniques of EXAFS, SEXAFS and XANES*, edited by D. C. Koningsberger, and R. Prins (Wiley-Interscience, New York, 1988).

[164] J. J. Rehr, and R. C. Albers, Reviews of Modern Physics **72**, 621 (2000).

[165] D. E. Proffit, D. B. Buchholz, R. P. H. Chang, M. J. Bedzyk, T. O. Mason, and Q. Ma, Journal of Applied Physics **106** (2009).

[166] D. Marasco, in *Materials Science and Engineering* (Northwestern University, Evanston, 2002), p. 144.

[167] D. A. Walko, O. Sakata, P. F. Lyman, T.-L. Lee, B. P. Tinkham, J. S. Okasinski, . . . M. J. Bedzyk, in Synchrotron Radiation Instrumentation: Eighth International Conference, edited by T. Warwick, J. Arthur, H. A. Padmore, and J. Stohr (American Insititute of Physics, New York, 2004), pp. 1166.

[168] M. J. Bogan, W. H. Benner, S. Boutet, U. Rohner, M. Frank, A. Barty, . . . H. N. Chapman, Nano Lett **8**, 310 (2008).

[169] S. Ikeda, K. Hirao, S. Ishino, M. Matsumura, and B. Ohtani, Catalysis Today **117**, 343 (2006).

[170] O. Rosseler, M. V. Shankar, M. K. L. Du, L. Schmidlin, N. Keller, and V. Keller, Journal of Catalysis **269**, 179 (2010).

[171] T. Menke, R. Dittmann, P. Meuffels, K. Szot, and R. Waser, J Appl Phys **106** (2009).

[172] S. T. Christensen, B. Lee, Z. X. Feng, M. C. Hersam, and M. J. Bedzyk, Applied Surface Science **256**, 423 (2009).

[173] D. P. Woodruff, Reports on Progress in Physics **68**, 743 (2005).

[174] L. Cheng, P. Fenter, M. J. Bedzyk, and N. C. Sturchio, Physical Review Letters **90** (2003).

[175] P. L. Cowan, S. Brennan, T. Jach, M. J. Bedzyk, and G. Materlik, Physical Review Letters **57**, 2399 (1986).

[176] R. Herger, P. R. Willmott, O. Bunk, C. M. Schlepuetz, B. D. Patterson, and B. Delley, Phys Rev Lett **98** (2007).

[177] O. Warschkow, M. Asta, N. Erdman, K. R. Poeppelmeier, D. E. Ellis, and L. D. Marks, Surface Science **573**, 446 (2004).

[178] K. Johnston, M. R. Castell, A. T. Paxton, and M. W. Finnis, Phys Rev B **70** (2004).

[179] A. Asthagiri, and D. S. Sholl, J Chem Phys **116**, 9914 (2002).

[180] H. Iddir, V. Komanicky, S. Ogut, H. You, and P. Zapol, Journal of Physical Chemistry C **111**, 14782 (2007).

[181] O. Auciello, J. F. Scott, and R. Ramesh, Phys Today **51**, 22 (1998).

[182] A. Mobius, C. N. R. Rao, A. Schofield, D. M. Edwards, A. S. Alexandrov, and J. E. Enderby, Philos T Roy Soc A **356**, 38 (1998).

[183] A. K. Tagantsev, V. O. Sherman, K. F. Astafiev, J. Venkatesh, and N. Setter, J Electroceram **11**, 5 (2003).

[184] T. Matsumoto, H. Tanaka, T. Kawai, and S. Kawai, Surface Science **278**, L153 (1992).

[185] M. M. Nowell, and D. P. Field, in Materials Reliability in Microelectronics VIII, edited by J. Bravman, T. Marieb, J. R. Lloyd, and M. A. Korhonen (Materials Research Society Symposium Proceedings, Warrendale, PA, 1998), pp. 115.

[186] G. S. Was, D. J. Srolovitz, and D. Liang, in Structure and Morphology, edited by S. Moss, D. Ila, R. C. Cammarata, E. H. Chason, T. L. Einstein, and E. D. Williams (Materials Research Society Symposium Proceedings, Warrendale, PA, 1997), pp. 311.

[187] A. Gungor, K. Barmak, A. D. Rollett, C. Cabral, and J. M. E. Harper, J Vac Sci Technol B **20**, 2314 (2002).

[188] J. Son, J. Cagnon, and S. Stemmer, J Appl Phys **106** (2009).

[189] V. Komanicky, K. C. Chang, A. Menzel, D. Hennessy, G. Karapetrov, and H. D. You, P Soc Photo-Opt Ins **6340**, U278 (2006).

[190] V. Komanicky, A. Menzel, K. C. Chang, and H. You, Journal of Physical Chemistry B **109**, 23543 (2005).

[191] S. T. Christensen, J. W. Elam, F. A. Rabuffetti, Q. Ma, S. J. Weigand, B. Lee, . . . M. J. Bedzyk, Small **5**, 750 (2009).

[192] J. W. Elam, M. D. Groner, and S. M. George, Review of Scientific Instruments **73**, 2981 (2002).

[193] A. Nelson, Journal of Applied Crystallography **39**, 273 (2006).

[194] J. A. Venables, *Introduction to surface and thin film processes* (Cambridge University Press, 2000).

[195] J. H. Van der Merwe, Interface Science **1**, 77 (1993).

[196] J. A. Enterkin, K. R. Poeppelmeier, and L. D. Marks, Nano Letters **in press** (2011).

[197] R. Lazzari, Journal of Applied Crystallography **35**, 406 (2002).

[198] K. Jacobi, M. Gruyters, P. Geng, T. Bitzer, M. Aggour, S. Rauscher, and H. J. Lewerenz, Physical Review B **51**, 5437 (1995).

[199] J. S. Pedersen, Journal of Applied Crystallography **27**, 595 (1994).

[200] C. Gatel, P. Baules, and E. Snoeck, Journal of Crystal Growth **252**, 424 (2003).

[201] T. Wagner, G. Richter, and M. Ruhle, Journal of Applied Physics **89**, 2606 (2001).

[202] N. A. Gjostein, in *Surfaces and Interfaces*, edited by J. J. Burke, N. L. Reed, and V. Weiss (Syracuse University Press, Syracuse, NY, 1976), pp. 271.

[203] C. L. Liu, J. M. Cohen, J. B. Adams, and A. F. Voter, Surface Science **253**, 334 (1991).

[204] L. Vitos, A. V. Ruban, H. L. Skriver, and J. Kollar, Surface Science **411**, 186 (1998).

[205] X. F. Lai, and D. W. Goodman, J Mol Catal a-Chem **162**, 33 (2000).

[206] C. E. J. Mitchell, A. Howard, M. Carney, and R. G. Egdell, Surface Science **490**, 196 (2001).

[207] D. E. Starr, S. K. Shaikhutdinov, and H. J. Freund, Topics in Catalysis **36**, 33 (2005).

[208] A. J. Francis, C. G. Roberts, Y. Cao, A. D. Rollett, and P. A. Salvador, Acta Mater **55**, 6159 (2007).

[209] C. P. Flynn, Physical Review B **73** (2006).

[210] G. Prevot, and B. Croset, Physical Review B **74** (2006).

[211] A. Asthagiri, and D. S. Sholl, Physical Review B **73** (2006).

[212] A. Marmier, and S. C. Parker, Physical Review B **69** (2004).

[213] J. N. Fiedor, A. Proctor, M. Houalla, and D. M. Hercules, Surf Interface Anal **23**, 204 (1995).

[214] R. L. Blake, Hessevic.Re, T. Zoltai, and L. W. Finger, American Mineralogist **51**, 123 (1966).

[215] S. Yamazoe, Y. Hitomi, T. Shishido, and T. Tanaka, Journal of Physical Chemistry C **112**, 6869 (2008).

[216] C. Lemire, S. Bertarione, A. Zecchina, D. Scarano, A. Chaka, S. Shaikhutdinov, and H. J. Freund, Physical Review Letters **94** (2005).

[217] G. C. Bond, Applied Catalysis a-General **157**, 91 (1997).

[218] J. Haber, and P. Nowak, Catalysis Letters **27**, 369 (1994).

[219] S. Surnev, M. G. Ramsey, and F. P. Netzer, Progress in Surface Science **73**, 117 (2003).

[220] G. Silversmit, D. Depla, H. Poelman, G. B. Marin, and R. De Gryse, Journal of Electron Spectroscopy and Related Phenomena **135**, 167 (2004).

[221] N. R. Shiju, M. Anilkumar, S. P. Mirajkar, C. S. Gopinath, B. S. Rao, and C. V. Satyanarayana, Journal of Catalysis **230**, 484 (2005).

[222] M. M. Koranne, J. G. Goodwin, and G. Marcelin, Journal of Catalysis **148**, 369 (1994).

[223] E. A. Kroger, F. Allegretti, M. J. Knight, M. Polcik, D. I. Sayago, D. P. Woodruff, and V. R. Dhanak, Surface Science **600**, 4813 (2006).

[224] M. Bedzyk, and G. Materlik, Surface Science **152**, 10 (1985).

[225] J. P. Perdew, J. A. Chevary, S. H. Vosko, K. A. Jackson, M. R. Pederson, D. J. Singh, and C. Fiolhais, Physical Review B **46**, 6671 (1992).

[226] G. Kresse, and J. Hafner, Physical Review B **47**, 558 (1993).

[227] G. Kresse, and J. Hafner, Physical Review B **49**, 14251 (1994).

[228] P. E. Blochl, Physical Review B **50**, 17953 (1994).

[229] G. Kresse, and D. Joubert, Physical Review B **59**, 1758 (1999).

[230] H. J. Monkhorst, and J. D. Pack, Physical Review B **13**, 5188 (1976).

[231] K. Senthil, and K. Yong, Nanotechnology **18** (2007).

[232] C. Y. Kim, J. W. Elam, P. C. Stair, and M. J. Bedzyk, Journal of Physical Chemistry C **114**, 19723 (2010).

[233] Z. Zhang, P. Fenter, L. Cheng, N. C. Sturchio, M. J. Bedzyk, M. L. Machesky, and D. J. Wesolowski, Surface Science **554**, L95 (2004).

[234] J. S. Okasinski, C. Kim, D. A. Walko, and M. J. Bedzyk, Physical Review B **69** (2004).

[235] D. P. Debecker, F. Bertinchamps, N. Blangenois, P. Eloy, and E. M. Gaigneaux, Applied Catalysis B-Environmental **74**, 223 (2007).

[236] D. P. Debecker, R. Delaigle, K. Bouchmella, P. Eloy, E. M. Gaigneaux, and P. H. Mutin, Catalysis Today **157**, 125 (2010).

[237] B. W. Lee, H. Cho, and W. Shin, Journal of Ceramic Processing Research **8**, 203 (2007).

[238] F. Bertinchamps, C. Gregoire, and E. M. Gaigneaux, Applied Catalysis B-Environmental **66**, 10 (2006).

[239] L. Cheng, in *Materials Science and Engineering* (Northwestern University, Evanston, 1998), p. 112.

[240] D. Waasmaier, and A. Kirfel, Acta Crystallogr A **51**, 416 (1995).

[241] D. T. Cromer, and D. Liberman, J Chem Phys **53**, 1891 (1970).

[242] D. T. Cromer, and D. A. Liberman, Acta Crystallogr A **37**, 267 (1981).

[243] J. C. Lin, in *Materials Science and Engineering* (Northwestern University, Evanston, 2009), p. 236.

Appendix A: Programs for XSW Data Analysis

A.1 Developments in XSW Analysis Program: SWAM

The core programs for the single crystal XSW data processing is to analyze the rocking curves and the X-ray fluorescence. Originally several Fortran programs were written by M. Bedzyk and J. Zegenhagen in 1984 and then developed further by Likwan Cheng[239] and Anathony Escuadro[35]. The Fortran program “SUGO” is used for data manipulation and later was translated to a Matlab based program “sugomat” by Zhan Zhang. Another important Fortran program, “SWAN”, was translated to a Matlab version, “SWAM”, by Jui-Ching Lin.

In the program SWAM, the atomic scattering factors are calculated analytically using the method presented by Wasmaier and Kirfel[240]. SWAM can also calculate some physical parameters such as Bragg angles, structure factors, and ideal Darwin widths for a given crystal under a chosen dynamical diffraction condition. Most importantly, the program calculates and convolutes the reflectivity curves from an ideal 2-bounce monochromator and a sample and fits the convolution result to the experimental rocking curve data. The result of the reflectivity fit is then used to perform a fit of the theoretical fluorescence yield to the experimental fluorescence yield data in order to obtain the coherent position (P_H), coherent fraction (f_H), and off-Bragg normalized fluorescence yield.

Previous version (version 3) is only capable of handling several limited elements, such as Si, Ti. The calculations of the anomalous scattering coefficients, f' and f'', are based on a tabulated list, which is limited by the energy range from 0 to 40 keV and the data resolution. Here we used a Cromer-Liberman equation[241] to theoretically calculate the anomalous scattering coefficients at any given energy for any element.

A.1.1 Guides to Some Important Routines

(a) *cromermat.m*

cromermat.m is the core routine in the new version of SWAM. The following database is used: (1) *matoele.dat*, which contains each element's atomic number, weight and symbol; (2) *fcoef.dat*, which is to calculate f_0, the non-dispersive part of the atomic scattering factor; (3) *XSECT.dat*, which is the list of the cross section value for each element.

f_0 is a function of the selected element and of $k = \sin\theta/\lambda$, where λ is the photon wavelength and θ is incident angle. f_0 is approximated by a summation of a series of Gaussian functions, $f_0(k) = c + \sum_{i=1}^{5} a_i \exp\left(-b_i k^2\right)$, where c, a_i and b_i are the coefficients tabulated in *fcoef.dat* database. This database can be downloaded freely from the ESRF website: http://ftp.esrf.eu/pub/scisoft/xop2.3/DabaxFiles/f0_WaasKirf.dat

The cross section database, *XSECT.dat*, has a number of orbitals. The first five records of each orbital are the cross section values at energy from about 1 to 80 keV approximately equally spaced in log(energy). The next five records are cross section values at energies selected by Gauss integration scheme if the function type is 0. (The function type is given in Cromer and Liberman[241]) The 11th value is read in for an energy equal to 1.001*(binding energy). If the X-ray energy is less than the binding energy, a function called "sigma3" will be used according to the reference of Cromer and Liberman[242].

The *cromermat.m* routine is used by *AtomS.m* and *calcf.m* to calculate f_0, f' and f'' and then to calculate the structural factor and other parameters.

(b) *AtomS.m*

This routine is used to calculated f_0, *f'* and *f''*. It is isolated from *calcf.m* to be a GUI based, user-friendly routine for a special use. It can calculate the atomic scattering factor for any element, cation or anion. For execution, it has to be placed in a directory containing *cromermat.m*, database files of *maofele.dat*, *fcoef.dat* and *XSECT.dat*. Type "AtomS" in the Matlab command window, and the GUI input panel should guide the user to finish the atomic factor calculation.

A.1.2 Flowchart of the Developed SWAM Program

SWAM is a Matlab based program and is therefore independent of the operating system (Mac, PC, LINUX). Once Matlab is open, simply key in "SWAM" at the command line (when the working folder is at the SWAM program folder) and the program will start. The GUI based panel will guide the user to do data analysis. The detailed instruction can be found in the Appendix of Likwan Cheng's PhD thesis[239]. Both the formats of the input data files, an XRR file and an XRF file, are (X, Y, ΔY) three-column data, separated by 'Tab', after the comments rows (begin with #, the number of comment rows are not limited). The first column is for the angular step number, the second column is for the experimental X-ray reflectivity (XRR) or XRF yield and the third column is the error. The XRR and XRF files can be obtained by cutting the output spreadsheet file from *sugomat*. The three functions in SWAM are: (1) **cr**: Compute the physical parameters for a single crystal dynamical diffraction condition, (2) **r0**: Calculate and fit the rocking curve, and (3) **f1**: Calculate and fit the fluorescence yield. The new computing algorithm for **cr** is shown in the flowcharts in Fig A.1 as an example. The flowcharts for **r0** and **f1** are the same as those in Jui-Ching Lin's PhD thesis[243].

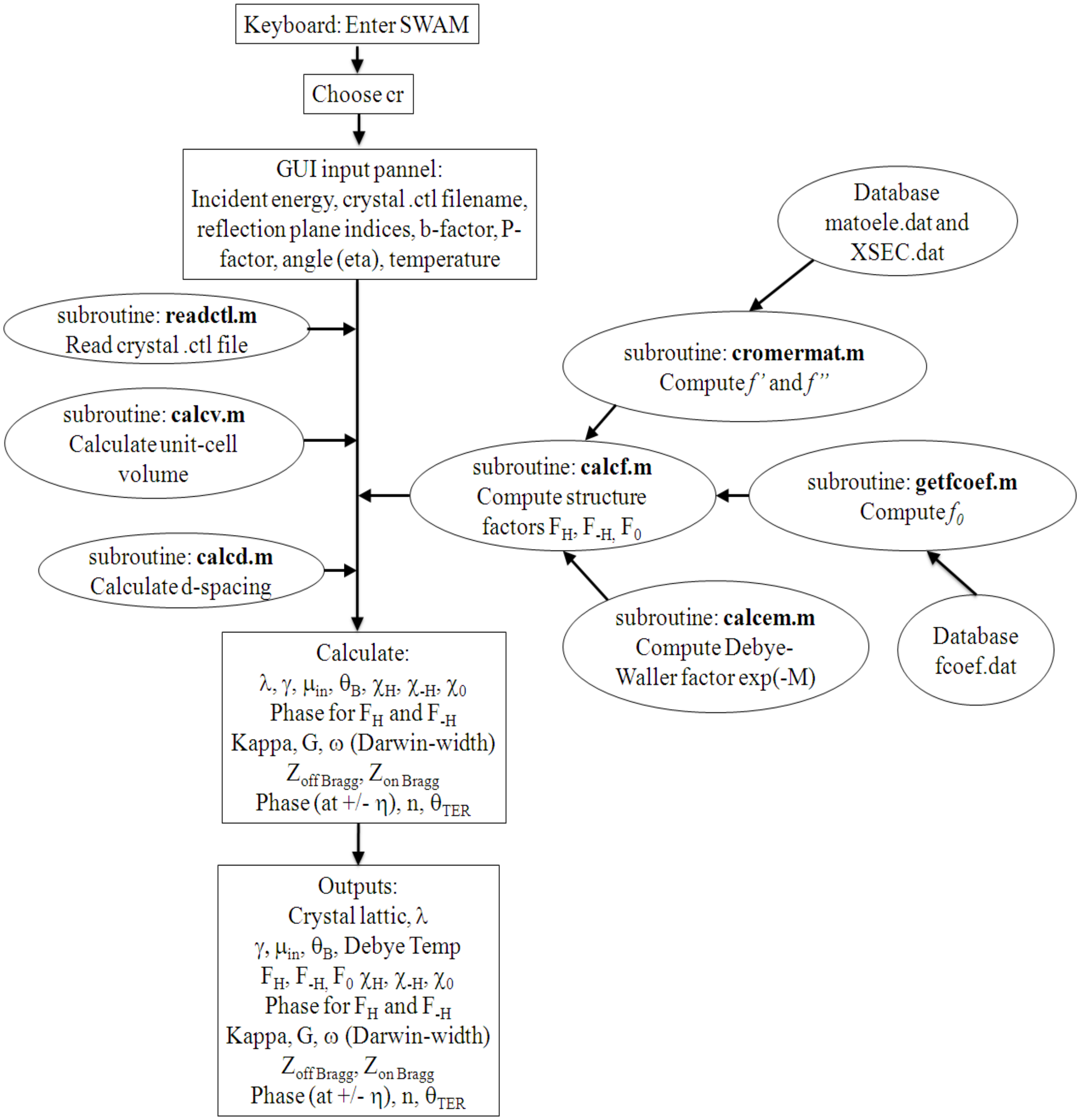

Fig. A1: Flowchart diagram of **cr** showing the algorithm for computing physical parameters for a single crystal under dynamical diffraction condition.

A.2 Using SUGOMAT for XSW Data Processing

The Fortran program SUGO is suitable for many kinds of XSW data processing. However, when working at synchrotron for a quick data analysis, it is not so convenient because one has to type in all information manually. Instead, sugomat can provide a quick data processing, and generate the normalized reflectivity and fluorescence files for obtaining coherent fraction and coherent position using program **f1**. We will first go through a step-by-step data analysis in sugomat, and then we will provide a script for the quick data analysis.

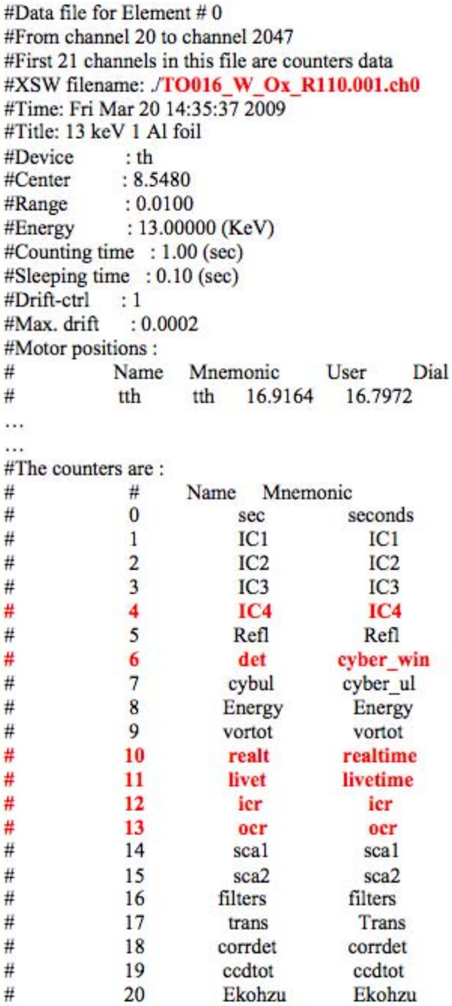

```
#Data file for Element # 0
#From channel 20 to channel 2047
#First 21 channels in this file are counters data
#XSW filename: ./TO016_W_Ox_R110.001.ch0
#Time: Fri Mar 20 14:35:37 2009
#Title: 13 keV 1 Al foil
#Device        : th
#Center        : 8.5480
#Range         : 0.0100
#Energy        : 13.00000 (KeV)
#Counting time   : 1.00 (sec)
#Sleeping time   : 0.10 (sec)
#Drift-ctrl     : 1
#Max. drift     : 0.0002
#Motor positions :
#             Name    Mnemonic       User       Dial
#              tth       tth     16.9164     16.7972
...
...
#The counters are :
#               #       Name    Mnemonic
#               0          sec             seconds
#               1          IC1               IC1
#               2          IC2               IC2
#               3          IC3               IC3
#               4          IC4               IC4
#               5          Refl              Refl
#               6          det             cyber_win
#               7          cybul            cyber_ul
#               8          Energy           Energy
#               9          vortot           vortot
#               10         realt            realtime
#               11         livet            livetime
#               12         icr               icr
#               13         ocr               ocr
#               14         sca1              sca1
#               15         sca2              sca2
#               16         filters          filters
#               17         trans             Trans
#               18         corrdet          corrdet
#               19         ccdtot           ccdtot
#               20         Ekohzu           Ekohzu
```

Fig. A2: A typical XSW data header. The red-marked rows are important data sets for XSW data processing. TO016_W_Ox_R110.001.ch0 is the filename.

Taking the analysis of W signal of the mixed VO_X-WO_X / α-$TiO_2(110)$ as an example, the raw XSW data file named as, “TO016_W_Ox_R110.001.ch0”, is placed in a folder for analysis. Fig. A2 shows the typical XSW data header. **IC4** records the X-ray intensity after the incident slit and is used for normalization. **det** records the reflectivity. The livetime fraction is given by, $ltf = (realt \cdot ocr)/(livet \cdot icr)$, where **ltf** is lifetime fraction, **realt** is real time of X-ray fluorescence counting, **livet** is live time, **icr** is the incoming rate of X-ray fluorescence, and **ocr** is outgoing rate. These values can be read directly from the XSW data file in their respective row. For example, **IC4** is saved in row 5 of the data file.

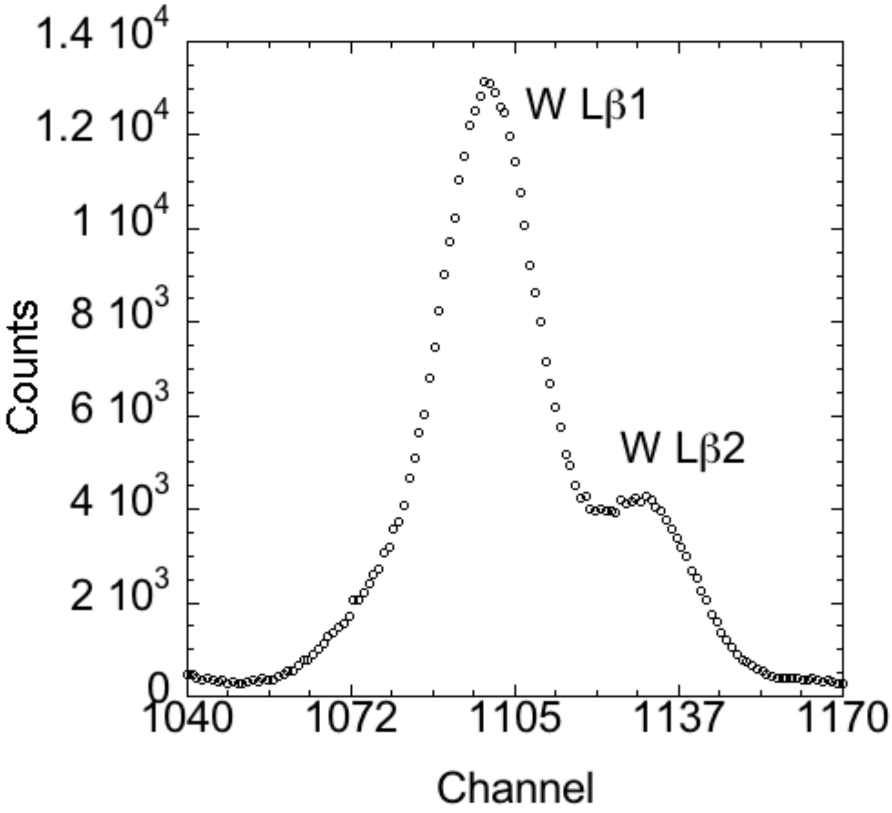

Fig. A3: Tungsten X-ray fluorescence (XRF) data read from energy-dispersive XRF detector

Figure A3 shows the W XRF spectrum read from “TO016_W_Ox_R110.001.ch0”. To extract W Lβ1 signal, we have to choose the proper background regions and fit two Gaussian functions at the same time. After typing “sugomat” in the Matlab command window, a GUI input panel will pop out, as shown in Fig. A4. The detailed use of each option can be found in Likwan Cheng’s PhD thesis[239]. From Figure A3, we can choose the left background region to be (1040, 1049), and the right background region to be (1161, 1170). The W Lβ1 peak position is around 1100, and the W Lβ2 peak position is around 25 channels higher than W Lβ1 peak position. The Full width at half maxima for each peak is around 23. The preliminary Gaussian fit window (after choosing “ad” command in Fig. A4) is shown in Fig. A5 and Fig A6. The user can fill in these initial values for the Gaussian fit. A detailed Gaussian fit by using “ga” has to be carried out after the preliminary Gaussian fit, and the FWHM values and peak positions in Fig. A6 will then have to be fixed, namely, 0 in the fraction steps.

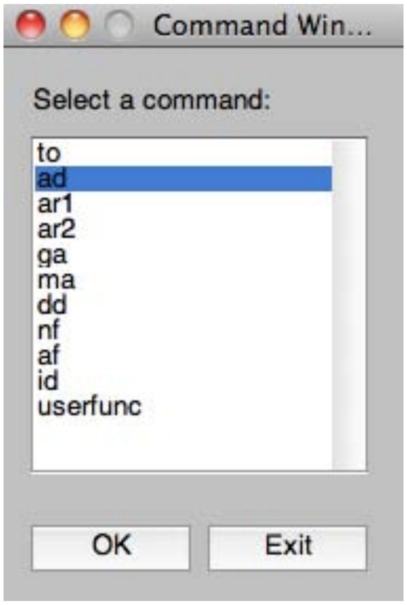

Fig. A4: The command main window of sugomat.

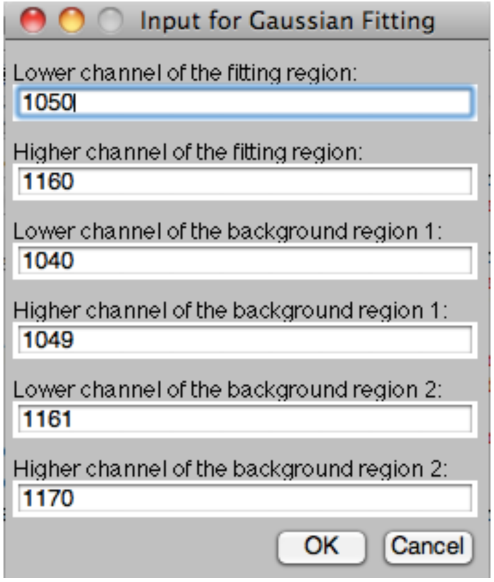

Lower channel of the fitting region: 1050

Higher channel of the fitting region: 1160

Lower channel of the background region 1: 1040

Higher channel of the background region 1: 1049

Lower channel of the background region 2: 1161

Higher channel of the background region 2: 1170

Fig. A5: The GUI panel for background input. These values are estimated from Fig. A3

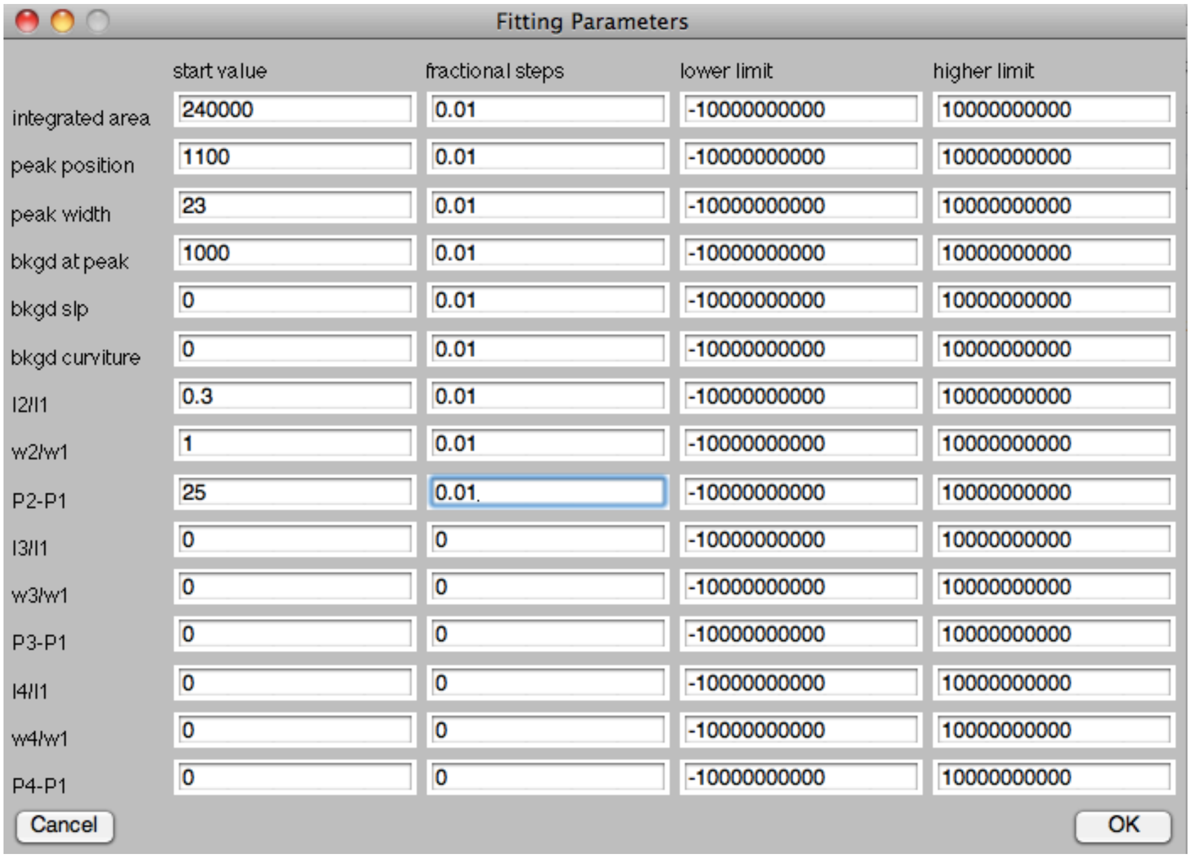

	start value	fractional steps	lower limit	higher limit
integrated area	240000	0.01	-10000000000	10000000000
peak position	1100	0.01	-10000000000	10000000000
peak width	23	0.01	-10000000000	10000000000
bkgd at peak	1000	0.01	-10000000000	10000000000
bkgd slp	0	0.01	-10000000000	10000000000
bkgd curviture	0	0.01	-10000000000	10000000000
I2/I1	0.3	0.01	-10000000000	10000000000
w2/w1	1	0.01	-10000000000	10000000000
P2-P1	25	0.01	-10000000000	10000000000
I3/I1	0	0	-10000000000	10000000000
w3/w1	0	0	-10000000000	10000000000
P3-P1	0	0	-10000000000	10000000000
I4/I1	0	0	-10000000000	10000000000
w4/w1	0	0	-10000000000	10000000000
P4-P1	0	0	-10000000000	10000000000

Fig. A6: The GUI input panel for initial Gaussian parameters, which are estimated from Fig. A3

To normalize data and obtain lifetime fraction, data manipulation is necessary. In the GUI option panel in Fig. A4, after choosing “ma”, a data manipulation GUI option panel pops out as shown in Fig. A7. A proper operation can then be chosen for data processing.

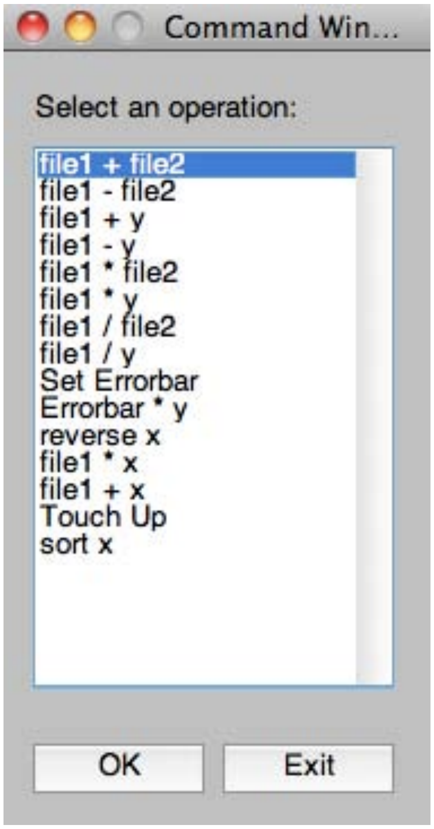

Fig. A7: The command window for data manipulation after choosing “ma” in Fig. A4

So far we have roughly showed how to do a step-by-step XSW data processing by sugomat. In the following, a script is provided for a quick data processing. The typical script is shown in Fig. A8. In this script, “id” means idle. It is a combination of the step-by-step procedures mentioned above for data extraction, manipulation and normalization. To execute this script, type “sugomat(1)” and choose this script file.

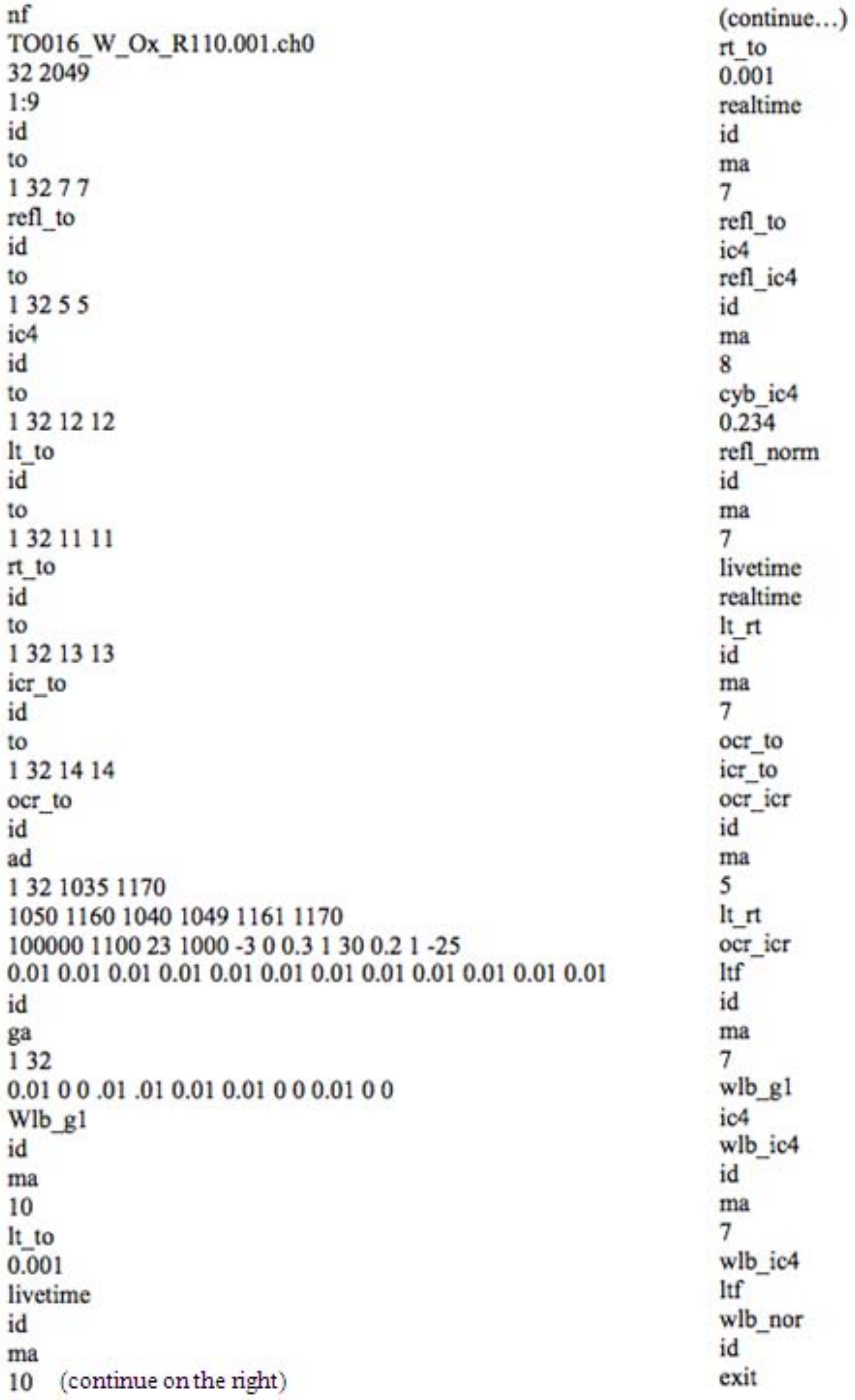

```
nf
TO016_W_Ox_R110.001.ch0
32 2049
1:9
id
to
1 32 7 7
refl_to
id
to
1 32 5 5
ic4
id
to
1 32 12 12
lt_to
id
to
1 32 11 11
rt_to
id
to
1 32 13 13
icr_to
id
to
1 32 14 14
ocr_to
id
ad
1 32 1035 1170
1050 1160 1040 1049 1161 1170
100000 1100 23 1000 -3 0 0.3 1 30 0.2 1 -25
0.01 0.01 0.01 0.01 0.01 0.01 0.01 0.01 0.01 0.01 0.01 0.01
id
ga
1 32
0.01 0 0 .01 .01 0.01 0.01 0 0 0.01 0 0
Wlb_g1
id
ma
10
lt_to
0.001
livetime
id
ma
10    (continue on the right)
```

```
(continue...)
rt_to
0.001
realtime
id
ma
7
refl_to
ic4
refl_ic4
id
ma
8
cyb_ic4
0.234
refl_norm
id
ma
7
livetime
realtime
lt_rt
id
ma
7
ocr_to
icr_to
ocr_icr
id
ma
5
lt_rt
ocr_icr
ltf
id
ma
7
wlb_g1
ic4
wlb_ic4
id
ma
7
wlb_ic4
ltf
wlb_nor
id
exit
```

Fig. A8: A Script for the quick XSW data processing. The whole script reads from the left column to the right column.

Appendix B: Global Fit of XSW Data Using Igor Pro

B.1 Global Fit Procedures

The important information obtained from XSW experiments is the atomic height and the distribution of the surface species. The atomic density map created from the summation of Fourier amplitudes and phases gives the direct view of the distribution of the measured element. The height of the element can also be obtained from the numerical analysis of the atomic density maps. Due to the lateral symmetry used in this summation, there is no deviation of the element from the high symmetry sites laterally. This is a so-called model-independent method. To get more accurate height and atomic distribution of the element at each adsorption site, a model-dependent analysis is necessary. This model is typically based on the relationship between the Fourier components and the element's distribution, as described in Eq. (B1)

$$f_H \exp\left(2\pi i P_H\right) = \sum_i c_i \exp\left(2\pi i \mathbf{H}\cdot\mathbf{r}_i\right), \qquad \text{(B1)}$$

where c_i is the occupation fraction at the i^{th} adsorption site and $\mathbf{r}_i$ refers to the position of the element at the i^{th} adsorption site. In order to determined the best-fit structural parameters and refine the model, a systematic method is needed to fit this model to all H=(hkl) XSW results. Since each set of XSW parameters (or Fourier components) is an independent measurement of the atomic-scale structure, it would be desirable if we could fit all the XSW measurements simultaneously to realize the benefit of a larger number of data points. This global analysis can be achieved by using the "Global Fit" procedure file in Igor Pro, which is a popular graphing and data analysis software package.

Anathony Escuadro's PhD thesis[35] provides a global fit procedure using Igor Pro version 4 and lower. As the development of the Igor Pro software, the Global Fit routine has changed significantly and some new functions have been added. Here we provide a global fit procedure based on Igor Pro version 6.

The Igor Pro documentation shows that the Global Fit procedure provides all the necessary functions to combined the individual data sets into a single data set in order to fit the multiple experiments as a single one. It also allows the fitting parameters to be defined as either global or local parameters. Instead of simply defined as global in old version of Igor Pro, the new version allows to defined "linked" parameters and "unlinked" parameters, which gives much more freedom to do the global fitting. The linked parameters are those that will be fit with the same value for all or some data sets, while unlinked parameters can have unique values for each individual data set. In our XSW measurement, it is assumed that each *hkl* measurement is probing the same surface/interface (i.e. the surface/interface structure is not changing significantly over the course of several XSW measurements). Therefore, in the general model described in Eq. (B1), the structural parameters, namely c_i and $\mathbf{r}i$, are considered as linked global parameters. The *hkl* diffraction plane indices and Fourier components are considered as the unlinked local parameters.

Besides using the build-in mathematical functions to fit the experimental data, Igor Pro allows users to define their own functions, enabling us to encapsulate our surface model into a form that Igor Pro and the Global Fit procedures can handle. Taking one set of Fourier component of the oxidized surface of 1/3 ML $WO_X/\alpha\text{-}Fe_2O_3(0001)$ as an example, we will go through a step-by-step procedure to show how to use the new version of Global Fit in Igor Pro 6.12 for XSW data analysis.

Table B1: A set of *in situ* XSW experimental and best-fit data of the Ox2 surface of the 1/3 ML W / α-Fe_2O_3 (0001) interface. Model independent parameters, f_H and P_H, are the measured H = *hkil* Fourier amplitudes and phases for the W distribution. These can be compared to the calculated f_H^C and P_H^C values determined from the best-fit of the model that is described by Eq. 5.2.

hkil	*0006*				$10\underline{1}4$				$01\underline{1}2$			
	f_H	f_H^C	P_H	P_H^C	f_H	f_H^C	P_H	P_H^C	f_H	f_H^C	P_H	P_H^C
Ox2	0.47(1)	0.59	0.11(1)	0.16	0.63(3)	0.62	0.44(1)	0.44	0.55(2)	0.65	-0.22(1)	-0.28

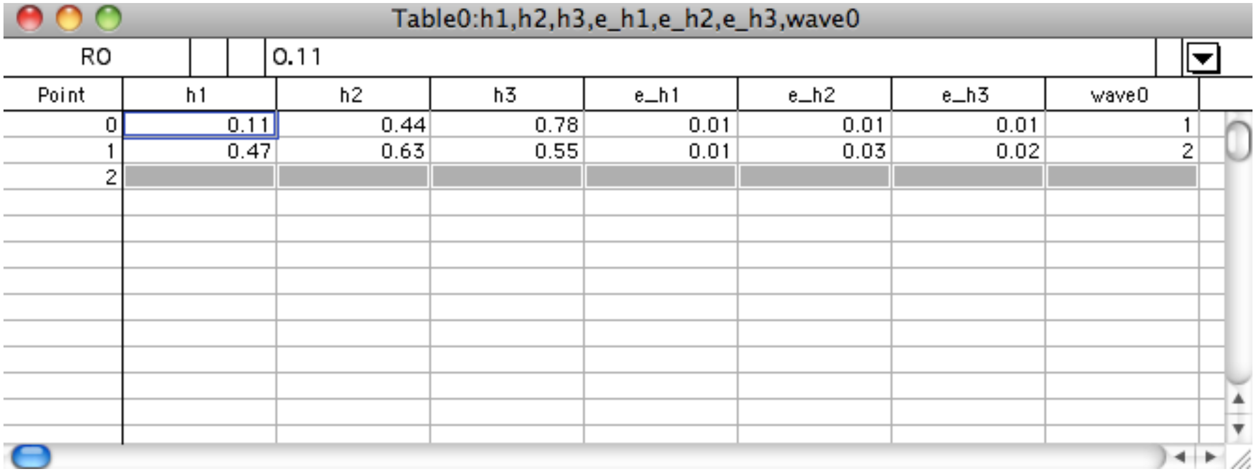

Table0:h1,h2,h3,e_h1,e_h2,e_h3,wave0

RO 0.11

Point	h1	h2	h3	e_h1	e_h2	e_h3	wave0
0	0.11	0.44	0.78	0.01	0.01	0.01	1
1	0.47	0.63	0.55	0.01	0.03	0.02	2
2							

Fig. B1: The data table for all Fourier components. The first row contains the P_H values and the second row contains the f_H values. e_hi is the associated error for each Fourier component.

The Fourier components as the data sets are input first in the table in Igor Pro, as shown in Fig. B1. There are six waves used in this global fit. The first row contains the coherent position values and their associated errors. The second row contains the coherent fraction values and their associated errors. Since each XSW dataset has two independent results (the coherent fraction and coherent position), we can use a linear fit to analyze the XSW results. The last column, “wave0”, is used in this linear fit function as the variables. In this case, the slopes and intercepts of the individual lines that are fit to the XSW data are calculated as a linear combination of the two XSW parameters. The model used for this global fit is shown in Eq. (5.1), which contains four global fit parameters to describe the W atomic distribution, namely, occupation fractions at the two adsorption sites on the α-Fe_2O_3(0001) surface, c_A and c_B, and the W vertical height to the oxygen plane at the two sites, z_A and z_B. These four parameters are defined as w[3], w[4], w[5] and w[6] in the global fit function, “xswParaFit”, as shown in Appendix B2. The rest three of the total seven fit parameters, w[0], w[1], and w[2], are used to describe the diffraction plane indices.

To use the Global Analysis control panel, select “Global Fit” from the Analysis section. After adding h1, h2 and h3 into Y Waves and wave0 into X Waves, select “xswParaFit” as the function for each wave from the “Choose Fit Function” pull-down menu, which displays the available fitting functions, including the built-in functions and any user-defined functions. Note that in the Data Sets portion of the control panel, it allows any number of data sets to be entered for global analysis. The data sets can be either entered via the “Add Data Sets” pull-down menu (or “Add/Remove Waves…” pull-down menu) in the Data Sets section or from an existing graph of the data to be analyzed. When using the pull-down menu, the user should specify both the Y Waves and the X Waves, if the appropriate X wave exits. If there is no specific X wave that corresponds with the Y Wave to be fit, the “_calculated_” wave should be selected as the matching X Wave. In our case, the individual XSW results are defined as a series of Igor Pro waves, as shown in Fig. B1. The whole Global Analysis panel is shown in Fig. B2. The global parameters in this model are marked with different colors in the control panel.

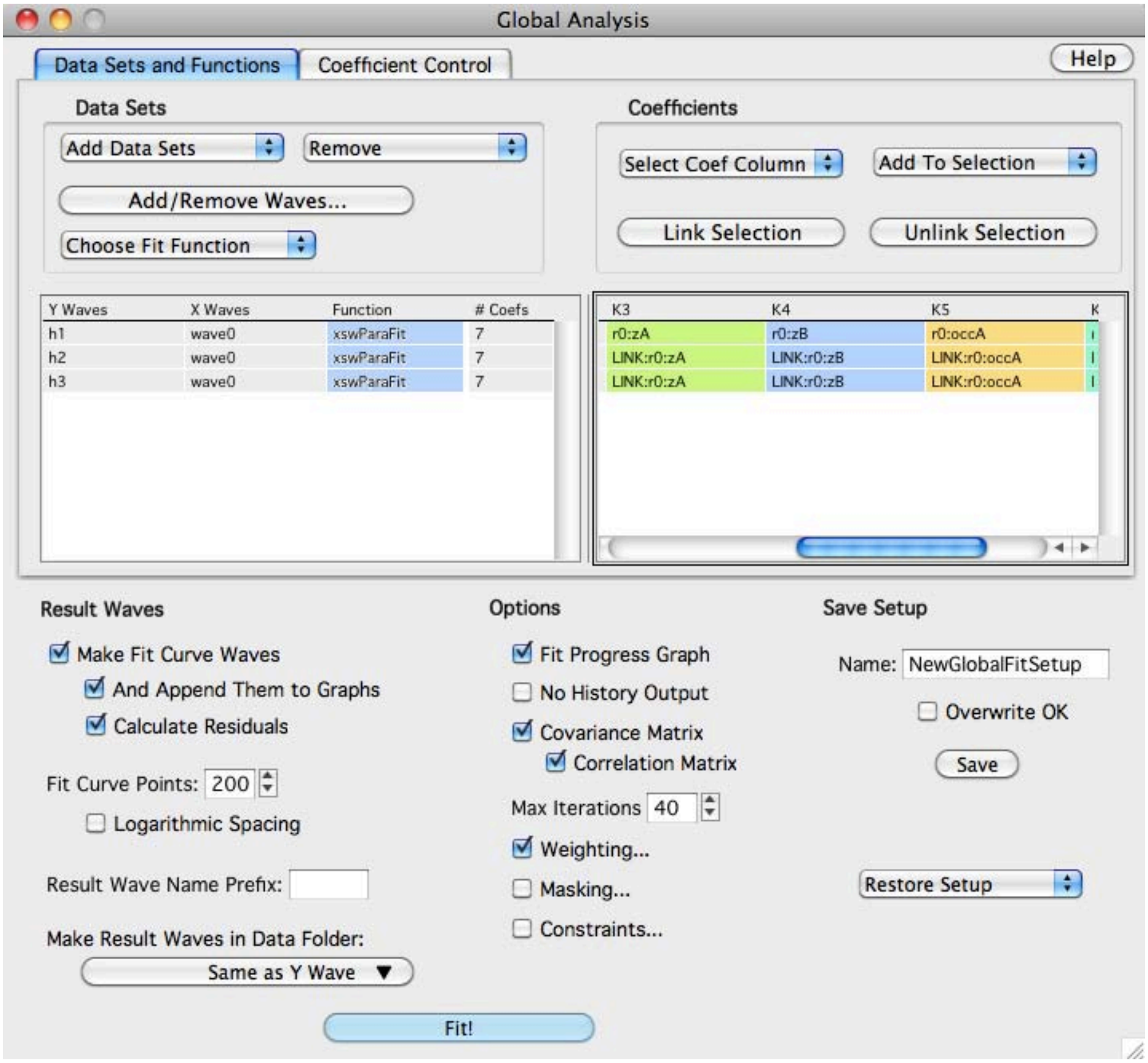

Y Waves	X Waves	Function	# Coefs
h1	wave0	xswParaFit	7
h2	wave0	xswParaFit	7
h3	wave0	xswParaFit	7

K3	K4	K5
r0:zA	r0:zB	r0:occA
LINK:r0:zA	LINK:r0:zB	LINK:r0:occA
LINK:r0:zA	LINK:r0:zB	LINK:r0:occA

☑ Make Fit Curve Waves
☑ And Append Them to Graphs
☑ Calculate Residuals
Fit Curve Points: 200
☐ Logarithmic Spacing
Result Wave Name Prefix:
Make Result Waves in Data Folder: Same as Y Wave

☑ Fit Progress Graph
☐ No History Output
☑ Covariance Matrix
☑ Correlation Matrix
Max Iterations 40
☑ Weighting...
☐ Masking...
☐ Constraints...

Name: NewGlobalFitSetup
☐ Overwrite OK

Fig. B2: The Global Analysis control panel of the Global Fit Igor Pro procedure. The fitting function, data sets and global parameters are specified in this panel.

The final step in preparing the fit is to enter the initial guesses for the various fit parameters. This is done in the “Coefficient Control” subpanel of the Global Analysis control panel. This subpanel contains a list of all the parameters defined in the fitting function and allows the user to specify an initial guess for the χ^2 fit. As shown in Fig. B3, these initial guesses are either held as constant during the analysis or given a start value. These constants are diffraction plane indices, and those variables are the global parameters that will be determined from the fit. Epsilon values in this panel are used to calculate partial derivatives with respect to the fit parameters, which in turn are used to determine the direction in which the χ^2 fitting routine proceeds.

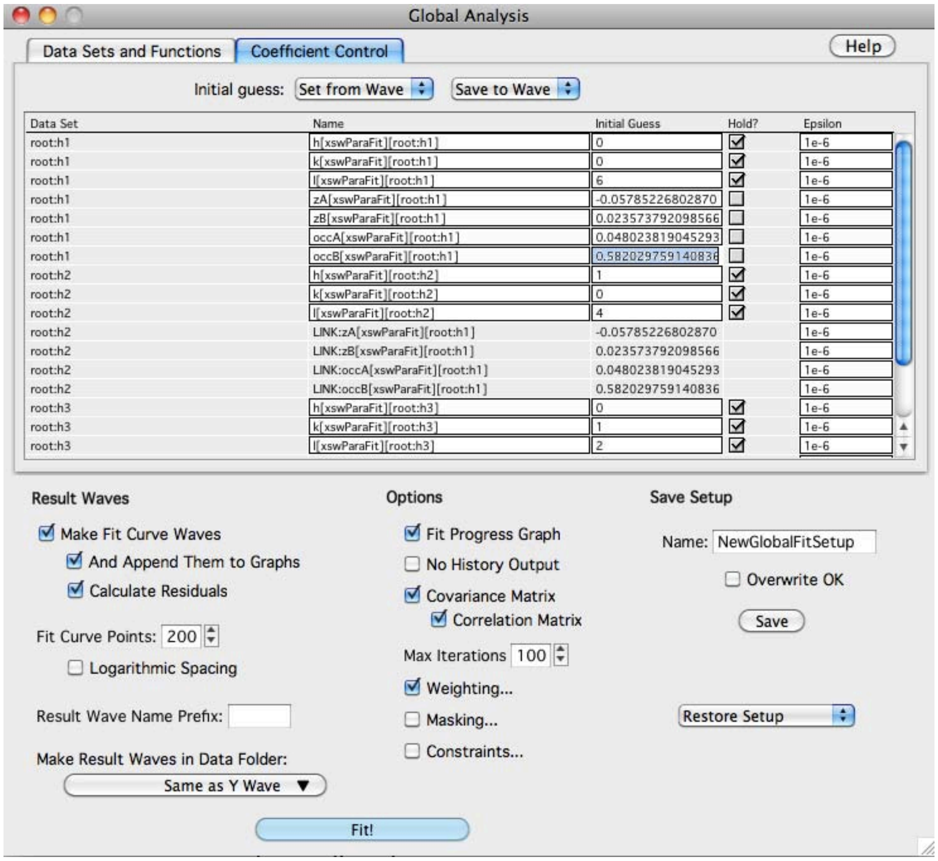

Initial guess: Set from Wave | Save to Wave

Data Set	Name	Initial Guess	Hold?	Epsilon
root:h1	h[xswParaFit][root:h1]	0	☑	1e-6
root:h1	k[xswParaFit][root:h1]	0	☑	1e-6
root:h1	l[xswParaFit][root:h1]	6	☑	1e-6
root:h1	zA[xswParaFit][root:h1]	-0.05785226802870	☐	1e-6
root:h1	zB[xswParaFit][root:h1]	0.023573792098566	☐	1e-6
root:h1	occA[xswParaFit][root:h1]	0.048023819045293	☐	1e-6
root:h1	occB[xswParaFit][root:h1]	0.58202975914083	☐	1e-6
root:h2	h[xswParaFit][root:h2]	1	☑	1e-6
root:h2	k[xswParaFit][root:h2]	0	☑	1e-6
root:h2	l[xswParaFit][root:h2]	4	☑	1e-6
root:h2	LINK:zA[xswParaFit][root:h1]	-0.05785226802870		1e-6
root:h2	LINK:zB[xswParaFit][root:h1]	0.023573792098566		1e-6
root:h2	LINK:occA[xswParaFit][root:h1]	0.048023819045293		1e-6
root:h2	LINK:occB[xswParaFit][root:h1]	0.582029759140836		1e-6
root:h3	h[xswParaFit][root:h3]	0	☑	1e-6
root:h3	k[xswParaFit][root:h3]	1	☑	1e-6
root:h3	l[xswParaFit][root:h3]	2	☑	1e-6

Result Waves

☑ Make Fit Curve Waves
  ☑ And Append Them to Graphs
  ☑ Calculate Residuals

Fit Curve Points: 200
  ☐ Logarithmic Spacing

Result Wave Name Prefix:

Make Result Waves in Data Folder: Same as Y Wave

Options

☑ Fit Progress Graph
☐ No History Output
☑ Covariance Matrix
  ☑ Correlation Matrix

Max Iterations 100

☑ Weighting...
☐ Masking...
☐ Constraints...

Save Setup

Name: NewGlobalFitSetup
☐ Overwrite OK

Fig. B3: The Coefficient Control panel lists all initial guesses for this global fit. The diffraction plane indices are given as constants and the four global parameters are given proper initial values for the fit.

Some optional fit attributes can be set at the bottom of the control panel. The most useful options are the "Weighting…" and the "Constraints…" parameters. These allow for the fine-tuning of the χ^2 fit routine by letting the user force some or all of the fit coefficients to remain within set limits, or select a separate set of error waves that will be used to weight the XSW data sets. These errors in our case are input as e_h1, e_h2 and e_h3, as shown in Fig. B1.

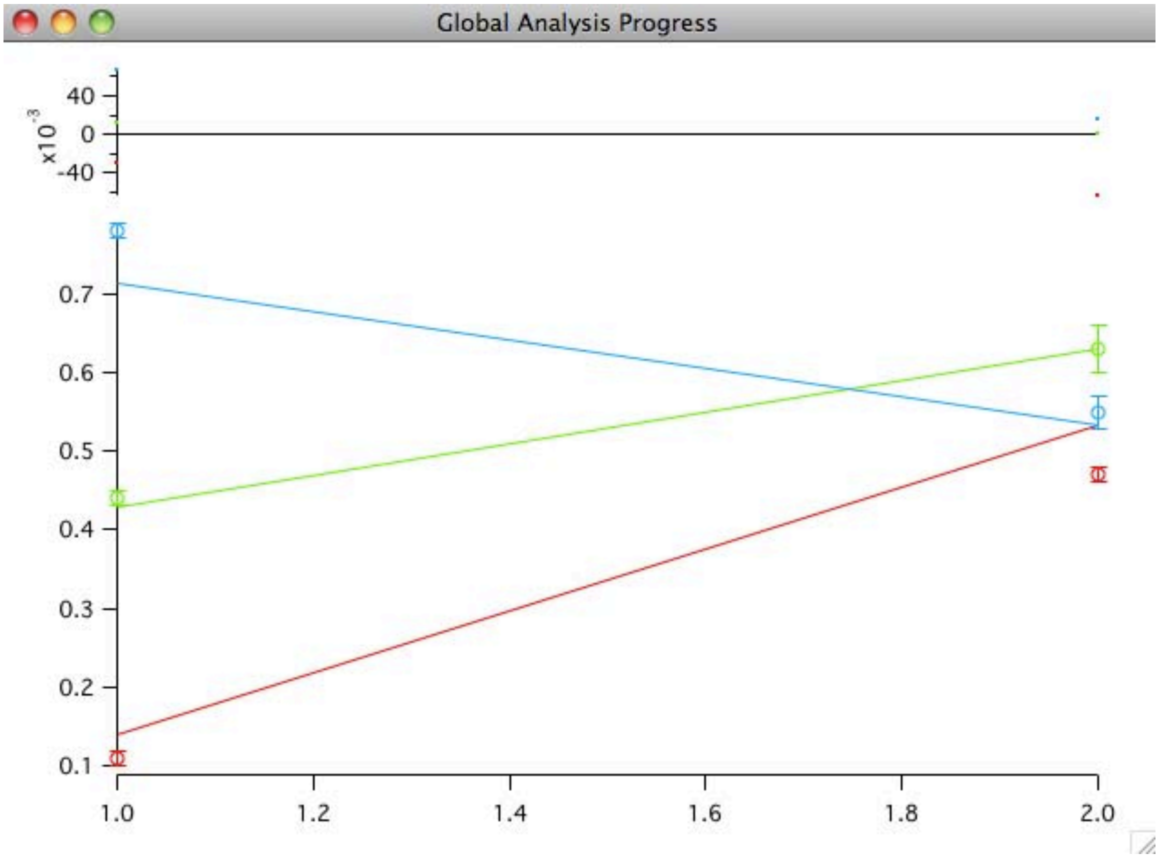

Fig. B4: Graph generated by Igor Pro that represents the global fit of the specified structural model to the XSW data. The upper part of this figure shows the calculated residual displayer after choosing "Calculate Residuals" in the Global Analysis control panel. The markers are the experimental values for the coherent fraction and positions, and the uncertainties in these values are shown as error bars. The colored lines connect the best-fit values for the XSW parameters.

With all these preparation above, the fit process can begin using the “Fit!” button on the Global Analysis panel. When the fitting routine is finished, information about the fit results is displayed in the command window, such as the best-fit values of the fit coefficients, the χ^2 value of the completed fit, and the calculated standard deviation of the fit parameters. The fit results can also be displayed graphically after selecting “Fig Progress Graph” to allow for a direct comparison between the experimental data and the best-fit parameters, as shown in Fig. B4.

B.2 Igor Pro Function for XSW Global Fit

The custom fitting function used with the Global Fit procedure in Igor Pro 6.12 to fit the multiple sets of XSW data is list below.

```
Function xswParaFit(w,xx) : FitFunc

Wave w
Variable xx
Variable real_ah, imag_ah, coh_f, coh_p, occA, occB
Variable /C Fm_rect, Fm_pol

	//CurveFitDialog/ These comments were created by the Curve Fitting dialog. Altering
them will
	//CurveFitDialog/ make the function less convenient to work with in the Curve Fitting
dialog.
	//CurveFitDialog/ Equation:
	//CurveFitDialog/ f(xx) = a+b*xx
	//CurveFitDialog/ End of Equation
	//CurveFitDialog/ Independent Variables 1
	//CurveFitDialog/ xx
	//CurveFitDialog/ Coefficients 7
	//CurveFitDialog/ w[0] = h
	//CurveFitDialog/ w[1] = k
```

```
        //CurveFitDialog/ w[2] = l
        //CurveFitDialog/ w[3] = zA
        //CurveFitDialog/ w[4] = zB
        //CurveFitDialog/ w[5] = occA
        //CurveFitDialog/ w[6] = occB

        occA=w[5]
        occB=w[6]

real_ah =
occA*cos(2*Pi*(2*w[0]+w[1]+3*w[2]*w[3])/3)+occB*cos(2*Pi*(w[0]+2*w[1]+3*w[2]*w[4])/3)
imag_ah =
occA*sin(2*Pi*(2*w[0]+w[1]+3*w[2]*w[3])/3)+occB*sin(2*Pi*(w[0]+2*w[1]+3*w[2]*w[4])/3)
Fm_rect = cmplx(real_ah,imag_ah)
Fm_pol = r2polar(Fm_rect)
coh_f = real(Fm_pol)
coh_p = imag(Fm_pol)/(2*Pi)
if (coh_p < 0.0)
        coh_p +=1
endif
return (2*coh_p-coh_f)+(coh_f-coh_p)*xx
End
```